THEORETICAL INVESTIGATIONS INTO SINGLE-ATOM CATALYSTS ON CERIUM DIOXIDE: DEPOSITION AND ACTIVATION

Nathan Daelman

UNIVERSITAT ROVIRA i VIRGILI

Theoretical investigations into single-atom catalysts on cerium dioxide: deposition and activation

Nathan Daelman

Eye to eye with platinum Cerberus – N. Daelman

DOCTORAL THESIS
2019

UNIVERSITAT ROVIRA I VIRGILI
THEORETICAL INVESTIGATIONS INTO SINGLE-ATOM CATALYSTS ON CERIUM DIOXIDE: DEPOSITION AND ACTIVATION.
Nathan Daelman

Nathan Daelman

Theoretical investigations into single-atom catalysts on cerium dioxide: deposition and activation

DOCTORAL THESIS

Supervised by
Prof. Núria López Alonso

Institute of Chemical Research of Catalonia
(ICIQ)
and Rovira i Virgili University (URV)

UNIVERSITAT ROVIRA i VIRGILI

Tarragona
2019

UNIVERSITAT ROVIRA I VIRGILI
THEORETICAL INVESTIGATIONS INTO SINGLE-ATOM CATALYSTS ON CERIUM DIOXIDE: DEPOSITION AND ACTIVATION.
Nathan Daelman

ICIQ
Institut Català d'Investigació Química
Avinguda Països Catalans 16
43007 Tarragona, Spain

UNIVERSITAT ROVIRA i VIRGILI
Carrer de l'Escorxador
43003 Tarragona, Spain

I STATE that the present study, entitled "**Theoretical investigations into single-atom catalysts on cerium dioxide: deposition and activation**", presented by Nathan Daelman for the award of the degree of Doctor, has been carried out under my supervision at the Institute of Chemical Research of Catalonia.

Tarragona, September the 3rd, 2019

Prof. Núria López Alonso

UNIVERSITAT ROVIRA I VIRGILI
THEORETICAL INVESTIGATIONS INTO SINGLE-ATOM CATALYSTS ON CERIUM DIOXIDE: DEPOSITION AND ACTIVATION.
Nathan Daelman

Sponsors

The work presented in this thesis was made possible by the economic support and collaboration of the ICIQ Foundation and the Spanish Ministerio de Economía y Competividad (MINECO), project number CTQ2015-68770-R. In addition, we thank BSC-RES for providing computational resources.

Barcelona Institute of
Science and Technology

Barcelona
Supercomputing
Center
Centro Nacional de Supercomputación

UNIVERSITAT ROVIRA I VIRGILI
THEORETICAL INVESTIGATIONS INTO SINGLE-ATOM CATALYSTS ON CERIUM DIOXIDE: DEPOSITION AND ACTIVATION.
Nathan Daelman

Acknowledgements

I would like to start off by thanking my supervisor, Prof. Núria López. Not only for her guidance and advice throughout my doctoral career and in the writing of this thesis, but also because it was predominantly her vision that pushed our breakthrough in the remarkable oxidation state dynamics of single-atom platinum. I myself would surely never have spotted its profound impact on the Heterogeneous Catalysis. I think the Nature Materials paper that we put out, is a testament to this vision. This immediately leads me to our co-author, Dr. Marçal Capdevila-Cortada. Almost as a mentor, did he teach me the fundamentals of Solid State computation and ceria catalysis. Although this learning period was cut short, as Marçal went on to make a marvelous career for himself, I was still able to function by myself thanks to him. Obviously, there is a whole team making the lab function, way too numerous for me to call each one out by name. Let me just thank all those who with whom I got to share interesting discussions (you know who you are ;)). This also includes the people who act as support in the background, but keep the whole place keeps running: thank you Núria Vendrell for helping me out with the treacherous path that is bureaucracy, and merci Martin for your patience in tweaking the cluster to my (by times outrages) needs. Also special mention to Edvin and Moises for the art direction of the thesis cover.

Secondly, I would like to acknowledge my collaborators. They are already mentioned several times in the course of this work, but that still does not do them justice. I am overjoyed that so many side-projects are sprouting from the original paper and am more than curious to see where they will lead to. Obviously, a single person cannot cover this much ground. So many of the advances here I owe to other brilliant minds. In chronological order, I extend my gratitude to Dr. Tobias Schäfer who's work has given me a better insight in the shortcomings of HF and DFT and how to correct for them via post-processing. He has also been extremely diligent an detailed in running the advanced MP2 methods for us on VASP6. Then there is Prof. Jörg Behler, and in fact his whole group, who warmly welcomed me in Göttingen. My thanks for the great times to Jan, Sebastian, Dilshana, Xaiza, Anton, and both Martins. And a shout-out to Martin Paleico as well as Rainer

for always being ready to help me out with any questions. I thought I had a basic grasp of neural networks before my stay, but I having had the opportunity to meet the machine learning community in beautiful workshop hosted by Jörg was eye-opening. Their presentations gave me a newfound appreciation of the effort that goes into creating these forcefields. Having seen the richness in techniques and the versatility of problems for which they can be used, I am convinced that this field will grow on to become a crucial part of Computational Chemistry. During my stay I also had the pleasure of getting to work with Minttu Kauppinen on the microkinetics. Never have I met a person who manages to pull out the best in me through intelligent and constructive questioning. The only shame is that we have not yet been able to meet in person, though maybe one day in the future.

Apart from the Science, one also needs lots of emotional support in times of writing. Luckily for me I could always fall back on my loving girlfriend Anna, and my two great friends (and co-workers) Mauro and Bob (Chuong Nguyen). Unfortunately, I could not spend as much time with all of them as I would have wished to, having to cancel far too often and far too many invitations. Nonetheless, they along with Núria kept looking after my physical and mental health. Let me also express my gratitude towards Bob for proofreading my Methodology section and giving me great feedback. Support also comes from afar when you work abroad, in this case from my friends and family at home. Here too we tend to have fallen somewhat out of contact, but I know that in times when it truly matters I can always fall back on you. I am sure that without my dad's hard labor as sole supporter of our five-head family I never would have it even this far. He managed to put me and my siblings through higher education. I cannot express how truly happy I am for my mom to have made this far despite her condition that she can (proverbially) see me graduate as a doctor. I mentioned before how Minttu challenges me in a constructive, but surely the same goes for my brother with whom I can always bounce off my ideas and vice versa. Lastly for my sister, who is just starting her adult life, I wish her much strength and prosperity.

Concerning dedication, I guess that in a way this thesis is dedicated to all of the people mentioned above. Then again, from where I am standing, this is more of a first step into an unexplored chemical territory rather than the end of a 'grand' opus. Therefore, it feels odd to call out dedications for something that is effectively a beginning. Rather, I hope that all of these people may be there with me as I progress down this road.

Contents

UNIVERSITAT ROVIRA I VIRGILI
THEORETICAL INVESTIGATIONS INTO SINGLE-ATOM CATALYSTS ON CERIUM DIOXIDE: DEPOSITION AND ACTIVATION.
Nathan Daelman

Abstract

This thesis centers around single-atom catalysts on reducible metaloxides, their stability and reactivity. Single atoms have namely shown to posses remarkable reactivity and are much more resource efficient. I will be focusing on the case of single-atom platinum, for which the quadruple coordination on (100) ceria is thermally stable with respect to the bulk phase, corresponds to the resting state. This coordination can be synthesized via vapor deposition or trapping of metal adatoms under lattice dynamics. Application of reductive pulses alters the coordination to become chemically more active. The nature or the reductant is of little importance, as both carbon monoxide and dihydrogen are work. The activated form has several low-lying minima corresponding to different oxidation states. Ab initio Molecular Dynamics demonstrated that at elevated temperatures (onset at around 450 K) the oxidation state changes, meaning that it is dynamic in nature. The benchmark backs this claim. The adatom retains the neutral and singly positive states for the majority of the time. The latter is quite exotic in organometallic compounds. This particular phenomenon empowers the high reactivity in oxidation reactions. A reaction path is constructed for each individual oxidation state and coupled were appropriate. The resistivity of the oxidation state dynamics was verified via additional Molecular Dynamics simulations. It is preserved under carbon monoxide adsorption, but breaks down after additional adsorbates and all oxidation states converge. Microkinetics show that peak performance is achieved at 450 K ($\sim$ 150°C). At higher temperatures the conversion is still complete but slows down. The catalyst is thus a prime candidate in the US Department of Energy 150°C challenge.

A mechanism was deduced from the local Density of States and a Born-Haber cycle. Volume expansion around a cerium ion predisposes its empty 4f states to electron donation. The cost for electron excitation from the adatom to the ion is off-set by the Coulomb interaction. In other words, the phonons assist in the polaron hopping by lowering the barrier. The same mechanism was studied for other elements from group 10. I verified that indeed nickel also has a dynamic oxidation state. In this case it is more shifted towards II+ mixed with some

I+. Neutral single-atom nickel was not observed in any Molecular Dynamics simulation. The reason for this shift stems from size effects. With palladium on the other hand an energy penalty for reorganizing its electronic structure breaks the oxidation state dynamics. Single-atom palladium is thermodynamically feasible, but only in a neutral state. A proof of concept for Phonon-Assisted Metal-Support Interaction along with the reaction paths were published in Nature Materials.

A further, grander benchmark has been initiated to confirm the stability if the Hubbard term in density functional theorem. Here, second order Møller-Plesset perturbation theory (MP2) is used to study two aspects of the bulk phase transition: geometry and thermodynamics. In the former the various levels of exact exchange and correlation are compared. The takeaway message is that balancing out incomplete expression is more important than obtaining a full contribution from either. More specifically, in cerium dioxide MP2 underestimates the experimental volume by 1% but is in perfect agreement with the experimental bulk modulus. Overall, HSE03 comes out on top for the geometries. In the case of dicerium trioxide (Ce_2O_3), exact exchange makes the volume expand. When offset with correlation as in HSE03, RPA, and MP2 the performance is equal. The reduction reaction is endothermic in all methods.

Lastly, I present a startup project for construction a ceria forcefield. This should allow for the model upscaling and thermodynamic integration over Molecular Dynamics simulations. In principle there is a large enough dataset for bulk and slabs to ensure a high-quality fit without over-fitting. The scope in this work is restricted to bulk ceria, which acts more as a test case. Several failed models are presented, their issues examined. These stem mostly from initial data conversion issues along with unphysical oxygen diffusion. From there on the first-ever working forcefield is generated and tested. This shows that the proof-of-concept indeed works. Finally, a strategy is presented on how to proceed with the network's expansion based on the current amount of slab structures. The possible applications of a fully-functioning Neural Network Potential are also brielfy discussed.

In summary, this thesis presents the basics of Phonon-Assisted Metal-Support Interaction for single-atom catalysts and their reactivity. It is mindful of the potential pitfalls of the state-of-the-art methods and tests novel approaches to improve accuracy and scale.

Chapter 1

Introduction

Climate change is no longer some far-off problem; it is happening here, it is happening now.

Barack Obama

1.1 DOE 150° Challenge

The field of Catalysis has and will always continue to play a key role in modernizing production chains to suit the societal needs for green, environment-friendly processes. The latest report from the Intergovernmental Panel on Climate Change (IPCC) titled the *IPCC's Fifth Assessment Report (AR5)* shows that this need is stronger than ever. Globally, the mean land and ocean temperatures have risen 0.85°C over the period from 1880 to 2012. The current growth is projected at 0.2°C per decade. Figure 1.1 contains a more detailed prognosis with different future scenarios. The descriptor that most determines the course is greenhouse gas emissions under the form of carbon dioxide. Panels a and b show how the next decade will be decisive for the entire century. Even under the most optimistic conditions, we will surpass the 1.5°C threshold.

In the meantime, classic fuel engines running on diesel and petrol still occupy 92.6% of the whole market. Even with stagnating sales numbers, last year still saw 16, 677, 937 new vehicle registrations in the United States of America (USA) and 15, 158, 874 in the European Union (EU).[1] Motorized land vehicles thus make up 82% of all petroleum consumption in the land transportation sector and 60% of the total in the USA.[2] As such, governments are forced to take action and impose stronger emission standards. Three greenhouse gases in particular are targeted,

namely carbon dioxide (CO_2), hydrocarbons such as methane (CH_4), and nitrous oxide (N_2O). The standard three-way car exhaust catalysts already breaks down the latter two and carbon monoxide (CO).[3] The EU currently enforces Euro6[4] and the USA Tier3. The former focuses more on CO and CO_2, while the latter on CH_4 and N_2O. With the rising global awareness of climate change, the US Department of Energy (DOE) has put out its vision for the automotive industry by 2020:[2] *reduce the activation temperatures (measured as* 90% *conversion) of the car exhaust catalysts from* 200° *to* 150° *C.* This is in anticipation of more fuel efficient and less consuming engines that will operate at lower temperatures. In absence of an effective recuperation route for CO_2, reducing fuel consumption and pollutant emission is the best strategy. It also guarantees less pollution at the startup, when the engine temperature still is low. Achieving their goal requires innovation from the manufacturing industry, chemical engineers, as well as material scientists to come up with novel catalysts. It is therefore called the DOE 150°C challenge.

In this work I examine a variation on the currently popular Pt and Pd catalysts which are common in diesel car catalysts.[3] The subject is quite topical, as it hinges on the recent advances in the shape and size control of metal nanoparticles deposited on metal oxides. I present the thesis that *single-atom Pt bears a variational oxidation state, giving it superior catalytic properties*. The majority of the same hypothesis has been recently published in Nature Materials.[5] The reactivity is tested on CO oxidation in a model environment for car exhaust catalysts.

The importance of CO oxidation Although carbon monoxide itself is not a greenhouse gas,[6] it obviously is a precursor to it and can cause health problems.[7] Symptoms include foremost restricted cardiovascular circulation, but can also branch out to the respiratory system, the central nervous system, and reproduction system as well as prenatal development. In larger concentrations, normally only found in poorly vented enclosures, it can even lead to ischemia (tissue damage due to a lack of oxygen) or death. Indeed, carbon monoxide is commonly known as a silent killer with its lack of color or odor. It binds to hemoglobin (Hb) to form COHb, which prevents further dioxygen (O_2) uptake in the blood. Indirectly, CO is also a precursor to ozone, which again causes respiration problems. Considering that transportation is the main source of ambient CO, curbing car emissions is the most efficient tactic to protect the general populations health, especially in high-density demographics.

In experiments, carbon monoxide is a popular molecule to probe the catalyst's

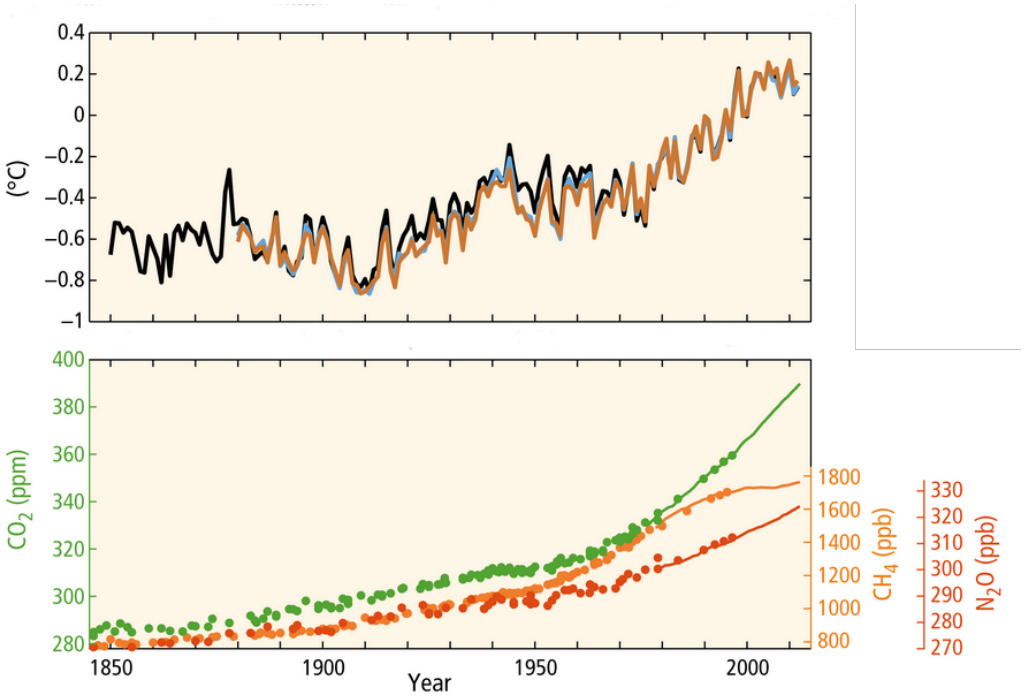

Figure 1.1: Top panel: Overview of the global mean temperature form 1850 till 2012. The color codes indicate different data sources. **Bottom panel:** Global emissions of greenhouse gases over the same time period as above. Note how the attention lies on three major compounds: CO_2, CH_4, and N_2O. Only CH_4 seems be slightly stagnating. Based of AR5.

adsorption sites and reactivity. Its compact size and simple geometry also prevents steric effects from interfering with the adsorption. Experimentalists use it to infer the metal's oxidation state via infra-red spectroscopy.[8] The lights-off turn-over frequencies of CO oxidations are also a common reactivity benchmark.[9] In many metal systems, it acts as a Lewis acid after adsorption. As such it is sensitive to reduction of the metal. In synthesis it can control nanoparticle sintering or wetting.[10] This ties in to the aforementioned size control for our catalyst.

1.2 Cerium oxide

Cerium is the most abundant of the rare-earth elements.[11] Obeying the law of demand, it is thus quite cheap and makes for an economically attractive raw material. Its oxides (ceria) partake in catalysis both directly as indirectly as a support for other active materials. As such, ceria can be found in traditional

three-way diesel exhaust catalysts. The three-way nomenclature refers to the simultaneous conversion of CO to CO_2, NO_x to N_2, and hydrocarbons to water and CO_2.[3] Ceria forms part of the catalyst in each reaction.

Ceria possesses three intertwined properties that explain most of its catalytic prowess:[12]

1. Low oxygen vacancy formation energy leads to readily interchange with the atmosphere. In reactions too, ceria can be a source of oxygen. At the same time, the spurious charge of the lattice oxygen remains in the matrix and settles onto the cerium ions. Although materials such as MoO_x sustain three different OSs of their metal,[13] cerium dioxide can only contain Ce^{4+} and its reduced state, Ce^{3+}. These electrons too can participate in reactions. The changing local behavior between Lewis acid and base earns cerium dioxide its place as a key redox catalyst in Heterogeneous Catalysis.

2. Facile migration of these oxygen vacancies (and their polarons).

3. An easy (local) conversion between both of its oxide structures. The change is facilitated by the alignment of the aforementioned vacancy sites.

The most stable version is the fluorite-type structure cerium dioxide (CeO_2)[14] version is called dicerium trioxide (Ce_2O_3). The former sees Ce atoms coordinate with seven neighbours in a hexagonal cell with sesquoide A-type structure. Their OSs then translate into a fully filled O 2p band (with some Ce 5d mixed in) and the empty Ce 5d conduction band. Between these lies a Ce 4f peak, which is the main distinguishing feature. In cerium dioxide it lies above the Fermi-level lies halfway between 2p and 4f, while in dicerium trioxide it lies just under. The 2p band then becomes valence band and the now empty 4f peak looses it sharpness by broadening out.

1.3 Modeling challenges for the future

Density functional theorem (DFT) calculations have become the standard in Heterogeneous Catalysis. The oldest approach, Local Density Approximation, was designed by the Solid State community[15] to capture the main electronic structure aspects of metals in a more efficient fashion than current-time quantum chemistry methods. The low-order scaling of DFT empowers larger slabs calculations. When extended in depth, bulk properties are better represented. It conversely also allows for larger surface areas to adsorb more complex molecules or model lower

coverages. Some materials still pose a challenge for current implementations, such as the Generalized Gradient Approximation.

In the case of ceria, self-interaction penalizes high electron densities. The material is computed to be ferromagnetic, although in reality it is an insulator. The state-of-the-art workaround exists in either equipping density functional theorem equiped with a Hubbar correction or employing hybrid functionals instead. The former retains all the benefits of DFT but requires an external parameter, while the latter is noticeably slower. This thesis predominantly contains Hubbard-enhanced calculations. The derivation of this parameter is discussed amply in subsection 2.1.4. Suffice to say for now that it depends on the orbital filling. Hence, any mayor changes to it, e.g. chemical reduction, warrant an adjustment in the parameter. This alters the energy reference and complicates the correct evaluation of the thermodynamics.[16] In the meantime, quantum chemistry methods have been making strides as well. Two new low-scaling perturbation implementations have been introduced to VASP,[17,18] making supercell calculations feasible. Compared to hybrid functionals which only include a portion of exact exchange, postprocessing methods for Hartree-Fock accounts for full exchange. The correlation energy also encompasses more quasi-particle paths than state-of-the-art post-processing methods for density functional theory, i.e. the Random Phase Approximation.[19] These innovations could set a new benchmark for DFT and gauge the accuracy of the Hubbard correction in reduced slab models.

As regular slab calculations have become common place, the community now turns its attention to constructing even larger, more inclusive models.[20] The emphasis lies on coupling a multitude of surface processes, including side reactions, landscaping and catalyst degradation. One approach in biochemical areas is to use forcefields. Due to their strong dependence on a parametrization scheme and low accuracy in comparison with ab initio methods, classical force fields are not applicable in Solid State or Heterogeneous Catalysis. The rise of Machine Learning has brought with it algorithms that automatically fit parameters. If the parameter construction is free from any physical presuppositions and purely mathematically based, the algorithm becomes universal. Neural Networks match these requirements perfectly, attaining ab initio accuracy when well-trained. Training requires a large amount of data to cover the chemical space of interest. Thus the focus of any practical implementation falls on sampling coupled with preliminary testing.

1.4 Motivation and objectives

The chapter 3 presents the study of single-atom depositions on cerium dioxide via DFT. It starts with platinum adatoms and later on broadens the scope to nickel and palladium. Due to the prevalence of platinum on ceria in car-exhaust catalysis, the emphasis will lie on one of the mayor reaction cycles: the oxidation of carbon monoxide gas into carbon dioxide. The electronic structure is fundamental to rationalizing its catalytic properties, and receives ample attention. A by point breakdown contains:

- Verify the existence of platinum single-atoms on various ceria surfaces and identify anchoring sites.
- Investigate the effect of ambient conditions, more specifically the presence of reductive components in the atmosphere, and how it influences the anchoring sites.
- Identify the various single-atom coordinations and their oxidation states.
- Present a model for the oxidation state distribution.
- In section 3.2, evaluate the reactivity of each state in carbon monoxide conversion via (a) a mechanistic deconstruction and (b) a micro-kinetic model based on the former.
- In section 3.3, expand the scope to other potential metals and compare their oxidation state distributions with those of platinum.

Chapter 4 addresses alternatives to the density functional methodology used above. There is no "one solution fits all" case. Depending on the specific requirements, I consider different angles of approach. These are always performed in collaboration with another expert.

The first project focuses on the accuracy of the electronic structure calculations, in particular under reductive circumstances. The aim in section 4.1 is to investigate the quality of various functional schemes with increasing accuracy up until second order Møller-Plesset theory. For the first trials, the scope is restricted to bulk phase only. Reduction is incorporated by comparing the CeO_2 and Ce_2O_3 phases. Concretely, the goals are:

- Present the latest developments in wavefunction methods for solid state.
- Apply the novel implementations on a simple test model: bulk ceria.

- Asses the impact of bulk reduction.
- Select other benchmark functionals to include atomic physics in a constructive, step-by-step fashion.
- Compare the wavefunction methods with density functional theory on (a) the geometry and (b) bulk modulus (forces).

The second project in section 4.2 revolves around constructing a high-dimensional Neural Network Potential. The emphasis lies solely on rational data generation, visualization of the chemical space, fitting, and evaluation of the fit quality. At a certain point, simulations naturally enter into the fit evaluation and I shall discuss a couple of preliminary results.

- Mapping out the chemical space.
- Outlining an approach for systematically producing data.

Lastly, I will summarize the findings of chapters 3 and 4 in the conclusions of chapter 5

Chapter 2

Theoretical background

"First I'll tell you about the picture of the universe painted by modern physics: the geometry of the universe is not physical." "Can you be a little less abstract?" "What if I put it this way: in the universe, apart from empty space, there is nothing."

Liu Cixin, Ball Lightning

2.1 Ab Initio methods

Electronic structure calculations underlie Computational Chemistry. When it is composed from first-principles or ab initio, theory stands on its own, free to investigate novel systems. Thanks to ab initio, Computational Chemistry is a branch of its own rather than a regurgitation of experimental analysis. In what follows, I shall give a bird-eye's view of this tremendously large and complex field. I shall introduce the concepts necessary to understand the methodology used in Chapter 3, starting from the very foundation.

2.1.1 Fundamentals of Quantum Chemistry

Dirac equation

The most encompassing formula of atomic quantum mechanics (QM) would be the Dirac equation.[21] For simplicity we first consider a particle of mass m and momentum p out of an external potential. Special relativity employs the Einstein notation, where a_μ is a four-dimensional vector that adheres to the Lorenz transformation between different frames. The dot product then evaluates to $a^\mu a_\mu = \left(a^{(t)}\right)^2 - \left(a^{(x)}\right)^2 - \left(a^{(y)}\right)^2 - \left(a^{(z)}\right)^2$ with $a^{(t)}$ corresponding the time-coordinate projected onto space and the other components to the actual spatial coordinates. With the light speed c, we then obtain:

$$p^\mu p_\mu - (mc)^2 = \left(\gamma^\kappa p_\kappa - mc\right)\left(\gamma^\lambda p_\lambda + mc\right) = 0 \tag{2.1}$$

The left-hand factor defines regular particles, while the right-hand describes anti-particles. Substituting the momentum vector p_κ with its functional counterpart yields the more well-known form:

$$\left(i\hbar\gamma^\kappa \partial_\kappa - mc\right)\Psi = 0 \tag{2.2}$$

Although momentum is a four-vector, the quantum field Ψ adheres to a different transformation rule. Note that in this convention, Ψ is not the wavefuntion. One mayor difference is that the quantum field does not preserve the total number of particles. Being clearly an eigenvector of $\gamma^\kappa \partial_\kappa$, Dirac's Ψ is also called a bispinor. The tensor γ_κ namely corresponds to a vector of (2×2)-matrices with the Pauli-matrices as their elements. These individual matrices have spinors for eigenvectors. The Pauli-matrices alone generate the entire Lie group of unitary (2×2)-matrices SU(2). The algebraic structure of this group is isomorphic with that of the Lie group of orthogonal (3×3)-matrices SO(3), which describe rotations in Cartesian space. The groups themselves however are not isomorphic. This leads to the particular effect where a full rotation in SU(2), corresponds to a 4π angle in SO(3). When moving on to non-relativistic quantum theory the Pauli-matrices are ignored and the bispinor symmetry lost. Due to its fundamental importance to the Pauli-exclusion principle and Fermi-Dirac statistics, it has to be reintroduced as spin. This is the single biggest mark of special relativity on atomic QM.

Other, non-spin related relativistic effects can still affect physical and chemical properties in specific cases. This strongly impacts group 11 elements in particular.[22] The example of (atomic) gold is most pronounced, where the 6s orbital

centered around the nucleus contracts and stabilizes (direct relativistic effects) and the nuclear charge screening destabilizes higher angular orbitals such as 5d (indirect relativistic effects). This results in the 5d/6s gap decreasing enough for the excitation spectra to appear in the upper visible spectrum. Hence, valence electrons are affected as well, not only core-electrons. This applies especially to heavy elements where the valence electrons gain a high kinetic energy.

To measure this impact, potential energy (V) now has to be added to the Dirac equation:[23]

$$\begin{pmatrix} V & c\boldsymbol{\sigma}\cdot\mathbf{p} \\ c\boldsymbol{\sigma}\cdot\mathbf{p} & V-2c^2 \end{pmatrix}\begin{pmatrix} \phi \\ \chi \end{pmatrix} = E\begin{pmatrix} \phi \\ \chi \end{pmatrix} \tag{2.3}$$

Here, ϕ and χ are the large and small components of the total quantum field Ψ, respectively. These names refer to their overall contribution to the total energy. The objective is to transform the quantum field Ψ to wavefunction in classical QM.

A first step would be to decouple both components and rewrite the four-component Hamiltonian in terms of the large component ϕ alone. The Foldy-Wouthuysen transformation (eq. 2.4) along with renormalization $\left(\hat{O}\right)$ then yield the two-component Hamiltonian $\left(\hat{H}_\phi\right)$.

$$\chi = \hat{X}\phi = \frac{1}{2c}\left(1+\frac{E-V}{2c^2}\right)^{-1}\boldsymbol{\sigma}\cdot\mathbf{p}\phi \tag{2.4}$$

$$\hat{H}_\phi = \hat{O}\hat{H}\hat{O}^{-1} = \sqrt{1+\hat{X}^\dagger\hat{X}}\left(V+c\boldsymbol{\sigma}\cdot\mathbf{p}\hat{X}\right)\sqrt[-1]{1+\hat{X}^\dagger\hat{X}} \tag{2.5}$$

Now, of the small component only its main contribution is taken into account. The expansion of the coupling operator $\hat{X}$ in terms of $\left(2c^2-V\right)$ yields the Hamiltonian kernel:

$$\hat{H}_\phi = V+\boldsymbol{\sigma}\cdot\mathbf{p}\left(\frac{c^2}{2c^2-V}\right)\boldsymbol{\sigma}\cdot\mathbf{p}-\boldsymbol{\sigma}\cdot\mathbf{p}\left(\frac{c^2}{2c^2-V}\right)\left(\frac{E}{2c^2-V}\right)\boldsymbol{\sigma}\cdot\mathbf{p}+\ldots \tag{2.6}$$

The first term only contains the direct (classical) potential. Retaining then the potential along with the next term for kinetic energy yields the zeroth order relativistic approximation (ZORA). More elaborate versions, such as the first order relativistic approximation (FORA), include higher order terms from $\hat{O} = 1+\hat{X}^\dagger\hat{X}/2+\ldots$ Remarkably enough, simply rescaling the ZORA Hamiltonian by $\left(1+\langle\phi|V+\boldsymbol{\sigma}\cdot\mathbf{p}\left(\frac{c^2}{2c^2-V}\right)\boldsymbol{\sigma}\cdot\mathbf{p}|\phi\rangle\right)^{-1}$ incorporates most of the FORA energy*, especially for the valence electrons. In the special case of one-electron atoms

*Rescaling with a number only affects the eigenvalues, not the eigenvectors.

and ions, this *rescaled ZORA*[24] even recovers the exact Dirac energies. For heavy elements on the other hand, these equations have to be solved self-consistently rather than adding them in a perturbative manner. Finally, the correspondence of the large and small components the mixing of particles versus anti-particles in eq. 2.3 shows that the remaining particle-component ϕ contains only its spin in a two-component form. This is then converted into a spin and wavefunction product.

It should be pointed out again that the Hamiltonian in eq 2.6 operates only on a single spin $\frac{1}{2}$ particle. The next part will focus on a multi-particle system in the classical limit.

Time-independent Schrödigner equation

The classical counterpart to the Dirac equation is the time-dependent Schrödigner equation:

$$\hat{H}\psi = i\hbar\frac{\partial\psi}{\partial t} \tag{2.7}$$

Within the context of this works, we are interested in the stationary solutions of this differential equation, meaning that the time component of the derivative is vanishing. When the system is time-symmetric, for example with Hamiltonian that does not depend on time, it coincides with the sum of the kinetic $\left(\hat{T}\right)$ and potential energy $\left(\hat{V}\right)$ similar to Newtonian mechanics. In eq. 2.8, the electrostatic potential has been fully written out, disregarding any electric or magnetic field applied from outside. The momentum operator $\hat{p}$ has been derived from its Fourier counterpart of the average $\mathcal{F}^{-1}(\bar{p})$. As by convention, $\mathbf{r}_i$ and q_i refer to the electron coordinates and charges respectively. Nuclear variables are in capitals.

$$\hat{H} = \hat{T} + \hat{V} = \sum_{i,I}\left[\frac{\hbar^2}{2}\left(\frac{1}{m_i}\nabla_i^2 + \frac{1}{M_I}\nabla_I^2\right) + \sum_{j,J}\frac{q_i Q_J}{\parallel \mathbf{r}_i - \mathbf{R}_J \parallel} + \frac{1}{2}\sum_{j=1}^{n}\frac{q_i q_j}{\parallel \mathbf{r}_i - \mathbf{r}_j \parallel}\right] \tag{2.8}$$

Employing separation of variables in eq. 2.9, there are now two differential equations: $\phi(t)$ for the time-dependent wavefunction and $\chi(\mathbf{r}, \mathbf{R})$ the spatial components. The time-dependent wavefunction becomes a first order differential equation with a trivial solution. It adds oscillations following a period of $\frac{2\pi}{E}$ to the wavefunction. Within the context of the probability density $\psi^*\psi$ however, the inner product yields a truly time-independent solution, hence the name.

The same conclusion applies to all derived quantum observables which are time-independent themselves. The spatial wavefunction on the other hand is rephrased as an eigenvalue problem. It garners the most focus when solving the the general time-independent Schrödigner equation for atomic, molecular, and crystal systems. Some of its particularities namely prevent an analytic solution for all but the one-electron case. In the following sections I shall explore some of the commonly applied approximations to derive an estimated solution.

$$\frac{i\hbar}{\phi(t)}\frac{\partial\phi(t)}{\partial t} = constant = \frac{\hbar^2}{2\chi(\mathbf{r},\mathbf{R})}\sum_{i,I}\left(\frac{1}{m_i}\nabla_i^2 + \frac{1}{M_I}\nabla_I^2\right)\chi(\mathbf{r},\mathbf{R}) + V(\mathbf{r},\mathbf{R}) \tag{2.9}$$

Born-Oppenheimer approximation

The general strategy for solving the (time-independent) Schrödigner equation is to build up the full system's wavefunction from the wavefunctions of individual building blocks, i.e. the electrons and nuclei. Most nuclei have well-localized wavefunctions (both in physical and reciprocal space) in comparison to electrons. They owe this to their difference in mass. Consequentially, they could be (as a first approximation) regarded as point particles that follow a classical behavior. Only hydrogen falls on the border. Being the lightest element of the whole periodic system, it tends to undergo typical quantum effects such as tunneling.[25] The implications are that we can simplify the Coulomb terms for nuclear repulsion and electron-nuclear interaction to those between point particles. Furthermore, the inertial effects of the high mass difference make that the nuclear motion is retarded, again with respect to the electronic motion. In the *clamped-nuclei* approximation the nuclear coordinates are fixed and their momentum (temporarily) neglected. As such, the focus shifts to solving the electronic part of Hamiltonian. The total wavefunction now simply factors out into a product of both: $\chi(\mathbf{r},\mathbf{R}) = \sum_i \chi_i(\mathbf{r};\mathbf{R})\,\phi_i(\mathbf{R})$, with $\chi_i(\mathbf{r};\mathbf{R})$ depending only parametrically on $\mathbf{R}$. By varying the nuclear coordinates as parameters in a self-consistent, electronic calculation one can map out the potential energy surface (PES) for a specific region.

Nonetheless, to obtain the total energy one should still add the nuclear kinetic energy. Even local minima of the ground-state PES still require a zero-point energy (ZPE) correction similar to the lowest energy state in a quantum well. Applying the total Hamiltonian to the product shows that the nuclear kinetic energy interacts both with wavefunctions individually:

$$\left[\hat{T}_N + \hat{V}\left(\mathbf{R}\right) - E_n\right]\phi_n + \hat{\Lambda}_{mn}\phi_m = 0 \tag{2.10}$$

χ_i still enters eq. 2.11 coupling the nuclear motion to the electronic potential and is called the adiabatic term $\left(\hat{\Lambda}\right)$. Its first term is diagonal, while the second term is anti-Hermitian and thus has vanishing diagonal elements. The latter couples two electronic ground-states through their associated nuclear geometries. Its off-diagonal elements can be expanded using the Hellmann-Feynman theorem to yield eq. 2.12.

$$\hat{\Lambda}_{mn} = \langle\chi_m|\hat{T}_N|\chi_n\rangle - \sum_{j}^{nuclei}\frac{1}{M_i}\langle\chi_m|\frac{\partial}{\partial R_j}|\chi_n\rangle\frac{\partial}{\partial R_i} \tag{2.11}$$

$$\langle\chi_m|\frac{\partial}{\partial R_i}|\chi_n\rangle = -Z_j\sum_{k}^{nuclei}\frac{\langle\chi_m|\frac{R_j-R_k}{|R_j-R_k|^3}|\chi_n\rangle}{\epsilon_m - \epsilon_n} \tag{2.12}$$

When diagonalized and adsorbed into the diabatic potential W, eq. 2.11 yields eq. 2.13.[26] This W potential can be considered a gauge-transformation of V. That makes it unique up to a phase factor $e^{-i\omega t}$.

$$\left[\hat{T}_N + \hat{W}\left(\mathbf{R}\right) - E_n\right]\chi_n = 0 \tag{2.13}$$

Unfortunately, the actual construction the second $\hat{\Lambda}$ term or its diagonalization are too involved for most practical applications. Thus, it is neglected leading to the actual Born-Oppenheimer approximation (BOA). Within BOA different nuclear motions have now been fully decoupled and there is no interaction between ϕ_m and ϕ_n anymore. Or stated differently, the BOA uses V instead of W. Eq. 2.12 shows that this can be done safely as long as the corresponding electronic ground states are well-separated in energy. When a nuclear geometry however couples two (near-)degenerate electronic states, as with conical intersections, the energy-contribution diverges.

In their original paper, Born and Oppenheimer used perturbation theory to expand the full Hamiltonian according to the relative electronic mass m/M and compute the five lowest order terms.[27] The expansion helps clarifying the physical interpretation of the coupling matrix. Its zeroth term corresponds to the electronic potential at a local minimum, or in other words the electronic solution in the clamped nuclei approximation. The higher order corrections account for coupling in between the nuclear motion, i.e. the missing Λ matrix. Second order adds vibrational motion upon which the fourth order terms correct and expand with rotation. The first and third order terms on the other hand are vanishing. From

there on out the pattern remains analogous so that the higher order terms further couple the vibrational and rotational motions.

Periodic Boundary Conditions

The focus now shifts to multi-particle equations. The simplest system contains two electrons and uses their individual wavefunctions χ_a and χ_b as a minimal basis set. The Hamiltonian in eq. 2.14 has two solutions: $(\chi_a \pm \chi_b)/\sqrt{2}$. They are (de)stabilized in equal amounts compared to the non-interacting systems.

$$\begin{pmatrix} H_{aa} & H_{ab} \\ H_{ba} & H_{bb} \end{pmatrix} = \begin{pmatrix} H_{aa} & H_{ab} \\ H_{ab} & H_{bb} \end{pmatrix} \tag{2.14}$$

Figure 2.1 extrapolates to a n electron system. The number of combinations increases while the spacing between the energy levels decreases. This is the origin of band structures in in Materials Science, where one effectively deals with limit case of $n \to \infty$. The definition of crystals as *systems with a translational symmetry at the atomic level* entails that the nuclear potential adheres to the same symmetry. As such, the Hamiltonian and its eigenfunctions must comply with the periodic symmetry.[28] This is formulated as Bloch's theorem in eq. 2.15.

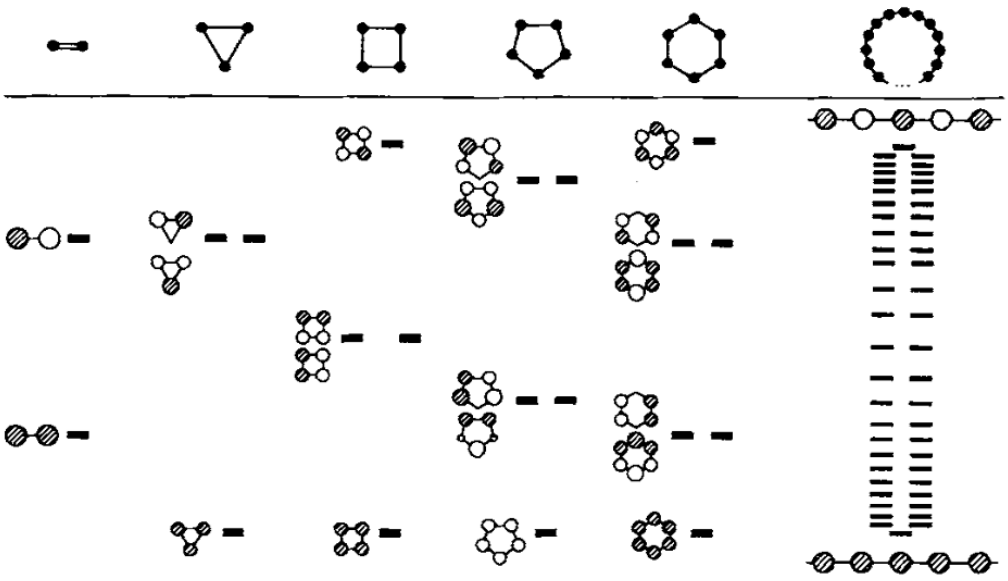

Figure 2.1: Illustration of level splitting and the onset of band formation under 1D symmetry with hydrogen. Taken from ref 29

In this context, **r** stands for a position vector within the primitive cell and **R**

for a translation vector consistent with the crystal symmetry. A new parameter $\mathbf{k}$ is also introduced as the wavenumber, fulfilling the same role as the coefficients in the n-copy interaction problem. From eq. 2.15 it is clear that this would be the variable of reciprocal space after Fourier transformation. This space contains a minimal periodic unit, just like the Wigner-Seitz primitive cell, called the Brillouin zone. Consequentially, all discernible k-points lie within its boundaries. Therefore, the reciprocal to $\mathbf{R} = \sum_{i=1}^{3} N_i \mathbf{a}_i$ is $\mathbf{k} = \sum_{i=1}^{3} \frac{m_i}{N_i} \mathbf{b}_i, m_i \in \mathbb{Z}$, with the reciprocal lattice vector $\mathbf{b}_i = 2\pi \frac{\mathbf{a}_j \times \mathbf{a}_k}{\mathbf{a}_i \cdot (\mathbf{a}_j \times \mathbf{a}_k)}$ for $(k = j + 1 = i + 2)$. In practical implementations, the unit cell stands in for the primitive cell. If the unit cell does not overlap with the primitive cell and is thus a supercell, the Bravais unit cell shrinks proportionally. This yields an inverse scaling relationship between the number of k-points and the lattice parameters along each axis. Since all physical quantum observables of a system commute with its Hamiltonian, they naturally inherit its symmetry. VASP exclusively works with a plane-wave basis set for the unit cell. Due to the mathematical similarity, its wavenumber $\mathbf{G}$ stands on the same level as $\mathbf{k}$, see the second equality in eq. 2.15. The main difference is that $\mathbf{G}$ is limited to the primitive cell or its images (if $\mathbf{k} \neq \mathbf{0}$). Instead of setting the limits of a vector box, the set is controlled using an upper-limit (ENCUT) on the wave energy $E_{cut} = \frac{\hbar^2}{2m} G_{cut}$.

$$\psi(\mathbf{r} + \mathbf{R}) = e^{i\mathbf{k}\cdot\mathbf{R}} \psi(\mathbf{r}) = \sum_{\mathbf{G}} c_{\mathbf{k}+\mathbf{G}} e^{i(\mathbf{k}+\mathbf{G})\cdot\mathbf{R}} \tag{2.15}$$

When examining phenomena at the crystal edges, the bulk models are traded in for slab models. These slabs are cutouts of the bulk along a specific Miller index with a certain depth perpendicular to the intersection plane. In asymmetric models, as used in this work, the bottom atom layers are kept fixed to simulate the bulk strain. Consequentially, the translational symmetry breaks down along the perpendicular direction. Various codes handle this loss of symmetry differently. On the one hand, there are programs such as Car-Parrinello code for the new Millenium (CP2K) that reformulate their sets of equations. Although physically they are entirely correct, this approach is quite involved and slows down the implementation. For planar-wave code like Vienna Ab initio simulation package (VASP) on the other hand, it is better to keep enforcing the periodic boundary conditions (PBCs). As a result, the user has to introduce a vacuum large enough for the slabs not to interact anymore. The interaction between the slab and its image can be mapped out using the working potential. The aim is to have the latter converge. A good rule of thumb for the vacuum would be a minimum length of 8 and 10 Å to be safe.

Lastly, I would like to remark, that many of the approximations in this section asymptotically convergence according to a specific parameter. Here, we have established at the least four such parameters, six even in the case for slabs. These parameters are linked to the energy and one cannot compute thermodynamic values by comparing systems with different, non-converged setups. When starting, one should always benchmark these parameters in order to determine the converge criteria.

2.1.2 Hartree-Fock approximation

In the following sections I shall present common approaches to solving the electronic part of the time-independent Schrödigner equation, elaborate on some of their particularities and, where necessary, point out common pitfalls. Many of these computational methods are variations on the so-called *variational theorem*. It states that a ground state solution minimizes the system's energy. The strategy thus shifts to solving a new set of coupled differential equations of a parametrized wavefunction.

I shall first develop the Hartree-Fock (HF) approximation according to the textbook of Szabo and Ostlund.[30] HF starts with separating the wavefunction into a product of spin-orbitals that each contain up to a single electron. This expression still breaks with the permutation symmetry underlying the Pauli-exclusion principle however. The symmetry can be reimposed by going off all possible permutations between the basis set functions and electrons while keeping track of the sign, which led to the definition of Slater-determinants. The exact Hamiltonian consists solely out of the sum of one and two-electron operators. The Fock operators partitions into operators that act upon individual electrons. This works straightforwardly for the kinetic energy and the Coulomb interaction with the nuclei are grouped together into $\hat{h}$. The remaining two-electron integrals fall into two categories:

1. **Direct energy $\left\{\hat{J}\right\}$:** the spin-orbitals for each electron *aligns* with its conjugate. This physically describes to two electron clouds interacting via the Coulomb potential, to which it evaluates in the classical limit.

2. **Exchange energy $\left\{\hat{K}\right\}$:** the spin-orbitals for each electron *mismatch* with its conjugate. This type of interaction is exclusive to QM, as no counterpart exists in classical mechanics (CM).

By evaluating only one integral, the interaction effectively becomes a one-electron operator. The sum of all contributions to the single-electron energy ϵ_a then becomes:

$$\begin{aligned}\hat{F}(\mathbf{r}_1)\,\chi_a(\mathbf{r}_1) &= \left\{\hat{h}(\mathbf{r}_1) + \sum_i \left[\hat{J}(\mathbf{r}_i) - \hat{K}(\mathbf{r}_i)\right]\right\}\chi_a(\mathbf{r}_1) \\ &= \hat{h}(\mathbf{r}_1)\,\chi_a(\mathbf{r}_1) + \sum_b \int d\mathbf{r}_2 \frac{1}{r_{1,2}}\left[\chi_b^\dagger(\mathbf{r}_2)\,\chi_b(\mathbf{r}_2)\,\chi_a(\mathbf{r}_1) - \chi_a^\dagger(\mathbf{r}_2)\,\chi_b(\mathbf{r}_2)\,\chi_b(\mathbf{r}_1)\right] \\ &= \hat{h}(\mathbf{r}_1)\,\chi_a(\mathbf{r}_1) + \sum_b \int d\mathbf{r}_2 \frac{\chi_b^\dagger(\mathbf{r}_2)\,\chi_b(\mathbf{r}_2)}{r_{1,2}}\left[1 - \hat{P}_{a,b}\right]\chi_a(\mathbf{r}_1)\end{aligned} \tag{2.16}$$

Here χ stands for a one-electron spin-orbital and $\hat{P}_{a,b}$ for the permutation operator working on $\chi_b^\dagger$ and χ_a. Note that in eq. 2.16 $\hat{J}$ and $\hat{K}$ cancel out when evaluated over χ_a. Hence, there is no self-interaction. DFT methods on the other hand, commonly suffer from this error, see 2.1.4. Applying now the variational principle to the Fock operators yields a set of coupled, single-electron eigenvalue problems. If a finite basis set is chosen and χ expressed as a linear combination of the basis set functions, it can even be rewritten into the Roothan equation of which the matrix form reads as:

$$\mathbf{FC} = \mathbf{SC}\epsilon \Leftrightarrow \epsilon = \mathbf{C^{-1}S^{-1}FC} \tag{2.17}$$

Based on previous the notation, **F** stands for the Fock matrix and likewise the diagonal matrix ϵ contains the eigenvalues. The columns in **C** define *chi* and lastly the overlap matrix **S** which evaluates the projection of all basis set functions $S_{i,j} = \left\langle \xi_i \middle| \xi_j \right\rangle$. If the basis set is orthonormal, the overlap matrix becomes identity: $\mathbf{S} = \infty$. The **F** and **S** matrices are all known, so **C** is rotated by a unitary matrix during diagonalization. The presence however of the spin-orbitals in the electron repulsion carries over to **F** as a dependence on **C**. Practically, this recurrence of the solution in the equation to solve is handled by starting from an initial guess, computing the new spin-orbitals $\xi_a^{(1)} = \sum_b u_{a,b}^{(1)} \chi_j$, and reinserting it into the Fock matrix. This process is carried out iteratively until new updates only marginally improve upon a pre-determined measure. The measure can compare **C**, but in `VASP` we employ the energy difference. The final wavefunction is then said to be *self-consistent*.

The procedure does not stop after the convergence of the Roothan equation however. Koopman's theorem sheds further light onto the physical interpretation of the eigenvalues. The ionization potential to remove/excite an electron in ξ_a from the wavefunction (without any relaxation) equals $\epsilon_a > 0$. Similarly, the electron-affinity for occupying a virtual spin-orbital χ_α is $-\epsilon_\alpha$. This entails that under the same conditions, the excitation of an electron from $\xi_a \rightarrow \xi_\alpha$ is $\epsilon_a - \epsilon_\alpha$. Here we

have been working under the assumption that the eigenvalues are sorted according to increasing value. Hence, the ground state which minimizes the overall energy, only has the n lowest orbitals occupied. The remaining virtual orbitals are a leftover from the mathematics, but will be useful in the post-processing. Contrary to this picture, the total HF energy is not the sum over all occupied spin-orbitals. This sum counts the electron repulsion twice, since $\langle b|\hat{J}_a|b\rangle = \langle a|\hat{J}_b|a\rangle$ and likewise for $\hat{K}$:

$$E_{\mathrm{HF}} = \sum_{i=1}^{n}\left[\epsilon_i - \sum_{j}^{n}\frac{1}{2}\langle\xi_i|\left(\hat{J}-\hat{K}\right)|\xi_i\rangle\right] \tag{2.18}$$

The solution in eq. 2.18 returns the ground state energy of the HF Hamiltonian. This expression actually is a *mean-field approximation* of the exact Hamiltonian. The Coulomb operator is approximated here by its average, excluding any fluctuations in the wavefunction. The residual error $E_{\mathrm{exact}} - E_{\mathrm{HF}}$ is referred to as *electron correlation* (E_c) and stems from two possible sources:[31]

1. **Static correlation:** the ground state wavefunction is ill described by only a single Slater determinant. A common workaround is to generate a linear combination of various determinants, also called multi-configurational methods. This kind of contribution is especially prevalent in (near-)degenerate systems.

2. **Dynamic correlation:** there is some mixing in from particle/anti-particle fluctuations. This effect is considered more or less universal and is often mitigated by including small contributions from excited states.

Most of the terms introduced here are key aspects that define electronic structure theory. Not only is HF key to understanding terms such as electron correlation, it also acts as the starting point for mounting a structured expansion. For example, looking at it from a different perspective eq. 2.18 is a first order correction to the zeroth order energy sum of Fock eigenstates ($\sum_a^{occ}\epsilon_a$). In the following subsection I shall develop perturbation theory, which adds a second order correction to the HF energy.

2.1.3 Post-Hartree-Fock: second order Møller-Plesset perturbation theory

In the previous section I introduced the concept of electron correlation. Since this is a difference in energy, the exact Hamiltonian $\left(\hat{H}\right)$ can be split up into the Fock

operator $\left(\hat{H}^{(0)}\right)$ and a correlation-operator as a perturbation $\left(\lambda\hat{V}\right)$ where λ is a scaling parameter. The eigenvalues and eigenfunctions of the exact Hamiltonian can then be developed as a Taylor series around the solutions to $\left(\hat{H}^{(0)}\right)$, labeled as $E_i^{(0)}$ and $\left|\Psi_i^{(0)}\right\rangle$. Note that these corrections do not follow the variational principle and are not evaluated self-consistently. As a downside, the computed energies also no longer form an upper-estimate to the (approximate) Hamiltonian's ground state energy.

$$\hat{H}_i^{(0)}\left|\xi_i^{(0)}\right\rangle = \epsilon_i^{(0)}\left|\xi_i^{(0)}\right\rangle \tag{2.19}$$

$$\hat{H}_i^{(0)}\left|\xi_i^{(1)}\right\rangle + \hat{V}\left|\xi_i^{(0)}\right\rangle = \epsilon_i^{(0)}\left|\xi_i^{(1)}\right\rangle + \epsilon_i^{(1)}\left|\xi_i^{(0)}\right\rangle \tag{2.20}$$

$$\hat{H}_i^{(0)}\left|\xi_i^{(2)}\right\rangle + \hat{V}\left|\xi_i^{(1)}\right\rangle = \epsilon_i^{(0)}\left|\xi_i^{(2)}\right\rangle + \epsilon_i^{(1)}\left|\xi_i^{(1)}\right\rangle + \epsilon_i^{(2)}\left|\xi_i^{(0)}\right\rangle \tag{2.21}$$

This formulation is called Rayleigh-Schrödigner perturbation theory.[17] When applied to HF, it is called Møller-Plesset perturbation theory (MP). Projecting back onto the ground state $\left|\xi_i^{(0)}\right\rangle$, the terms $\left\langle\xi_i^{(0)}\middle|\hat{H}_i^{(0)}\middle|\xi_i^{(2)}\right\rangle = \epsilon_i^{(0)}\left\langle\xi_i^{(0)}\middle|\xi_i^{(2)}\right\rangle$ cancel out. Furthermore, Brillouin's theorem states that for the HF ground states are orthogonal to any single electron excitations, so that $\left\langle\xi_i^{(0)}\middle|\xi_i^{(1)}\right\rangle = 0$. All that remains is the second order contribution $\epsilon_i^{(2)}$ and the perturbation on the other side. Applying Brillouin on eq. 2.20 we retrieve $\epsilon_i^{(1)} = \left\langle\xi_i^{(0)}\middle|\hat{V}\middle|\xi_i^{(0)}\right\rangle$. Knowing that the HF energy in eq. 2.18 is a first order correction, we obtain an explicit expression for the perturbation operator $\hat{V} = -\left(\hat{J} - \hat{K}\right)/2$ and consequentially the second order energy:

$$E_a^{(2)} = \sum_{i,j\neq i} \frac{\left|\left\langle\xi_i^{(0)}\middle|\hat{V}\middle|\xi_j^{(1)}\right\rangle\right|^2}{\epsilon_i^{(0)} - \epsilon_j^{(0)}} \tag{2.22}$$

$$= \frac{1}{2}\sum_{a,b}^{occ}\sum_{\alpha,\beta}^{virt} \frac{\langle a,b|\frac{1}{|\mathbf{r}-\mathbf{r}'|}|a,b\rangle\left[\langle\alpha,\beta|\frac{1}{|\mathbf{r}-\mathbf{r}'|}|a,b\rangle - \langle\alpha,\beta|\frac{1}{|\mathbf{r}-\mathbf{r}'|}|b,a\rangle\right]}{\epsilon_a + \epsilon_b - \epsilon_\alpha - \epsilon_\beta} \tag{2.23}$$

In eq. 2.23 only the interactions between occupied (a, b) and virtual orbitals (α, β) remain. Remark that this approach only returns an energy correction, but no updated wavefunction, Density of States (DOS), nor forces in `VASP`. This restricts the method to single point calculations only.

Low-scaling implementations

The second order correction $E^{(2)}$ of MP2 can be split into direct $\left(E_d^{(2)}\right)$ and exchange $\left(E_x^{(2)}\right)$ contributions. Both contributions contain double excitations formed out of pairs of two-electron interactions. These form the bottleneck. In reciprocal space, the integrals can be split k-point. This process lends itself well to parallelization. Moreover, each two-electron integral can be factored here out into a product of single electrons overlap integrals. The latter scale linearly with respect to the number of occupied (a) and virtual (α) orbitals. This entails that the total complexity of the procedure in reciprocal space scales as $O\left(N_a^2 N_\alpha^2 N_{\mathbf{G}}\right)$, where $N_{\mathbf{G}}$ denotes the number of k-points. The total order is thus quintic. For molecular systems on the other hand there already exist linear-scaling algorithms based on Gaussian basis sets and one-electron integrals. Afterwards, the integrals are transformed back to real space via inverse Fast Fourier Transform (FFT), which has been well-studied and optimized.[32]

The runtime in PBCs is further reduced by using a coarser auxiliary basis set for the overlap integrals. Later on the results are extrapolated to the full-size basis set limit. In `VASP`, the auxiliary set is independent of the k-mesh. It is instead fully determined by its real-space counterpart, the cutoff energy `ENCUTGW`. Its default value is $\frac{2}{3}$ of `ENCUT`. In the following paragraphs, I shall present two workarounds to achieve more favorable scaling. Both have been implemented by Dr. T. Schäfer in `VASP6`[17,18] and we are testing them out on ceria bulk phase (see Section 4.1).

Laplace-transformed method

Figure 2.2a shows the major steps of the Laplace-transformed second order Møller-Plesset perturbation theory (LTMP2) implementations.[17] The main strategy is to separate out the virtual orbitals first. This would result in lowering the $O\left(N_\alpha^2\right)$ contribution to $O(N_\alpha)$. This is done by rewriting the denominator in terms of its Laplace transform over τ, which is an exponential. This product is grouped with the single-electron products of the nominator yielding overlap matrices between virtual and occupied orbitals. These matrices can be evaluated beforehand (step I) and subsequently summed over one set (in this case the virtual orbitals) to yield the total effect (step II) on an occupied orbital a. Remark that the latter now acts as a parameter. The exponential factor is a remnant of the denominator.

As such, the virtual part in the total order has been moved to a step before of $O(N_\alpha)$. In its place are now the Laplace integral and the FFT to switch to reciprocal space. The damping of the τ exponent reduces the cost of computing the former. It is evaluated numerically, using a quadrature with a default of six

weight points. As such it is mostly independent of the system's size and acts rather as a pre-factor to the total order. The expression for this order is now $O\left(N_a^2 N_{\mathbf{G}} N_{\mathrm{FFT}}\right)$, with N_{FFT} the size of the FFT grid points.

In the reciprocal space, each k-point has its own unique set of local eigenfunctions and values. As such, the eigenfunctions are determined by two parameters: $\phi_{a,\mathbf{k}}$ Their two-electron integrals are only non-vanishing when crystal momentum is conserved, i.e. $\mathbf{k}_1 + \mathbf{k}_2 = \hat{T}\,(\mathbf{k}_3 + \mathbf{k}_4)$. One vector can be offset by the translation symmetry $\hat{T}$, so any such integral depends on only three wavenumbers. The updated transformation function then looks like:

$$\left|w_{a,\mathbf{k}}^{\mathbf{G},\mathbf{q},\tau}\right\rangle = \sum_{\beta} e^{\left[\epsilon_{a,\hat{T}(\mathbf{k}-\mathbf{q})} - \epsilon_{\beta,\mathbf{k}}\right]\tau} \left\langle \beta, \mathbf{k}\middle| e^{-i(\mathbf{G}-\mathbf{q})\hat{\mathbf{r}}}\middle| a\hat{T}\,(\mathbf{k}-\mathbf{q})\right\rangle_{\Omega_0}$$

The index Ω_0 refers to the primitive cell volume as the minimal periodic unit in physical space. The size of $N_{\mathbf{G}}$ is further halved by employing time symmetry. This symmetry is only valid when no external field is applied to the system and spin-orbit coupling is ignored. Under time symmetry, the HF eigenfunctions are symmetric under inflection of the wavenumbers $\mathbf{k}$. This is due to $\mathbf{k}$ controlling the momentum of the plane wave basis set. Likewise, the transformation has the symmetry:

$$\left|w_{a,+\mathbf{k}}^{+\mathbf{G},+\mathbf{q},\tau}\right\rangle = \left|w_{a,-\mathbf{k}}^{-\mathbf{G},-\mathbf{q},\tau}\right\rangle$$

Stochastic method

A flow chart of the stochastic version[18] is shown in Figure 2.2b and builds on LTMP2. The bottleneck in LTMP2 still contains the double summation over the occupied orbitals. By estimating instead the energies, one can reduce the order. This approach only pays off if the number of data points is significantly smaller than the total set of states. The latter obviously depends on the energy accuracy $\delta E^{(2)}$ needed. The stochastic variable X^{τ} at in the τ grid is generated from a linear combination of HF orbitals of the similar occupation. Its random coefficients p_a are independently and uniformly distributed.

Steps 0, I, and II now scale as $O(N_\theta N_{\mathbf{G}} N_{a/\alpha})$, $O\left(N_\theta N_{\mathbf{G}}^{aux} \log\left(N_{\mathbf{G}}^{aux}\right)\right)$, and $O\left(N_\theta^2 N_{\mathbf{G}}^{aux}\right)$, respectively. The *aux* superscript refers to a finer, auxiliary FFT grid used in `VASP`. N_θ meanwhile denotes the sampling size. Virtual orbitals receive the same treatment, so the same scaling applies, hence $N_{a/\alpha}$. Because the current implementation operates at gamma-point exclusively, there is no dependence on N_{FFT} anymore. If a higher k-point sampling is needed, the images can always be accounted for as a supercell.

Rather than generating a single set of X^τ and updating the statistics gradually, one can also use two parameters to produce a larger sample. The two-electron integrals can then combine different sets, yielding correlated stochastic variables in step II:

$$\left\langle k_\theta^\tau l_{\theta'}^\tau \middle| \alpha_\theta^\tau \beta_{\theta'}^\tau \right\rangle, \theta \neq \theta' \tag{2.24}$$

Step III on the other hand forms no part of the bottleneck. Maintaining a fixed convergence criterion $\delta E^{(2)}$, the sample size is written as $n = n_L N_\theta^2$ where n_L denotes the total number of right-hand loops in Figure 2.2b. The order of the total step 0 then becomes $O(nN_{\mathbf{G}}(N_a + N_\alpha)/N_\theta)$, showing how correlated sampling benefits the overall speed. In the limit of a sample big enough to reach convergence after one cycle ($n_L = 1$), the order scales down to $O\left(\sqrt{n} N_{\mathbf{G}} N_\alpha\right)$. This optimal case also assumes that the impact of the virtual states is much larger than that of the occupied.

The second order exchange $E_x^{(2)}$ contains more involved integrals, for which step I scales as $O\left(N_\theta^2 N_{\mathbf{G}}^{aux} \log\left(N_{\mathbf{G}}^{aux}\right)\right)$. Under the same optimal conditions as before, the order diminishes to $O\left(nN_{\mathbf{G}}^{aux} \log\left(N_{\mathbf{G}}^{aux}\right)\right)$. Under a fixed $\delta E^{(2)}$, the sample size n depends quadratically on the system size and the scaling becomes cubic at each step. If we relax the criteria to a fixed relative error, n becomes independent of system size. Step 0 then becomes quadratic, step II linear and the bottleneck shifts to step I. Finally, in the optimum of all possible scenarios where the number of virtual orbitals (N_α), compared to the sample size $\left(\sqrt{n}\right)$, is small enough for the prefactors to dominate, the scaling can even become linear. This indicates that the advantage of stochastic MP2 compared to LTMP2 is not always clearcut. If used properly however and with some leeway towards the accuracy, the scaling can reduce favorably enough that only HF poses a bottleneck on the system size.

2.1.4 Kohn-Sham formulation of Density Functional theory

Nowadays, postprocessing methods for Hartree-Fock (post-HF) methods are barely used outside of benchmarking. This is due their demanding combinatorics of two-electron integrals in the post-processing.[33] In 1964, Hohenberg and Kohn proposed an alternative,[34] stating:

"It is proved that there exists a general functional $F[n(\mathbf{r})]$, independent of $v_{ext}(\mathbf{r})$, such that $E \equiv \int v_{ext}(\mathbf{r}) n(\mathbf{r}) d\mathbf{r} + F[n(\mathbf{r})]$ has as its minimum value the correct ground-state energy associated with $v_{ext}(\mathbf{r})$."

The external potential $v_{ext}(\mathbf{r})$ refers to the PES, which itself is determined by the nuclear coordinates (see section 2.1.1 for a more elaborate discussion). This

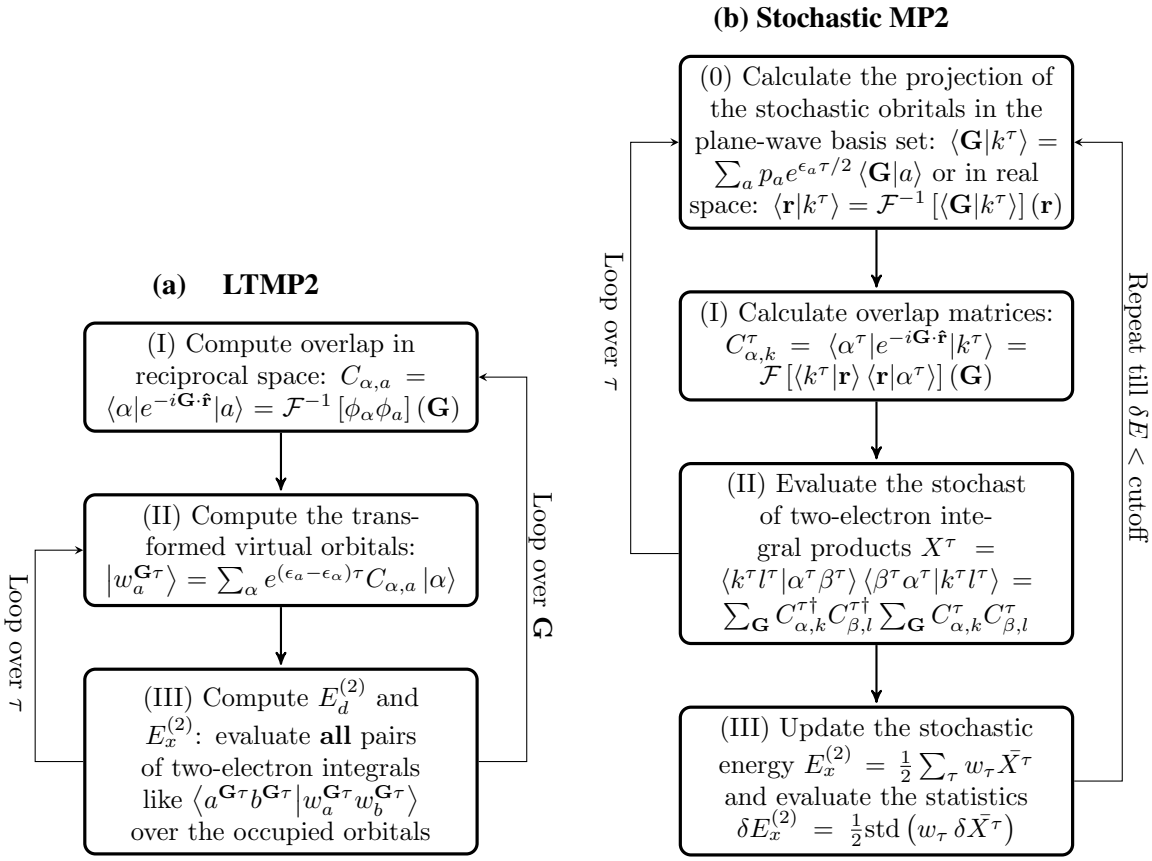

Figure 2.2: Flow charts of two low-scaling MP2 implementations. Both compute the second order direct $\left(E_d^{(2)}\right)$ and exchange $\left(E_x^{(2)}\right)$ contributions by factoring out the two-electron integrals. **a:** LTMP2 which distinguishes itself from quintic scaling MP2 in the separation and presummation of the virtual orbitals in step II. **b:** second order Møller-Plesset perturbation theory with stochastic orbitals (stochatic MP2) builds on LTMP2 but estimates the contributions instead of sampling the full space. This version only works at gamma-point. Steps I and III yield the same observables. Latin letters refer to occupied states and Greek to virtual. The ϕ stand for the corresponding HF eigenfunctions

quote covers a lot of ground, so usually it is split up into two conclusions. Firstly, the uniqueness theorem establishes a two-way link between the external potential and the electron density. Moreover, this link is universal, regardless of the details of $v_{ext}(\mathbf{r})$. Analysis schemes such as Atoms in Molecules[35] support this claim by illustrating how molecular properties can be derived from the density. The local maxima for example correspond to the nuclear positions and their relative values correlate with the nuclear charge. As such, one can reverse engineer

the atomic structure from the electron density. Another implication is that the wavefunction description contains redundant information, which can be stripped during integration to obtain the electron density.

The second theorem sets up a framework to derive the density from the external potential by reintroducing the variational principle for the ground-state. Its impact is seminal. It implies that much of the same apparatus developed above can be recycled. It were Kohn and Sham who eventually laid the groundwork for actually solving the Schrödigner equation using the universal functional.[36] They separate out the Coulombic interaction among electrons and electrons with nuclei from $F[n(\mathbf{r})]$, retaining another universal functional $G[n(\mathbf{r})]$. The only supposition is the clamped nuclei approximation. This new functional inherits the uniqueness and variational properties from the former. Next the assumption of the non-interacting electron gas is introduced in order to split off its kinetic energy from $G[n(\mathbf{r})]$. All the remaining interactions, aside from direct Coulomb, are gathered in the exchange-correlation (xc) functional. Since the exchange energy is known from HF, it can be evaluated over the density, leaving only correlation. The latter can be retrieved by using the correlation in a uniform electron gas, ϵ_c, as a standard unit and weighing according to the density. This then yields the following exchange(x)-correlation(c):

$$E_{xc}[n(\mathbf{r})] = E_x[n(\mathbf{r})] + \int n(\mathbf{r})\,\epsilon_c(n(\mathbf{r}))\,d\mathbf{r} \tag{2.25}$$

If the density is sufficiently slowly varying, $\epsilon_c(n(\mathbf{r}))$ can incorporate the exchange into the integrand as $\epsilon_{xc}(n(\mathbf{r}))$. This simplification does negatively impact the long-range description of the atomic potential. A stable density also has to be *stationary*, i.e. $\int \delta[n(\mathbf{r})]\,d\mathbf{r} = 0$, which leads to a series of one-particle equations:

$$\left[-\left(\epsilon_i + \frac{1}{2}\nabla^2\right) + v_{ext}(\mathbf{r}) + \int \frac{n(\mathbf{r}')}{|\,\mathbf{r}-\mathbf{r}'\,|}d\mathbf{r}' + \frac{dn(\mathbf{r})\,\epsilon_c(n(\mathbf{r}))}{dn(\mathbf{r})} + \int \frac{\sum_j \psi_j(\mathbf{r})\,\psi_j^*(\mathbf{r}')}{|\,\mathbf{r}-\mathbf{r}'\,|}\psi_i(\mathbf{r}')\,d\mathbf{r}'\right]\psi_i = 0 \tag{2.26}$$

The fourth term $(dn(\mathbf{r})\,\epsilon_c(n(\mathbf{r}))/dn(\mathbf{r}))$ has a definition similar to a chemical potential $\mu_c(n(\mathbf{r}))$ from the correlation's contribution to the electron density. This connects a part of the electron potential to a thermodynamic concept that will fill up sparse regions. The solutions are called Kohn-Sham (KS) orbitals and define the electron density $n(\mathbf{r}) = \sum_i \lambda_i\,|\,\psi_i(\mathbf{r})\,|^2$ with λ being the occupation

number. The appearance of the KS orbitals in the Hamiltonian necessitates a self-consistent approach.

Now that both exchange and correlation interactions have been relegated to a single functional, all that remains is to determine its mathematical expression. This task is far from trivial, as in a sense this term summarizes the unknown aspects of electronic structure theory. Mainly, there are two philosophies to constructing functionals. On the one hand there are the *empiricists* who fit a wide range of variables. This often leads to hyper-specialized functionals with little expansion capabilities. The *reductionists* on the other hand, try to derive functionals entirely from QM. They employ simple models that act as limiting cases for the electron gas. Considering their impact on the Solid State community and the insights that are to be gained from them, this thesis will explore the reductionist's view. The red thread throughout comes in the form of a classification system created by John Perdew.[15] It counts how many exact physical constraints (or insights) each functional meets and explores how to add the missing ones without losing the former. Perdew has been termed this approach *phytting*. Alluding to the Biblical verses of Genesis 28.10-12, the classes are hierarchically ordered in *Jacob's Ladder*. Its rungs lead from the Hartree-world up to the 'heaven' of exact xc. As of the time of this writing, a total of 17 constraints are known:

1. **Exchange:**

   (a) **Negativity:** the exchange contribution always lowers the energy ($E_x < 0$).

   (b) **Spin scaling equality:**[37] the total exchange energy in spin-polarized systems is well-defined. It amounts to a sum over the separate spin-densities.

$$E_x\left(n_\alpha, n_\beta\right) = \frac{1}{2}\left[E_x\left(n_\alpha, n_\alpha\right) + E_x\left(n_\beta, n_\beta\right)\right] \tag{2.27}$$

   (c) **Uniform density scaling:**[38] varying the uniform electron gas along all three spatial dimensions, results in a linear behavior of the correlation energy.

$$E_x\left[\gamma^3 n\left(\gamma \mathbf{r}\right)\right] = \gamma E_x\left[n\left(\mathbf{r}\right)\right], \gamma \in \mathbb{R} \tag{2.28}$$

   (d) **Fourth order gradient expansion:**[15] the exchange energy can be expanded to fourth order.

$$E_x^{\mathrm{GE4}}\left[n\left(\mathbf{r}\right)\right] = \int n\left(\mathbf{r}\right) E_x^{\mathrm{uniform}}\left[n\left(\mathbf{r}\right)\right] - 2.382 \times 10^{-3} \frac{\mid \nabla n\left(\mathbf{r}\right) \mid^2}{n^{4/3}\left(\mathbf{r}\right)} - 3.633 \times 10^{-5} \frac{\mid \nabla^2 n\left(\mathbf{r}\right) \mid^2}{n^2\left(\mathbf{r}\right)} + 9.083 \times 10^{-5} \frac{\mid \nabla n\left(\mathbf{r}\right) \mid^2 \nabla^2 n\left(\mathbf{r}\right)}{n^3\left(\mathbf{r}\right)} + \alpha_x \frac{\mid \nabla n\left(\mathbf{r}\right) \mid^4}{n^4\left(\mathbf{r}\right)} d\mathbf{r} \quad (2.29)$$

(e) **Finite non-uniform scaling limit**

(f) **Thight lower bound for two-electron densities**

2. **Correlation:**

(h) **Non-positivity:** the correlation energy will never destabilize the system ($E_c \leq 0$).

(i) **Second order gradient expansion:** In a slowly-varying density of a closed-shell system $\left(n_\alpha\left(\mathbf{r}\right) = n_\beta\left(\mathbf{r}\right) = n\left(\mathbf{r}\right)/2\right)$, the kinetic energy density τ can be written out in function of the density and its first-and second gradients using the second order gradient expansion (GE2). This expansion can be used in the Fourth order gradient expansion.

$$\left[\tau_\alpha\left(\mathbf{r}\right) + \tau_\beta\left(\mathbf{r}\right)\right]^{\mathrm{GE2}} = \frac{3}{10}\left(3\pi^2\right)^{2/3} n^{5/3}\left(\mathbf{r}\right) + \frac{1}{72}\frac{\mid \nabla n\left(\mathbf{r}\right) \mid^2}{n\left(\mathbf{r}\right)} + \frac{1}{6}\nabla^2 n\left(\mathbf{r}\right) \quad (2.30)$$

(j) **Uniform density scaling to the high-density limit:** The correlation energy converges to an asymptotic value as density of the uniform electron gas increases.

$$E_c\left[\gamma^3 n\left(\gamma\mathbf{r}\right)\right] = \mathbf{constant}; \gamma \to \infty \quad (2.31)$$

(k) **Uniform density scaling to the low-density limit:** In the low-density regime, the energy of an uniform electron gas scales linearly.

$$E_c\left[\gamma^3 n\left(\gamma\mathbf{r}\right)\right] = \gamma E_c\left[n\left(\mathbf{r}\right)\right]; \gamma \to 0 \quad (2.32)$$

(l) **Zero correlation energy for one-electron densities:** the correlation energy is vanishing when there is only a single spin-state, i.e. $n_\alpha = n\left(\mathbf{r}\right)$ and $n_\beta = 0$.

(m) **Finite non-uniform scaling limit**

3. **Exchange and correlation:**

   (n) **Size-extensivity:** This is a more rigorous definition of *size-consistency* in terms of linked diagrams. Since in the context of DFT linked diagrams are undefined, both terms overlap. Size-consistency then entails that evaluating the energy of a system of non-interacting constituents (e.g. atomic distances diffusing away) yields the sum of the individual constituents.

   (o) **General Lied-Oxford lower bound:**

$$E_{xc} \geq -1.679 \int n^{4/3}(\mathbf{r})\, d\mathbf{r} \tag{2.33}$$

   (p) **Weak spin-polarization dependence in low-density limit**

   (q) **Static linear response of the uniform gas**

   (r) **Lieb-Oxford lower bound for two-electron densities**

Most of these constraints apply to an electron gas with uniform density and certain limiting cases. Although any aspiring functional should fulfill all of them, they cover predominantly theoretical cases. It is important to note that there's no guarantee that a functional on a higher rung will outperform one form a lower rung in every real-world application. The reason for these cases can usually be traced back to error-cancellation. The main concern is that error-cancellations in lower-rung functionals with respect to higher-rung are due to the 'wrong' reasons. For a good example of the inherent dangers of non-physical error-cancellations, one can look the at trend in functionals that has emerged over the past decades. Newer functionals are ever more biased towards better energy accuracies (for their applications in reaction mechanisms) without much regard for the electron density.[39] Any systematic advantages of a higher rung however stem from the ideal cases approximating the system's physical reality at a local rather than a global level. Jacob's Ladder also guarantees that the highest rung corresponds with the Universal Functional and would therefore be fully accurate.[15] Now that these general remarks have been covered, I shall briefly introduce each rung and its specifics:

1. **Local Density Approximation (LDA):** here the electron gas is modeled as a uniform electron gas. Correlation is introduced via the Pauli exclusion principle, forcing electrons to occupy ever higher states. Both correlation

and exchange energies are defined only in terms of the spin-resolved electron densities $n_\alpha(\mathbf{r})$ and $n_\beta(\mathbf{r})$, making it fully local. LDA fulfills the following constraints: 1(a-c) and 3(n,q). The size-consistency (3n) is instrumental for obtaining consisting adsorption/desorption energies. The other constraints enforce a correct description of the uniform electron gas. The conceptual similarities with metals explain the revolutionary success that LDA had in these systems. As noted before, this implies that it should also function well for slowly varying electron densities, which can be locally approximated as being uniform. Its main drawback is that it often overestimates atomization energies. This is partially attributed to the correlation energy being overestimated almost twofold compared to advanced post-Hartree-Fock methods.

2. **Generalized Gradient Approximation (GGA):** For slowly-varying densities, the leading correction is the second gradient correction approximation (GE2), which adds $C_{x/c} \mid \nabla n(\mathbf{r}) \mid^2 / n^{4/3}$ to both the LDA exchange and correlation energies. The defining feature here are the gradient variables $\nabla n_\alpha(\mathbf{r})$ and $\nabla n_\beta(\mathbf{r})$. Since the density now requires information at $\mathbf{r}$ and from its immediate surroundings $\mathbf{r} + \Delta\mathbf{r}$ for numerical gradient, it has become semi-local. If implemented as is however, the correlation energy will turn out positive for realistic materials. This breaks with constraint 2(h), leading overall worse results than LDA. The problem traces back to a faulty description of the correlation holes. One way to circumvent these issues, is to apply a cutoff to the correlation interaction. The cutoff radius does not significantly alter the form of the correlation energy in slowly-varying (i.e. near-uniform) densities, but it does for the exchange term. Instead, the high-density limit of the exchange is used as an approximation ($C_x \approx -C_c(\infty)$), analogous to the correlation behavior (see 2j). The cutoff radius can either be fitted or derived using fundamental parameters only. The latter category is called *non-empirical*, of which the most well-known GGA functional used in Solid State Physics and Heterogeneous Chemistry is Perdew, Burke and Ernzerhof functional (PBE).

3. **meta-generalized Gradient Approximation (meta-GGA):** as pointed out in GGA, both previous rungs break down at low-densities and strongly interacting systems. From an energetic point of view, the error there comes from the unphysical direct interaction an electron with itself, or *self-correlation*. That is to say: $E_x[n_{1e^-}(\mathbf{r}), 0] \neq 0$. Self-correlation in turn causes incorrect symmetry-breaking of the density and an increased energy. The workaround starts from correctly identifying and then eliminating one-electron regions. To this end the kinetic energy density $\tau(\mathbf{r})$, defined as $\sum_{i,\sigma}^{occ} \left[\nabla\phi_{i,\sigma}(\mathbf{r})\right]^2$, is

introduced as another variable.[40] Within the one-electron regions, the spin kinetic energy as a known behavior: $\tau_\sigma = \mid \nabla n_\sigma(\mathbf{r}) \mid^2 / 8 n_\sigma(\mathbf{r})$.

As such, a properly constructed meta-GGA is then free from self-correlation error, while still obeying all previously set constraints. The kinetic energy is related to the Laplacian of the density $\nabla^2 n(\mathbf{r})$, as in the exact second order expansion of 2(i). Therefore, it is not uncommon for this variable to be the defining trait of meta-GGA. As such, the constraints 1(d) can also be enforced now, yielding the exact exchange up to fourth order. With $\nabla^2 n(\mathbf{r})$ added, meta-GGAs are now no longer (semi-)local with respect to the density. In the construction of their KS orbitals however, they still are. Hence, the evaluation of their functionals is barely more demanding than GGAs. The biggest hurdle in their implementation is the evaluation of the functional derivative. It can be mitigated via orbital averaging, but remains complex.

4. **Exact exchange and compatible correlation (XXMC):** The next step would be to obtain an exact exchange functional. The xc energy is defined in terms of a coupling constant between the exchange and correlation. Both separate out into individual terms:

$$E_{xc}^{exact} = \frac{1}{2} \int \int \frac{n(\mathbf{r}) \bar{n}_{xc}(\mathbf{r}, \mathbf{r}')}{\mid \mathbf{r} - \mathbf{r}' \mid} d\mathbf{r} d\mathbf{r}' = E_x^{exact} + E_c^{exact} \tag{2.34}$$

$$\bar{n}_{xc}(\mathbf{r}, \mathbf{r}') = \int_0^1 \frac{\langle \chi_\alpha | \hat{n}(\mathbf{r}) \hat{n}(\mathbf{r}') | \chi_\alpha \rangle}{n(\mathbf{r})} - \delta(\mathbf{r} - \mathbf{r}') \, d\alpha = n_x(\mathbf{r}, \mathbf{r}') + \bar{n}_c(\mathbf{r}, \mathbf{r}') \tag{2.35}$$

Here, α toggles the electron-electron interaction between *off* (0) and *on* (1). Consequentially, at $\alpha = 0$ all correlation vanishes. The xc benefits from mixing some exact exchange: $E_{xc}^{XXMC} = E_{xc}^{GGA} + \alpha \left(E_x^{exact} - E_x^{GGA} \right)$. In fact, it is mandatory in the high-density limit. Remark that the integral now entails full non-locality for the densities (and the KS orbitals alike). From tests on atomization energies, the optimal coupling constant α is found to be 0.25. To satisfy the high-density limit however, α has to be 1.00. So clearly, a compromise has to be made. At the same time, an exact exchange functional adheres to Coulomb's law in the long-range, while its energy equals $-\frac{1}{2} \int \int \frac{n(\mathbf{r}) n(\mathbf{r}')}{|\mathbf{r} - \mathbf{r}'|} d\mathbf{r} d\mathbf{r}'$ for one-electron densities.

Correcting the exchange would be the first big step to describing excited systems, their time-dependence, and related quantities such as polarizabil-

ity. In atomic systems it would also improve the sp and sd transfer energies, as well as core-valence excitations for obvious reasons. Unfortunately, the solution is not as easy as naively adding exact exchange. Both exchange and correlation holes observe long-range interactions that compensate for one and another. Since the exact exchange is added to a meta-GGA basis, the correlation is still semi-local, creating an imbalance. This effect plays a large role in multi-atomic systems. In 2001, when the Ladder was first proposed, there were two major routes to circumvent this issue. One approach is to add a region-selective exchange correction to the correlation functional. When tuned to exchange-dominated regions, the xc will have an exact exchange functional. Outside those regions, it reverts back to the xc in meta-GGAs. This method is called hyper-generalized Gradient Approximation (hyper-GGA)[15] and it selectively curbs the long-range effects of the exchange functional. Alternatively there is the Correlation Factor Model, which constructs a special xc density from the exchange density, using the correction factor. It is computationally quite demanding due to its non-locality and spherical averages for the exchange holes.

5. **Exact exchange and exact partial correlation:** On the last defined rung, the non-local functionals employ occupied and unoccupied KS spin-orbitals alike. The exact correlation can be developed into series of which only a part gets evaluated. Hence the name *partial correlation*. As mentioned in the previous rung, having the correlation compensate for the exchange in the long-range interactions is key. There is still much work left in this field, but two general strategies are being pursued. One is interpolating the expressions for the W_λ integrand in $E_{xc}\left(n_\alpha, n_\beta\right) = \int_0^1 W_\lambda\left(n_\alpha, n_\beta\right)$. The expressions at interval edges of λ are known, as they correspond the weak and strong interactions, respectively. To evaluate the integral, one needs Interaction Strength Interpolation. The end result yields exact correlation in the high-density limit. Another approach consists of using the Random Phase Approximation (RPA) with the right functional. This technique is discussed in greater detail later on (see section 2.1.4).

6. **Exact Density Functional Theory**

It is safe to say that the lower two rungs (LDA and GGA) have been well-covered in the past decades. Currently, some attempts at meta-GGAs[41] and hyper-GGAs[42] have been made, but these methods are still far from commonplace.

There are two possible caveats with GGA. The first lies in the actual parametrization of the (second order expansion of the) exchange (eq. 2.36) and

correlation (eq. 2.37) functionals. Here, $s = \frac{\nabla n(\mathbf{r})}{2k_{x/c}n(\mathbf{r})}$ stands for the dimensionless density gradient, which denotes the deviation from the homogeneous gas ($s = 0$). By toggling the strength of the added gradient term (μ), one skews the functional to retrieve better atomization and total energies (strong dependence) or better lattice parameters and surface energies (weak dependence). From expanding the exchange energies of neutral atoms in terms of their core-charge, one can derive that μ should be $20/81$. To describe instead slow-varying densities (such as the variance electrons in solids) $\mu = 10/81$ is preferable. This is another consequence of the GGA expression being incomplete, forcing the user to compromise.

$$E_x^{GGA}[n(\mathbf{r})] = \int \epsilon_x^{unif}[n(\mathbf{r})] \left\{1 + \mu s_x^2 + \cdots\right\} d\mathbf{r} \tag{2.36}$$

$$E_c^{GGA}[n(\mathbf{r})] = \int \left\{\epsilon_c^{unif}[n(\mathbf{r})] + \beta s_c^2 + \cdots\right\} d\mathbf{r} \tag{2.37}$$

To conclude, I will briefly introduce a couple of functionals that are relevant to Solid State calculations.

1. **PBE:** is a non-empirical GGA functional that respects the constraints 1(a-c), 2(h-k), and 3(n-q). It bears the strong μ-value match slow-varying, high-density regions as found in atoms and molecules. While LDA underestimates the lattice parameters values by about 1%, PBE overestimates their experimental value nearly equally. This obviously cascades into all lattice-derived properties, such as bulk moduli, phonon frequencies, magnetism, and ferroelectricity. When it comes to surfaces, both LDA and PBE over-stabilize the surface energies and over-bind adsorbates, although PBE is less severe. In the low-frequency regime (wave-vector $< 2k_F$), this response function is nearly frequency-independent. It can thus be approximated by LDA response, which is completely frequency-independent. For GGA to meet the same requirement, the quadratic exchange and correlation terms should cancel, i.e. $\mu = \pi^2\beta/3$ or $\beta = 0.0375$.

2. **PBEsol:**[43] focuses, as the name suggests, on the solids and bears the μ-value complementary to PBE. Since its exchange functional has changed now, its correlation should change to match it. The β_{sol} parameter is fitted to the homogeneous gas in the jellium model. The xc of this model can be expanded into geometric descriptors, such as volume (V) and area (A): $E_{xc}^{jellium} = \epsilon_{xc}^{unif} V + \epsilon_{xc}^{surf} A + \cdots$ Either one of these descriptors can be fitted to. Using for example the area, yields $\beta_{sol} = 0.046$. Perdew, Burke and Ernzerhof functional adapted for solids (PBEsol), with only a

2.7% overshoot, then matches the experimental values much better than LDA (27%) or PBE (−11%). PBEsol even becomes exact in the limit of extremely compressed solids as their density reaches near-uniformity and the exchange term dominates. Lastly, I would like to point out that the altered β_{sol} breaks with the exact XC-response to an external, wave-like, perturbing potential.

3. **Strongly constrained and appropriately normed (SCAN):**[41] This is the first-ever functional to satisfy all 17 conditions and falls within the meta-GGA category. The SCAN functional employs an enhancement factor $F_x(s, \alpha)$ in the exchange energy:

$$E_x[n(\mathbf{r})] = \int n(\mathbf{r})\, \epsilon_x^{unif}[n(\mathbf{r})]\, F_x(s, \alpha)\, d\mathbf{r} \tag{2.38}$$

The kinetic offset $\alpha = \frac{\tau - \tau^{single-orbital}}{\tau unif}$ measures the binding character, e.g. covalent single bond ($\alpha = 0$), metallic nature ($\alpha \approx 1$), weak bonded ($\alpha \gg 1$). Contrary to other meta-GGAs, SCAN has different $s \to \infty$ limits for the various α zones as shown in Figure 2.3. Most meta-GGAs instead converge to the Lieb-Oxford limit (3r). The correlation enhancement on the other hand is interpolated between $\alpha = 0$ and 1, after which it is extrapolated to $\alpha \to \infty$. Despite its improved performance on atoms and molecular systems, trials with ceria indicate that it fails at charge localization after vacancy formation.

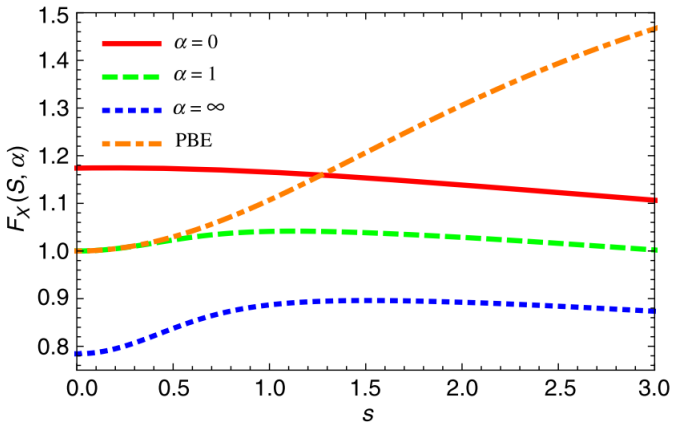

Figure 2.3: The exchange enhancement factor $F_x(s, \alpha)$ for a spin-unpolarized system of various kinetic offsets. The orange line compares it to PBE.

The second caveat to GGA comes from the self-correlation error mentioned in meta-GGA. This error is particularly high in cases where the valence electrons, often from the d or f-orbitals, strongly interact. Rare-earth metals and their oxides fall within this category. I shall discuss three types of alternative solution to this error besides meta-GGA. Each one has been used in Chapter 3.

Hubbard correction

In his original paper, Hubbard described how transition and rare-earth metals display both a band structure and an atomic structure.[44] His work laid the foundation for an ad hoc energy term that pushes the system's atomistic properties to the foreground. In the original version, two terms $E_{Hubbard}$ and E_{dc} are added.[45] $E_{Hubbard}$ is based on the HF energy between spin-orbitals of the same atom and azimuthal quantum number l. The individual integrals are weighted by the parameters F_0, F_2 and F_4 (F_6 in case of f-orbitals). E_{dc} on the other hand prevents double-counting and is expressed as:

$$E_{dc} = \frac{1}{2}\sum_i \left[U n_i \left(n_i - 1\right) - J\left(n_i^{\alpha}\left(n_i^{\alpha} - 1\right) + n_i^{\beta}\left(n_i^{\beta} - 1\right)\right)\right] \tag{2.39}$$

The parameters U and J regulate the total number of valence orbitals per atom and the individual spin-orbitals, respectively. This means that double-counting only has to be accounted for in magnetized systems. Both parameters depend on the F-set, where U bears a one-on-one connection with F_0, and J with the rest. A major disadvantage of this formulation is its basis set dependence. This means that any matrix construction cannot simply be diagonalized. In order to preserve one of the fastest, most optimized algorithmic steps Cococcioni and de Gironcoli removed the higher order F parameters and put F_0 center stage:

$$E_U\left(\mathbf{n}_{I,\sigma}\right) = E_{Hubbard}\left(\mathbf{n}_{I,\sigma}\right) - E_{dc}\left(\mathbf{n}_{I,\sigma}\right) = \frac{U_{eff}}{2}\,\mathrm{tr}\left[\mathbf{n}_{I,\sigma}\left(1 - \mathbf{n}_{I,\sigma}\right)\right] \tag{2.40}$$

U_{eff} underlines that the effect in J are either negligible or can be incorporated into U as $U_{eff} = U - J$. The parabolic function (after diagonalization into an occupation matrix) has its zero points at $n_{eigen} = 0$ or 1. This means that any partial occupation results in an energy penalty. Under the assumption that the atom's surroundings provide an infinite electron reservoir, the chemical potential between two filled shell states is a linear interpolation. Under the effect of the residual Hartree energy, which is a mostly quadratic function, the curvature is incorrect. Normally, the xc pads this error out from the third rung on. Here, U_{eff} amounts to the same when it is equal to $\frac{d^2E}{dN^2}$, where N is the on-site occupation with

the density $n(\mathbf{r})$. In actual solids, the curvature also incorporates hybridization effects which should persist under the Hubbard correction. Thus when computing U_{eff}, their contributions have to be subtracted. Since the non-interacting part from LDA (or whichever functional for that matter) experiences the same hybridization, it can be used to filter these effects out. The Janak theorem allows us to recast U_{eff} in terms of first order derivatives $\sum_i \frac{d\epsilon_i}{dN} - \frac{d\epsilon_i^{KS}}{dN}$ with ϵ_i and ϵ_i^{KS} being the eigenvalues of the total and non-interacting functional respectively.[46] By defining a perturbation to the system as the flux with the electron reservoir, one can also use the density response functions to obtain $U_{eff} = \sum_i \chi_i^{-1} - \chi_{0,i}^{-1}$. Later I shall show how this formulation is the same integration kernel in RPA. In that sense, this flavor of the Hubbard correction only retains a local scope[†] of RPA. In the linear response theory U_{eff} is then derived by first numerically computing the response, i.e. the second derivative of the on-site occupation with slight shifts in the applied potential. The advantage in this formulation is that the energy shift is a one-dimensional variable, whereas the electrons can be rearranged in several ways of which only the minimum energy counts. The χ_0 term then is the immediate (i.e. non-selfconsistent) response of the density, while χ allows it to screen the electron flux in a self-consistent manner. This approach based on linear response theory (LPT) is internally consistent. Actual applications of LPT are restricted to a finite-size supercell as reservoir. The supercell is then scaled until the responses converge. To achieve convergence faster, an additional charge neutrality condition is added as a background charge. As such, the leading terms in the interaction of the perturbation with its images cancel. Even when both responses converge, their inverses might require larger supercells. Therefore, the results are extrapolated to larger cell sizes. In this section I have only discussed how to converge the Hubbard parameters using the energy. Considering the central role of the electron density in any quantum observable one could construct other, analogous procedures. The same holds, in case one wants to reintroduce spin-effects with the J parameter.

To finish this section, I shall briefly discuss role of Hubbard in ceria (CeO_2 and Ce_2O_3) systems. CeO_2 is a common catalyst in redox reactions, where electron transfer processes are key. It is clear that reducing the formal oxidation state from Ce^{4+} to Ce^{3+} leads to a change in occupation. Unless the chemical potential remains constant (like in Figureeffig:hubbard), the energy curvature changes with the occupation number and also the (effective) Hubbard parameter(s). Eventually, in a chemical reaction all that matters are relative energies rather than absolute. A good case study examined the first dehydrogenation step in the catalyzed formaldehyde conversion.[16] The issue is exactly as postulated above: passing

[†]In the sense of density fluctuations.

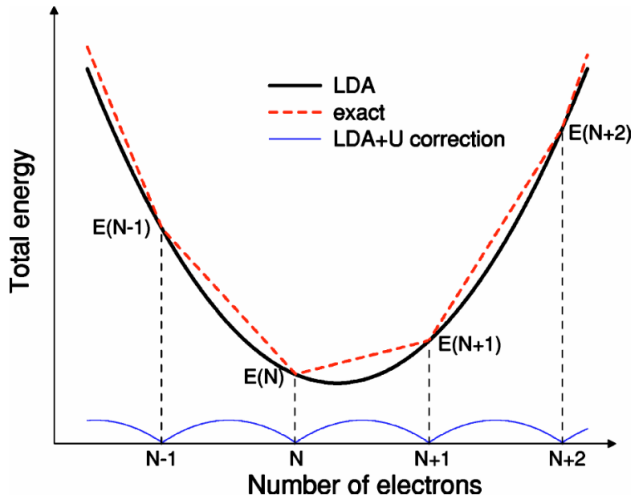

Figure 2.4: Example of a LDA (red dashed) fitting of the energy profile (black solid). The Hubbard parameter (blue solid) corrects for the energy difference, depending on the partial occupancy. Taken from ref. 46.

a threshold, the reaction energies in the Ce^{3+} system linearly stabilize with increasing U_{eff}. The threshold is reached once the transfered electron localizes at the target site. At the same time, the Ce^{4+} system is independent from the Hubbard term. Remarkably, the transition state of the electron transfer ends up lying right in between both endpoints. Since only one example of each type exists, it is difficult to extend these conclusions to other reactions. It is known however from experimental results that $U_{eff} < 5.5$ eV forms an upper-limit to the reaction barrier.

Post-DFT: Random Phase Approximation

In the discussion on Jacob's Ladder, at the fifth rung the RPA was put forth as a feasible approach. The fifth rung tackles exact correlation, which when off-set with (exact) HF exchange, removes all self-interaction energy.[47] Up to date, no functional exists which incorporates RPA directly as an energy term. Instead, RPA is applied as a post-processing methods for density functional theory (post-DFT) correction to the ground state energy. Although in theory this post-processing can still happen in a self-consistent manner, computational cost and memory limitations force most applications to adopt a LDA or GGA reference wavefunction.

The name RPA refers to the early work of Bohm and Pines, where they decouple the response of the homogeneous electron gas to external perturbation into

the plasmonic motion of the whole gas and the individual particles' movements.[19] Since the phases of these individual electrons are out of sync, their contributions average out to zero. Only including the plasmonic response then yields the random phase approximation. This model would later on form the basis for modern RPA implementations. The most common one starts from the adiabatic connection (AC). Within this context, the total Hamiltonian is approximated with a switch variable λ running from 0 to 1: $\hat{H}(\lambda) = \hat{H}_0 + \lambda\hat{H}_1(\lambda)$, so

$$E(\lambda = 1) = \langle\Psi_0|\hat{H}_0|\Psi_0\rangle + \int \langle\Psi_\lambda|\hat{H}_1(\lambda) + \lambda\frac{d\hat{H}_1}{d\lambda}|\Psi_\lambda\rangle\, d\lambda \tag{2.41}$$

Here, the reference Hamiltonian $\hat{H}_0$ corresponds to the single particle energies from the mean-field approximation. It is extended to include electron-electron interactions, and for the intent of RPA also the xc hole. This hole refers to the depletion in certain regions as a consequence to renormalized density fluctuations. The grand physical insight comes from the fluctuation-dissipation (FD) theorem that links the xc hole to a path integral of the linear response term χ^λ, or polarization. This response term calls back to the plasmon movement from before and can thus be expressed in terms of Green functions.[48] The linearity refers to how the energy scales along path. Remark that the path is chosen so not to disturb the density. As such, the response function can then be written out as:

$$\begin{aligned} E_{xc}^{RPA} = E_x^{exact} + E_c^{RPA} = &-\int \sum_{ij}^{occ} \frac{\psi_i^*(\mathbf{r})\,\psi_j(\mathbf{r}')\,\psi_j^*(\mathbf{r})\,\psi_i(\mathbf{r}')}{|\,\mathbf{r}-\mathbf{r}'\,|} d\mathbf{r}d\mathbf{r}' \\ &+ \frac{1}{2\pi}\int \mathrm{tr}\Big(\log\Big(1-\chi^0(i\omega)\,v\Big) + \chi^0(i\omega)\,v\Big)d\omega \end{aligned} \tag{2.42}$$

$$\chi^\lambda_{RPA}(\mathbf{r},\mathbf{r}',i\omega) = \chi^0(\mathbf{r},\mathbf{r}',i\omega) + \int \chi^0(\mathbf{r},\mathbf{r_1},i\omega)\,\frac{\lambda}{|\,\mathbf{r_1}-\mathbf{r_2}\,|}\,\chi^\lambda_{RPA}(\mathbf{r_2},\mathbf{r}',i\omega)\,d\mathbf{r_1}\mathbf{r_2} \tag{2.43}$$

Eq. 2.42 separates the response function into the HF exchange (based on the KS orbitals) and adiabatic connection applied to fluctuation-dissipation (ACFD)-RPA correlation terms.

The strength of RPA shines within the greater framework of functional construction since it bridges approaches from mean-field theory and quantum chemistry. Its Goldstone diagrams are namely explicitly known and can very easily be compared with those of MP2, single-particle Green functions G multiplied with the screened interaction matrix W (GW)[49]), and Coupled Cluster with double excitations only (CCD). In each of these cases, RPA either partially overlaps or

constitutes a full subset of an infinite summation. Diagrammatically, the correlation energy accounts for all particle-antiparticle rings in a photon propagation. These rings add up to a geometric series that converges. The leading term in the series corresponds to the direct energy in MP2. In GW, a product of the Green functions from $\hat{H}_0$ and underlying self-energy matrix can be treated in the AC scheme to retrieve RPA. Even though RPA is free of self-energy, it is not for self-polarization. The latter is the erroneous incorporation of the electron (or a hole) into its own screening. In the case of CCD, one obtains an assortment of diagrams. The ring diagrams are found by solving the equation $B + AT + TA + TBT = 0$, where B stands for the classical Coulomb interaction between occupied and virtual orbitals, A for the excitation energies and exchange interaction, and T the weight matrix to be solved. The RPA correlation energy is simply the Coulomb interaction with the solution: $E_c^{RPA} = \frac{1}{2}\,\mathrm{tr}\,(BT_{sol})$. Conversely, this direct ring CCD can also be interpreted as the interaction between plasmon oscillations of two electron gases.[50] One only accounts for single-electron excitations, while the other also allows de-excitation. The combination leads back to a double excitation. In the short-range (SR), the xc hole is not strictly negative anymore and errors start to appear. Perdew and coworkers showed that mixing in correlation energy from LDA or GGA corrects for these errors, leading to a version called RPA+.[51] Even so, the difference between RPA and RPA+ is only appreciable in systems with a vanishing long-distance interactions, such as atoms. The atomization energies of molecules or the surface energies of metals on the other hand already achieve chemical accuracy. The latter can be explained by the exactness of RPA at high densities.

To finish this part, I shall briefly discuss the importance of RPA in the case of CO adsorption onto copper (Cu) (111).[19] Despite its simple appearance, many functionals wrongly adsorb CO at the hollow site rather than on top, where it is less coordinated.[52] Climbing the Ladder, LDAs and GGAs fail qualitatively. Only by mixing in exact exchange with PBE0 (PBE0) is qualitative agreement reached. Still, both sites lie close in adsorption energy (less than 0.1 eV difference) and in a reaction path, both would adsorb CO equally. Clearly, exact exchange has to accommodated for with (near-)exact correlation. Regardless of the starting functional, be it PBE or PBE0, non self-consistent RPA yields the same adsorption energy distribution. The difference remains 0.22 eV, consistent with experimental findings. Remarkably, in the overall trend the absolute adsorption energies also drop as one climbs the Ladder. This shows that a overall the xc hole has a negative contribution to the bonding energy. From an implementation point of view, note that overcome the computational cost, RPA was performed on Cu clusters rather than an extended slab. The clusters then were gradually grown until

the RPA correction converged with respect to PBE. Regarding the scaling, RPA with projector augmented wave (PAW) orbitals naturally scales with an order of $O\left(N_{PAW}^2 N_{occ}^2 N_{eig}\right) \sim O\left(N^4\right)$. Atom-centered orbitals used to have more issues $\left(O\left(N^6\right)\right)$, but by recasting it into plasmon-pole formulation and applying the resolution-of-identity technique, RPA also scales as $O\left(N^4\right)$. Table 2.1 compares the scaling of several aforementioned methods.

Table 2.1: Overview of the most important algorithms discussed in this chapter and their scaling. The methods (grey) are divided in the initial calculations and available post-processing. Stochatic MP2 has varying scaling depending on the error margin allowed and other conditions (see 2.1.3).

start	HF			DFT(+U)
	$O(3)$			$O(3)$
post	MP2	LTMP2	stochatic MP2	RPA
	$O(5)$	$O(4)$	$O(4) - O(1)$	$O(4)$

Hybrid functionals

Similar to RPA, the AC can also derive different schemes, depending on the particular choice of reference $\hat{H}_0$ and expansion $\hat{H}_1$ Hamiltonians. In any derivation however, the main objective is to account for the electron gas screening two interacting electron charges. Whereas Hubbard and RPA correct screening via correlation, *hybrid functionals* mix HF exchange in with that of DFT. Their success is based on the apparent inclusion of static correlation that delocalizes the DFT exchange hole. In this section, I shall discuss two families of hybrid methods and how they interlink. The first family, Heyd–Scuseria–Ernzerhof functional (HSE)[53] originates from the observation by Kohn that the exchange interaction in insulators decays exponentially with the band gap. Systems with a vanishing band gap, such as metals, display an algebraic decay on the other hand. Considering that long-range (LR) DFT exchange can be efficiently computed with the fast multi-pole method but HF cannot, the HF scope is reduced to SR interaction only. Using the errorfunction and its complement, the Coulomb operator is separated into the its LR and SR parts respectively. This yields a steady decrease (SR)/increase (LR) of both components rather than a hard cut-off. A screening parameter ω controls the point where one component overtakes the other. In HSE03 this point lies at approximately 0.143 Å(ω = 0.3 Å^{-1}), while in HSE06 it shifts closer to 0.095 Å(ω = 0.2 Å^{-1}). Considering the distinct advantages of Perdew's PBE, this functional is mixed in, yielding:

$$E_{xc}^{HSE} = \alpha E_x^{HF,SR}(\omega) + (1-\alpha) E_x^{PBE,SR}(\omega) + E_x^{PBE,LR}(\omega) + E_c^{PBE} \quad (2.44)$$

Note that in the limit of vanishing SR ($\omega \to \infty$) the PBE xc is retrieved. The value of the mixing parameter α now can either be fitted or theoretically. In case of the latter perturbation theory returns $\alpha = 1/4$. The theoretical value also makes that in the limit of vanishing LR ($\omega \to 0$), one obtains PBE0. In the case of magnetic systems with many low-lying minima, such as the light-harvesting Prussian Blue and $BiVO_4$, an α-value of 0.13 (HSE03) yields better band gaps.[54] Lastly, it should be mentioned that slight alterations on the expansion of the errorfunction allow HSE to retrieve the Lieb-Oxford lower-bound (condition 3(o)). Even though other HSE implementations fail at this, the energy difference in the xc is within the order of mHartree ($\sim$ 27 meV).[55]

The PBE0 model which was mentioned briefly before, is remarkable in that it falls at the intersection of two hybrid families. The first one, HSE, was discussed above. The second is called AMC*n*, where the *n*-parameter denotes the number of (emperical) parameters.[56] The most general version is AMC3, which mixes two rungs (LDA and GGA) with HF:

$$E_{xc}^{AMC3} = E_{xc}^{LDA}\alpha_1 \left(E_x^{HF} - E_x^{LDA}\right) + \alpha_2 \Delta E_x^{GGA} + \alpha_3 \Delta E_c^{GGA} \quad (2.45)$$

By adsorbing the LDA terms into the GGA, AMC3 simplifies to AMC1:

$$E_{xc}^{AMC1} = E_{xc}^{GGA}\alpha_1 \left(E_x^{HF} - E_x^{GGA}\right) \quad (2.46)$$

The same perturbation theory still holds, so that theoretically α_1 should equal 1/4. In which case there are no empirical parameters left anymore and one obtains AMC0 (also called mPW0). The AMC0 is competitive with B0LYP. Up to now I have not specified the GGA functional for AMC. Choosing PBE for AMC0 then retrieves PBE0. Figure 2.5 gives a summary of the discussion.

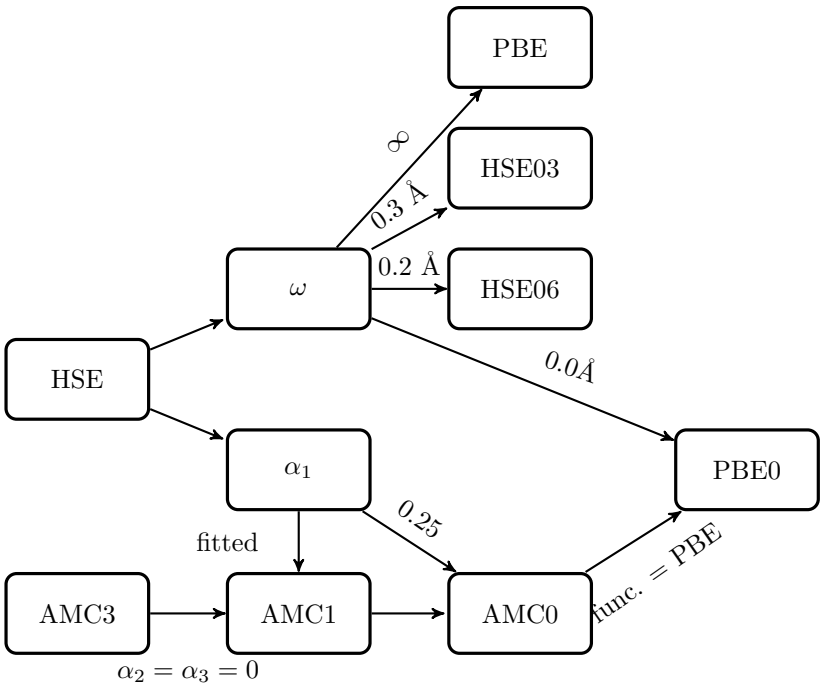

Figure 2.5: Schematic representation of how the HSE and AMC families cross. The nodes contain either a hybrid functional or a parameter. Each arrow shows which variables to change to alter the functional. PBE0 is a special case where both families converge using only fundamental constants.

Correlation energy: MP2 vs RPA Both MP2 and RPA are post-processing methods that start from different point, but account for additional correlation energy. In MP2, the pertubator consists out of the direct $\left(\hat{J}\right)$ and exchange $\left(\hat{K}\right)$ components. Figure 2.6 shows both in the same order. The exchange now happens between virtual orbitals, but apart from that is completely identical to Fock exchange. Since this added exchange is a consequence of the changing determinant, it is still regarded as correlation. Figure 2.7 on the other hand shows that the leading RPA matches the direct MP2 contribution. The higher order terms account for the ripple effect of the excitation, i.e. screening effects. The electronic fluctuations averaging out and excited electron coupling sounds reminiscent of the van der Waals (vdW) model for instantaneous dipole interaction. In the LR limit, RPA indeed converges to the correct r^{-6} behavior. Hence, RPA incorporates dispersion effects. The same goes for MP2.

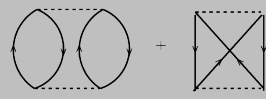

Figure 2.6: Goldstone diagram of MP2

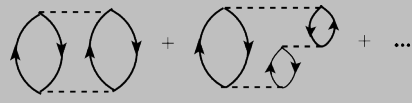

Figure 2.7: Goldstone diagram of RPA

2.1.5 D3: Grimme's method

When scaling up to the inter-molecular level, the forces at play are usually divided into permanent electrostatics (e.g. Coulomb, dipoles, quadrupoles, etc.) and dispersive forces, which arise from coupled fluctuations in the electronic density. At long range, these interactions are poorly accounted for by most correlation functionals. Dipole fluctuations namely entail (short-lived) electronic excitations. This type of interactions becomes dominating for large neutral molecules without any fixed poles and play a role in their physisorption in Heterogeneous Catalysis. Apart from RPA there exist ad-hoc solutions for these cases. Overall, there are three ways of correcting:

1. **Density-based approaches** such as vdW-DFT use an adiabatic integral to add explicitly add long-range interactions. This approach is in essence exact, but in practice has to be approximated.

2. **Dispersion-correcting potentials** apply a projection-based correction to

the electron-density. It is similar in spirit to the PAW-pseudopotentials (PPs), but with any cut-off radius. The major downside to this approach is that it does not capture the right asymptotic behavior $\left(\sim r^{-6}\right)$ in at the extreme long-range. In practice, it does capture dissociation well, as long as the products are not removed too far.

3. **DFT-D methods** employ a series approximation to dispersion. The series' coefficients are derived from the atomic polarizability.

When appropriate, I applied Grimme's D3 method[57] from the latter family to adsorbing molecules. To better highlight some of the particularities of this implementation, I will be comparing it to its predecessor, DFT-D2. As mentioned above, both methods develop the dispersion interaction into a series of the form:

$$E_{\mathrm{vdW}} = \sum_{A,B} \sum_{n=6,8,10,\cdots} s_n \frac{C_n^{AB}}{r_{A,B}^n} f_{d,n}\left(r_{A,B}\right) \tag{2.47}$$

The functions $f_{d,n}$ damp out the correction at low to mid-ranges in order to avoid double counting. The coefficients C_n^{AB} are defined per atom pair A and B. Whereas in D2 they were interpolated empirically,[57] D3 uses the exact Casimir-Polder formula:

$$C_6^{A,B} = \frac{3}{\pi} \int_0^\infty \alpha^A\left(i\omega\right) \alpha^B\left(i\omega\right) d\omega \tag{2.48}$$

$$C_8^{A,B} = 3C_6^{A,B} \sqrt{s_{4,2}^2 \sqrt{Z_A} \frac{\left\{r_A^4\right\}}{\left\{r_A^2\right\}} \sqrt{Z_B} \frac{\left\{r_B^4\right\}}{\left\{r_B^2\right\}}} \tag{2.49}$$

Here, $\alpha^A\left(i\omega\right)$ stands for the polarizability of atom A and has been pre-computed with time-dependent DFT. Higher order terms can be derived through a recursion formula. In practice however, D3 runs up to the 8^{th} order. D2 on the other hand, only contains the 6^{th} order term. The developers place much more trust in their coefficients than those of D2, as they put $s_6 = 1$ to enforce correct asymptotic behavior. Only when the functional itself already accounts or part of the long-range dispersion (e.g. B2PLYP) can s_6 be diminished to balance the energy out.

The coefficients may seem static, but in D3 they are tailored to account for the local geometry. This feature makes up for the lack of any density-based information. Admittedly, D2 already accounted for carbon hybridization, but

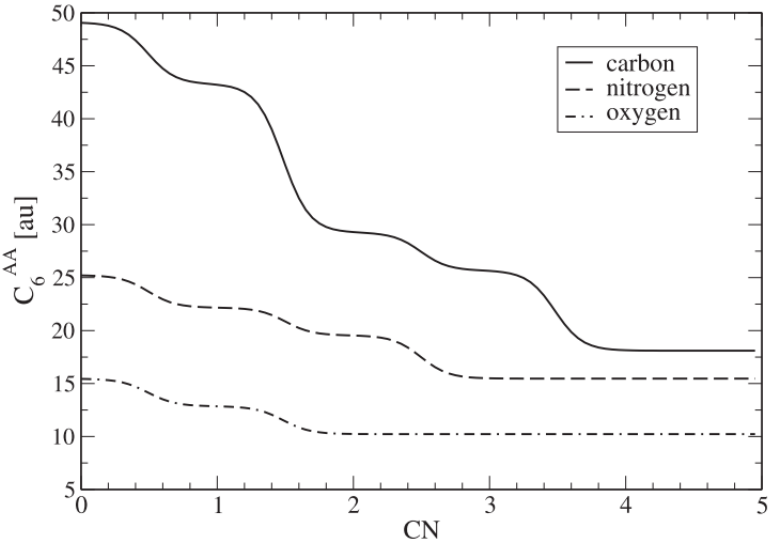

Figure 2.8: Two-dimensional interpolation of the C_6 coefficient between two C, N, and O atoms. Each plateau coincides to a different bond order, increasing from 0 at the left to its full valence at the right. Taken from ref. 57.

it fell short in some cases[‡] and the concept was never expended upon to other atoms. D3 captures the atomic environment by a single real number, namely the fractional coordination number (fCN). All other atoms in the system are taken up in this environment, but weighed using a logistic function of the scaled covalent single-bond radii: $(R_{A,cov} + R_{B,cov})\,/r_{AB}$. This way, any atom having crossed the radial sums is fully counted. Next up, the fCNs have to be combined in order to form two-component coefficients. These components are derived via a two-dimensional Gaussian interpolation scheme that rescales a reference coefficient. The interpolation is done over a grid of anchoring data points and should retrieve both stable coordinations (plateaus) and bond breaking (smooth regions). Figure 2.8 shows the interpolation scheme for CC, NN and OO pairs. Remark how the number of plateaus decreases when moving along the periodic table, accounting for the actual oxidation states.

Apart from the pair-wise interaction, D3 also accounts for triple-atom interactions. The expression is analogous to the pair-wise series, but limited to the 6^{th} order. In addition, it also contains angular information now. When all angles are smaller than 90°, as in densely packed systems, the interaction becomes repulsive.

Before concluding this section, I would also like to point out a couple of flaws

[‡]During a chemical reaction, the change in hybridization was accompanied by an energy jump between states was not continuous nor differentiable.

in D3:

1. There are no parameters to account for the change in polarizability after the electron transfer nor was this accounted for in the data set.

2. In metal systems the covalent radii have to be artificially shrunk.

2.1.6 Pseudopotentials

The valence electrons contribute much more to chemical and transport properties than the core electrons. Since the latter require a higher cutoff energy to be properly described, it would be advantageous if their computation could be circumvented. So instead, the potential energy from each nucleus takes in its surrounding core electrons. The latter are only computed once (in the case of `VASP` by the software distributer) and left unchanged after. This is called the frozen core approximation. The resulting potential is called a PP and has the general form:[58]

$$\hat{v}_{ps} = \hat{v}_{eff} + \sum_{i=1}^{n} \left(\epsilon_{eff} - \epsilon_{c_i}\right) |\chi_{c_i}\rangle \langle\chi_{c_i}| \tag{2.50}$$

Here, c_i counts the core electrons, χ_{c_i} are their one-electron wavefunctions, and ϵ_{c_i} the corresponding energies. Since the density $|\psi_{c_i}|^2$ is mostly centered around a specific nucleus, the PP can be assumed to be local in nature, even though formally it is not. Similarly, $\hat{v}_{eff}$ is the unshielded, electrostatic potential from the nucleus in question and ϵ_{eff} the ground state energy. Solving the modified Hamiltonian $\left(\hat{H}_{ps}\right)$ with the modified wavefunction $\left(\chi_{ps}\right)$ retrieves ϵ_{eff}. The PP thus only modifies the wavefunction around the nuclei but not the single valence electrons' energies.

In the long range, this modified wavefunction $\left(\chi_{ps}\right)$ should still overlap with the original wavefunction $\left(\chi_{eff}\right)$. The point where they start diverging would be the core radius (r_c). Inside the core, the modified wavefunction no longer has to contain nodes as did the original. Indeed, the computational benefit exactly comes from its smoothly decay to zero as it approaches the atom's center. This is commonly referred to as the *softness* of the PP. When expressed as in eq. 2.50, the modified wavefunction has a norm of $1 - \sum_{i=1}^{n} \left|\left\langle \chi_{c_i} \middle| \chi_{ps} \right\rangle\right|^2$. When its norm is not unitary, various observables need to be rescaled throughout the calculations. Constraining $\hat{v}_{\mathrm{ps}}$ to the sum of weighted spherical Bessel-functions remedies this issue, making it now norm-conserving and its radial part (formally) local. `VASP` comes with three major distributions of PPs: ultrasoft pseudopotentials (USPPs),

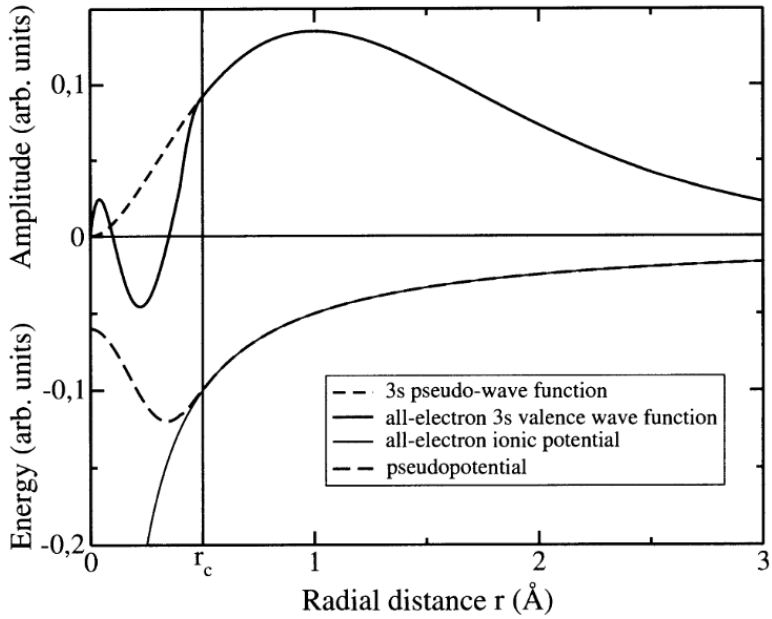

Figure 2.9: A demonstration of norm-conserving pseudopotentials (NCPPs). The upper part compares the all electron (AE) wavefunction (full line) with the pseudo- (PS) wavefunction (dashed line). Analogously, the bottom showcases the exact and PP. Taken from ref. 58.

PAW potentials, and PAWs suitable for GW calculations. The former two employ two Bessel-functions per nucleus in `VASP`.

1. **USPP:**[59] It has been determined that NCPPs require a core radius that matches the outermost (local) maximum of the AE wavefunction to reproduce the PS charge density. This results in complex, contracted atoms, e.g. first-row 3d and rare-earth, having unusual high cutoff energies. This goes against the entire philosophy behind PPs. The most straightforward solution simply extends the core radius further out. Obviously, freezing ever larger portions of the wavefunction is detrimental to the general applicability of these NCPPs.

   Vanderbilt came up with a workaround, USPPs, where the NC condition is relaxed and amended with augmentation charges. These make up for the difference in charge density between the AE and PS wavefunctions within the core radius. Up to this point, this is still an exact frozen-core approach. In practice however, the augmentation functions are only constructed to retrieve the exact moments in the core radius (pseudization). Now, the

USPP is exact up to first order charge density changes with respect to the reference system. The speedup is significant, especially in 3d elements.

2. **PAW:**[59] One of the main implementation hurdles of USPPs is the large number of parameters that go into it. As such, extensive testing is needed before a generally applicable set can be published. PAW instead writes the AE wavefunction out as a linear transformation of the pseudo-wavefunction (see eq. 2.51). The same transformation is applied to the Hamiltonian. On-site projection operators $|p_i\rangle$ are used to determine where to correct the pseudo-wavefunction, hence the name.

   Similarly to USPP, small on-site augmentation charges have to be added. The main difference lies in that PAW does not pseudize its augmentation values. Instead it projects them directly from the AE wavefunction onto a second radial basis set that is centered around the nucleus. Since PAW uses two kinds of basis sets, so one-electron properties (e.g. the overlap charge density) end up containing four terms (see eq. 2.52). There is another central assumption begin made however, namely that the partial waves $\chi_a(\mathbf{r}) = \langle \mathbf{r}|a\rangle$ form a complete set. In that case, the last two, mixed terms vanish and performance rates rise.

$$|\chi_{AE}\rangle = \left[1 + \sum_i \left(\langle\phi_{i,AE}| - \left|\phi_{i,ps}\right\rangle\right)|p_i\rangle\right]\left|\chi_{ps}\right\rangle \tag{2.51}$$

$$\begin{aligned}\left\langle\chi_b^{AE}\middle|\mathbf{r}\right\rangle\left\langle\mathbf{r}\middle|\chi_a^{AE}\right\rangle = &\left\langle\chi_b^{ps}\middle|\mathbf{r}\right\rangle\left\langle\mathbf{r}\middle|\chi_a^{ps}\right\rangle + \left\langle\chi_b^{ps}\middle|\mathbf{r}\right\rangle\left\langle\mathbf{r}\middle|\chi_a^{aug}\right\rangle \\ &+ \left\langle\chi_b^{aug}\middle|\mathbf{r}\right\rangle\left\langle\mathbf{r}\middle|\chi_a^{ps}\right\rangle + \left\langle\chi_b^{aug}\middle|\mathbf{r}\right\rangle\left\langle\mathbf{r}\middle|\chi_a^{aug}\right\rangle\end{aligned} \tag{2.52}$$

3. **PAW for GW:**[60] Building on the aforementioned central PAW assumption, there is one case in particular where it breaks down. Both post-HF (e.g. MP2) and post-DFT methods (e.g. RPA and GW) include a large set of virtual orbitals. The high-energy/momentum range of these orbitals are very delocalized, being more similar to planar waves than a bounded state. Hence, the projection $\langle p_a|\chi_\alpha\rangle$ becomes too small. In Fourier space this is even clearer, as bound states χ_a all lie around the gamma point. In the case of the late 3d transition metals, the deviation from NCPPs can be up to 80%.

   There are two ways to correct this error. One would be to derive the exact formulation and apply an energy correction a posteriori. Alternatively, considering how the augmented charges are not complete, the NC condition has

to be reintroduced. In VASP, the approximately norm-conserving potentials (10% to 20% deviation) were constructed. In a first attempt, the core radius is adjusted. If it becomes too small (too hard pseudopotential) or too large (too poor applicability), the pseudo-wavefunction is adjusted to become NC again.

2.2 Algorithms for probing the PES

One of the most fundamental aspects in computational chemistry consists of finding points of interest on the PES, at least in a preliminary step and mapping a trajectory between them. There is a particular interest for minima that correspond with reactants, products, or reaction intermediates and saddle points. Retrieving the former is often referred to as *geometry optimization*, for which I shall present three possible methods, based on ref. 32. Bear in mind that these are not necessarily global. In some fortunate cases the same algorithms might also retrieve saddle points, although there exist more specialized options that are discussed subsections 2.2.2 and 2.2.2. Once the topology has been determined, the focus then shifts to building up a reaction network. All the methods presented here were implemented in building the reaction networks in Chapter 3.

2.2.1 Geometry optimization

Descent methods

The most straightforward approach to optimizing a geometry would be to follow the PES downhill to a minimum. Lacking a global view of the PES, one makes due with only the local curvature. A naïve approach would simply (numerically) identify the local gradient, extrapolate a linear path from there and minimize it. This approach is called the *steepest descent* method and it suffers from one big caveat: it has poor efficiency. Upon arriving at the path's minimum namely, a new direction has to be selected. The new gradient always lies at a 90° angle with respect to the old path by virtue of the 1D-minimum. This would be fine in principle, but slight variations in the hyperplane bisecting the PES manifold might prevent it from having reached the true minimum in that general direction. As such, the trajectory starts oscillating between two directions and ends up following a jagged zigzag path, see Figure 2.10. Conversely, this can also prevent it from exploring a larger region on the manifold.

The performance is boosted when coupling two vectors instead, one acting as the driver $\mathbf{h}_i$ moving the system downhill and the other as the rudder $\mathbf{g}_i$, adjusting

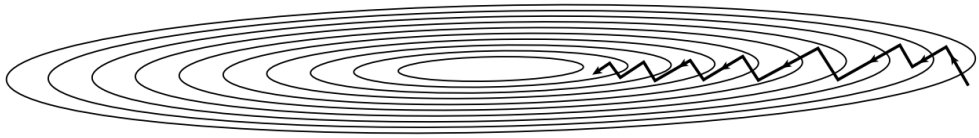

Figure 2.10: Illustration of the zigzagging behavior of Steepest Descent in a local minimum. Picture taken from ref. 32.

the orientation. Both are constructed recursively out of the previous step and each other. The rudder at the next step $\mathbf{g}_{i+1}$ is made to be orthogonal to previous vectors $\mathbf{g}_i$ and $\mathbf{h}_i$. The first orthogonality fulfills the rudder role, the second allows for new directions to be explored. In practice, $\mathbf{g}_i$ coincides with the local downhill gradient, so both the derivative and previous movement are $\mathbf{h}_{i-1}$ both taken into account. The updated driver, which performs the actual steps, is the sum of of the previous the driver and rudder:

$$\mathbf{h}_{i+1} = \frac{\mathbf{g}_{i+1}^2}{\mathbf{g}_i^2}\mathbf{h}_i + \mathbf{g}_{i+1} \tag{2.53}$$

These kinds of algorithms are called *conjugate gradient descent*. Their name derives from the conjugacy requirement: $\mathbf{h}_i\mathbf{H}\mathbf{h}_j = 0$ and in fact all previous j steps and $\mathbf{H}$ the Hessian matrix. This ensures that the driver always explores new directions along the Hessian and leads to the performance boost. Remark that actual implementations the explicit presence of $\mathbf{H}$ is removed, so the Hessian never has to be computed or stored.

The specific implementation presented here is from Fletcher and Reeves. Compared to steepest descent, the driver here stabilizes the erratic movements of the rudder/gradient by keeping the focus longer in the local region. It works perfectly for (near-)parabolic functions, where it only requires one step in each direction. In practice however, the involvement of the gradient makes computing the Hessian obsolete. Polak and Ribiere expanded the scope by slightly modifying effect of $\mathbf{h}_{i-1}$ on the next step $\mathbf{h}_i$. When the rudder is hardly changing, the driver is 'reset' to gain speed.

Quasi-Newton

The Newton-Raphson method is a standard way of finding a zero point. This is done by successively finding the zero point of the extended tangent to the local function point and jumping back to the function, steadily closing in to zero point. Finding (local) minima works analogously by applying Newton-Raphson

on the manifold's derivative. Obviously, the tangent is now constructed using the Hessian. Here is where the method distinguishes itself from the conjugate gradient. In principle both are analogous, but the former only required a N-sized gradient vector while Newton-Raphson stores a $(N \times N)$ matrix.

Quasi-Newton methods on the other hand employ an approximate Hessian and update it so in the long-range limit it matches the real Hessian. Throughout, the approximation is kept positive-definite and symmetric. As such, the optimizer is pushed towards the minima. On manifolds with inflection points (i.e. vanishing second derivatives), this remarkably works out better than using the real Hessian due to the positive-definite criterion. Still, even under optimal circumstances a large position update might still place the minimizer outside of the convex region. In `VASP` `POTIM` attenuates the initial step. In general a propagation step looks like:

$$R_i = -H^{-1} \cdot \nabla f\left(\mathbf{R}_{i-1}\right) + R_{i-1} \tag{2.54}$$

giving the added benefit of optimal performance at quadratic regions, such as near the minimum. The updating step in the meantime in approach of Davidon, Fletcher, and Powell reads:

$$\begin{aligned} H_{mn}^{(i)} = H_{mn}^{(i-1)} + \frac{\left(\mathbf{R}_i - \mathbf{R}_{i-1}\right)_m \left(\mathbf{R}_i - \mathbf{R}_{i-1}\right)_n}{\left(\mathbf{R}_i - \mathbf{R}_{i-1}\right) \cdot \left(\nabla f\left(\mathbf{R}_i\right) - \nabla f\left(\mathbf{R}_{i-1}\right)\right)} \\ - \frac{\left[\mathbf{H}^{(i-1)} \cdot \left(\nabla f\left(\mathbf{R}_i\right) - \nabla f\left(\mathbf{R}_{i-1}\right)\right)\right]_m \left[\mathbf{H}^{(i-1)} \cdot \left(\nabla f\left(\mathbf{R}_i\right) - \nabla f\left(\mathbf{R}_{i-1}\right)\right)\right]_n}{\left(\nabla f\left(\mathbf{R}_i\right) - \nabla f\left(\mathbf{R}_{i-1}\right)\right) \cdot \mathbf{H}^{(i-1)} \cdot \left(\nabla f\left(\mathbf{R}_i\right) - \nabla f\left(\mathbf{R}_{i-1}\right)\right)} \end{aligned} \tag{2.55}$$

Since both methods perform equally well, VASP implements both under the tags `IBRION` = 2 and 1, respectively. In principle, `IBRION` = 1 is advised when starting close to the minimum. Starting in the saddle region, it can even in some cases be used to minimize along the $(N-1)$ dimensions to retrieve the saddle point.

2.2.2 Retrieving saddle points

Nudged Elastic Band method

Within the framework of transition state theory (TST), one can construct a reaction coordinate that crosses a transition state between two intermediates. The reaction coordinate then describes the position along a trajectory on the PES. The intermediates are considered (local) minima, meaning that they have a positive curvature in every direction. Similarly, the transition state is usually regarded as

a saddle point[§], with one negative curvature along the trajectory. Looking for a transitions state then becomes a matter of constructing a trajectory that coincides with the minimum energy path (MEP).[61]

One approach is that of elastic band methods, where the trajectory is sampled with a couple of images that are connected via an interpolation function. Apart form the PES gradient or true force, each image also feels a spring force that establishes the trajectory. To obtain a true MEP, each image then undergoes an optimization procedure analogous to the ones outlined above (see subsection 2.2.1). Although, Henkelman's (and VASP's) implementation use the Verlet algorithm. A common pitfall of these methods is that the spring forces will tend to straighten out the MEP. In regions where the PES strongly curves, overly rigid springs then start *corner cutting*.

A special subclass, called the nudged elastic band method (NEB) method,[62] remedies this issue. Here, both the true force on the image and its spring forces are projected out onto the perpendicular and parallel sides of the MEP, respectively. This process is called *nudging*. As such, the spring forces are solely responsible for maintaining the right image spacing. They do not interfere with the MEP optimization guided by the real force components. Of course, a tangent to the image has to be constructed in order to define these directions. The straightforward approach would be to take the difference vector of the two adjacent images and normalize it. By constructing the tangent from the sum of two normalized difference vectors, each between the image itself and one adjacent image, the image spacing is kept fixed. Note that these definitions do not apply to the images at both ends. These are kept fixed during the optimization, as to impose boundary conditions. Henkelman later added two modifications to the original algorithm in order to circumvent NEB breakdowns.

The first tackles kinks in the MEP by tweaking the tangent's definition.[62] These kinks form in regions where the spring force strongly outweighs the true force. Inflection points between the minima and saddle point are a good example (see Figure 2.11). Once they are formed, these points are hard to remove through simple optimization. Rather, the kinks tend to fluctuate back and forth between each step. To understand this better, assume an hypothetical MEP lying in a parabolic trench with a constant slope of F along the path. When a single image is then perturbed from its position dx, it experiences a restoring spring force of $-kdx$ pulling it back. At the same time its higher energy neighbor feels a destabilizing force of $dx/2RF$ due to a badly aligned tangent. When the destabilizing force becomes greater than the restoring, the band becomes locally

[§]In TST a transition state does not need to pose an actual energy barrier. Any entropic effect that allows the reactants to remain in thermal equilibrium is valid as well.

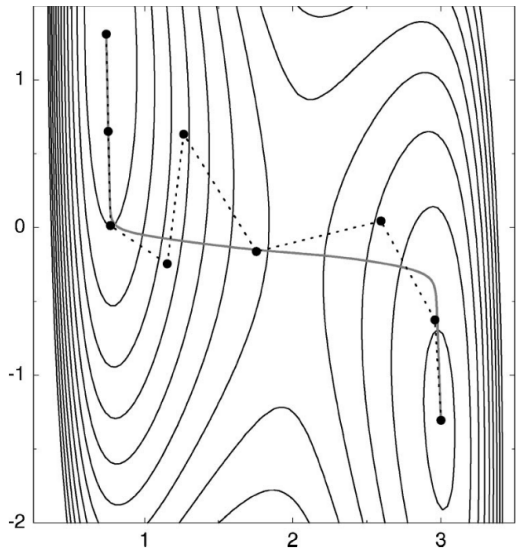

Figure 2.11: Comparison between original NEB algorithm with kinks (dashed line) connecting the images (dots) and minimum energy path (solid line). The PES is based on a two-dimensional LEPS model. Taken from ref. 62.

unstable and a kink appears. Since the image spacing R depends on the number of images, NEBs always become unstable after superseding an upper-limit of images. In test cases of simple 2D-periodic PES for example, this number lies around 13 images. One could try and prevent any kinks by mixing some of the perpendicular spring component to straighten out sharp angles. This approach however, would basically be reverting back to a generic elastic band method. Instead, the paper presents a solution where the normalized tangent only includes the difference vector of the image with its neighbor that lies higher in energy. In cases where both neighbors lie higher or lower in energy, a weighted average is made over both. This mixing ensures a smooth transition around the saddle point, where the adjacent image in the tangent switches. Since the tangent's definition changed, the forces should be altered to ensure equal spacing, see below. More importantly, this approach retains the most important benefit of the NEB method, which is to assign clearly defined roles to each force acting on the image.

The second correction, manages the equal image spacing enforced above. Although this works perfectly for images near the constraints, a good description of the saddle point region prefers a higher image density here. Incorporating the parallel component of the real force would push the images towards minima along the path. By simply inverting their sign, the images will group around the saddle point of interest. This version is called the climbing-image nudged

elastic band method (CI-NEB)[63] and is no more computationally demanding than a regular NEB. In practice, a couple of initial runs are performed without climbing images using only the corrected tangent. Once a good starting MEP is obtained, only the highest-energy image starts climbing. At the same time, all spring components are removed from its expression. Remark that this does not mean that the highest-energy image can now diverge from the trajectory: it still has its real force components projected using its neighbors. As long as the MEP under consideration contains only a single saddle point, it will eventually converge to it. Figure 2.12 shows how significant the impact of CI-NEB can be. It corrects the barrier height by 1 eV compared with an interpolation.

The other images still feel spring force, so they follow the highest-image. Since the latter does not necessarily lie in the middle of the MEP anymore, each side will have a different inter-image distance. As pointed out before, a higher density of images around the saddle point is preferable. With one image actively climbing to the saddle point, this can be achieved by increasing the spring coupling with its surrounding images. In practice, the spring constant is defined linearly in terms of the image energy. This all then culminates in the following set of equations for the total force $\mathbf{F}_i^{tot}$ of image i, its parallel $\left(\mathbf{F}_i^{\parallel}\right)$ and perpendicular $(\nabla E^{\perp}(\mathbf{R}_i))$ components, the force on the climbing image $\mathbf{F}_{i_{max}}$, the improved spring constants k_i', and the improved tangent τ_i. Finally, it should be noted that the most symmetric spacing around the saddle region is achieved by choosing E_{ref} to be the energy of the highest end point.

$$\mathbf{F}_i^{tot} = \mathbf{F}_i^{\parallel} - \nabla E^{\perp}(\mathbf{R}_i) \tag{2.56}$$

$$\mathbf{F}_i^{\parallel} = k_i' \boldsymbol{\tau}_i \left(\mid \mathbf{R}_{i+1} - \mathbf{R}_i \mid - \mid \mathbf{R}_i - \mathbf{R}_{i-1} \mid\right) \tag{2.57}$$

$$\nabla E^{\perp}(\mathbf{R}_i) = (1 - \boldsymbol{\tau}_i) \nabla E(\mathbf{R}_i) \tag{2.58}$$

$$\mathbf{F}_{i_{max}} = \nabla E^{\parallel}(\mathbf{R}_i) - \nabla E^{\perp}(\mathbf{R}_i) = -\nabla E(\mathbf{R}_{i_{max}}) + 2\tau_{i_{max}} \cdot \nabla E(\mathbf{R}_{i_{max}}) \tau_{i_{max}} \tag{2.59}$$

$$k_i' = k_{max} - r\Delta k \begin{cases} r = 1 \text{ if } E_i < E_{ref} \\ r = \left(\frac{E_{max} - E_i}{E_{max} - E_{ref}}\right) \text{ if } E_i > E_{ref} \end{cases} \tag{2.60}$$

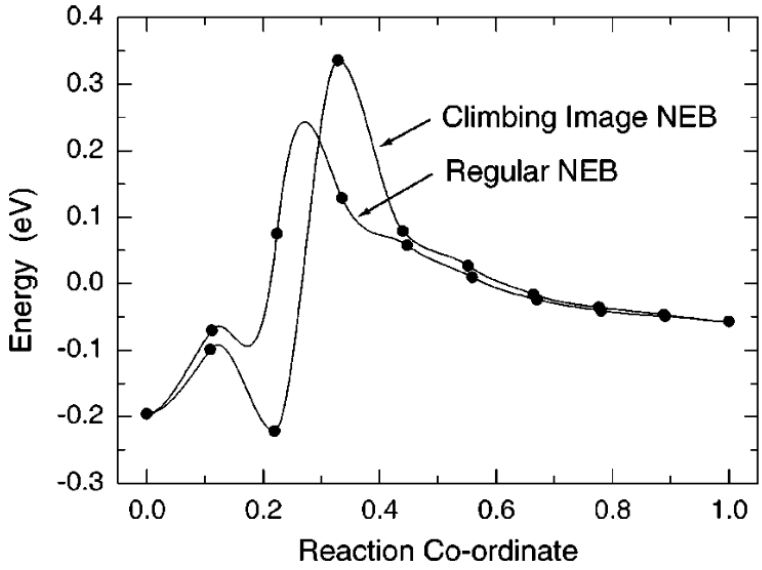

Figure 2.12: Calculation of the MEP between methane adsorption onto a Ir (111) surface. The MEP was computed using both the original NEB and CI-NEB. It demonstrates how the CI-NEB manages to pinpoint the saddle point with an image. This results in the barrier height increasing with about 1 eV than if it were calculated through interpolation. The reaction coordinate also shifts more towards the center using the CI-NEB. Taken from ref. 63.

$$\boldsymbol{\tau}_i = \begin{cases} \diamond\boldsymbol{\tau}_i^+ = \frac{(\mathbf{R})_{i+1}-(\mathbf{R})_i}{|(\mathbf{R})_{i+1}-(\mathbf{R})_i|}; \text{ if } E_{i-1} < E_i < E_{i+1} \\ \diamond\boldsymbol{\tau}_i^- = \frac{(\mathbf{R})_i-(\mathbf{R})_{i-1}}{|(\mathbf{R})_i-(\mathbf{R})_{i-1}|}; \text{ if } E_{i-1} > E_i > E_{i+1} \\ \diamond\boldsymbol{\tau}_i^+ \max(\mid E_{i+1}-E_1 \mid, \mid E_i - E_{i-1} \mid) + \boldsymbol{\tau}_i^- \min(\mid E_{i+1}-E_1 \mid, \mid E_i - E_{i-1} \mid); \\ \text{if } E_{i-1} < E_{i+1} \text{ and } E_i \text{ is an extremum} \\ \diamond\boldsymbol{\tau}_i^+ \min(\mid E_{i+1}-E_1 \mid, \mid E_i - E_{i-1} \mid) + \boldsymbol{\tau}_i^- \max(\mid E_{i+1}-E_1 \mid, \mid E_i - E_{i-1} \mid); \\ \text{if } E_{i-1} > E_{i+1} \text{ and } E_i \text{ is an extremum} \end{cases} \tag{2.61}$$

Dimer method

The dimer method (DM)[64] follows a pair of images (or a dimer) on the PES. The dimer moves as to align its midpoint with a saddle point. This corresponds to the parallel forces of both images canceling out. In practice, its image spacing is kept fixed, so the dimer's movements are constrained to rotation around its

midpoint and translations. The algorithm starts with rotations to align the dimer's axis with the lowest curvature, along which a saddle point likely lies. This part immediately forms the bottleneck and has therefore been most scrutinized. The lowest curvature coincides with the total force perpendicular to the dimer axis vanishing, or in a words an energy minimum can be handled by any of the minimization methods in subsections 2.2.1. The translation is much simpler in that only maximizes one dimension. A conjugate descent with small step sizes works best here. Obviously, the parallel force component has to be directed towards the maximum, i.e. $\mathbf{F}' = \mathbf{F}_{tot} - 2\mathbf{F}_{\parallel}$. One caveat is that when the dimer enters a shallow minimum it could take a long time to leave. This is because it orients itself along the contour lines, tracing them out in a spiraling path. Therefore it is better to redefine translation force to $\mathbf{F}' = -\mathbf{F}_{\parallel}$ in convex regions. The algorithm then alternates between rotation and translation steps.

Now that the move set for the dimer has been presented, it is appropriate to look at the dimer setup. As mentioned before, the dimer consists out of closely lying, near-identical images. In VASP, the second image is defined by a vector with the same number of unfrozen atom coordinates after the regular position of image one. A good starting point would be the lowest (or most negative) curvature derived from the Hessian in a frequency calculation. In that case, the initial rotation should not change the orientation. The vector's norm is normalized, to ensure a predefined image spacing. Care should be taken that the spacing is large enough for the difference in forces on both images to be physical, rather than numerical noise. Typically, the spacing (and likewise the translational step size) should not fall below 10^{-3} Å.[65] An improved version circumvents this limit by focusing on the midpoint and its tangent rather than the two images.[66] At the same time, the evaluation of the gradient can be replaced for linear extrapolation. Thus, each step now requires only a minimum of 4 gradient evaluations (2 for rotation and 2 for translation). The downside is a drop in curvature accuracy from $O\left(\Delta R^2\right)$ to $O(\Delta R)$. Diminishing the step size ΔR makes up for it. In other words, the improved dimer method (IDM) prefers a larger number of steps to readjust more rapidly to the altering PES.

One of the defining strengths of the IDM is how it can start from a minimum and retrieve a saddle point. This is great for cases where the next reaction step is unknown or hard to guess. Generally speaking, there could be several saddle points near the minimum. I shall therefore briefly discuss two strategies for exhaustively sampling all saddle points in the direct vicinity. Firstly, one can try various starting images. Fixed-temperature Molecular Dynamics (MD) seems like a great way to generate new pool of structures. These tend to lie along the same low-curvature modes however and could systematically exclude specific saddle points. Tests have

shown random displacements (according to a Gaussian distribution) outperform the dynamics' pool. The second strategy is to vary the initial search direction rather than the starting image. Only slightly tweaking the algorithm allows for the exploration of higher-curvature directions in a hierarchical order. First the lowest curvature is identified and then its vector component is subtracted from the forces. As such, the rotation procedure excludes any hyperplane containing that direction and reorients to the next lowest curvature instead. This orthogonality constraint is very similar to the one presented in section 2.2.2. The DM can also be used in conjunction with a regular NEB to pinpoint a specific saddle point. The NEB does not have to be run until convergence, but just long enough to obtain a rough MEP estimate. The dimer can then either take its starting images from those adjacent to the suspected saddle point or instead from the interpolated image and its tangent.[62]

2.2.3 Ab initio Molecular Dynamics

An Ab Initio Molecular Dynamics (AIMD) simulation consists out of a trajectory that maps out the PES and configuration space. The path progresses in small time steps of Δt after which each vector, i.e. position, momentum and force, is updated. The exact expression for these updates is what controls the system. In 1984, Suichi Nosé proposed an approach to systematically explore the canonical ensemble (T,V,N) or the constant pressure ensemble (T,P,N).[67] The system is simulated as being brought into contact with an energy reservoir that introduces temperature fluctuations. This is done via the introduction of a novel, 'virtual' variable s, which rescales all particle velocities equally. The Hamiltonian adds this s-variable as an additional object with is own potential:

$$H = \sum_i \frac{m_i \mathbf{v}_i^2}{2} + V(\mathbf{r}_i) + \frac{Q}{2}\left(\frac{ds}{dt}\right)^2 + (f+1)\, k_B T_{ext} \log(s) \tag{2.62}$$

Here, f stands for the number of degrees of freedom (DOF), T_{ext} for the external temperature, and Q controls the time scale of the temperature fluctuations. Their average over a whole period yields the externally set energy per DOF. Similarly, from the equipartition theorem $\sum_i \frac{\mathbf{p}_i^2}{2m_i} = \frac{k_B f}{2} T$, it can be shown that the thermostat really enforces the average temperature: $\langle T \rangle = T_{ext}$. This entails that both heat baths obtain equilibrium, given enough time. Other important quantities such as the Hamiltonian, translational and rotational momentum are also all conserved throughout the simulation. Hence the simulation is time-reversible. Since velocity is made up from two components, any of those two can

adsorb s, becoming either effective space or time. The latter is physically more sound for systems with a fixed volume and demonstrates that in reality the Nosé thermostat readjusts the time step to obtain equilibration. The actual mechanics behind it can be derived by taking the derivative with respect to s, yielding

$$Q\frac{d^2s}{dt^2} = \sum_i \frac{\mathbf{p}_i^2}{m_i s^2} - \frac{(f+1)}{s}k_B T_{ext} \tag{2.63}$$

Around the equilibrium this reduces to the regular second order differential equation for the harmonic oscillator. Although Nosé claimed to have proven that this approach reproduces the canonical ensemble, subsequent works have shown both theoretically and via numerical simulation that it often falls short in one key condition: ergodicity. The ergodic hypothesis postulates that a time-averaged observable of the trajectory coincides with a similar average over the ensemble. In other words, when simulating for long enough the frequency by which each state appears in the trajectory corresponds to its ensemble weight. Together with connectivity, it allows for the derivation of ensembles from Markov chains.[68] Paradoxically enough, any set of equations that accurately describes the canonical ensemble will become unstable over time. Once high momentum vectors start to appear, the time step becomes too large leading to non-physical collisions. At that point, the total systems energy increases due to potential interaction. This confirms that time scaling is necessary but not enough.

Hoover reasoned that if the kinetic energy alone could not provide adequate control over the ensemble sampling, then some of its higher moments should contain errors.[69] Correction of these errors could fix the ergodicity. Since the average kinetic energy $\langle K \rangle$ is already being controlled (via T_{ext}), Hoover decided to add another variable for the fluctuation $\left\langle K^2 \right\rangle$. This gives the new series of equations:

$$\begin{aligned}
\frac{d\mathbf{q}_i}{dt} &= \mathbf{p}_i \\
\frac{d\mathbf{p}_i}{dt} &= -\nabla_{\mathbf{q}_i} V - \left(\zeta + \xi p_i^2\right)\mathbf{p}_i \\
\frac{d\zeta}{dt} &= \frac{1}{\tau_\zeta^2}\sum_i \left(p_i^2 - 1\right) \\
\frac{d\xi}{dt} &= \frac{1}{\tau_\xi^2}\sum_i p_i^2\left[p_i^2 - 3\right]
\end{aligned} \tag{2.64}$$

The virtual variable s has been swapped for an explicit scaling function ζ, free from its own potential. The τ scalars tweak the response rate of the control

variables. Both the zeroth and sixth moment now give the right distributions. Strangely enough, the explicit addition of the sixth moment with its own control variable leads to instability at small time steps. Numerical experiments show that the phase space is much better covered using two control variables, rather than one. This then defines the Nosé-Hoover thermostat.

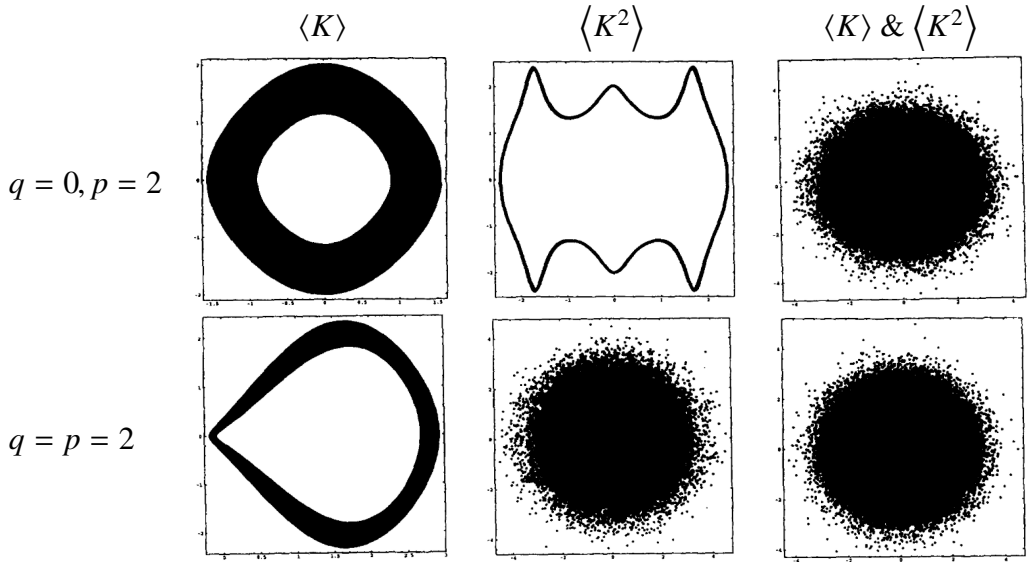

Figure 2.13: Comparison of momenta (header) in simulations of a one-dimensional harmonic oscillator from eq. 2.64. Clearly a combination of first-and second order momenta greatly benefits the ergodicity. Each trajectory of up to 200,000 points starts from the $\{q, p\}$ parameters on the left-hand side and $\zeta = \xi = 0$. The horizontal axis displays p and the vertical axis q. Based on fig. 1 from ref. 69.

As the AIMD progresses through the phase space, the electronic structure has to be updated. The most straightforward way would be to relax it after each step. This is called the Born-Oppenheimer Molecular Dynamics (BOMD). Conversely, one could use the energy-time relation $H|\Psi\rangle = i\hbar\frac{\partial|\Psi\rangle}{\partial t}$ to propagate the electronic wavefunction with the time step Δt. This Car-Parinello approach is much faster, but also requires shorter time steps. `VASP` only implements BOMD, although it does generate an estimate of the new electronic wavefunction after propagation.

2.2.4 Microkinetics

Many Computational Chemistry applications rely on the ability to model reaction mechanisms in catalysis. There are several ways to go about it, each with a

different level of assumptions. The most physically complete methods sample various trajectories and weigh them accordingly. BOMD (see subsection 2.2.3) could be classified in this category. In practice however, it is far too costly due to the low frequency of reaction events. A faster alternative will be presented in section 2.3. In this subsection however, I shall be discussing microkinetic models. Micorkinetics focuses on the temporal behavior of the concentrations present in the reaction network. Information on the spatial distributions is relegated to the model reactor and simplified via integration. The model breaks down the reaction network into cycles of elementary building blocks, namely reaction steps. These are defined using the minima and saddle points discussed in detail above. The transition state theory (TST) powers this process, as it allows for individual reaction steps to be represented by the MEP.

Transition State Theory

TST[61] models each reaction step as the system passing from a reactant region to a product region. The system can temporarily reside at the dividing plane between both before passing on. Two important restrictions apply however. Firstly, each region acts as an energy basin with a partition function Z that is in thermal equilibrium. The ensemble controlling that equilibrium can be either micro-canonical or canonical[¶]. This thesis exclusively uses the latter. The theory allows for perturbations to disturb the basin, as long as its response time is far smaller than the frequency of crossing events. Consequentially, any non-thermodynamical effects are disregarded. As such, TST cannot model molecular beam experiments for example. Eq. 2.65 describes the flow rate k^{TST}. The dimensionality of the transition state (TS) is one lower than that of the reactant as it consists solely out of paths $\mathbf{\Gamma}$ that cross the hyperplane along the unit normal $\mathbf{n}$. The partition function at the hyperplane then becomes $Z^{tst} = \int \exp\left(-\frac{V(\mathbf{r})}{k_B T}\right) \delta\left[\mathbf{n} \cdot (\mathbf{r} - \mathbf{\Gamma})\right] d\mathbf{r}$. If the Z^{tst}/Z^{R} ratio with the destination/reactant reservoir (R) shrinks, the phase space volume can become too small in comparison to the funnel that leads up to the dividing surface. In that case the dividing plane might become part of the basin and TST fails as well.

The second restriction states that the dividing plane acts as a point of no return. Once reached, a reactant will not fall back to the original basin. This is accounted for by only including the forward half of the crossing speeds $\mathbf{v}_{\perp}$. Applying the equipartition theorem yields the general formula on the right-hand side of eq. 2.65. In reality, product paths can be erratic and traverse the boundary several times. Hence, k^{TST} poses an upper-limit estimate of the actual rate. At

[¶]The macro-canonical ensemble is ruled out due to preservation of atoms and electrons.

the level of chemical reactions, there are usually also two processes constituting a dynamic equilibrium. These are easily incorporated by establishing two opposite flows passing through the same surface. Lastly, the surface is often constructed to contain a saddle point (and lie orthogonal to the reaction coordinate), but it does not have to. Contrary to popular belief, it does not even require a potential energy barrier separating both basins. An entropic barrier, i.e. a very selective condition that disqualifies most reactants, suffices. This remark plays a crucial role in adopting TST for physisorption, where no bonds are broken.

$$k^{TST} = \frac{\langle \mathbf{v}_\perp \rangle}{2} \frac{Z^{tst}}{Z^R} = \frac{k_B T}{\sqrt{2\pi m_{eff} k_B T}} \frac{Z^{tst}}{Z^R} \tag{2.65}$$

Reaction mechanisms at the surface

As mentioned before, each mechanism can be split into reaction steps. When such a step consists out of a single transition state connecting two intermediates and no other intermediates can be found, it is considered *elementary*. The rate of elementary steps scales with the number of inciting collisions. Hence, it increases linearly with the concentration of species involved. As such, a conversion reaction $A \rightarrow B$ has a reaction rate of $r_B = k[A]$. Here, letters in square brackets indicate the species' concentration over time and if they carry a subscript 0, it refers to the initial concentration. In elementary reaction steps, the rate constant k^{Arr} in eq. 2.66 converts to the Arrhenius equation. The partition function Z^{tst} now spans the tangent space according to the harmonic oscillator approximation. In the case of a bimolecular reaction, $A + B \rightarrow C$, the rate now becomes bilinear: $r_c = k[A][B]$. When a molecule dissociates, the directions are simply reversed. In the odd case where the concentration $[A]$ is large enough for the change to be negligible, the reaction order drops to zero. This means that the product is steadily produced ($r_A = kt + [A]_0$). For the first and second order reactions this behavior is exponential or hyperbolic, respectively.

$$k^{Arr} = \frac{k_B T}{h} \frac{Z^{tst}}{Z^R} e^{-E_b/k_B T} \tag{2.66}$$

In Heterogeneous catalysis, the surface first has to trap the reactants before proceeding. In essence the physisorption model equates to a gas effusing through a hole of a similar cross-section A as the target site. Since the hole is small in comparison with the molecules, only those with the right orientation and a momentum perpendicular to the wall pass through. Eq. 2.67 expresses the sticking coefficient of a gas per unit of volume V. Using the ideal gas law

($PV = nk_BT$), it is rewritten in terms of the partial pressure P and molar amount of particles n.

$$k^{stick} = \frac{k_B T A}{V\sqrt{2\pi m k_B T}} = \frac{PA}{n\sqrt{2\pi m k_B T}} \tag{2.67}$$

These elementary reactions can be combined to produce more complex mechanisms. For example, a species A adsorbs onto the surface ($A + * \rightleftarrows A^*$). From there on it reacts with a species B in the gas phase, desorbing instantaneously as a species C ($A^* + B \rightleftarrows C$). The first step is expected to proceed much faster than the latter, which imposes the bottleneck. Under these conditions, one may assume that gas phase A and adsorbed A^* are in a quasi-equilibrium. This is very useful, because it provides a value (called the Langmuir adsorption isotherm) for $[A^*]$ and $[*]$ in the bottleneck rate $r_2 = k_{2+}[A^*][B] - k_{2-}[C][*]$. This is called the Eley-Rideal mechanism and its overall rate can be found in eq. 2.68. The capital letters K stand for the equilibrium constants of reaction step 1 or 2.

$$r = \frac{k_{2+}K_1[*]_0\left([A][B] - [C]/K\right)}{1 + K_1[A]} \tag{2.68}$$

The reaction network modeled in section 3.2 assumes no reactions in gas phase. Instead, all reactivity takes places between two adsorbed species on the surface. In this case, the species A and B both compete over the same adsorption site. When they lie in proximity of another, they react to form C. The latter diffuses in a separate step. The reaction rate of the Langmuir-Hinshelwood mechanism in eq. 2.69 bears a striking resemblance to the one of Eley-Rideal. This is because the C production is now rate-determining and the adsborbates each have their own quasi-equilibrium. The most notable difference lies in the order of the denominator and $[*]_0$, but both stem from the forward term $r_{3+} = k_{3+}[A^*][B^*]$. Although Langmuir-Hinshelwood is a fair representation of the CO oxidation on Pt_1/CeO_2, this reaction network has channels crossing and off-cycle reactions. Therefore, we prefer to construct a set of simple, non-linear differential equations and propogate them using a common integrator, such as fourth order Runge-Kutta.

$$r = \frac{k_{3+}K_A K_B[*]_0^2\left([A][B] - [C]/K\right)}{\left(1 + \sum_J K_J[J]\right)^2} \tag{2.69}$$

Reactor types

The reactor type refers to the microkinetics' model for the spatial distribution. Rather than having an explicit dependence, as with kinetic Monte-Carlo (KMC),

Table 2.2: Comparison of the different type of reactor models. Both the molar (n) and the concentrations (c) balances are compared, or their flows $\dot{n}$ and $\dot{c}$. Note that in the static case of BR the variable is time (t), while in the other reactors are understood in terms of residence time $\left(\tau = \frac{V_{\text{reactor}}}{\dot{V}_{\text{input}}}\right)$.

	BR	CSTR	PFR
molar balance	$\frac{dn}{dt} = rV$	$\frac{\dot{n}-\dot{n}_0}{\tau} = r\dot{V}$	$\frac{d\dot{n}}{d\tau} = r\dot{V}$
concentration balance	$\frac{dc}{dt} = -kc$	$\frac{\dot{c}-\dot{c}_0}{\tau} = -kc$	$\frac{dc}{d\tau} = -kc$

the quantity being measured is adjusted.[70] Each model is an abstraction of industrial tanks and this is where they lend their name from. The simplest two-phase reactor is the batch reactor (BR). It starts out with a fixed gas mass that does not change during the reaction. Physically, this corresponds to a heated and stirred tank with no inlet or outlet flow. Typically, the reactant concentrations in a BR keep decreasing until dynamic equilibrium. From there on out, the concentrations flatline. When instead a constant flow is pumped through the reactor, one obtains a continuously stirred tank reactor (CSTR). The gas resides some time inside the tank, where it reacts, and the outgoing mixture flows under the modified partial pressures. Since the gas mixture is pumped out before necessarily reaching equilibrium, flat concentration lines now coincide with the steady-state limit.

The three-way catalyst in automobiles has a gas flow running through, but it does not really store a portion as with CSTR. Instead it would be more correct to consider it as an elongated tube. Assuming that the flow strength does not prohibit the the fluid from interacting with the coated reactor walls (turbulent flow), we find ourselves with a plug flow reactor (PFR). Table 2.2 shows that the molar ($\dot{n}$) and concentration ($\dot{c}$) flows of PFRs are the continuous version of CSTRs. This means that a PFR can be modeled as a series of serial, interconnected CSTRs with matching in and outflows. Because the flow now is steady, the balance in PFR is mathematically similar to that of BR, except for the time aspect.

2.3 Alternatives to ab initio: Machine Learning

Computational models in Materials Science and Heterogeneous Chemistry often have to be restricted in size out of consideration for the computational resources. This in turn of course limits the scope. DFT can account for up to 200 to 300 atoms maximum, which would be enough for small nanoparticles (NPs) with many degrees of freedom restricted. Larger NPs and extended surfaces are often modeled as slabs with PBCs. Expanding to even larger systems would require

forcefields. These suffer from the caveat that they do not allow for bond breaking. Considering the nebulous nature of bonds in Solids as is already, this prevents any serious application.

The rise of machine learning techniques promises an alternative. Now, force fields can be automatically fitted to the PES and adapt naturally rather than having to rely on approximations or manual parametrization. There are two main technologies that are useful for this: Neural Networks (NNs) and Bayesian Inference.[71] When considering a high-dimensional PES, the former is the most adequate approach by far. The potentials constructed this way can reach the accuracy of the (ab initio) code that generated their training set, while performing only slightly slower than classical force field methods. The scaling for the model still remains linear. This makes them highly suited to perform large-scale MD, sampling of low-frequency processes (via meta-dynamics), and any application for which kinetic Monte Carlo is suitable.

2.3.1 Neural Networks

NNs are popularly compared to the inner workings of a brain, from which the method derives its name. The comparison makes sense in that both contain several nodes (neurons) branching out and forming connections. These nodes (neurons) bundle the receiving information but only pass it on (fire) when a certain threshold is met. In principle each node (neuron) from one layer (part) is connected to all nodes (neurons) of its neighboring layers (parts). These connections are strengthened during training (learning) to improve the NN's performance (brain's cognition).

$$\mathrm{f}{:}\mathbb{R}^n \rightarrow \mathbb{R}^m; \mathbf{o} = \mathrm{f}_j \left[\mathbf{b}_j + \mathbf{M}_{j-1,j}\mathrm{f}_{j-1}\left[\cdots \mathbf{b}_2 + \mathbf{M}_{2,3} \cdot \mathrm{f}_1\left[\mathbf{M}_{1,2} \cdot \mathbf{i}\right]\right]\right] \tag{2.70}$$

In more mathematical terms, the network is an elaborate vector function, as shown in eq. 2.70, that is fitted to a training set. Its layers are stored as transformation matrices $\mathbf{M}_{j-1,j}$. The threshold in turn is modeled using an activation function f_j on the resulting vector. Threshold or activation functions are vanishing in one direction to act as an off-switch. Conversely, it can also be constructed to approach unity along the other direction, which places an upper bound on the signal strength. This has the added benefit of parameterizing the signal strength with the matrix elements alone. The successive application of a matrix and activation function constitutes an intermediate layer j. Often such a layer also comes equipped with its own bias node $\mathbf{b}_j$ that stands loose from the output. Two special layers that fall outside of this definition are the input $\mathbf{i}$ and output layer $\mathbf{o}$. The

former is the starting vector before any matrix operations. Their dimensions are determined by the dataset and remain fixed throughout.

The actual architecture of the NN, is determined by the number and dimensions of intermediate layers. These variables are called hyperparameters (HPs), as they are fixed before training commences. The user should not arbitrarily choose these HPs, since they influence the network's performance both in terms of accuracy and evaluation time. It is instead standard practice to compare the results between a handful of different HP sets using a validation set or to rely on literature. Special distinction is made however between NNs with a single intermediate layer and deep neural networks (DNNs), which have more than one. DNNs introduce nonlinear behavior into the fit and are usually treated as a black box. In many cases, two or three intermediate layers suffice.

The training procedure evaluates the error (or loss function) between the NN output and the dataset. The derivative of the loss function with respect to each weight is computed by applying the chain rule in the opposite direction (i.e. starting from the output side). Note that the impact of the weights in a previous layer depends on the strength of their connecting nodes. Next, an optimizer minimizes the derivatives and these are subsequently updated until convergence. This algorithm is called back-propagation. The training can be considerably sped up by choosing a good initial approximation. Nguyen and Widrow generated a scheme[72] based on the knowledge that smooth activation functions only allow for a small range of nodal input to produce a linear signal. Outside of this range the nodal output becomes constant and largely unimportant. The range is controlled by the weight at that node, while the bias controls its position. By evenly spreading out these values to cover the range of interest, each node can be assigned a different role which is updated after the first back-propagation cycle.

When training a NN, the dataset is split into two or three categories:

1. The *training set* contains the data used for the actual training process. The data points are used to determine the loss function.

2. The *test set* is evaluated by the NN to determine how well the interpolation works.

3. In some cases a *validation set* is added to objectively evaluate the accuracy between various NN architectures. This set is especially useful when scanning the HP space.

To enforce consistency, all three sets are usually partitions form the total data set In case the optimized NN performs poorly on the training set, it is considered

to have a high bias. When the performance on the training set is equally good as on the test, over-fitting has occurred and the NN is said to have a high variance. In many fitting problems the user has to try and strike a balance between the bias and variance. This can be done by either adding more nodes or cutting out those that have low weights and only generate noise. A good ratio in size would be 70, 20, and 10% for the training, test, and validation sets respectively.

2.3.2 Neural Network Potentials

In Chemistry, NNs are mostly used to fit the PES and the end result is called Neural Network Potentials (NNPs). Despite the name, they function like regular force fields in that they predict both the energy and atomic forces using geometric data. NNPs do not make any physical presuppositions, employing only their training data. While this gives them some generality, it also hinders any extrapolation. The original implementations failed to bank on their universality however by acting directly on the Cartesian coordinates or a Z-matrix. As a result, their input format was overly rigid: the number and order of the elements has to remain constant throughout the training and later on in deployment. Hence, models could be scaled up, defeating one of the main purposes for NNPs. To expand the algorithms' applicability some mathematical restrictions had to be set in place:

1. Any permutations in the input coordinates should not affect the output.
2. Translation and other symmetry operations on the input coordinates yields the same output.
3. The NNP can rescale to match the system size. This means that the input should be flexible and adapt to a fixed layer size.

Depending on the application, special layers along with various modifications can be added to the NN. In this thesis, I will focus on fitting the PES using the methods developed by Behler and Parinello,[73] called High-Dimensional Neural Network Potentials (HDNNPs). Rather than enforcing the restrictions above in the NN architecture, HDNNPs apply a transformation to the input coordinates before feeding them to the network. This version works for molecules and condensed matter alike, although I shall be focusing on the latter exclusively.

2.3.3 Symmetry functions

Instead of using the atomic coordinates, the periodic system is rewritten in terms of fingerprints. These fingerprints constitute a particular kind of metric in the

chemical space. Hence, the structure similarity (in geometry, forces, and energies) should be reflected in their values. In molecules, a topological approach is popular,[74] but the connectivity in bulk systems is much more complex. Some methods directly try to capture it, like permutation invariant polynomia (PIP),[75] but they are severely limited in complexity. Most instead center around the constituent atoms and its surrounding topology, e.g. Smooth Overlap of Atomic Positions (SOAP),[76] and symmetry functions (SymFuncs).[73] Considering their role in HDNNPs, I shall be focusing on the latter.

SymFuncs project a neighborhood around each atom onto a separate number. There are three reasons to restrict the function to its immediate environment:

1. Under periodicity many incarnations of the same element are likely to become indistinguishable. That is to say, each element is embedded in the same system.

2. The local character of the function makes it more easily transferable between systems. This ties in with the previous argument. Indeed, while systems may vary overall, they can still retain similar sites.

3. Less input to process during training, the faster the learning process.

So, only a the immediate sphere of radius r_c around the atom of interest is considered for the projection. The Behler group have their own program for HDNNP fitting, `RuNNer`. It contains two type of cutoff functions in eqs. 2.71 and 2.71 that rescale the any point at a distance r from the central atom. Both decrease monotonically to mimic, qualitatively at least, the diminishing impact of atoms further away.

$$f_1(r, r_c) = \begin{cases} \frac{1}{2}\left[\cos\left(\frac{\pi r_{ij}}{r_c}\right) + 1\right]; r \leq r_c \\ 0; r > r_c \end{cases} \tag{2.71}$$

$$f_1(r, r_c) = \begin{cases} \frac{1}{2}\left[\tanh^3(1 - \frac{r_{ij}}{r_c})\right]; r \leq r_c \\ 0; r > r_c \end{cases} \tag{2.72}$$

In `RuNNer`, the geometry is developed into radial and angular distributions. The radial distribution only requires an atom pair. Since the separation can take different ranges depending on the element, the projection is defined for all their pair combinations individually. In the case of ceria with two elements for example, there will be a group of projections for Ce-Ce, O-O, and Ce-O each.

Every contribution within the cutoff sphere is summed together. This similarly applies to the angular distributions, but with elemental triplets. Now that a vector covers the phase space, the actual projection can focus on specific regions.

There is however one other constraint. A NNP trains on and returns both energy and forces. Due to the different format and dimensions between the outputs (number versus vector), they require their own NNs. To enforce consistency then, the force NN is the derivative of the energy NN. From eq. 2.70 we know that the derivative propagates through the linear combinations and ends up at the cutoff functions. These therefore have to vanish in a continuous manner at the border, as do their first derivatives. Not only does it prevents output inconsistencies, it also guarantees a smooth change in the force vector once a new atom enters the cutoff sphere during a MD simulation.

Considering the locality and continuity of the zeroth and first order derivatives, a Gaussian function makes for a prime choice to measure radial distributions between the central atom i and another atom j. The choice of η and r_s parameters shifts Gaussian's peak. By generating a set of parameters one obtains a vector that focuses on different regions in space. In a sense, one could also state that it act as a soft, lower cutoff within a hard, upper cutoff. The lower cutoff should stop at the minimal bonding distance of the element pair in question to prevent any redundant information and slow down the training procedure. In fact, `RuNNer` automatically evaluates the entire SymFunc's span and throws a warning if it is too small.

$$G_2^{(i)}\left(r_{ij}, \eta, r_s, r_c\right) = \sum_j f\left(r_{ij}\right) e^{-\eta\left(r_{ij}-r_s\right)^2} \tag{2.73}$$

The angular distribution works on top of the radial, although it counts as different set of vector entries. Now, a triangle of atoms is built where each pair lies within the cutoff radius around the enter atom. The main angle θ_{ijk} is measured between atoms j and k around the central atom i. Since the potential should be periodic, eq. 2.74 uses the cosine of the main angle. To avoid cancellation due to negative values, its scope is restricted to the positive half of the period. As such, angles of 180° are poorly described. That is to say, perturbations in angle there only result in small numerical feedback. Therefore, a second set of projectors, rotated 90° is used for them. The λ parameter toggles between both.

$$\begin{aligned} G_3^{(i)}\left(\theta_{ijk}, r_{ij}, r_{ik}, r_{jk}, \eta, \zeta, \lambda, r_c\right) = \sum_{j,k} & f\left(r_{ij}\right) f\left(r_{ik}\right) f\left(r_{jk}\right) \\ & \left[\lambda \cos\left(\theta_{ijk}\right) + 1\right]^{\zeta} e^{-\eta\left(r_{ij}^2 + r_{ik}^2 + r_{jk}^2\right)} \end{aligned} \tag{2.74}$$

Finally, it should be pointed out that the projections shown here do not guarantee a unique number for each neighborhood. Mathematically, the injection property is not met. However, one-to-one map of the environment to its fingerprint necessitates injection and surjection. The latter is also does not hold when the image space is $\mathbb{R}$, but can an easily be enforced by restricting the image space to the projections' limits. The injection on the other hand can be mended by choosing a set of projectors and expanding the fingerprint to a vector. By keeping the covariance between the indexes to a minimum (no redundant information), the vector's rank can be exhaustively increased till convergence. Figure 2.14 shows the overall composition scheme for a symmetry vector (SymVec).

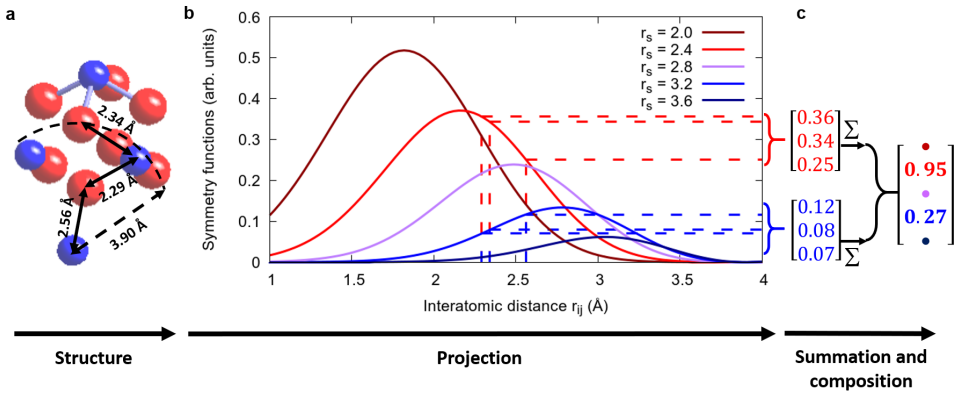

Figure 2.14: Illustration of radial SymVecs implementation. **a:** Primitive cell of bulk cerium dioxide (CeO_2) where blue stands for cerium and red for oxygen atoms. The full arrows denote the inter-atomic distances that are fed into symmetryfunction. The dashed arrows on the other hand denote the cutoff radius. **b:** Sampling of the Gaussian radial functions (eq. 2.73) with a cutoff radius of 3.9 Å(eq. 2.71). The η parameter of the radial function is kept constant at -2 Å^{-2}, while the peak r_s is shifted according to the legend in the top-right corner. The dashed lines project the inter-atomic distances in panel a onto the SymFunc of the corresponding color. **c:** Construction of the vector. The group the projections of panel b together into vectors. Here only two of the five entries are actually sampled.

2.3.4 Atomic energies and the grand scheme

After the projection, each atom has a SymVec that describes its neighborhood. These vectors act as the input to the NNP. As mentioned before, energies and forces are outputted. The forces acting on each individual atom are directly outputted by standard ab initio code, so there is a one-to-one mapping with the

vectors. Each force component receives its own NN with different parameters. With the energies, the situation is not that clear: there is only one value for the entire system. Therefore, a new observable is defined associating an atomic energy to each index. Mind that this concept is purely mathematical construction, since no quantum operator can be constructed to define atomic energies. As such it has to be constrained for the sum of over all the atomic energies to return the system's energy. The energy NN outputs atomic energies, but it is the system's energy that is evaluated with the training set. Although `RuNNer` loops over all atoms, the NN parameters used are always the same. This effectively increases the input data and smaller training loops by the system's size. In total there are four different NNs being trained. The formulation of NNs as in eq. 2.70 allows for the construction of a derived network. Still, the energy results can disagree with those of the forces, even at the data level. When evaluating the residual error of the output vector $\begin{bmatrix} E & F_x & F_y & F_z \end{bmatrix}$, it is clear that the force has a larger impact since it contains more components. To rectify this, the residual errors are weighted. The default setting equalizes both observables and can be further toggled to accommodate for high bias fitting of one observable. Figure 2.15 gives a schematic overview of the NNP architecture.

2.3.5 Future challenges in Machine Learning

The NNP as presented up till now only considers local interaction. Any interaction that stretches beyond the cutoff radius is effectively masked. To accommodate for this weakness, the HDNNP first separates out any long-range interactions from the total energy. `RuNNer` can account for two types: electrostatic potentials and dispersion. The former receives its own NN where the SymVecs are fitted to the individual atomic charges, similar to the atomic forces. The Coulomb energy is then computed via Ewald summation and subtracted from the total energy. Experience shows however that corrections from the Coulomb scheme are marginal due to shielding. Analogously, vdW corrections based on Grimme's method (see subsection 2.1.5) are only parametrized by the elemental pairs and a coordination number. They can be computed exactly, as is, and again subtracted from the system's energy. This also allows for the mixing of datasets with and without vdW corrections. The schematics already account for both implementations.

Some systems still fall outside of this scope however. For one, the atomic charges that underlie long-range electrostatics are themselves still local in nature. Next, the reconstructed energies and forces currently do not contain any higher order moments. Another problem is the case where the electron density is no longer well-described by its environment. The reduction of zinc oxide makes

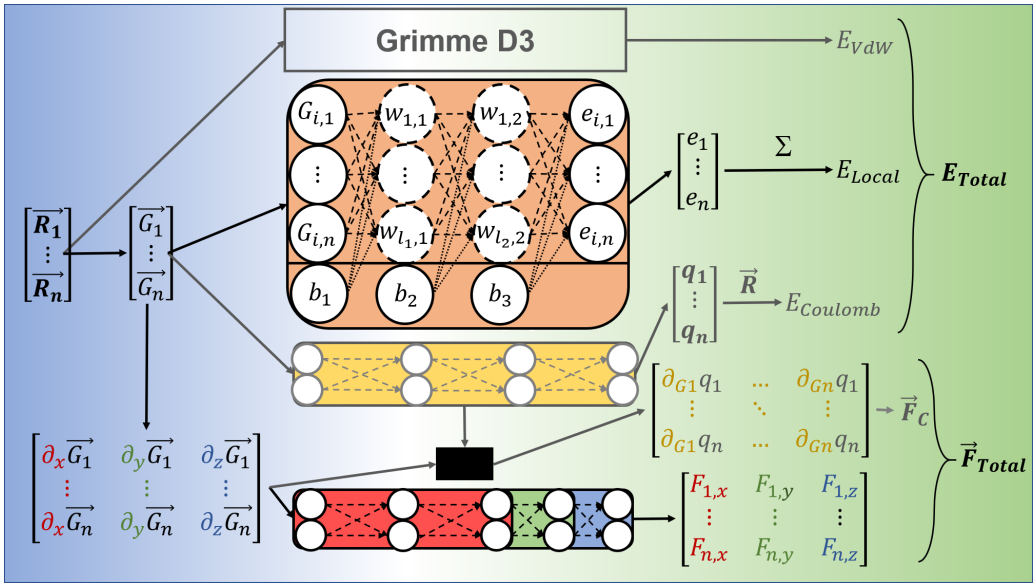

Figure 2.15: Full Neural Network architecture as implemented in `RuNNer`. The input side is shaded blue and starts from the atomic coordinates $\mathbf{R}_i$, which are converted into SymVecs $\mathbf{G}_i$ (see Figure 2.14). From there on out, the vectors are fed into various, independent NNs. A general sample is given in the atomic energy NN (orange) with layers j, weights $w_{i,j}$ and offset b_j. The dashed arrows show the connectivity. Dashed nodes are submitted to an activation function. The resulting atomic energies e_i are summed to obtain the local energy. In specific cases where long-distance interaction becomes important, the contributions of electrostatics and dispersion can be accounted for via optional routes (gray). For the former another NN (yellow) is trained to predict the atomic charges. Along with the coordinates they derive the Coulomb energy. The dispersion energy is computed directly from Grimme's method (see section 2.1.5). Lastly, the force components are processed analogously to the local energy in the RGB colored NNs. The input is changed to the spatial derivative of the SymVecs though. The Coulomb forces are computed from the same charge network after derivation to the SymFuncs. The whole process described here breaks down forward evaluation. For training of the NN, back-propagation loops over the scheme in reverse, updating the weights using the Kalman filter.

for a good example. Here, the foreign electron occupies the conduction band and becomes delocalized. Lastly, the rapidly growing configuration space limits actual applications to a few elements only. One line of research focuses on the systematic expansion of the Behler-Parinello approach with improved long-range interactions. The field of machine learning has honed many varieties on the NN. One such version is based on the optical nerve and is widely implemented in image

recognition. A convolutional neural network (CNN) uses kernel to agglomerate pixels according to different patterns. Afterwards, it passes them through regular NN layers. As such, it spots patterns of different sizes, generating new images with various kernels. All the while, the final pictures are still processed as a whole. A recent implementation applies it to hexagonal patterns with remarkable results:[77] the CNN manages to reliably extrapolate the potential. The image is generated by smearing out the atoms using Gaussian functions. Nonetheless, this method faces its own hurdles. First and foremost, the kernels now require a fixed size equal to the training set (pixel) dimensions. Hence, the main exploit of NNP to model larger models is lost. Apart from that, the kernels have to be preset by the user. In other words, the user has to bestow insight into the symmetry of the data beforehand.

Overall, what sets most artificial potentials apart from each other is the choice of descriptors and metrics. A whole plethora has been generated and tried. Since each study works with different datasets and often on specific systems it is hard to judge, but currently the SymVecs are the state-of-the-art implementation. For the Machine Learning community to develop better methods and break through in the Chemistry community, it will have develop a consensus on how to compare the performance of individual algorithms and which systems to fully characterize first. This will be its biggest challenge in the near future.

Chapter 3

Single-atom catalysts of Group 10 elements on ceria

We are not going in circles, we are going upwards. The path is a spiral; we have already climbed many steps.

Hermann Hesse, Siddhartha

3.1 Pt single-atoms and dynamic charge transfer

3.1.1 The Pt/ceria interface

The combination of platinum (Pt) NPs on a ceria support works so well, it has become synonymous with car-exhaust catalysts. More specifically, the three-way catalyst consists out of a matrix with pores. The pores are covered by 10 – 30% of ceria with Pt, palladium (Pd), and ruthenium (Ru) deposited on top.[3] The first two play a key role in the oxidation of CO to CO_2. Where in the gas phase the rate-determining step is the O-O bond breaking into radicals (5.182 eV), this shifts to the CO recombining with the activated oxygen atom (1.036 eV) on the heterogeneous catalyst's surface. The support actually assists in the catalysis, as oxygen is consumed at the ceria side* while CO adsorbs onto the metal.[78] From thereon, the adsorbates must migrate towards the metal/support boundary to recombine.

*This makes sense, considering the high oxygen storage capacity of ceria.

Here, time-resolved resonant X-ray emission spectroscopy (RXES) revealed a second contribution from ceria to the reaction. The concentration of Ce^{3+} matches the CO conversion rate stoichiometrically, suggesting that both are products and that CO actually recombines with lattice oxygen. Hence, the atmospheric oxygen supply merely serves to replenish the surface vacancies. During the reduction in preparation of the reaction, the Ce^{3+} concentration hits a lower bound which depends on the temperature. Within the temperature range of 24°C to 44°C this level fluctuates between 0.75% and 2%. Since the presence of Pt seems to activate reduced cerium ion with oxidation state III+ (Ce^{3+}) for oxidation, the remaining centers are thought to lie too far away from the boundary. This should then extend to other reactions, earning them the name of *spectators*.

A similar conclusion was reached independently using synchrotron-radiation photoelectron spectroscopy, scanning tunneling microscopy, and DFT calculations.[79] The sizes cover a wider range and are shown to converge to a concentration of 16.7% in the limit of large NPs. This new value turns out much larger than the one in the previous work. The reason is that here it was measured at ultra-high vacuum (UHV), not in an oxidizing atmosphere. The twist however lies in that the electrons in these Ce^{3+} ions do not originate from any surface vacancies, but rather the metal itself. Moreover, the model predicts that the charge depletion is at its strongest for NPs with a radius around 1.5 nm ($40 < \#\text{atoms} < 90$). Focusing in on this region has shown that this electron exchange influences Pt nanoclusters strongly enough to coin the name Electronic Metal-Support Interactions (EMSI).[80] The name itself is a throwback to the more general Strong Metal-Support Interactions (SMSI).

The effect was first observed in water splitting over Pt clusters, a key step in the water-gas shift reaction (WGS) reaction. Conversion reaches a peak at cluster sizes of 1.7 nm with a gain of more than a six-fold.[81] Other metals, such as Cu and gold (Au), follow a similar trend but drop off more slowly with increasing particle size. Only nickel (Ni) was found to posses a peak at the same size as Pt and the same asymptotic behavior, although it does not live up to the same activity. DFT verified that Pt_8 outperforms Pt_{79} and Pt (111). Not only is the process exothermic, contrary to Pt (111) it only has a barrier of 0.62 eV. At the end of the splitting the activated OH group stays on top where it is open to any attack from CO, while the proton migrates down close to the boundary.

Interestingly, a modest covering of titania (TiO_2) with CeO_x of 11% produces peaks twenty-folds taller than on Pt (111). Hence either titania interacts with ceria to modify its properties or this is a ceria size effect. Ref. 81 noted that as the NP grow, the Pt 5d band becomes more pronounced and fills up to the Fermi-level, deactivating the synenergy of this two-phase support. The other

route was investigated in refs. 82 and 83. The study determined two separate effects for the Pt_8 cluster deposited on ceria. Firstly, spontaneous, metal-to-oxide electron transfer as observed above. This already occurs from the moment of deposition and does not need temperatures higher than room temperature[†]. Calculations explain this as the Pt 5d orbitals nearly forming a band that bridges the ceria HOMO(O 2p)-LUMO(Ce 4f) gap. Since the empty 4f orbitals lie just above the Fermi level, most energetic constrains for electron excitation/reduction of cerium ions have been removed. Along with previous observation, this shows that the band has to be carefully tuned. Secondly, when the system meets a key condition, oxygen spills over onto the metal cluster (*reverse spillover*) at elevated temperatures of 700 K. The condition: downscale the ceria support to nanoscale itself. Due to the strain, small ceria NPs are more accepting of vacancies than their extended surface counterparts. Combined with the oxygen uptake on the Pt side, the overall process even becomes exothermic by -0.51 eV on $Ce_{40}O_{80}$. The reverse spillover also leaves surface vacancies behind, which result in more Ce^{3+}. Although both phenomena contribute to the phase potential, the authors also remarked a drop in the region of $300 - 450$ K.

The takeaway message from this brief overview is that a sustained charge flow from Pt to ceria generates a non-zero potential between both. A portion of the Ce^{3+} actively participate in catalysis and are therefore detrimental to the overall reactivity. When sizing down the NPs to clusters the potential remains but affects the cluster's shape. In the following section, I shall discuss the existence of single-atom (SA) Pt and how the trend outlined above continues.

[†]To the knowledge of the author no lower temperature limit has ever been established.

Strong Metal-Support Interactions (SMSI) This term originates from the work of Tauster[84,85] of titania supports and chemisorption behavior. The old picture of oxide supports was they did not interfere with the properties of the metal nanoparticles (NPs) resting on top. Tauster disputed this simplistic view by claiming that certain oxides do interact with their support. The first reported case consists of Pd deposited titania, which after heating in a reducing environment would grow over and eventually encapsulate the metal. Simultaneously, the reactivity decreases with the loss of active surface area. The encapsulation is fully reversible via oxidation, highlighting its chemical nature. This effect extends to other metals such as Ir, Ru, Rh, Pt. Some oxides do still abide by the old model, such as alumina or silica.

It was theorized that a metal-metal bond formed via electron donation from the under-coordinated metal to the oxide. As the range of unique properties grew for metal/oxide combinations susceptible to SMSI, the term started referring to the bonding itself. New phenomena included dispersion of the metal instead of the oxide and enhanced catalytic reactivity. Farmer and Campbell demonstrated that ceria are capable of the former in the case of silver.[86] They did this by comparing the energetics of Ag NP growth on MgO and ceria. There is a clear break in trend for the chemical potentials. Ceria yields much lower potentials, i.e. more stable, NPs than those of the same size on MgO. This entails that ceria can accommodate smaller NPs. Moreover, ceria with a higher degree of reduction or defects excel at supporting small NPs. One theory as to why these benefit dispersion points to the repulsive effects of lattice strain around each particle. Thinner slabs or those with more vacancies can namely reshape themselves better to correct for the lattice mismatch. The surface then accommodates for the resulting strain by counteracting it in the perimeter around the particle.

There is some dispute in the current academic debate about the actual nature of this bonding: in how far is it covalent, to what degree does charge transfer play a role, and in which direction does it go[a]? EMSI, a variety on SMSI, displays a strong perturbation in the electronic structure of the NPs. Investigation revealed that depletion of the d-band of Ag on hollandite manganese oxide promotes the EMSI character and reactivity.[88] This depletion is coupled to Ag-O bond formation with progressively shorter lengths. At the same time, EMSI also reduces the internal Ag-Ag bond distance, condensing the NP. The final Ag NPs carry on average a partial charge between 0 and 1 e^-. The d orbitals remain partially empty after bond formation, signaling a full electron transfer (ET). This theory would explain why mostly reducible metal oxides are sensitive to this type of interactions.

[a] Some studies suggest that the charge density could also flow from the oxide to the metal.[87]

3.1.2 Pt_1/ceria in the literature

The stability of the Pt catalyst plays a major role in the overall performance of the three-way catalyst. When undergoing several heating and cooling cycles between usage of the car, the smaller NPs disappear to Ostwald ripening.[89,90] As discussed above, the small NPs are more reactive so them disappearing leads to a decline in performance. The group of John Jones however reasoned that by capturing the mobile surface atoms before they are adsorbed by the larger NPs, this loss can be turned into a profit.[91] They prepared a batch of Pt NPs deposited on La-Al_2O_3 mixed with several types of ceria NPs. The particles are then allowed to sinter under an air current at 800 K. A combination of microscopy (HAADF scanning tunneling electron microscopy) and spectroscopy (X-ray defraction) verify that the Pt NPs dissolve. Rather than being lost to the bulk and becoming non-reactive, the SAs are trapped at surface defects sites.[91] The authors note that the reactivity seems to be higher on polyhedral NPs and nanorods, which predominantly expose (111) and (110) surfaces. Based on this postulation, several theoretical models where proposed. The most prominent model stabilizes Pt at a monolayer (ML) surface step site between two (111) plateaus.[92] In the study, two types of steps were considered. They differ from each other by a row of oxygens acting as an intermediate stepping stone between both layers. Both bind Pt much more strongly than the regular, pristine surface. At the step with the row, Pt integrates itself in a square-planar coordination (4O) geometry with four oxygen atoms and is oxidized to Pt^{2+}. When the row is removed however, the local geometry does not support a four-coordination and Pt is only partially oxidized. It is clear that this second setup is strained, as the row-enhanced step sustains a Pt coverage of $\theta_{Pt} = 2/3$, whereas without Pt clusters already at $\theta_{Pt} = 1/3$. The excess electrons are adsorbed by the cerium ions, although photoelectron spectroscopy indicates a pattern breaking of lower Ce^{3+} concentrations. Instead it is shown that atmospheric oxygen can accumulate at the step and participate in PtO_4 formation with one oxygen ligand sticking out. The additional -1.60 eV gain allows even for a full coverage at the step. Other studies validate that square-planar PtO_4 is the most stable surface coordination.[93] The geometry falls in line with observations from other fields such as organic metal chemistry.[94] The surface direction of the model corresponds to the (100) Miller index, which have been found to sustain SA Pt in other calculations.[95]

3.1.3 Constructing a model: Pt-4O

Considering how the surface step between two (111) plateaus lies along the (100) Miller plane, we decided to construct another model on a pristine (100) surface.

Apart from dispersing Pt atoms via Ostwald-ripening, one can also deposit Pt via volatilization into PtO_2.[96,97] In this state, both oxygen atoms remain attached to the Pt atom as ligands that integrate into the lattice. Of all three major surface cuts, oxygen-terminated (100) provides the perfect environment to form square-planar Pt. To keep our model stoichiometric however, we produce the same coordination using only original lattice oxygens. The work of Capdevila-Cortada[98] shows how in the process of heating up to 800 K, the surface switches between the oxygen and cerium-termination. The latter exists out of low-lying pyramid-like structures, that can wedge dispersed Pt atoms in between them. At the 800 K mark these structures break down to the oxygen-termination, but not necessarily the oxygen ring around Pt. Experiments back up the computational claims that the lattice oxygens become mobile at these elevated temperatures.[99] The regular parallel row pattern found in most literature breaks and rearranges itself into various patterns, each with its own coordination environment for prospective SAs. Obviously, this form of SA Pt enclosure is much more complex than the vapor deposition route and can produce a larger variety of starting points. Still, considering the relative stability and lattice dynamics it poses a notable alternative. The major difference for modeling both preparation methods is the production of Ce^{3+} ions in case of enclosure (and also the bonding energy). The maximum Pt loading before clusters start to appear is so low (3 wt%[100]) that the difference in oxygen storage capacity (OSC) between both becomes negligible. Moreover, by using the reduced version we can also track the Ce^{3+} dynamics.

The stoichiometric PtO_4 system is referred to as Pt-4O in the paper, and from here on out I shall adopt the same notation. In this model the Pt binding thermodynamics are further impacted by the added variable of the relative Ce^{3+} positions. Most computational works content themselves by allowing the system to relax to a single, uncontrolled electron(ic) configuration (EC). This EC is then assumed to be the global minimum. We on the other hand follow a different philosophy and choose a specific EC by predetermining the Ce^{3+} positions. To investigate the extent of this effect, we then sample all 28 combinations of how to distribute two electrons over a (3×3) supercell. This yields a much more representative distribution. Paper figure (pFig.) 1 showcases the various energy levels compared to the Pt bulk cohesion energy (left y-axis) and the most stable SA Pt coordination (right y-axis). This last reference energy is exothermic by 0.3 eV with respect to Pt bulk (the solid brown line). Hence, SA Pt is resistant against sintering, and the surface dynamics outlined above form a thermodynamically viable route for trapping Pt atoms. It is clear that confined within a 11.649 Åradius, the impact of the distribution is appreciable: the energy span between the two extrema measures 0.7 eV. Despite the considerable energy range, many

levels group together in tightly packed bands. This suggests that any energy level is attainable via small, incremental energy steps. To test this out, we performed BOMD on a (2×2) supercell. The cell was gradually heated from 0 to 300 K, after which it equilibrated for 1.5 ps before further heating to 600 K. As predicted, the polaron onset ($Pt^{+} \rightarrow Pt^{0}$) happens at 600 K (0.052 eV thermal energy) after 2.42 ps. Throughout the simulation Pt-4O retains its oxidation state (OS) II+ nor does it break open. Only during polaron hopping events where one electron delocalizes does the metal oxidation state (mOS) become less defined.

Catalytically, SAs do not live up to the reactivity of NPs.[101] Several studies show however that applying a short reductive pulse (or a series of pulses, interspersed with oxidative periods) transforms the system. Afterwards, the reactivity sky-rockets, meaning that the catalyst has been activated. The same studies contradict each other however in how strong the boost is. One theory proposes that upon steam treatment at 800°C after calcination, the Pt adatom is buried in subsurface layers, from where it enhances the reactivity via vacancy formation.[102] In this scenario a 100% conversion rate is achieved just below 150°C. The same authors later present an improved reduction process that should promote (re-)agglomeration instead,[97] as with regular NPs. Now, full conversion is achieved at 125°C using impregnation methods or even at 75°C with vapor deposition, both after activation obviously. Still, the authors claim that the same NP distributions are attained and instead attribute the differences to reducibility of the ceria support. Gänzler and coworkers in fact managed to find the optimal NP size (1.4 nm) with the largest inter-facial, active area.[10] They are prepared via short, reducing pulses of either CO or dihydrogen (H_2). These clusters attain only half a conversion rate at 158°C however. It is thusly clear that there is no consensus yet on the mechanism behind this reactivity, except that an activation step is required.

We on the other hand, postulate that the SAs are preserved after activation. Our theory hinge on the pulsations in ref. 10, because overexposure would convert the catalyst back into larger, non-optimnal NPs. In the following paragraph I shall dissect the activation step in our scenario.

3.1.4 Activating the catalyst: Pt-3O

As described in the previous paragraph, the SAs after deposition differ from the active catalyst. We considered both reductive routes (CO and H_2) and constructed a full reaction mechanism in pFig. 4a. The left-hand cycle 1 showcases both activation procedures. In the case of CO activation, the gas adsorbs on top of Pt, proceeds to abstract a single oxygen ligand and then desorbs as CO_2. H_2

on the other hand, homolytically splits between Pt and a neighboring ligand. Next, the hydrogen atom at the Pt side migrates over to the OH group where the whole desorbs as water gas. Energetically, both reaction mechanisms have their bottlenecks at the opposite ends. In the CO activation it is the C-Pt bond breaking (E_a= 0.97 eV) right before desorption, while with the H_2 activation it occurs as the H-H bond breaks during chemisorption (E_a= 1.35 eV). The difference in activation energys (E_as) along with the entropy loss upon adsorption, help to explain why CO is the preferred reactant.

The end result of both pathways is the same: the oxygen ring around Pt is broken up, resulting into a Pt-3O (PtO_3) coordination. Although an oxygen atom has been abstracted and the surface has been reduced as a consequence of it, I must again point out that for the following we used a stoichiometric system. As such we decouple the effects of the coordination from those of the surface reduction. Latter on, I shall also touch on the latter. Compared to the well-defined Pt-4O, the bonding situation in Pt^0-3O is a bit awkward. For one, at equilibrium one ligand clearly has a longer bond length (2.843 Å) than the other two that lie at 90° (2.003 Åon average). More importantly however, we do not know its mOS from literature. For an elaborate discussion on why these are not interchangeable, the reader is kindly referred to the side box 3.1.4. Therefore, we sampled three mOSs (0, I+, and II+) in a fashion similar to the energy levels of Pt-4O. The results are also listed in pFig. 1, in the middle section.

What stands out most is how the energy range of mOS I+ pans out almost symmetrically around mOS 0[‡], demonstrating how the Ce^{3+} configurations can equally benefit or disrupt the system and likewise for mOS II+ with respect to I+. Consequentially, the Pt^{2+}-3O is the most stable configuration and we can safely conclude it captures its chemical nature of best. Still, even the ground state still lies 0.23 eV above the most unstable Pt-4O configuration and 0.61 eV above the Pt bulk cohesion energy. It is therefore safe to assume that this system can only be produced via the activation mechanism. The BOMD simulation supports this analysis, as even before reaching 600 K the system already converts (see Suppl. Video 2). Remarkably enough the stoichiometric system does not convert back to the more stable Pt-4O but instead to a SA Pt with a two-fold coordination, Pt-2O. Yet, a single oxygen diffusion would have been all that was needed to achieve Pt-4O, while now the simulation performed two subsequent diffusion steps. The Pt-2O coordination on the other hand fits naturally in the regular row-termination studied in most papers. In the temperature range of 300 to 600 K it is overtaken by a zigzag pattern corresponding to the local coordination for

[‡]I.e. the center of the mOS I+ levels almost corresponds to the mOS 0 energy, with the latter lying just below it.

Pt-3O.[98] Although at a larger scale the ratio surely still applies, there clearly is another driving force at play in the direct vicinity of SA Pt. As mentioned before, Pt-3O has one weakly bonded ligand and unsurprisingly this ligand breaks off first (at around 300 K). More so than being simply thermally driven however, the diffusion seems to be initiated by a polaron hopping event to a Ce site neighboring the oxygen. It is reasonable to presume that the volume expansion pushed the oxygen out under an angle. This interpretation falls in line with the trajectory. The qualitative correspondence between the energy levels and the BOMD also validates our approach of mapping the minima out first. We conclude that Pt-3O at room temperature and above is a transient state that connects Pt-4O to Pt-2O. In the next paragraph I shall present the Pt-2O system and verify if its reactivity is really enhanced with respect to Pt-4O.

Before moving on, let me first address the recurring topic of stoichiometry. In paper supplementary figure (pSFig.) 12 we compared such systems (top panel in green) to Pt-nO with a surface vacancy concentration of $\theta_{vac} = \frac{1}{9}$. There are several signs that this results in too high Ce^{3+} concentrations. Hence we would be forced to use larger, computationally more expensive supercells and account for an exponentially increasing number of configurations. To discount the reaction thermodynamics (i.e. $Ce_{36}O_{72} \rightarrow Ce_{36}O_{71} + \frac{1}{2}O_2$) and only retain relative energies, we change the reference system to a cell of the same dimensions with a vacancy at the same location ($Ce_{36}O_{71}$). The vacancy location is chosen so to least interfere with the SA. Since the reference is already reduced, the same configuration variance holds. Hence, there exists no single Pt bulk line, but rather a region between the extrema. Below this region, the SA levels are thermodynamically stable and similarly all those that lie above are unstable. Those between both boundaries are in a dynamic equilibrium with Pt bulk. Any conversion depends on the specifics of the polaron trajectories. Either these rearrange themselves vertically in the diagram and leave the brown regions, or they convert to a lower lying Pt bulk level which itself is metastable.

Let us now examine the impact on Pt-nO. Firstly, Pt-4O remains in mOS II+, for the 167 ECs tested. Of all configurations sampled, none fall below the previous minimum. It is however possible to further destabilize the system up to 1.3 eV. In several cases however, Ce^{3+} resides in the subsurface of the system. From experiments we know that this is possible, but very unlikely considering their limited penetration depth.[103] Instead, polarons have the tendency to disperse out and driven by the polaron-vacancy interaction, the latter will follow them.[104] Together with the fact that SA Pt only exists at low loadings, this knowledge supports our motivation to restrict our scope to stoichiometric slabs. Pt-3O exemplifies the detrimental impact of Ce^{3+} overpopulation on the energetics if

we would account for vacancies. The osmotic (and spatial) pressure(s) reduce(s) Pt^{2+} to Pt^{+}, which contrary to Pt-4O, becomes much more stable. Even Pt^{0}-3O is tenable now with only a 0.2 eV gap between the mOS 0 and I+ ground states. It is unclear what the impact would be on the conversion to Pt-2O in this setup. The latter is still more favorable from a energetic (and entropic) perspective, but not as strongly anymore. We verified that all of these observations are truly caused by reduction and not for example by the change in lattice strain[§] by applying an intermediate reduction under the form of H_2 adsorption.

Charge or oxidation state? Inspired by a Nature Materials Perspective,[105] I want to clarify the terminology used in this body of work. Often the terms *charge* and *OS* are used arbitrarily, as if they are synonymous. This could not be further from the truth. Atomic charge is not a quantum observable, meaning that there is no theoretically sound definition. Any formulations of a partition scheme have to be based on another physical observable then. The OS on the other hand, captures the amount of valence electrons involved in bonding or band formation and is fully physical. The two can be linked by using the polarization constructed to recuperate the lattice dynamics as a partitioning. Focusing on the chemical properties of SA Pt/CeO_2, I prefer to talk about the OS. Contrary to the many types of charge schemes, ab initio does not directly report the OS.
Instead, we (the authors of ref.[5]) opt to use the magnetic moment of the Ce ions $\left(\mu^{Ce}\right)$. Ce^{4+} is spin-restricted, so it bears no μ^{Ce}. When an electron transfers, it is housed unshielded in a new orbital and the $\mu^{Ce^{3+}}$ lies close to $1\mu_B$. Still, during BOMD simulations the μ^{Ce} adopts a far wider range of values, starting from $0.5\mu_B$ up to full $1\mu_B$. To track the mOS we need an exact threshold. PSFig. 14 lists the BOMD statistics of the Pt-2O and Pt-3O systems, which counts the mOS lifetimes for different μ^{Ce} cutoffs. We settled on $0.8\mu_B$ cutoff as a compromise.

[§]Lattice strain is induced by the removal of an oxygen ion and the Ce^{3+} expansion. These are conflicting effects that also end up favoring intermediate mOSs.

Is there however a more direct way for elucidating the Pt OS? Could one analogously to Ce, use the μ^{Pt}? In pFig. 1 we plotted the total magnetic moments on both species. $\mu^{\text{Pt-2O}}$ correlates with $\mu^{\text{Ce}^{3+}}$ so that $0.0\mu_B$ corresponds to Pt^0, $0.5\mu_B$ to Pt^+, and $1.0\mu_B$ to Pt^{2+}. Pt-3O starts off along the same trend, but at Pt^{2+} the signal suddenly vanishes. The uniformity suggests a diamagnetic rather than a paramagnetic state, probably due to bond formation with the ligands. The DOS in pFig. 3 confirms a strong mixing of the Pt and O states close to the Fermi level. As a result, it is impossible to distinguish between Pt^0 and Pt^{2+} based on $\mu^{\text{Pt-3O}}$ alone. Similarly, $\mu^{\text{Pt-4O}}$ also vanishes. Of course, Pt^{2+}-4O is the sole mOS, so a descriptor only serves for verification purposes. Only Pt-2O seems viable, but spurious μ^{Pt} values of $0.75\mu_B$ cannot be indexed either.
We conclude that the complexity of the Pt electronic structure prevents any definitive mOS assignment. Experimentalists often employ X-ray photo-emission spectroscopy (XPS) shifts to determine the OS. We computed the computational counterpart, core-level binding energies and managed to obtain a qualitative correspondence in pSFig. 2 with XPS data.[93] Lastly, we did check the correlation between Bader charge scheme and the mOS. The figure can be found in figure 3.1. There is vague trend, but the fitting quality is poor $\left(R^2 = 0.78\right)$ which would result in descriptor with a mediocre signal-to-noise-ratio.

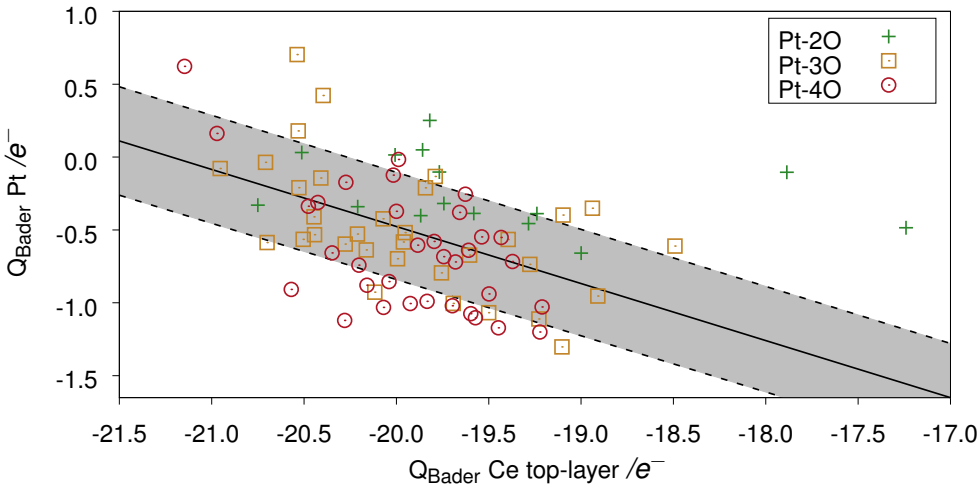

Figure 3.1: Linear regression between the Ce and Pt Bader charges (e^-) for Pt-nO. The solid line shows the regression curve and the dashed lines the standard deviation. The grey zone thus covers 68.2% of all data. The Ce charges cover the entire top surface layer, where the transferred electrons localize. Both charge distributions are calibrated to their valence shell electrons.

3.1.5 Activated form: Pt-2O

The previous paragraph concluded that the activated form Pt-3O is unstable at operation temperatures and spontaneously converts to Pt-2O. This suggests that Pt-2O might be the actual catalyst. I shall address the Pt-2O reactivity shorty, but first delve into its physical properties. Following the same approach as with Pt-3O, we again sampled the energy levels of the OS 0 to II+. The results can be found at the left-hand side of pFig. 1. Firstly, it is clear that now there are less states, since many converged to the same configuration. Secondly, none of the levels fall under the solid reference line, meaning that Pt-2O can be adsorbed by large NPs. This should not pose any trouble since repeated redox cycles disperse out the larger NPs.[10,106] There might still be competing, smaller NPs though. Due to a higher surface-to-volume ratio and accompanying low coordinations, these clusters are energetically less stable. This translates itself into a higher surface energy and lower chemical potential.[90] As a new reference, we constructed a spherical NP of around the optimal (reactive) size, i.e. 2 nm, and relaxed it. The structure can be found in pSFig. 4. Deposition effects that depend on the NP/CeO_2 interaction and the angle with the surface were ignored to reduce the computational effort. Disregarding these effects, we used the average bonding energy per atom to construct a novel, dashed reference line. Remark that this choice results in the strictest lower-bound, since the contribution of bulk atoms tends to stabilize the cohesive energy. Compared to the novel reference now, Pt-2O would need to oxidize to II+ before sintering. As such, we have demonstrated that Pt-2O is a metastable state that requires small cluster environments to thrive.

Comparing the mOS, I+ comes out as most stable by and far: all of its levels lie below the other mOS. Pt^0 and the Pt^{2+} minimum align, but considering how the latter as more unstable states, it should be less stable overall. The relative energy difference between all minima is low enough to be overcome by thermal energy (0.3 eV). Hence, it is unclear if at non-zero temperatures Pt^+-2O will still be the main species. Instead we could have phase changes between OSs and phase lines where two mOSs coexist. To test out this hypothesis, we performed the same BOMD setup as before. The Pt-2O remains stable up until at the least 600 K average temperature. The results after heating are shown in pFig. 2a,b. Monitoring a SA Pt, we see it exchange electrons readily with the oxide and assumes various mOSs as a function of time. Since this behavior started at 300 K, we presume that we are not sampling on a phase line but that instead this is the phase itself. In other words, past a certain temperature the mOS is not well-defined anymore. This is, to the authors' knowledge, the first record of a dynamically changing OS and thus a completely new phenomenon. As the mOS

determines the metal center's chemistry, the consequences are two-fold. Firstly, a single catalyst can now act as three separate ones and on a macro scale we may expect a temperature sensitive distribution.Secondly, the average time each mOS lasts, i.e. its lifetime, will determine the window of opportunity for a chemical attack. Any slowly progressing mechanisms are thus shut out. To get a flavor for both, we performed a statistical analysis on the BOMD results as shown in pFig. 2d. In total, mOS 0 and I+ are equally represented and II+ seems only present as noise. SA Pt does not simply oscillate between both mOS however. Instead, Pt^0 is found to have a much longer lifetime with outliers of up to 5 to 12 ps, while Pt^+ at most lives 2 ps. Moreover, Pt^+ populates a much wider range at the low lifetime intervals. The only Pt^0 presence in that region on the other hand lies at less than 0.1 ps, which can be discarded as noise. It is therefore our impression that the activation barrier of mOS 0 is higher than the one for I+. Once a single electron has been transferred, the barrier to a second seems quite low even though the state itself is energetically unstable. Hence we do not expect much contribution from II+ in general. Any discrepancies between mOS 0 and I+ on the other hand will reflect the impact of the attack window. The prominence of stable Pt^0 appears quite exotic, but it has actually been observed on copper oxides as well.[107]

Considering the novelty of this phenomenon, we constructed a first model to better understand it. Principally, there are two mayor contributions at play here. One is the Coulomb attraction between the oxidized SA and the Ce^{3+} sites. This generates the various energy levels and their alignment. It is examined by the Born-Haber cycle in pSFig. 6. The other is the local lattice expansion to accommodate the transferred electron. One can reasonably expect a mirror contraction of the oxygen ligands around Pt due to charge depletion. Considering how this aspect is arguably better understood, I shall be focusing in on it. To decouple the electrostatics from the charge transfer, we took the lowest minima of each Pt-2O mOS and removed the electron source, i.e. SA Pt. The rest of the slab was kept fixed, as instead it would relax back to the regular row-termination. We then focused on the changes in the local Density of States (LDOS) in pFig. 3, panels a-d. Comparing the pristine slab (panel a) with the one deformed by Pt^0 (panel b), the geometric impact of the SA is localized to the oxygens ligands. Their $2p_y$ orbitals (on the axis along the Pt bond) destabilize by up to 0.5 eV, as the energy contribution from Ce(5d) diminishes.[108]This behavior only grows more strongly as the ligands move further off-center (towards the former SA Pt location). On the Ce-side, the ET induces a volume expansion. Both phenomena are so intertwined however, that a cerium ion with oxidation state IV+ (Ce^{4+}) center with above average space has lower lying 4f orbitals. It is in other words more predisposed to reduction than other centers. Due to the asymmetry

in the mOS I+ case (panel c) one Ce^{4+} site is compressed and undergoes the opposite shift. After two mock ETs (panel d), the symmetry is restored. With two competing sites, the stabilization reduces significantly although it still remains present. This ties in with earlier observations that a (3×3) supercell becomes too small to sustain more than two surface Ce^{3+} ions. To see if the ETs occur spontaneously, we aligned the atomic levels of a non-interacting SA Pt (panel f) with the pristine slab. This was done by placing a Pt atom above the SA adsorption site, and aligning instead the respective O(2p) levels of the central atomlayer in the solid. The atom is suspended at nearly equal distances between the slab (7.1 Å) and its image (8.2 Å). All dipole corrections are turned off. A caveat in this approach, is that the Fermi level in DFT extends over the whole system.[109] This means that the Fermi levels of the slab and atom are the same, enforcing a last type of interaction. In the case of panel f, this results in the depletion of certain Pt orbitals. The symmetry breaking in turn results in the spread of the Pt DOS. To circumvent this issue, we introduced the constraint of the Pt^0-O bond in the form of two water ligands (panel e). The Pt orbitals now fall just under the vacant Ce(4f) orbitals, and no ET occurs.Any subtle shift in the vacant orbitals however, will push the system off-balance and induce changes in the mOS. From the discussion above it is clear that lattice vibrations can fulfill this role. To underline the phonon contribution and the role of SMSI that not only supports but apparently also aligns the Pt orbitals, we coin this phenomenon Phonon-Assisted Metal-Support Interaction (PAMSI).

3.1.6 Benchmarking

Now that all key players, i.e. Pt-*n*O, have been introduced, I shall discuss the benchmarking of our computational methods. All results displayed up to now were computed using Perdew, Burke and Ernzerhof functional equiped with a Hubbard correction (PBE+U) with an effective Hubbard parameter of U= 4.5 eV. One weakness of the density functional theorem equiped with a Hubbar correction (DFT+U) approach is the dependence of the ET energy on U.[16] Since linear response theory (LRT) yields different U values depending on the occupation, we extended the range of U values under consideration. pSFig. 5 is a variation on figure 1a with U= 3.5 eV (top) and U= 5.5 eV (bottom) added. Throughout each panel the reference lines and mOS 0 are untouched, since there is not ET present. The ionic mOS in Pt-3O and Pt-4O are much more sensitive to the change, as their centers gradually move down with U. In the meantime, their relative stability seems unaffected and the distribution's range is maintained. Consequentially, the Pt-3O mOS becomes indeterminate or is instead reaffirmed. Fundamentally, Pt-

2O behaves the same although less pronounced. At no point does the separation between the mOS becomes larger than 0.3 eV and at the least two mOS overlap. As such, the prerequisites for the dynamic behavior are always met. Lastly, I round this topic off with two more observations: although they have to be pointed out, the influence of the U should not be overstated. Both extremes (but U= 5.5 eV in particular) have outliers in the Pt-4O column. This suggests that we are already hitting on the boundaries of what is sensible and there is no need to extend the U scope. Secondly, LRT returns PBE+U with an effective Hubbard term of $U \approx 4.25$ eV for Ce_2O_3.[14] Considering how the main difference lies in the (partial) occupation of the 4f orbitals, we have an estimate for the deviation. Thus a correction of the U will have a minor impact, not strong enough to break the PAMSI in Pt-2O.

We expanded the benchmarking with other functionals and post-DFT corrections. We performed HSE (paper supplementary table (pSTab.) 3) and RPA (pSTab. 5) calculation on the mOS minima of each coordination. Overall, the methods slightly destabilize the atomic deposition energies. Both HSE approaches push a more metallic character (mOS 0). It has been shown that adding more exact exchange widens the ceria band gap.[87] Since the gap is already larger than with PBE+U, the level alignment favors SA Pt and the ET diminishes. This cannot be the full explanation however, as Heyd–Scuseria–Ernzerhof functional with the cutoff radius at 0.3 Åand 13% of exact exchange (HSE03) displays a wider spread. While the HF exchange mixing has been halved from 25% to 13% in comparison with Heyd–Scuseria–Ernzerhof functional with the cutoff radius at 0.2 Å (HSE06), its reaches does extend further now. The impact on the band gap of the former change is clear in pFig. 9.

RPA on the other hand was done on top of PBE.To ensure an ionic character, the HF and virtual orbital calculations started from the PBE+U charge density. Now, long-range correlation is added, which promotes the mOS II+. The trend brake with the other mOSs suggests that RPA's preference for Pt^{2+} comes from the mutual Ce^{3+} interaction.

3.2 Single-atom Pt as a catalyst

Having established the dynamic nature of the mOS, I shall now zoom in on the Pt-2O reactivity. One of the most well-studied reactions of Pt/CeO_2 is CO oxidation to CO_2. Considering how CO is already being used to activate SA Pt, it also constitutes a popular choice for testing subsequent reactions. Figure 4b,c outline the reaction profile. Since there are three possible starting mOS, we propagated a

unique reaction channel for each. Moreover, to trace the mOS distribution of each state we performed a short BOMD (10.5 ps) at 600 K without prior heating. Since transition states are by definition meta-stable, the BOMDs were only performed for the intermediate structures. For the assignment of the OS, we still count the number of Ce^{3+} centers like before. As more species adsorb, the pool of potential electron donors grows. Therefore the OS distributions do not necessarily refer to the mOS, but rather the whole structure of catalyst and adsorbates. One could in theory elucidate the mOS via core-level binding energies compared with XPS data or benchmarks. With the former unavailable and the latter outside of the paper's scope, I shall only discuss the total compound oxidation state (tOS)here.

We considered O_2 and CO adsorption for the first step. Both options and the follow-up steps proceed without any reaction barriers. Because O_2 slightly destabilizes SA Pt after adsorption and because initial CO uptake is more exothermic by ~ 0.5 eV, we preferred the latter route. PAMSI continues under after CO adsorption, though the distribution now shifts to strongly favor higher tOS. In fact, tOS 0 is quasi non-existent. Most likely, a part of these electrons originate from the σ donation to Pt according to the Blyholder model.[110] In the order of uptake, first CO and then O_2, two different coordinations emerge. The O_2 molecule nestles its lower atom in the trench next to the SA, integrating into the lattice. The atom on top angles towards the Pt. The CO molecule, which originally lay center above Pt, now has to tilt any of two ways. It can either lean over to the form a bond with the O_2 or it rotates away from the adsorbate under a 117° angle. The coordination in the first case is called a percarbonate and it is the precursor to CO_2. For this case, the tOS reduces to 0 and no further electron transfer dynamics (ET dynamics) is observed. Considering the overall percarbonate coordination and the formal charge of a lattice oxygen, the ET likely occurred internally. The other option reflects a side-mechanism that as re-enter the cycle as long as it does not poison the catalyst. The barrier with percarbonate is 1.60 eV and the overall step is endothermic by 0.61 eV. The high activation energy comes from the Pt electronic structure having to rearrange as CO rotates, and the 3.184 Ågap between Pt and O_2 that needs to be closed. Here, two BOMDs were performed. The former deforms the coordination geometry to an equilateral triangle (without bond breaking). In this state the is dynamic but with a clear preference for II+. If the system is heated more gently, it retains the regular geometry. Similar to the percarbonate system, the tOS remains 0 throughout. This validates that the position as lattice oxygen drives the ET, rather than the C-O bond. From percarbonate the reaction proceeds fluently towards the release of CO_2. The barrier depends on the mOS in the Pt-3O state. We did not perform a BOMD for Pt-3O and its tOSs were obtained via optimization calculations. Since the system is non-stoichiometric, the range of

levels has altered however. No tOS II+ was retrieved.

3.2.1 Microkinetic model

The absence of any large reaction barriers (disregarding the off-cycle step) suggests that the mechanism presented above can explain the high turn-over frequency (TOF) witnessed in experiments. In an attempt to quantify its reactivity, we started constructing a microkinetic model of CO oxidation by Pt-2O. The results in this section come from simulations performed by Minttu Kauppinen from the Honkala group. The input energies were provided by myself. A recent review in Nature Catalysis highlights the current state-of-the-art in first-principle microkinetics and the roadblocks ahead.[20] While it extensively addresses automated techniques driven by machine learning, these seem to be employed solely for fitting the ground state PES. In the following reaction network we go beyond and expand on that vision by including electronically excited states, namely Pt^0 and Pt^+.

The actual model itself demands several prerequisites. Firstly, it has to revolve around a catalyst that is recuperated at the end of the reaction. Since the last step in pFig. 4b leaves the system in a non-stoichiometric Pt-3O coordination, it fails to meet this requirement. There are two ways to close the cycle. As hinted at several times, the additional lattice oxygen atom can migrate away from Pt and recombine with a surface vacancy elsewhere. The latter is supplied via a Mars-van Krevelen (MvK) reaction in oxygen lean conditions.[111] Considering the disparity in reactivity between SA Pt and MvK, the latter would impose the bottleneck. The alternative that lies better in line with the expected performance boost would be a second CO oxidation step at Pt-3O, removing the remaining lattice atom.

Similar to steps II-III$_{a,b}$, CO adsorbs on Pt under an angle. This angle can lie at 180° or 0° with respect to the non-stoichiometric oxygen atom. As such, there are three different modes of approach:

1. CO rotates in a 180° around Pt and along the axis perpendicular to the support.

2. CO rotates again in a 180° angle over Pt. The axis of rotation now is parallel with the O-Pt-O coordination.

3. CO attacks O directly from a 0° angle above. In contrast with the other mechanisms, this one only involves the adsorption and desorption steps, separated by a single energy barrier.

All approaches yield the same TS and therefore we implemented the simplest: option 3. With the cycle closed, we impose one constraint to reduce complexity:

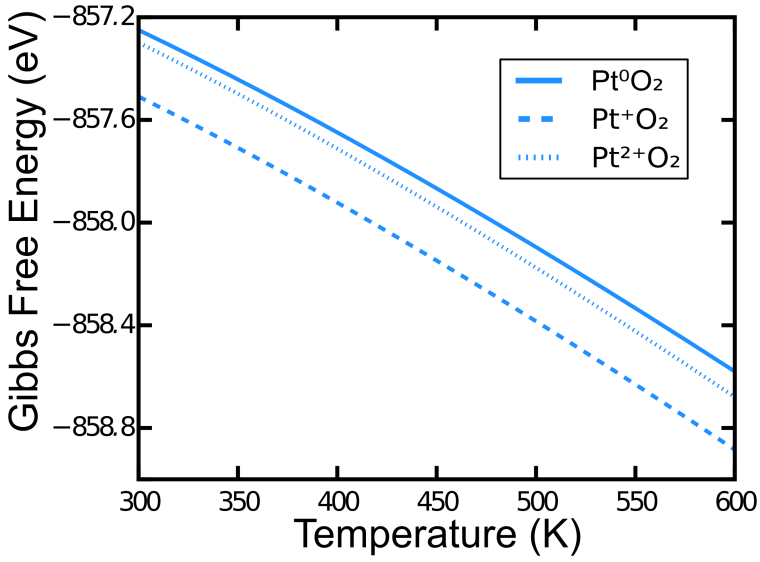

Figure 3.2: Gibbs free energy (eV) dependence on temperature (K) of the various Pt-2O mOS. The tangent is fully regulated by the entropy contribution. In this case it is only configurational and vibrational in nature. Since all lines are parallel, the vibrational entropy clearly overshadows the configurational within this temperature range. Courtesy of Minttu Kauppinen.

a reaction step between two intermediates preserves the tOS, unless the OS space is reduced. A single intermediate itself can change OS. The only exception lies at III_b, where conversion between tOS 0 and the ionic states warrants another primitive step (see pSFig. 11). The polaron hopping barriers for these OS changes are usually computed via a CI-NEB,[104] or alternatively via an intersection of PES with different ECs. The latter method is reminiscent of Marcus theory.[112] As of date, erratic electron localization interferes with the images' energy. A plausible solution would consist of combining transmission probabilities with the polaron band structure. This does not necessarily result in a reaction barrier, but rather a temperature-dependent probability function. For testing purposes we employ a global hopping barrier of 0.3 eV as an approximation. The value is based on the results in ref. 104.

The energy levels reported above exist out of internal energy, but for canonical ensemble, we need Gibbs free energy. In the case of surface species, lattice expansion is not accounted for and the free energy can be relaxed to Helmholtz energies, which require only entropy. In total there are four sources of entropy for surface species:

1. **Coordination entropy:** the DOF in the equilibrium geometry. The role of

this entropy for the (100) surface has been heavily explored in refs. 98 and 99.

2. **Configuration entropy:** the various possibilities in Ce^{3+} allocations. It is vanishing in the case of Pt^0-nO.

3. **Electron(ic) configuration entropy:** the level splitting of the 4f electrons in Ce^{3+}.[113]

4. **Vibrational entropy:** this work does not look into excited vibrational states but employs frequency calculations solely for the ZPE.

Type 1 lies outside the scope of this work and type 3 is insignificant in this temperature range. Figure 3.2 showcases the Gibbs free energy of Pt-2O with only type 2 and 4 entropy. The trends are nearly linear and remain equidistant. This indicates that the entropy is the same for all. Since type 4 entropy is constant between the same coordinations, this must be the dominant contribution by far. If type 2 entropy did matter, there should be line crossing at some point. While there is a slight widening in the mOS 0 and II+ gap towards the high-temperature range, within the range of interest type 2 entropy is negligible.

In accordance with the philosophy put forth in the Nature Catalysis review,[20] we also pay attention to catalyst stability and longevity. As such, future additions will most likely include the activation and deactivation step connecting Pt-2O to Pt-4O. This should significantly help finding the optimal CO/O_2 mixture. All runs were performed in a BR to test. Considering the thermodynamics involved, this means that if the catalyst is active it will eventually achieve full conversion. A PFR which better resembles the car-exhaust catalyst (and its timescales) is being constructed in the meantime.

Figures 3.3-3.6 compares three simulations at different temperatures: 300, 450, and 600 K. They will be discussed in that order. The initial coverage corresponds to the Pt-2O coverage in the DFT slab model. Starting near room temperature (300 K) then, figures 3.3 shows how the system adsorbs both gas reactants from the atmosphere, only to enter the off-cycle. Effectively the catalyst is being poisoned. Moreover, it withdraws less O_2 from the atmosphere than CO. Indeed, some of the Pt-2O with CO adsorbed remains, acting as a second poisoning mechanism. The small amounts here insinuate that slight temperature increases can remedy this last issue. Interestingly as well, the main tOS is I+. This makes sense from an energetic point of view for SA Pt (I) and its CO (II) reduced counterpart, but not for the oxidized version (III_b). This shows the limitations of PAMSI at this temperature.

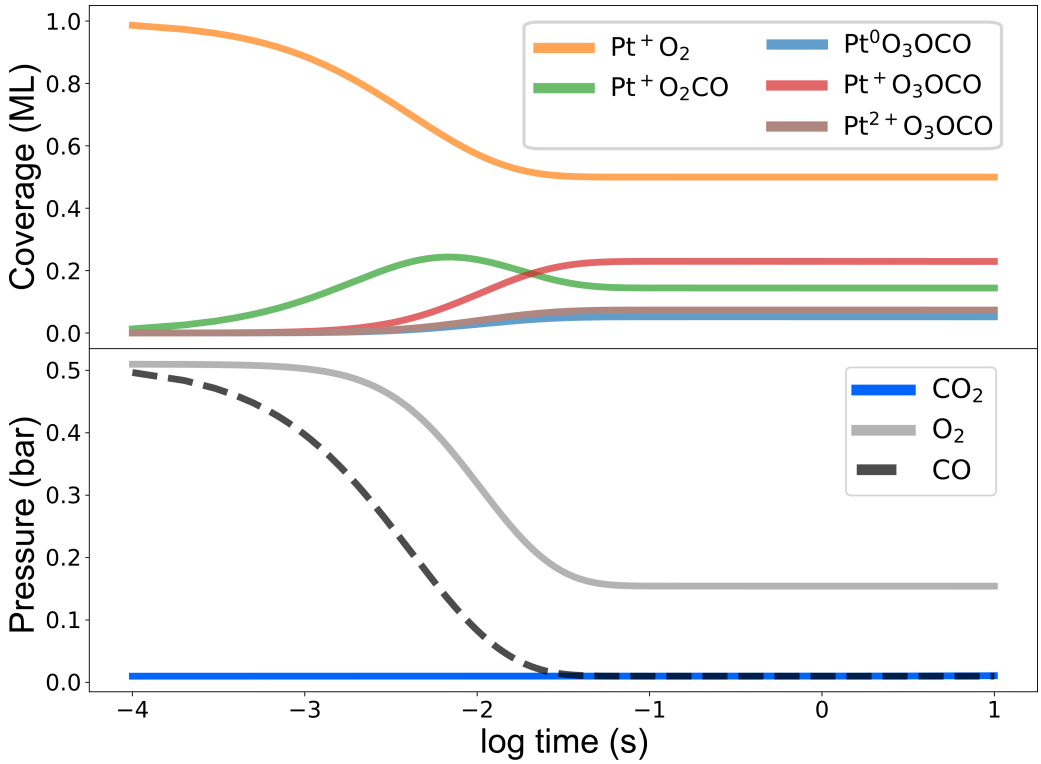

Figure 3.3: Microkinetics simulations of CO oxidation over Pt-2O at 300 K from 10^{-4} to 10 s. **Top panel:** the surface species coverage expressed in monolayers. Since this data is based on ref. 5, a ML of 1 signifies $\theta = \frac{1}{9}$. The system starts out at 1 ML of Pt-2O in its most stable form (mOS). Only species with concentrations higher than 0.01 ML are depicted. **Bottom panel:** gas phase pressures measured in bar. The initial gas mixture is (1:1) for CO-O_2.

Figure 3.4 is a continuation of figure 3.3. The time-scales of minutes to hours here are irrelevant for any practical applications in the automotive industry, as the fumes do not linger that longer in the exhaust pipe. Still they offer valuable academic insight. After 10^3 s, the off-cycle does manage to surpass the highest barrier in the entire reaction cycle (1.60 eV). The other tOSs follow suit, although it is not clear whether this is due to PAMSI or on their own accord. A more detailed, step-by-step tracing of the microkinetics could shed light on this question. As their concentration drops, the (II)-(III_b) is unbalanced towards the right and (II) also gradually converts. The reaction halts at non-stoichiometric Pt-3O, meaning that the catalyst is not recuperated and thus remains poisoned. Due to the particular partial gas pressure ratio, all CO is eventually converted into CO_2, but O_2 is also completely consumed. If this ratio is altered, so will surface catalyst coverages

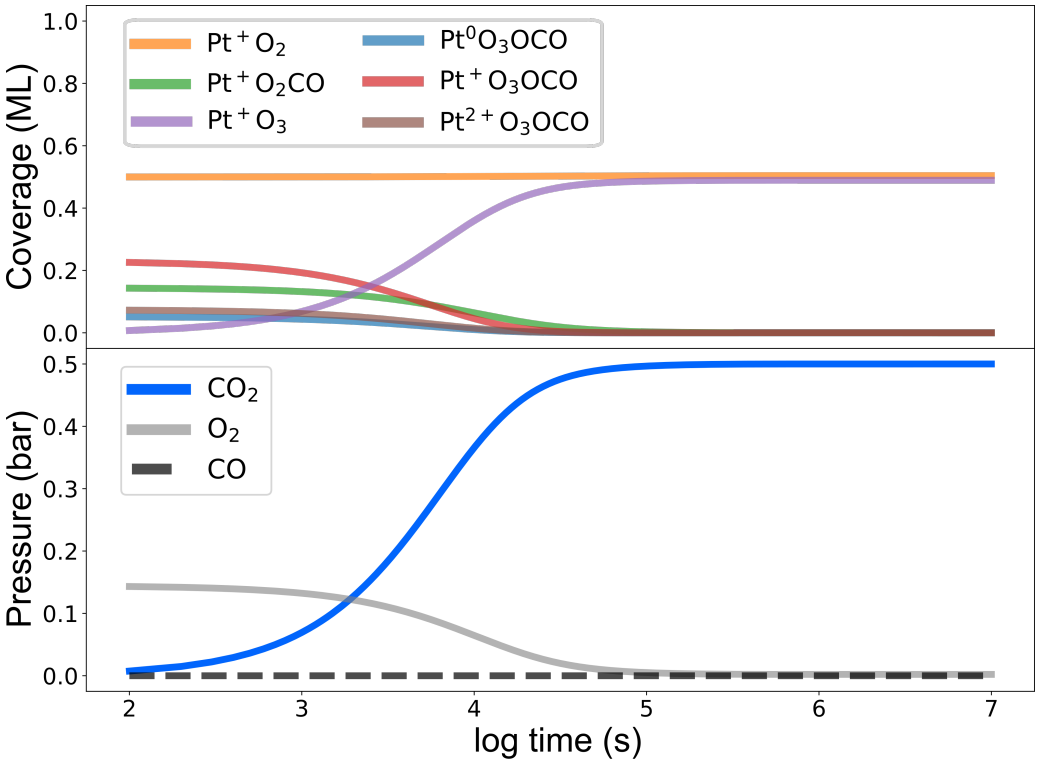

Figure 3.4: Microkinetics simulations of CO oxidation over Pt-2O at 300 K from 100 to 10^7 s. This figure is a continuation of figure 3.3. It shows CO conversion to CO_2 as well as catalyst poisoning in the form of non-stoichiometric Pt-3O (purple).

and gas mixtures.

Figure 3.5 verifies that at the DOE's target temperature (450 K), the poisoning is resolved and the catalyst rendered active. Conversions starts much more rapidly at mere milliseconds and takes up to an entire second for full conversion. This solidifies SA Pt as a candidate, although the 90% threshold will have to be verified with the PFR. It also offers one possible explanation of the experimental results in section 3.1.2. Although the reaction still follows the same off-cycle path, its bottleneck lies at (II) rather than (III_b) as before. Since this step is connected to the O_2 uptake, an increase in its partial gas pressure could also improve its reaction velocity. The tOSs 0 and II+ still do not accumulate during the reaction. Considering the starting mOS and the energetics, there is likely no time for the dynamic electron transfers (DETs) to form them. Still, even though DET does not empower multiple channels, the mechanism behind it (PAMSI) allows for the existence of Pt^+. Thus, the insights of section 3.1.5 are fundamental to the catalytic activity displayed here.

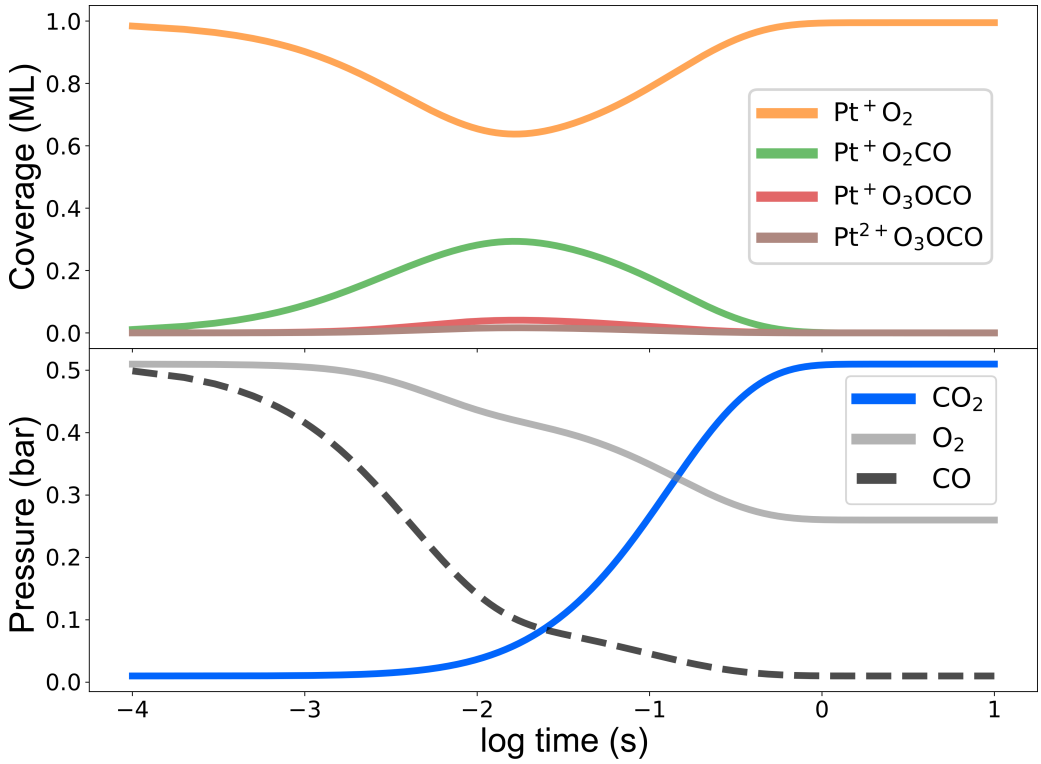

Figure 3.5: Microkinetics simulations of CO oxidation over Pt-2O at 450 K from 10^{-4} to 10 s. The setup and time length is the same as in figure 3.3. Some species are not displayed anymore since they react too fast to accumulate. The bottleneck under these operating conditions is the oxidation of CO adsorbed onto Pt-2O.

At 600 K the conversion still occurs, but figure 3.6 shows that it is slower than at 450 K by a factor of 100. The figure shows not surface coverages since there is no accumulation. The Pt-2O ratios of mOS I+ and II+ are likely due to the change in configuration entropy (see figure 3.2). Hence the on-surface reaction steps are not slowing the conversion down at all. Rather, it is more likely that diffusion events of the adsorbates to the gas phase now form the bottleneck. Alternatively, the lack of any buildup could signal an error on the side of the microkinetics. These higher temperature regimes should therefore be considered with caution.

As a finishing words, I would like to stress that these results are still a work in progress. Academically, they should provide experimentalists with a criterion to elucidate the nature of the activated catalyst. Technologically, the regular operational exhaust temperature of diesel cars lies at 550 K.[114] Therefore a mixture of SAs for the start-up and small NPs for afterwards would cover the full operation cycle in current-day engines. The fuel-efficient, low-temperature engines of

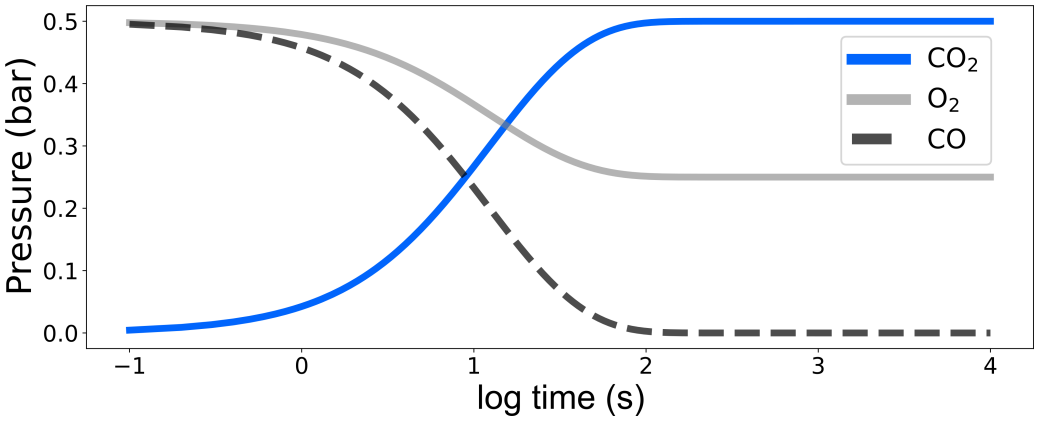

Figure 3.6: Microkinetics simulations of CO oxidation over Pt-2O at 600 K from 0.01 to 10^4 s. No surface coverages are shown because only Pt^+-2O exists (0.979 ML) and a little bit of Pt^{2+}-2O (0.018 ML). Since conversion still occurs, the other intermediates must react too fast to accumulate.

tomorrow on the other hand might not have any need for the NPs.

3.2.2 Stability of Pt-2O

A mayor point of concern for any catalyst is its resistance against degradation. It was established above that Pt-2O in particular is only against Ostwald ripening in the regime of smaller NPs. When the NPs become size of clusters however, the NP model breaks down and a more atomistic approach is needed. The first step to agglomeration would be a dimer formation between two SAs. The thermodynamics are listed in pSFig. 2. Relaxation of a Pt dimer in a (3×3) supercell always results in the separation of both Pt atoms. The repulsive force between both atoms can be overcome if the system is enclosed by lattice oxygen from both sides. The energies showcase that forced dimerization leads to a more ionic character. Still, for this model to actually occur, both atoms should be trapped in a trench and be steadily pushed towards each other. As demonstrated before however, the Pt-3O structure is unstable and therefore unlikely to impose any boundary conditions on the SA. Therefore the setup remains more theoretical than realistic. Apart from the bonding problem, there is also the question of the Pt mobility. Regardless of mOS, SA Pt needs to overcome a $\sim$ 3 eV barrier to diffuse along the trench. Trench hopping will be even more expensive and has to be induced by surface restructuring. Considering the awkward coordination at the TS, adsorbates might stabilize the SA. Obviously, O_2 incorporated into the lattice only serves to block and lock Pt in place. CO adsorption on the other hand

greatly reduces the barrier to around 0.4 eV. SA Pt now becomes mobile at around the same time PAMSI activates. The same observations were made in similar systems.[115] Lastly, the Pt-2O configuration has the perfect geometry to form PtO_2 and desorb. Moreover, under (not too) oxidative conditions the vacancies are refilled in favor of better thermodynamics. Even then, the reaction is endothermic by approximately 1 eV and even higher barrier. Thus it makes more sense for PtO_2 to deposit than for Pt-2O to volatize.

In conclusion, Pt-2O becomes mobile on the surface under CO exposure but this does not lead to dimerization. We know from literature that defect sites can still trap SA Pt.[9,92,116] Since Pt retains its SA nature even after trapping, this setup amounts to a dormant catalyst. The activation of these structures will most likely bear a resemblance to that of Pt-4O, but the specifics lie outside the scope of this work. Overall, Pt-2O is robust against most forms of degradation, and incorporation of such reactions into the microkinetic model would barely benefit its accuracy.

3.3 Scope of PAMSI

Up to now we have focused on the study of dynamic electron transfer and its impact on reactivity to a single case. There is however no reason to assume that it is confined to the combination of Pt and ceria. Thanks to the phonon-induced activation via PAMSI, we can actually list mandatory attributes for potential metal and reducible oxide combinations:

1. **Stability:** PAMSI is very much an adatom effect. Therefore, the SMSI should be strong enough for the oxide to support the adatom. Not only does the metal have to be dispersible at elevated temperatures, pristine lattice support has to be competitive with defect sites. The higher coordination numbers in the latter inhibit some of the other prerequisites.

2. **Level alignment:** the highest occupied molecular orbital (HOMO) of the SA-O lies closely to the vacant cation states. The importance of good level alignment is balanced with the size of the adjustments. High coordination numbers tend to deplete properly aligned systems and therefore kill off PAMSI, such as is the case with Pt-4O.

3. **Flexibility:** the surface should easily distort under phonon vibrations. This serves two purposes: (a) It alters the SA-O bonding distance. Since different bonding types accompany other mOS, bond formation could act as an

inciting event to ET. (b) It creates more space for the cation to accommodate the additional electron. The second mechanism only applies to cations whose volume expands after donation. In cases of partial or full shell filling this reduction-volume relation breaks.

4. **Level adjustment:** as a consequence of prerequisite 2, the vacant cation orbitals should lower enough in energy (or conversely, the SA orbitals increase) to overlap with the electron donor (acceptor). As such, ET will occur spontaneously. Even if the overlap is not complete, the barrier is still lowered and other processes, e.g. electron excitation, could activate the ET. The sole caveat is would be that these have to occur on the same short time-scales of lattice vibrations above the Debye temperature (hot polarons).

Pinpointing other systems that support SA metals with a variational mOS, would indicate whether this list of conditions is also complete. On the necessity of condition 2, it is not clear if mechanisms 2a and 2b are equally important. If IIb were to dominate for example, it would restrict potential candidates on the oxide side.

As a first approach, we investigate group 10 which contains Ni and Pd alongside Pt. Normally, elements from the same group share the same valence filling and consequentially are chemically similar. In group 10 however, the subshell occupation in gas phase slightly varies between each element. In order of increasing mass their computed valence configurations (Figure 3.2) are Ni($3d^9 4s^1$), Pd($4d^{10}$), and Pt($5d^9 6s^1$).In bulk form, each metal adopts the $d^9 s^1$ configuration.

We apply the same procedure to SA Ni and Pd, and start by comparing the energy levels in figure 3.7. Both Ni and Pd adatoms are extremely stable and resilient against sintering. This suggests that it should be possible to synthesize Ni-2O and Pd-2O. For Ni, mOS II+ comes out as most stable, followed closely by I+ at 0.14 eV difference. Some low-lying II+ states even overlap with the I+ minimum. Experience with Pt suggests that such an energy span may become dynamically active under PAMSI. The difference between mOS 0 and I+ is 0.33 eV larger however. So, although SA Ni^0 should be stable, its concentrations will be negligible. Remark that in Homogeneous Catalysis Ni^+ is at best considered a transient state, although there is no consensus about its existence.[117] Pd on the other hand retains its metallic properties: there is a 0.69 eV energy gap to the first excited state, Pd^+, and Pd^{2+} was not retrieved in any of the calculations.

To verify their validity, I performed a quick, preliminary BOMD scan using a (2×2) supercell at gamma-point. The slab was heated directly from 0 to 900 K at the same pace as with Pt-2O but without any intermittent equilibration

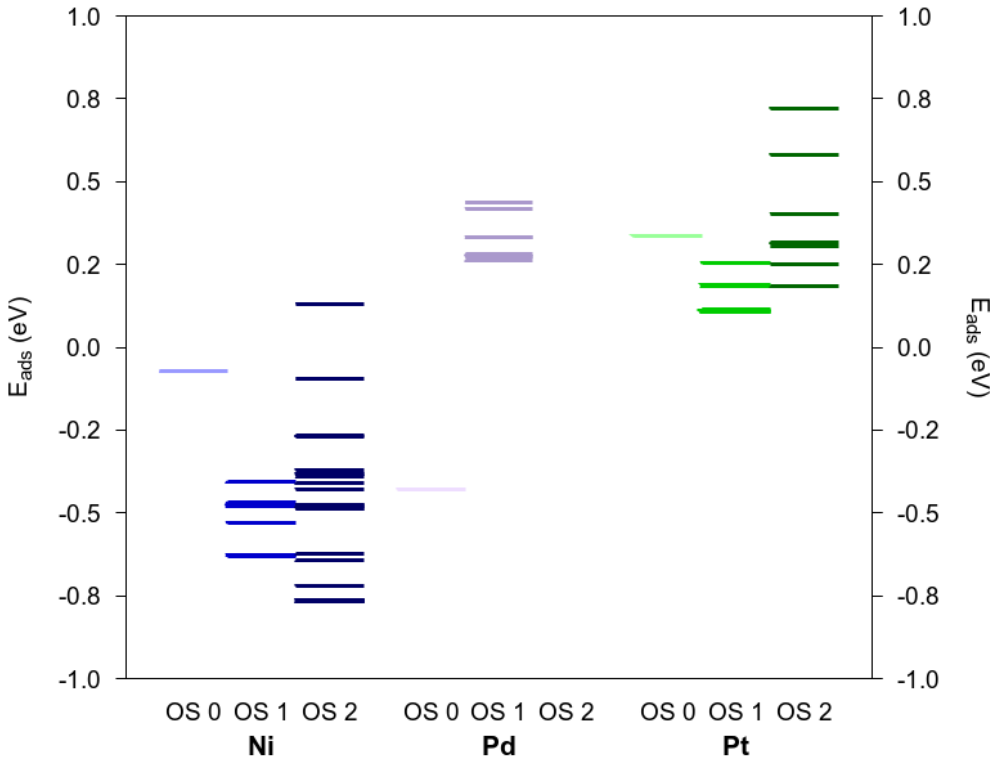

Figure 3.7: Comparison between the energy levels of SA Ni (blue), Pd (purple), and Pt (green) deposited in a 2O configuration on a cerium dioxide (3×3) supercell. The dispersion energies of each system are reported with respect to the row-terminated surface and their respective bulk energy. The zero line determines thermodynamic stability against large-particle sintering. In the case of Pd, no mOS II+ state converged.

periods. At higher temperatures, real ceria samples will start reshaping.[98] An overview of the Ni-2O mOS and the surface cerium ions is given in figure 3.8. I initialized the system at mOS I+ to allow Ni to obtain an estimate of the minimum energy barrier required for ET. At the threshold of 48.0 K (0.004 eV) Ni converts to II+. This is notably the most stable mOS, as the system resides most of it time here. Occasionally it reverts back to Ni^{+} but never Ni^{0}. Ni^{+} only appears in brief temperature windows/time intervals, so its potential role in reactions appears minor. Since the system has no time to equilibrate however, the data is not suitable to perform a statistical analysis on. At first glance it agrees with the predictions of the level diagram. The Ni-2O dynamics display an inverted behavior with respect Pt-2O, where mOS 0 and I+ are promoted. This translates to a complementary OS and different catalytic behavior, in this case better suited

for reductive species. The definitive BOMD results will incorporate a larger k-mesh and adequate equilibration. Meshes containing Ni and Pt will thus convert a wider range of substrates. Pd instead started at mOS 0 due to it being the global minimum by far. Even at 900 K, there is no fluctuation in magnetization or Ce^{3+} formation. Since the descriptors are static, no figure is added. With this we have concluded that Pd breaks with PAMSI.

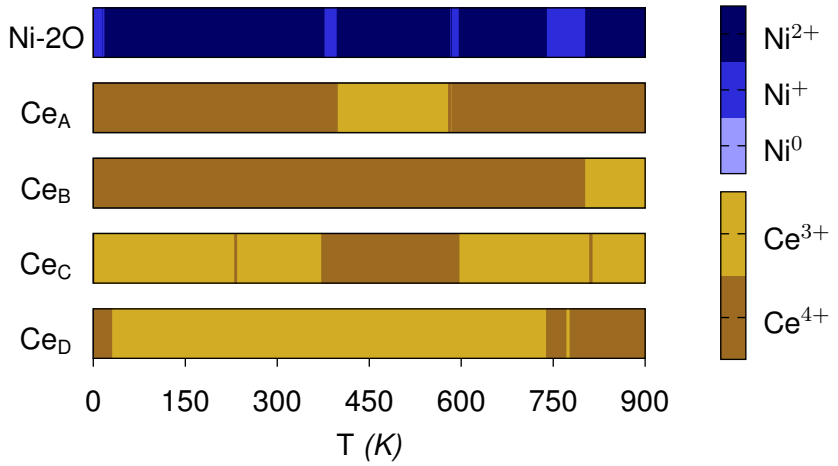

Figure 3.8: BOMD simulation of Ni-2O. The OS of Ni and the top surface layer cerium ions are traced out. No residual charge was found in the lower layers. The changing shades indicate DET. The run consists out of heating the slab from 0 K to 900 K in over 1500 fs. The slab itself is a 9 atomlayer thick, (2×2) supercell with a k-mesh at gamma point.

Oddly enough we observe a trend brake in group 10. In the case of Pd neither its size, mass effects nor electro-negativity can be the cause. To apply the theory of PAMSI, we compare again the LDOS. Since the contribution of phonons has already been elucidated, we focus on the metal's alignment. Figure 3.9 lists all three metals with the same setup in pFig. 3f, with two symmetrical water ligands. The distance of the bond lengths is adapted to match that of the SA's M^0-O bond. This ensures a realistic state localization.

The Pd d states have the same symmetry as Pt, while the Ni states overlap more (i.e. less symmetry breaking). Rather, the structure is more akin to a admixture of spherical and ML_2 symmetry. This shows that the interaction between the adatom and lattice has not reached its full potential. Along with the observation that the Ni-O bond length does not SMSI as well as PAMSI. Still, both interactions persevere.

Prerequisite 2 is fulfilled as each metal system aligns itself well with the Fermi

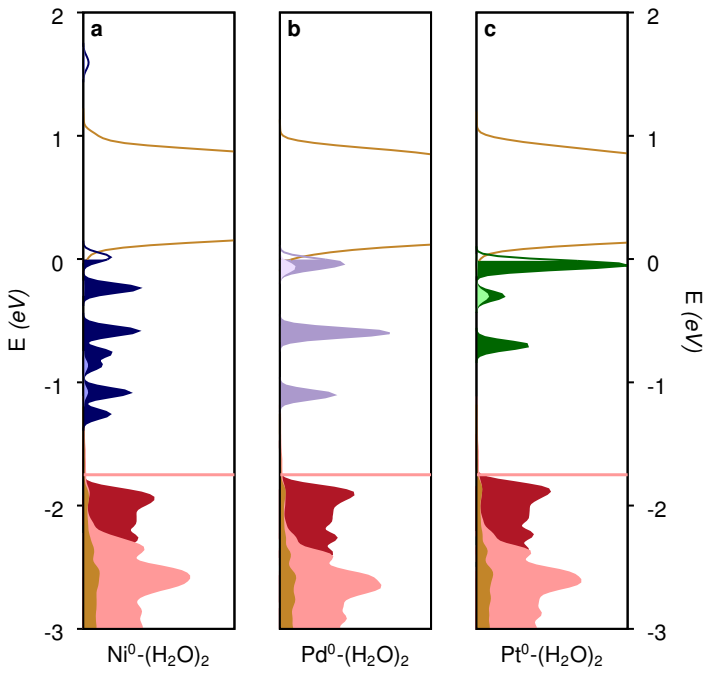

Figure 3.9: Comparison of the LDOS alignment between group 10. Each DOS corresponds to M-$(H_2O)_2$ non-interacting between slabs. The M-O was altered to the bond distance of the M^0-2O: Ni (1.76 Å), Pd (1.77 Å), and Pt (2.01 Å). The dipole moment has been switched off. Color code: Ni (blue), Pd (purple), Pt (green), surface oxygen (red), bulk oxygen (pink), Ce^4+ (brown). Bright metal colors refer to the s and dark to the d states. The pink line shows the top of the (slab's) valence band.

level. Since all other requirements are also met, Pd should also undergo DET. Thus, we are presented with a case that demands additional conditions. Apart from alignment, we also have the Born-Haber cycle. The ionization potential of Pd overlaps with that of Pt.[118] Table 3.1 however shows that $Pd^0 - (H_2O)_2$ formation is endothermic. While the bulk cohesion and SA deposition energies are exothermic with, they remain the least stable of the whole group by about 1 eV. Since Pd-O in the complex is anti-bonding, the basic energy costs of the Born-Haber cycle put the thermodynamics at a disadvantage. Both lattice distortions and electron excitation (quantified as ionization potential) require energy. This cost is not recuperated anymore by the covalent bond, and The Coulomb interaction alone cannot suffice. As such, ET becomes unfeasible.

This explanation still fails to address the stability of Pd^0-2O with respect to the bulk phase. Moreover, the Pd gas phase complex is about 2 eV less stable than its Ni and Pt counterparts, while the SA lies around 1 eV higher. Clearly some

Table 3.1: Binding energies (eV) of various structures with group 10 elements: individual atom, metal bulk, atom with two water ligands, and single-atom deposited in 2O configuration respectively. The atomic energies correspond to the total PBE energy, whereas the others are the binding energies with respect to the atom reference.

	E_{Atom}	E^{atom}_{Bulk}	$E^{atom}_{M^0-(H_2O)_2}$	$E^{atom}_{M^0-2O}$
Ni	−0.71	−4.76	−1.34	−4.83
Pd	−1.48	−3.74	0.71	−4.17
Pt	−0.50	−5.59	−1.90	−5.25

contributions from the slab selectively stabilize the mOS 0. The charge scheme in Figure 3.2 demonstrates that the SA lies somewhere between the bulk and complex. The latter however bears a significantly higher total charge than the SA, contrary to the other elements. Considering how the oxygen atoms are already reduced, this charge includes their lone pairs. This corroborates that the ligand is exerting Pauli pressure. Ionized lattice oxygen on the other hand are less prone to invade the Pd's space. In other words, the complex is an outlier. No such obvious difference exists between the bulk and SA however. At the least, not at the level of the l quantum number. The LDOS confirms that the d states of SA Pd fall into three peaks, enforcing symmetry between d_{xz} and d_{z^2} as well as s and d_{yz}. This corresponds better with the spherical symmetry of the atom than the bulk which breaks all symmetry. Also numerically, the difference in atomic energies matches that of the SA deposition energies closely. We conclude that the energy penalty due to breaking the electronic configuration of atomic Pd negatively impacts and in fact inhibits any ET dynamics. In terms of conditions, we require that (4) the interaction between the adatom and the ligands (in a reduced state) is bonding.

To the author's knowledge, thin film depositions of Ni on ceria have been investigated but no single-atom dispersion.[119] The lowest coverage (half a monolayer) starts out metallic at room temperature. Upon heating, the support will oxidize it to Ni^{2+} NPs. The population of particles with diameters less than 0.4 nm is suitable for SA formation.[106] Ni nanoclusters have been flagged for EMSI,[81] just like Pt. As long as downscaling does not affect their similarities, SA Ni can be expected to undergo PAMSI. Pd has also been found to disperse into single-atoms.[120] Their dispersion was verified both on ceria nano-octahedra and cubes. All three mOS were identified via Fourier-Transformed Infrared Resonance (FTIR) spectroscopy of the Pd-CO bond vibration. The Pd^{2+} dominates in concentration and most likely corresponds to a 4O configuration.[121] For the other two states it is unclear. Pd^0 does not necessarily correspond to the 2O configuration discussed here, but could also be an artifact of incomplete dispersion. Rather,

Table 3.2: Charges of various structures with group 10 elements: individual atom, metal bulk, atom with two water ligands, and single-atom deposited in 2O configuration respectively. The charge was computed by VASP via integration over the charge densities within the Wigner-Seitz radius. Complete partition of the physical space by these radii would yield 10 e^-. In the case of an individual atom, there is charge leakage due to the cell's volume (3375 Å). All values in gray are in absolute terms (e^-). The white cells show the s, p, and d orbital contributions (in %) from projection. The mixing in from p orbitals is considered noise and should physically be indexed as s contribution.

	Orbital	Atom	Bulk	M^0 $(H_2O)_2$	M^0-2O
Ni	tot	8,81	9,31	9,46	9,35
	s	0,04	0,05	0,05	0,06
	p	0,00	0,05	0,04	0,05
	d	0,96	0,90	0,91	0,89
Pd	tot	8,65	9,36	10,11	9,33
	s	0,00	0,05	0,07	0,06
	p	0,00	0,05	0,05	0,05
	d	1,00	0,90	0,88	0,89
Pt	tot	8,36	9,21	8,72	8,76
	s	0,05	0,07	0,06	0,07
	p	0,00	0,06	0,02	0,03
	d	0,95	0,87	0,92	0,90

we only investigated this system to compare with Pt-2O and retain the maximum number of parameters. The FTIR frequencies are of on-top CO adsorption only, which is suggestive of our model. X-ray diffraction measurements would be able to seal that discussion. The Pd^+ is theorized to be yet another PdO species. The relative intensities are constant among support types. SA Pd also converts CO with a performance similar to that of SA Pt after activation. Pd does not require such a step. Overall, the active catalyst in the experiments most likely is not captured by our model here. If it is Pd-4O however, it could be converted into Pd-2O.

Chapter 4

Method development

The secret of life, though, is to fall seven times and to get up eight times.

Paulo Coelho, The Alchemist

4.1 Wavefunction methods

All results up to now have been mostly based on DFT+U. The obvious caveat that the Hubbard term introduces an external parameter which is sensitive to ET.[16] Hence, there is no straightforward manner to improve on the accuracy of our calculations and distinguish artifacts from physical phenomena. In this respect the quantum-chemist's approach to post-HF procedures is much more intelligible. Up until recently, such methods were prohibitively consuming for slab models. `VASP6` addresses the need for post-HF by providing two new implementations of MP2: a low-scaling, $\left(O\left(N^4\right)\right)$ LTMP2 and a stochastic version $\left(O\left(N^3\right)\right)$. In a collaboration with Dr. Tobias Schäfer from Prof. Georg Kresse's group, we are testing the feasibility of applying these methods in high-correlation oxides. More specifically, we are studying the phase transition of Ce_2O_3 to CeO_2 by means of oxygen expulsion. Considering the preliminary steps, we restrict the scope to bulk systems but with the intention to later incorporate slab models too. In a real-world setting an ab initio code should reproduce the crystal geometry, the cohesion energy, and electronic structure well. Since MP2 is a correction to the HF energy, the code does not yield the electronic structure nor any forces. The same applies to RPA and GW for that matter. Comparing cohesion energies only makes sense

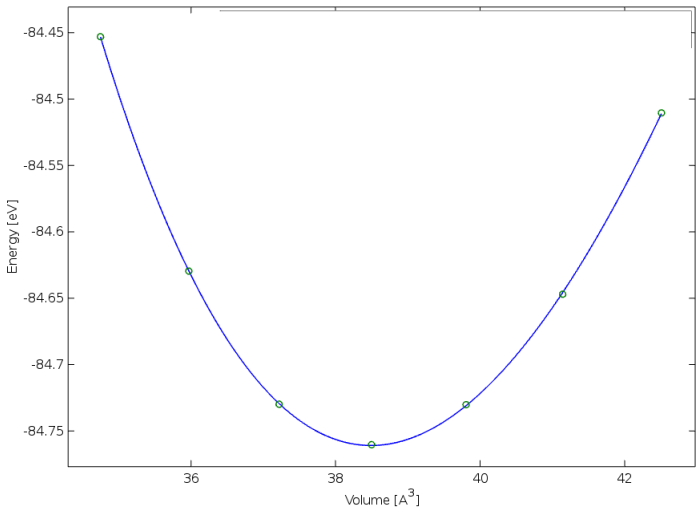

Figure 4.1: Determination of the lowest-energy (eV) volume ($Å^3$). The geometry is only changed by equally stretching the lattice parameters. The Birch-Murnaghan formula is fitted against the data. The example here is that of CeO_2 computed with LTMP2 (cutoff energy 500 eV) starting from HF. Courtesy of Dr. Tobias Schäfer.

for the relaxed bulk structures. In order to circumvent this blockade, we started from a primitive unit cell relaxed under PBE+U. By toggling the lattice parameter we then scan the volume range. The optimal lattice parameter is determined via fitting the scan to the fourth order Birch-Murnaghan equation.[122]

As such, we obtain not only the primitive cell volume at equilibrium but also the oxides bulk modulus B_0, i.e. its response to volume perturbations, at that equilibrium structure. The bulk modulus equates to strain induced force gradient, corrected for the net force:[123]

$$B = \left[\frac{4}{9a}\frac{\partial^2}{\partial a^2} - \frac{8}{9a^2}\frac{\partial}{\partial a}\right] E\,(a) \tag{4.1}$$

In eq. 4.1, a stands for the cubic lattice parameter. In terms of figure 4.1, it could be understood as the local curvature. Both descriptors were then converged to their k-mesh at a cutoff energy of 500 eV. Convergence with respect to the cutoff energy was then verified by comparing with the 600 eV value. In the case of RPA, the cutoff energy had to be increased to 700 eV. Two routes were tried: a functional approach and a post-HF. The former starts from the hybrid functional Heyd–Scuseria–Ernzerhof functional with the cutoff radius at 0.3 Å (HSE03), a popular alternative to DFT+U in CeO_2,[14] and the RPA corrected HSE03. RPA also accounts for the HF exchange energy. Thus a separate, non-selfconsistent

HF calculation is run based on the HSE03 charge density (HF/HSE03). Post-HF obviously starts from self-consistent HF. This allows for a nice comparison between the effects of different wavefunctions within the HF scheme. Lastly, MP2 adds correlation energy to HF. Remember that MP2 accounts for more quasi-particle diagrams than RPA.

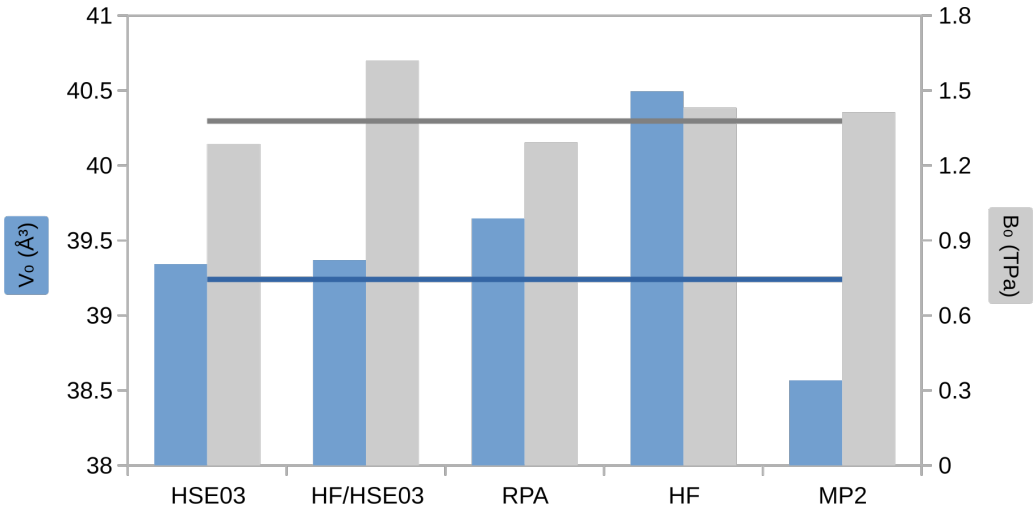

Figure 4.2: Method benchmarking on CeO_2: a comparison between a functional approach from HSE03 to RPA and a post-HF approach, LTMP2. The equilibrium volume V_0 (blue) and bulk modulus at equilibrium B_0 (grey) are used as descriptors. These values were computed using the fit shown in figure 4.1 and then converged with respect to the cutoff energy and k-mesh. The horizontal lines indicate the experimental reference data extrapolated from ref. 124.

Starting with CeO_2, figure 4.2 lists all six approaches. The experimental reference data are taken at room temperature (300 K).[124] Since static ab initio calculations assume at the absolute zero, the actual reference value was extrapolated to 0 K using a quadratic fit. HSE03 seems to lie at a sweet spot for both descriptors. The importance of the charge distribution in the geometrical equilibrium becomes clear when comparing HF/HSE03 with regular HF. The former retains the same V_0, whereas the latter clearly overestimates the volume. The HF/HSE03 bulk modulus already hints at HF being off equilibrium by overshooting the experimental B_0. In HF the overshooting is tempered by the strong volume expansion. RPA behaves the exact opposite of HF/HSE03 with respect to HSE03 and instead expands the volume while maintaining the bulk modulus. This duality probably best exemplifies the contrast between exchange and correlation. HF overshoots B_0 by as much as HSE03 and HF/HSE03 undershoot it. MP2 manages to correct on

this, yielding the most accurate bulk modulus. This suggests that MP2 describes the expansion curve best. Contrary to before, here correlation drives the volume down. The MP2 volume is off by 2%, the highest error margin of all methods.

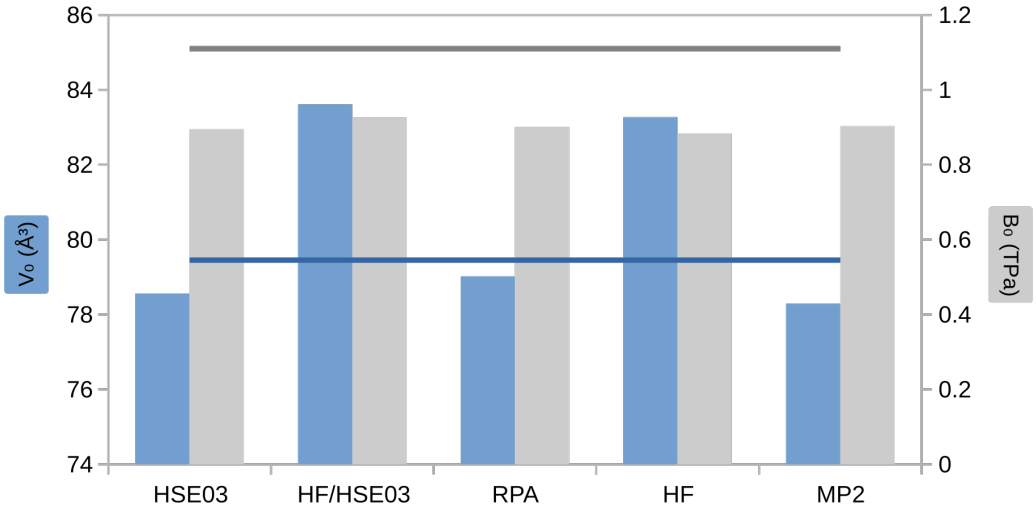

Figure 4.3: Method benchmarking on Ce_2O_3 with the AF spin alignment: a comparison between a functional approach from HSE03 to RPA and LTMP2. The methodology is similar to the one presented in figure 4.2. The experimental reference data taken from the quasihydrostatic measurements in ref. 125. There was not enough data to extrapolate from room temperature towards 0 K. This is indicated with a dashed reference line.

The reduced oxide, Ce_2O_3, carries unpaired spins around its cerium nuclei. It therefore assumes an anitferromagnetic (AF) and ferromagnetic (FM) state. Calculations predict the former to be the ground state.[14] In reality Ce_2O_3 is paramagnetic, but has been found to have weak AF at ambient pressures.[125] Figure 4.3 lists all calculations. These now demonstrate more agreement, especially in terms of the bulk modulus which only varies marginally. Mixing in too much exact exchange results in expansion, regardless of the wavefunction this time. Correlation helps even out the exchange effects. Considering its remarkable performance, HSE03 seems to strike a perfect balance between both although neither are exact. If anything, this suggests that higher-level methods are rather wasteful without adding much to the geometry description.

The FMc case is quite delicate to compute and thus only partially done. By lack of any alternative, the same experimental references from above are used in figure 4.4. Obviously the volume line will slightly move upwards.

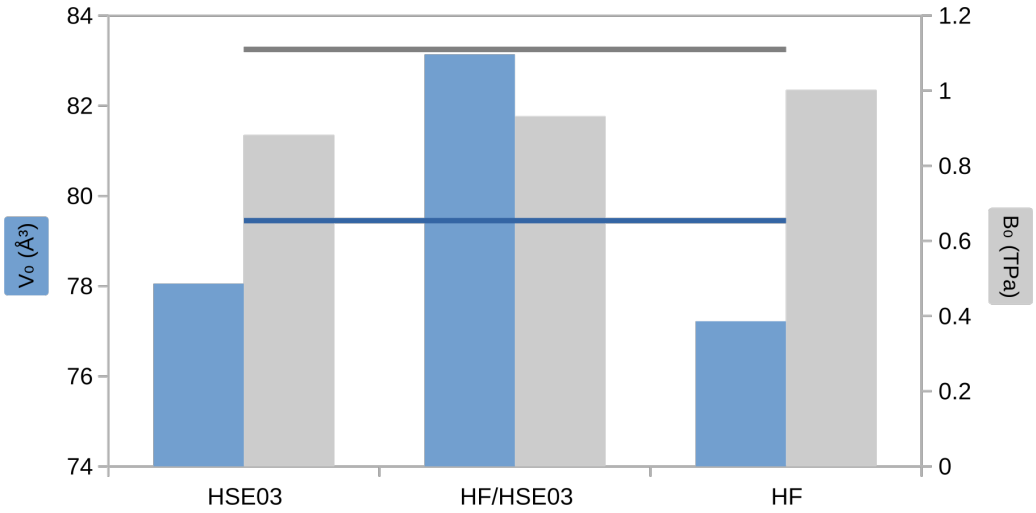

Figure 4.4: Method benchmarking on Ce_2O_3 with the FM spin alignment: a comparison between several functional approaches from HSE03 to RPA and HF. MP2 data is not yet available for this system. Since most experimental data does not distinguish between both magnetic states, the same experimental reference is used as in figure 4.3. The dashed line shows the same reference value as before.

4.2 Development of a ceria Neural Network Potential

Up to now the PAMSI phenomenon has been established and microkinetics has confirmed its impact on reactivity. Although the techniques employed are state-of-the-art, their limitations impede a full characterization of PAMSI:

1. The (3×3) supercell sizes are by far the biggest systems we can reasonably perform at the moment. This restriction largely stems from the need for full configurational sampling. Experimentally, the maximal SA Pt loading lies at 3 wt%,[100] while the computational setup is sampling at 11 wt%. The inter-vacancy interaction then increases as an artifact and could destabilize SA Pt.

2. The AIMD simulations for direct verification are limited in length: 112, 522 of total CPU hours (or about two-and a half months) were needed to produce 27 ps. While these timescales give a flavor of the mOS lifetimes and distribution (see pFig. 2d), they are not thermodynamically relevant. Consequentially, they cannot be used as identifiers in any experimental mean field measurements.

3. The microkinetics assume a spatial average of the reactor and disregard other surface processes which could affect the SA coordination. KMC works around this issue, given that is each process barrier is correctly computed.

In summary, most of the limitations can be traced back to the model's size and the simulations' timescales. Other research fields, such as Biochemistry, remedy these issues via forcefields or molecular mechanics (MM). The versatile nature of the chemical bond in Solid State introduces severe accuracy errors:

1. MM do not allow for bond breaking, which is arguably the essence of any chemical reaction.

2. The bonding nature in ceria lies somewhere in between (heterogeneous) covalent and ionic.[108]

3. Both Pt/Ni-O bond studied here balance between single (unsaturated) and double (saturated).

As is, the use of MM for these systems would be inappropriate. Section 2.3 introduces a novel formalism based on machine learning: HDNNPs no longer operate in terms of bonds but instead of (local) geometries. Since these potentials are data-driven, they can obtain accuracies of the same level as their training set. In other words, there is a technique that promises ab initio (PBE+U) levels of accuracy with linear time scaling and a slightly larger prefactor than MM.

The objective of this section is to present a scheme for preparing and expanding the input data set for `RuNNer`. `RuNNer` is the in-house software of the Behler group from the University of Göttingen,[73] where I performed my academic stay. The program has three modes: (1) projection of the atomic environment onto a SymVecs; (2) training of the NN; and (3) computing the energy and forces of novel structures via forward-propagation. Mode 2 fits the parameters of a NN to the energies and force components.

4.2.1 Data preparation

This section will be concerned with the HDNNP construction for CeO_2 bulk as proof of concept. The original data batch was generated using a BOMD simulation of a primitive cell at gamma-point for $10,000$ steps at 800 K. The temperature oscillations from the Nosé-Hoover thermostat were very wide (ranging up to 3889 K in one case) introduce a degree of randomness in the configurations under the volume restraints. The BOMD remains stay in the same energy basin,

revisiting previous geometries. In principle, the full trajectory can be converted and processed by the NN, but the mode 2 learning step poses the bottleneck. Due to the correlation between images and its temporal neighbors, BOMD data can filtered out with minimal loss of information.

One filtering option is to extract structures at a fixed interval. If the interval however coincides with the oscillations' period an integer plural, it will consistently select structures from the same energy regime. This scenario would exacerbate the correlation, rather than eliminating it. Instead, I designed a filter myself with the help of Sergio Pablo García Carrillo for the programming. Its purpose is not limited to removing correlation, but doing so in a homogeneous fashion: each input structure bears an equal weight in the NN, so oversampled regions in the training set may introduce a bias. This *binning* algorithm considers the chemical space via geometry, energy and forces. Since the geometry and forces are individual for the atoms, they are measured using the root mean square (RMS) deviation with respect to an arbitrary reference structure. Obviously, this restricts the filter to systems of equal size, number of elements, and atoms. As such it is well-suited for MD trajectories. With the 3D space established, it is then divided into voxels (0.02 eV/Å $\times$ 0.02 AA $\times$ 0.01 eV) to impose a local density estimate. From each voxel a fixed number of points (in this case 5) are selected at random. The reason for selecting multiple points is to retain more data. While the selected points are very similar (coming from the same voxel), the slight deviations allow for fine-tuning of the I/O relationship. In other words, they function as an error bar. If the voxel contains less, its density is considered too low and it is entirely discarded.

After binning, 2815 structures were retained, which were calculated with a higher accuracy in a k$(7 \times 7 \times 7)$ grid. This data set was split into 1955 training and 860 test points. The NN training was repeated until convergence over 20 cycles with a $5:1$ force to energy weight ratio. The same procedure was followed for each other HDNNP. The radial SymFuncs are controlled via two parameters (η and r_s), see 2.3. Originally, the η parameter alone was interpolated between the minimum inter-atomic distances and the cutoff radius. The end result is labeled HDNNP**a**. Panel a in figure 4.5 shows that the network reproduces the both energies and forces with minimal error margin. The range of data is still limited however. Therefore, the first dataset was expanded by compressing and stretching the lattice parameters in steps of 1 up to 5% and producing $35,849$ structures in total. The subsequent range expansion in HDNNP**b** is evident in panel b of figure 4.5. Mode 3 of `RuNNer` is limited to single-point calculations. An interface[126] between `RuNNer` and `LAMMPS` called `N2P2` was used to perform MDs. The MDs span a $(3 \times 3 \times 3)$ supercell and run in steps of 0.0001 fs. In both HDNNP

simulations an oxygen diffusion at the early onset causes severe structural damage and the model breaks down.

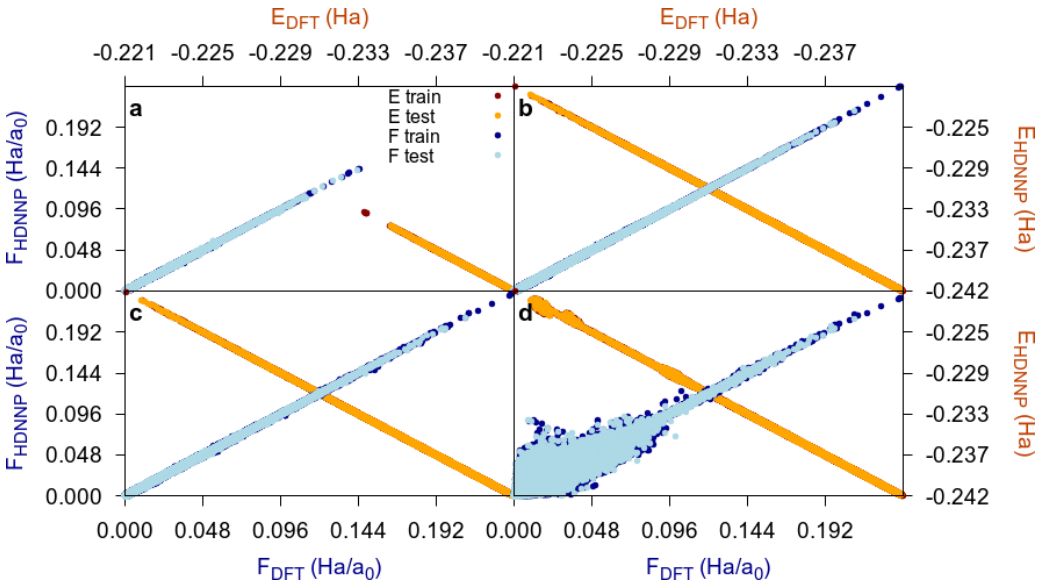

Figure 4.5: HDNNP performance in system energy (Hartree) and atomic force (Hartree/Bohr) predictions. Four different setups are considered: **a:** a 5.491 Å, fixed lattice bulk (dataset 1) with η sampling; **b:** the expanded bulk system (dataset 2) with η sampling; **c:** the expanded bulk system (dataset 2) with r_s sampling; and **d:** the expanded bulk system and additional (2×2) slabs (dataset 3) with r_s sampling. A linear relationship indicates that the HDNNP retrieves the DFT data. In the case of the energies, the (upper) x-axis has been inverted for better visibility. A distinction is made between the training and testing data. Since the NNs were optimized for the former, it should outperform the latter. The performance of the training data instead is a measure of the interpolation quality of the fit.

Sampling the r_s parameter instead of η generates HDNNP**c**. Figure 4.6 shows how this approach is much more adapt covering the inter-atomic distances. The η range on the other hand yields SymFuncs which are barely indistinguishable. It is a testament to the power of NNs to still produce good quality fits from such restricted input. The distance distributions confirm that dataset 1 was far too sparse. Dataset 2 increases the sample size, but not range. Only in the long-distance ranges ($\sim$ 8.5 a_0) of Ce-Ce and Ce-O does expand the range. Therefore, a third dataset was created by adding two sets (100) slabs of p (2×2) dimensions. The first has the regular row-termination (2O), while the other has peroxide like structures that have significantly shorter O-O distances compared to 2O. As such, the repulsive part of the O-O bond would be accounted for in HDNNP**d** and

prevent the inciting breakdown event. In the 5 to 7 a_0 region, there is little sampling and even none in the case of O-O. It therefore seems that several of these SymFuncs could be removed, leaving only those around the short-distance peaks (in purple). These SymFuncs (e.g. the dark-blue peaks) do serve a purpose, in breaking the symmetry between the left and right sides the purple peak.

Up to this point, I have not mentioned yet the angular SymFuncs. These function similar to their radial counterparts but with a ζ parameter that controls the range of angles included. In small cutoff radii they add little information and as such their impact has not yet been systematically investigated. For now, their radial setup has mimicked that of the regular radial SymFuncs.

4.2.2 Performance

The impact of HDNNP**c** and HDNNP**d** is not that clear in figure 4.5. In case of the latter, there is even an increase in the error margin. Since this error is restricted to small forces, this should not have a significant effect in MD simulations. Figure 4.7 shows the overall performance of both HDNNPs. In each case, the same $(3 \times 3 \times 3)$ supercell was pre-heated for 0.2 fs, after which the actual simulation ran for 1.0 fs as an NVT ensemble. Such a run typically requires only 12 min on a single processor, compared to 397 min of total CPU time for a single-point (SP) of the same system in `VASP 5.4`. The change in SymFuncs clearly improves the results as well, since the models retain their integrity well after pre-heating. The stability is temperature-dependent and the breakdown occurs sooner at higher temperatures. At temperatures as cold as 150 K, the system remains stable throughout. This may seem unsurprising, but neither HDNNP**a** nor HDNNP**b** reached this level. Only in the case of 600 K seemingly falls outside of the temperature trend, since it survives $\sim$ 0.1 fs longer than 450 K. Each simulation was run only once, so this could be just an outlier. More sampling would be needed to determine that, although this is not the aim of this project.

HDNNP**d** on the other hand never showed any signs of breaking down, unless pushed to the maximum sampling temperature of 900 K. The same oxygen diffusion mechanism again starts the chain reaction. Figure 4.7 shows a before and after snapshots. The criterion for breakdown is a deviation from the total energy (after pre-heating) of more than the acceptable accuracy (1 kcal/mol or 0.043 eV). Remark that in a system of 324 atoms with a total energy of -2574.7882 eV, this is a very strict accuracy. The inciting event occurs earlier however earlier on at around 0.7 fs, when both potential and kinetic energies start to diverge. In all other HDNNP**d** trials the energies keep following an inverted path, which validates their stability.

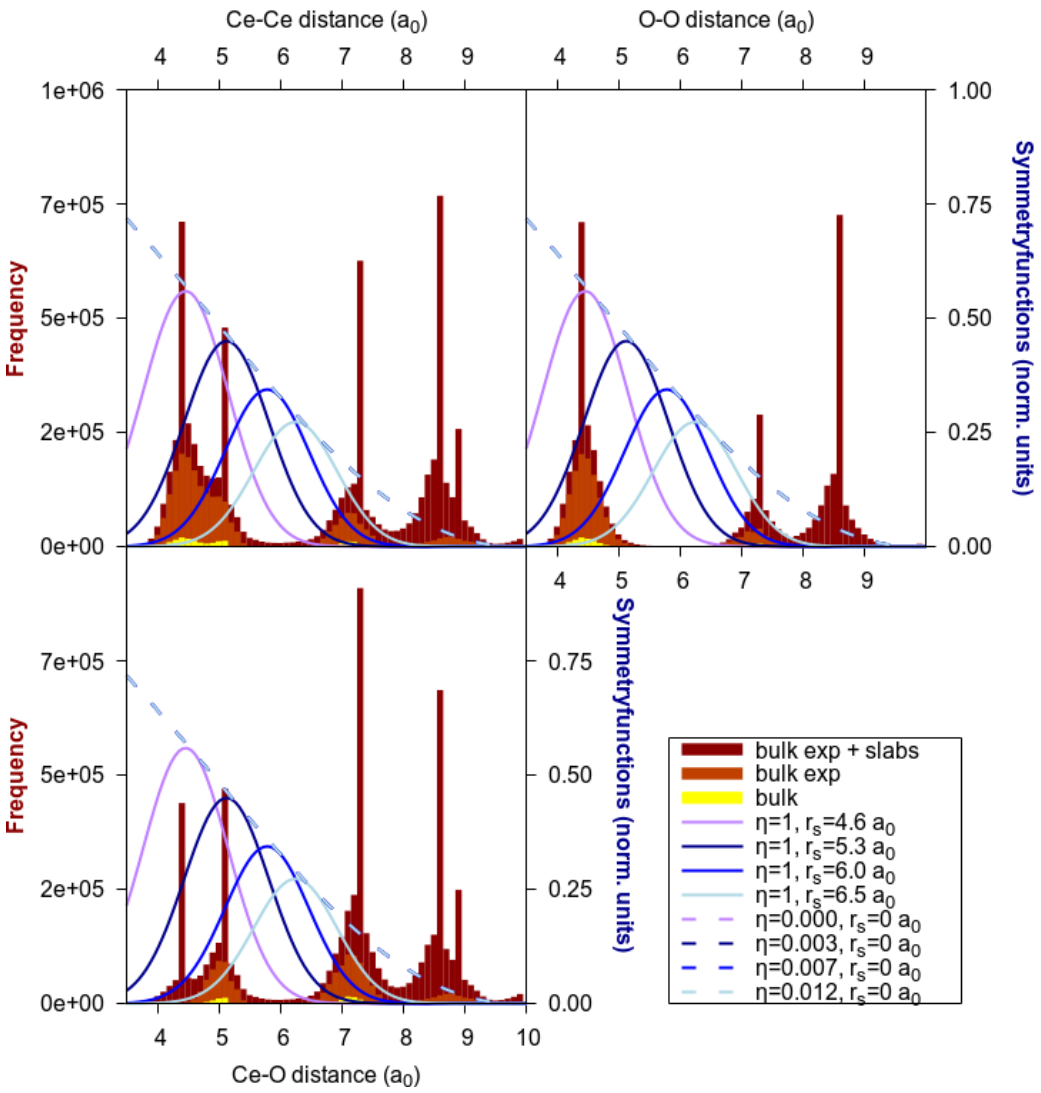

Figure 4.6: Inter-elemental distance distribution for Ce-Ce, O-O, and Ce-O respectively. The three different data sets used in the four setups are marked in various shades of red. Sampling of the η parameter is dashed lines, r_s sampling in solid lines. For further reference, see the legend at the right-hand bottom side. The script to sort the distances was written by Sergio Pablo García Carrillo.

4.2.3 Outlook

The HDNNP**d** is the first working prototype for CeO_2 bulk (up to 750 K). Some applications require higher temperatures than the those currently achieved. Firstly, the (100) surface reconstruction happens around 800 K. While the temperature

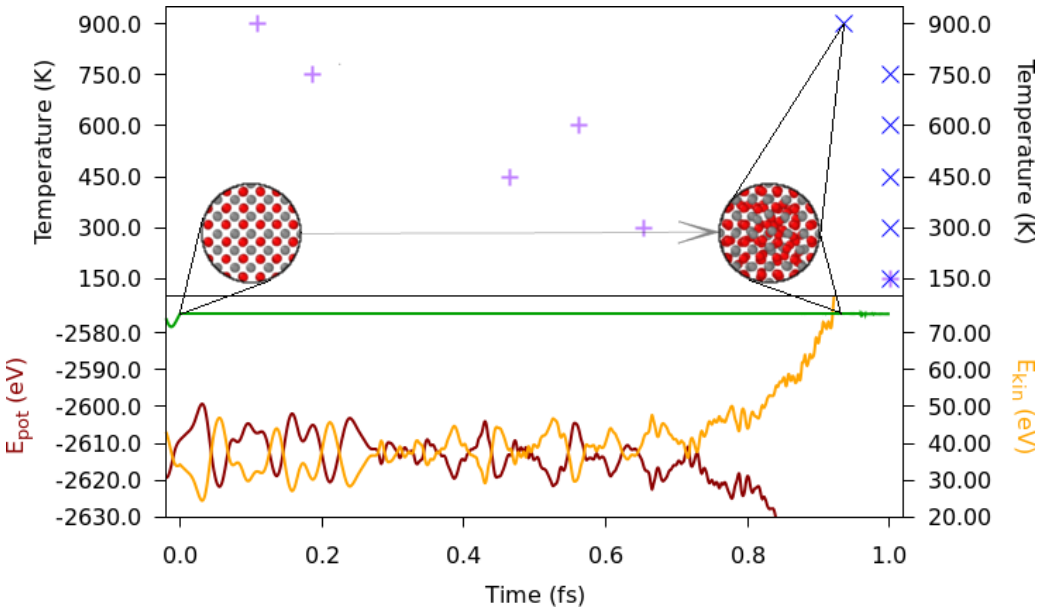

Figure 4.7: Top panel: LAMMPS stability test of the HDNNPs on CeO_2 bulk models. The models were equilibrated for 0.20 fs, after which the actual test starts 0.0 fs and runs for 1.00 fs. The time until energy leakage is plotted against the average Nosé-Hoover temperature (K). Only the setups c (purple crosses) and d (blue x's) from figure 4.5 are considered, since the setups a and b fail even before equilibration. The insets show a portion of setup d at 900 K at the beginning (left) of the test and when it breaks (after 0.93 fs). **Bottom panel:** example of a test simulation, in this case setup d at 900 K. The red line shows the bulk potential energy, while the the orange line shows the kinetic energy. Remark how both are anti-symmetric so their sum (the total energy in green) remains constant. The breakdown criterion is when the total energy deviates more than the chemical accuracy (0.043 eV).

oscillations at 750 K will likely reach the activation barrier, all models up to now have broken down due to faulty oxygen diffusion. Meanwhile, NP synthesis and aging employ temperatures of around ~ 1100 K. Figure 4.6 shows that there is still room for improvement by shifting or adding SymFuncs to the long-range distance. Meanwhile, the performance costs can be maintained by broadening a single SymFunc (using the η parameter) to cover the whole low-density region. It is not clear yet in how far a rendition of long-distance interaction will improve the model's stability, These interactions tend to be weak, although they could be the cause of the error margin in the low force scale (see figure 4.6d). In short, with an overview of the radial distribution, the SymFuncs can easily be optimized for max performance.

From here on out, the potential can be further tailored to address several phenomena. To name a few:

- **Bulk phase transitions:** In the previous section 4.1 the reduction from CeO_2 to Ce_2O_3 was discussed. Many intermediate states exist between limits and their phase diagrams have already been drawn.[11] Powerful MM simulations however can investigate the kinetics behind the phase transitions, their onset and spread through the material. Even now, anomalous phase transitions are being discovered in ceria.[127]

- **Neutral surfaces and NPs:** The oxide's surface is key to its chemical properties. Although training a model to perform a reaction is a challenge of its own,[128] the ceria morphology is already complex enough to be a full topic of its own.[98,99,129] Because defect sites play major role in SA trapping,[92] it would already be worthwhile to simulate step sites as well. The role of bulk remains crucial, as it allows for regulation of the slab thickness. Moreover, if high-index slabs are included, one can build even NPs.

- **Surface oxygen vacancies:** Redox processes are fundamental for the ceria reactivity. The approach of Behler and Parinello works outstandingly in the short range. Since electron localization is correlated to the local expansion in the Ce radius, the NNP should be able to track mOS. This is only theoretical, as it has not yet been performed by any group to the author's knowledge. In a test scenario vacancies would be perfect, since they conserve the number of Ce^{3+} centers (stability test) and have already been well-studied at smaller scales.[104,130]

With the exception of bulk Ce_2O_3, all other applications require slab structures. Our group has an impressive database (207, 092 structures) of neutral slabs from previous activities. Since these structures were generated in BOMD, they suffer from the same correlation. After binning, only 30, 730 structures remain. Figure 4.8 gives an overview of the chemical space covered. Each set was filtered separately, so homogeneity does not apply between the sets. This can be easily mitigated by producing more data in the sparser sets. From a data foundation, structures no longer have to be generated using inefficient BOMDs. Instead, an already existing structure could be slightly perturbed* using random fluctuations (analogous to the approach in 2.2.2). This would be perfect for points at the edges or outliers. Once a reasonably stable HDNNP has been trained, it can be pushed

*Within a physically meaningful contest.

to its breaking point. The inciting event can then be isolated and computed as a SP. In this manner holes in the energetic boundary can be systematically patched.

When it comes to vacancies, one can randomly remove oxygen atoms from the pre-existing structures. Caution has to be taken here to relax the slabs, so that the electrons localize into Ce^{3+} centers. Hence this step in the data generation is much more costly than the single-point calculations described before. Another potential pitfall with the Ce^{3+} centers, is the long-range interaction. While this was mentioned above already, it is important to realize that the cutoff radius divides both areas. Shortcomings in the long-range could therefore resolved by expanding the SR scope. Work on the (111) surface shows that Ce^{3+} centers tend to stay around their vacancies, but with PAMSI this is not a given. If the geometry of the electrons' sources determine their localization, then the cutoff radius might have to be expanded. This could pose an issue for the bulk primitive cells, as any radius extending beyond the PBC will generate artifacts with its own image. In this scenario, the bulk cells should be enlarged, scrambled and recomputed.

In conclusion, given the current NN setup and amount of data, large-scale neutral slab and NP should be feasible in a short time. The introduction of charged sites is unprecedented, but would greatly enhance the applicability of the ceria HDNNP. Above, I have presented a brief cost-benefit of its implementation.

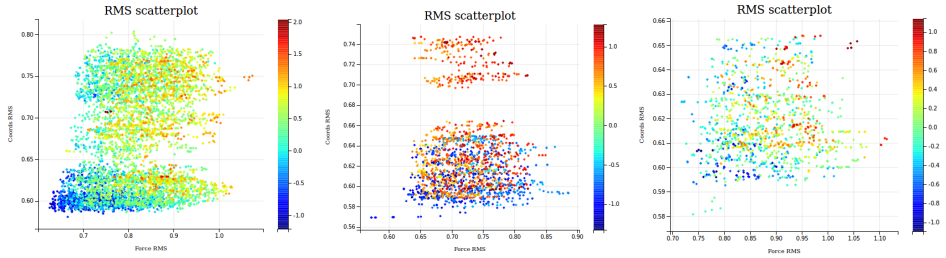

(a) (100) p (2×2)
$45,267 \rightarrow 6705$ pts

(b) (100) p (2×2) O-O
$18,000 \rightarrow 1990$ pts

(c) (100) p (2×2) 4O
$4000 \rightarrow 1325$ pts

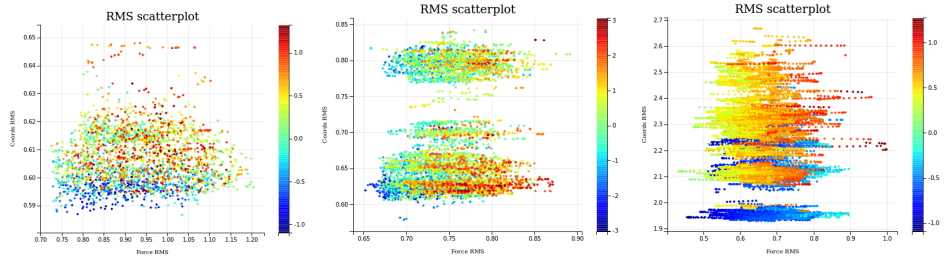

(d) (100) p (2×2) CeO_4
$29,976 \rightarrow 2820$ pts

(e) (100) p (4×4)
$49,370 \rightarrow 7345$ pts

(f) (110) p (2×2)
$20,000 \rightarrow 3490$ pts

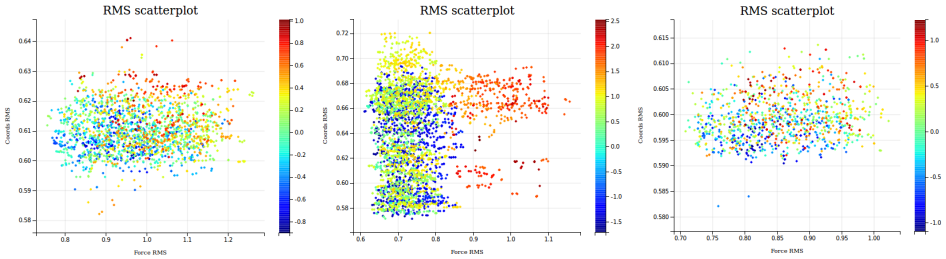

(g) (111) p (2×2)
$10,000 \rightarrow 2125$ pts

(h) (111) p (2×2) O-O
$24,479 \rightarrow 3850$ pts

(i) (111) p (3×3)
$6000 \rightarrow 1080$ pts

Figure 4.8: Overview of the in-house slab data after the binning filter. The x-axis shows the RMS force distribution, the y-axis the RMS geometries, and the color gradients the energy. Each panel has a different reference structure as well as range, so they cannot be readily compared amongst each other. They do reveal data pool separation (figures 4.8b and 4.8e), or even skewness (figure 4.8h). The subcaptions denote the type of data as well as the number of data points before and after filtering. Some naming conventions are less evident: O-O stands for slabs where two lattice oxygen atoms are bonding, forming a peroxo-like structure. 4O stands for oxygen rings. These can act as traps for SAs as shown in ref. 5. Lastly, CeO_4 are slabs with a Ce-termination rather than O. These geometries have pyramid shapes and are discussed in ref. 98.

Chapter 5

Conclusions

You must know that a person's ability to discern the truth is directly proportional to his knowledge.

Liu Cixin, The Three-Body Problem

The outset of this doctoral thesis was to model SA Pt on ceria, determine their electronic structure and frame it in the context of catalysis. As such I have presented a square-planar coordination surrounded by oxygen ligands on the pristine surface of nanocubes. This coordination can be synthesized from bulk platinum via surface wetting or instead via gas phase deposition. The system is stable without the need for surface defects. It has a low activity, but under reductive conditions this setup is activated via removal of two oxygen ligands. The resulting form is still stable against sintering by small nanoparticles, dimer formation, and evaporation. The electronic state of this species encompasses several low-lying minima corresponding to different oxidation states. Some of these states are unexpected for single-atoms, such as a neutral charge, while others are exotic in general, namely singly positive platinum. I modeled each state accounting for entropy of the charge residing in the slab. On top, I performed Born-Oppenheimer Molecular Dynamics and demonstrated that all three oxidation states are attainable at moderate temperatures (from 450 K on). At 600 K, the single-atom alternates between them. The electron transfer dynamics are governed by lattice vibrations that lower the polaron hopping barrier. To distinguish this phenomenon from other Strong Metal-Support Interactions and capture the mechanism, the term Phonon-Assisted Metal-Support Interaction (PAMSI) is coined.

The activated form catalyzes CO oxidation. Mechanistic pathways have been constructed for all three channels with cross-over reactions. The operating temperatures of the catalyst were verified using micro-kinetics. Disregarding any activation or deactivation steps, the single-atom catalyst attains peak performance at around 450 K ($\sim 150°$)C. These are the target temperatures for car-exhaust catalysts set by the DOE challenge. This makes that our model catalyst is an excellent candidate that requires little modification of the current commercially available standards. The reactivity of the model catalyst is traced back to predominantly the positive platinum oxidation state.

In order to better evaluate the impact of PAMSI, I started screening novel combinations of metals and oxide supports. Due to their chemical similarity with platinum, I commenced with elements from group 10 on the same ceria support: Ni and Pd. In contrast with Pt, these SA dispersions are in principle stable against all sizes of their NP counterparts. I found that nickel bears a dynamic oxidation state as well. The size effects negatively impact the range however and exclude the neutral OS from the batch. Palladium on the other hand, retains a single, classical OS. Due to its reordering of the electronic configuration, it incurs an energy penalty which is detrimental to PAMSI.

In Chapter 4, novel modeling techniques were tested out on ceria. Firstly, I presented a benchmark performed on the bulk phase comparing HF, HSE03, RPA, MP2, and experimental results. The focus lies especially on MP2, which was done in collaboration with Dr. Tobias Schäfer using the new `VASP` LTMP2 algorithm. These are the first-ever converged wavefunction results for the most common ceria phases. A general trend emerges of how the exchange hole pushes the lattice to expand, while correlation tends to make it contract. In Ce_2O_3 this effect is much more contrasted than CeO_2. Overall, HSE03 seems to have the best error cancellation between both. For the bulk modulus, the trend is less clear, but MP2 comes out on top. In the case of Ce_2O_3 there is no noteworthy change.

Secondly, several NNPs were constructed during my three-and a half month stay at the group of Prof. Jörg Behler. The emphasis lay on light-weight, primitive cell bulk structures for testing. Sampling over the Gaussian peak centers (r_s) for the radial SymFuncs proved much more effective in simulations then width (η) sampling. This also showed that there is more to a HDNNP's performance than can be measured via bias and variance. With the addition of a small amount of slab structures, the latest rendition of the potential is stable up to 900 K. As such, the conclusion is that machine learning techniques could generate an alternative to classical forcefields, at least in the case of ceria. Further improvements will consist of SymFunc expansion into the long range and addition of more data. Currently we posses slightly less slab structures than bulk, but considering their

size they contain more atomic environments. Moreover, if a HDNNP simulation only fails in specific cases, these incidents can be captured and added/plugged.

Chapter 6

Bibliography

[1] European Automobile Manufacturers Association. Economic and Market Report: EU Automotive Industry Full-year 2018. Tech. Rep. February, ACEA (2019).

[2] Zammit, M. *et al.* Future Automotive Aftertreatment Solutions: The 150°C Challenge Workshop. Tech. Rep., Pacific Northwest National Laboratory (PNNL), Richland, WA (United States) (2013).

[3] Chorkendorff, I. & Niemantsverdriet, J. W. *Concepts of Modern Catalysis And Kinetics* (Wiley-VCH, 2003).

[4] Nesbit, M. *et al.* Comparative study on the differences between the EU and US legislation on emissions in the automotive sector. Tech. Rep., EU Policy Department A (2016).

[5] Daelman, N., Capdevila-Cortada, M. & López, N. Dynamic charge and oxidation state of Pt/CeO_2 single-atom catalysts. *Nature Materials* (2019).

[6] van den Hout, K. *et al.* Ambient air pollution: Carbon Monoxide Position Paper. Tech. Rep., TNO Institute of Environmental Sciences, Energy Research and Process Innovation (1999).

[7] U.S. Environmental Protection Agency. Quantitative Risk and Exposure Assessment for Carbon Monoxide – Amended. Tech. Rep., USEPA (2010).

[8] Yang, X.-F. *et al.* Single-Atom Catalysts: A New Frontier in Heterogeneous Catalysis. *Accounts of Chemical Research* **46**, 1740–1748 (2013).

[9] Flytzani-Stephanopoulos, M. & Gates, B. C. Atomically Dispersed Supported Metal Catalysts. *Annual Review of Chemical and Biomolecular Engineering* **3**, 545–574 (2012).

[10] Gänzler, A. M. *et al.* Tuning the Pt/CeO_2 Interface by in Situ Variation of the Pt Particle Size. *ACS Catalysis* **8**, 4800–4811 (2018).

[11] Trovarelli, A. & Fornasiero, P. *Catalysis by ceria and related materials*, vol. 12 (Imperial College Press, London, 2013), second edn.

[12] Capdevila-Cortada, M., Vilé, G., Teschner, D., Pérez-Ramírez, J. & López, N. Reactivity descriptors for ceria in catalysis. *Applied Catalysis B: Environmental* **197**, 299–312 (2016).

[13] Rellán-Piñeiro, M. & López, N. One Oxygen Vacancy, Two Charge States: Characterization of Reduced α-MoO 3 (010) through Theoretical Methods. *The Journal of Physical Chemistry Letters* **9**, 2568–2573 (2018).

[14] Da Silva, J. L. F., Ganduglia-Pirovano, M. V., Sauer, J., Bayer, V. & Kresse, G. Hybrid functionals applied to rare-earth oxides: The example of ceria. *Physical Review B - Condensed Matter and Materials Physics* **75**, 19–24 (2007).

[15] Perdew, J. P. Jacob's ladder of density functional approximations for the exchange-correlation energy. In *AIP Conference Proceedings*, vol. 577, 1–20 (AIP, 2001).

[16] Capdevila-Cortada, M., Łodziana, Z. & López, N. Performance of DFT+ U Approaches in the Study of Catalytic Materials. *ACS Catalysis* **6**, 8370–8379 (2016).

[17] Schäfer, T., Ramberger, B. & Kresse, G. Quartic scaling MP2 for solids: A highly parallelized algorithm in the plane wave basis. *The Journal of Chemical Physics* **146**, 104101 (2017).

[18] Schäfer, T., Ramberger, B. & Kresse, G. Laplace transformed MP2 for three dimensional periodic materials using stochastic orbitals in the plane wave basis and correlated sampling. *The Journal of Chemical Physics* **148**, 064103 (2018).

[19] Ren, X., Rinke, P., Joas, C. & Scheffler, M. Random-phase approximation and its applications in computational chemistry and materials science. *Journal of Materials Science* **47**, 7447–7471 (2012).

[20] Bruix, A., Margraf, J. T., Andersen, M. & Reuter, K. First-principles-based multiscale modelling of heterogeneous catalysis. *Nature Catalysis* (2019).

[21] Griffiths, D. *Introduction to Elementary Particles* (Wiley-VCH, 2008), second edn.

[22] Schwerdtfeger, P. Relativistic effects in properties of gold. *Heteroatom Chemistry* **13**, 578–584 (2002).

[23] van Lenthe, E., Baerends, E. J. & Snijders, J. G. Relativistic regular two-component Hamiltonians. *The Journal of Chemical Physics* **99**, 4597–4610 (1993).

[24] van Lenthe, E., Baerends, E. J. & Snijders, J. G. Relativistic total energy using regular approximations. *The Journal of Chemical Physics* **101**, 9783–9792 (1994).

[25] Basdevant, J.-L. & Dalibard, J. *Quantum Mechanics* (Springer, Paris, 2002), first edn.

[26] Bear, M. *Beyond Born-Oppenheimer: Conical Intersections and Electronic Nonadiabatic Coupling Terms* (John Wiley & Sons, Inc., 2006).

[27] Born, M. & Oppenheimer, R. Zur Quantentheorie der Molekeln. *Annalen der Physik* **389**, 457–484 (1927).

[28] Kittel, C. *Introduction to Solid State Physics* (John Wiley & Sons, Inc., Berkely, 2005), eighth edn.

[29] Hoffmann, R. How Chemistry and Physics Meet in the Solid State. *Angewandte Chemie International Edition in English* **26**, 846–878 (1987).

[30] Szabo, A. & Ostlund, N. S. *Modern Quantum Chemistry: Introduction to Advanced Electronic Structure Theory* (Dover Publications , Inc., Minealo, New York, 1996), first edn.

[31] Ramos-Cordoba, E., Salvador, P. & Matito, E. Separation of dynamic and nondynamic correlation. *Physical Chemistry Chemical Physics* **18**, 24015–24023 (2016).

[32] Press, W. H., Teukolsky, S. A., Vetterling, W. T. & Flannery, B. P. *Numerical Recipes: The Art of Scientific Computing* (Cambridge University Press, 2007), third edn.

[33] Ochsenfeld, C., Kussmann, J. & Lambrecht, D. S. Linear-Scaling Methods in Quantum Chemistry. In *Reviews in Computational Chemistry Volume 23*, vol. 23, chap. 1, 1–82 (J. Wiley & Sons, Inc., 2007).

[34] Hohenberg, P. & Kohn, W. Inhomogeneous Electron Gas. *Physical Review* **136**, B864–B871 (1964).

[35] Bader, R. F. W. Atoms in molecules. *Accounts of Chemical Research* **18**, 9–15 (1985).

[36] Kohn, W. & Sham, L. J. Self-Consistent Equations Including Exchange and Correlation Effects. *Physical Review* **140**, A1133–A1138 (1965).

[37] Oliver, G. L. & Perdew, J. P. Spin-density gradient expansion for the kinetic energy. *Physical Review A* **20**, 397–403 (1979).

[38] Levy, M. & Perdew, J. P. Hellmann-Feynman, virial, and scaling requisites for the exact universal density functionals. Shape of the correlation potential and diamagnetic susceptibility for atoms. *Physical Review A* **32**, 2010–2021 (1985).

[39] Medvedev, M. G., Bushmarinov, I. S., Lyssenko, K. A., Sun, J. & Perdew, J. P. Density functional theory is straying from the path toward the exact functional. *Science* **355**, 49–52 (2017).

[40] Adamo, C., Ernzerhof, M. & Scuseria, G. E. The meta-GGA functional: Thermochemistry with a kinetic energy density dependent exchange-correlation functional. *The Journal of Chemical Physics* **112**, 2643–2649 (2000).

[41] Sun, J., Ruzsinszky, A. & Perdew, J. P. Strongly Constrained and Appropriately Normed Semilocal Density Functional. *Physical Review Letters* **115**, 036402 (2015).

[42] Huang, Y.-W. & Lee, S.-L. Hybrid DFT and hyper-GGA DFT studies of the CO adsorption on Pt nanoclusters: Effects of the cluster size and better CO LUMO description. *Chemical Physics Letters* **492**, 98–102 (2010).

[43] Perdew, J. P. *et al.* Restoring the Density-Gradient Expansion for Exchange in Solids and Surfaces. *Physical Review Letters* **100**, 136406 (2008).

[44] Hubbard, J. Electron correlations in narrow energy bands. *Proceedings of the Royal Society of London. Series A. Mathematical and Physical Sciences* **276**, 238–257 (1963).

[45] Liechtenstein, A. I., Anisimov, V. I. & Zaanen, J. Density-functional theory and strong interactions: Orbital ordering in Mott-Hubbard insulators. *Physical Review B* **52**, R5467–R5470 (1995).

[46] Cococcioni, M. & de Gironcoli, S. Linear response approach to the calculation of the effective interaction parameters in the LDA+U method. *Physical Review B* **71**, 035105 (2005).

[47] Ren, X., Rinke, P. & Scheffler, M. Exploring the random phase approximation: Application to CO adsorbed on Cu(111). *Physical Review B* **80**, 045402 (2009).

[48] Paulsson, M. Non Equilibrium Green's Functions for Dummies: Introduction to the One Particle NEGF equations. *arXiv:cond-mat* (2002).

[49] Chen, W. & Pasquarello, A. Accurate band gaps of extended systems via efficient vertex corrections in GW. *Physical Review B* **92**, 041115 (2015).

[50] Scuseria, G. E., Henderson, T. M. & Sorensen, D. C. The ground state correlation energy of the random phase approximation from a ring coupled cluster doubles approach. *The Journal of Chemical Physics* **129**, 231101 (2008).

[51] Yan, Z., Perdew, J. P. & Kurth, S. Density functional for short-range correlation: Accuracy of the random-phase approximation for isoelectronic energy changes. *Physical Review B* **61**, 16430–16439 (2000).

[52] Feibelman, P. J. *et al.* The CO/Pt(111) Puzzle. *The Journal of Physical Chemistry B* **105**, 4018–4025 (2001).

[53] Heyd, J., Scuseria, G. E. & Ernzerhof, M. Hybrid functionals based on a screened Coulomb potential. *Journal of Chemical Physics* **118**, 8207–8215 (2003).

[54] Hegner, F. S. *et al.* Cobalt Hexacyanoferrate on BiVO4 Photoanodes for Robust Water Splitting. *ACS Applied Materials and Interfaces* **9**, 37671–37681 (2017).

[55] Heyd, J. & Scuseria, G. E. Assessment and validation of a screened Coulomb hybrid density functional. *Journal of Chemical Physics* **120**, 7274–7280 (2004).

[56] Adamo, C. & Barone, V. Toward reliable density functional methods without adjustable parameters: The PBE0 model. *The Journal of Chemical Physics* **110**, 6158–6170 (1999).

[57] Grimme, S., Antony, J., Ehrlich, S. & Krieg, H. A consistent and accurate ab initio parametrization of density functional dispersion correction (DFT-D) for the 94 elements H-Pu. *The Journal of Chemical Physics* **132**, 154104 (2010).

[58] Groß, A. *Theoretical Surface Science*. Advanced Texts in Physics (Springer Berlin Heidelberg, Berlin, Heidelberg, 2003), 1st edn.

[59] Kresse, G. & Joubert, D. From ultrasoft pseudopotentials to the projector augmented-wave method. *Physical Review B* **59**, 1758–1775 (1999).

[60] Klimeš, J., Kaltak, M. & Kresse, G. Predictive GW calculations using plane waves and pseudopotentials. *Physical Review B* **90**, 075125 (2014).

[61] Mills, G., Jónsson, H. & Schenter, G. K. Reversible work transition state theory: application to dissociative adsorption of hydrogen. *Surface Science* **324**, 305–337 (1995).

[62] Henkelman, G. & Jónsson, H. Improved tangent estimate in the nudged elastic band method for finding minimum energy paths and saddle points. *The Journal of Chemical Physics* **113**, 9978–9985 (2000).

[63] Henkelman, G., Uberuaga, B. P. & Jónsson, H. A climbing image nudged elastic band method for finding saddle points and minimum energy paths. *The Journal of Chemical Physics* **113**, 9901–9904 (2000).

[64] Henkelman, G. & Jónsson, H. A dimer method for finding saddle points on high dimensional potential surfaces using only first derivatives. *The Journal of Chemical Physics* **111**, 7010–7022 (1999).

[65] Heyden, A., Bell, A. T. & Keil, F. J. Efficient methods for finding transition states in chemical reactions: Comparison of improved dimer method and partitioned rational function optimization method. *The Journal of Chemical Physics* **123**, 224101 (2005).

[66] Olsen, R. A., Kroes, G. J., Henkelman, G., Arnaldsson, A. & Jónsson, H. Comparison of methods for finding saddle points without knowledge of the final states. *The Journal of Chemical Physics* **121**, 9776–9792 (2004).

[67] Nosé, S. A molecular dynamics method for simulations in the canonical ensemble. *Molecular Physics* **52**, 255–268 (1984).

[68] Schnakenberg, J. Network theory of microscopic and macroscopic behavior of master equation systems. *Reviews of Modern Physics* **48**, 571–585 (1976).

[69] Hoover, W. G. & Holian, B. L. Kinetic moments method for the canonical ensemble distribution. *Physics Letters A* **211**, 253–257 (1996).

[70] Salmi, T. O., Mikkola, J.-P. & Wärnå, J. P. *Chemical Reaction Engineering and Reactor Technology* (CRC Press, 2011).

[71] Todorović, M., Gutmann, M. U., Corander, J. & Rinke, P. Bayesian inference of atomistic structure in functional materials. *Nature Partner Journals Computational Materials* **5**, 35 (2019).

[72] Linan, M. N., Gerardo, B. & Medina, R. Modified weight initialization in the self-organizing map using Nguyen-Widrow initialization algorithm. *Journal of Physics: Conference Series* **1235**, 012055 (2019).

[73] Behler, J. & Parrinello, M. Generalized Neural-Network Representation of High-Dimensional Potential-Energy Surfaces. *Physical Review Letters* **98**, 146401 (2007).

[74] Hert, J., Keiser, M. J., Irwin, J. J., Oprea, T. I. & Shoichet, B. K. Quantifying the Relationships among Drug Classes. *Journal of Chemical Information and Modeling* **48**, 755–765 (2008).

[75] Li, J., Jiang, B. & Guo, H. Permutation invariant polynomial neural network approach to fitting potential energy surfaces. II. Four-atom systems. *The Journal of Chemical Physics* **139**, 204103 (2013).

[76] Bartók, A. P., Kondor, R. & Csányi, G. On representing chemical environments. *Physical Review B* **87**, 184115 (2013).

[77] Ryczko, K., Mills, K., Luchak, I., Homenick, C. & Tamblyn, I. Convolutional neural networks for atomistic systems. *Computational Materials Science* **149**, 134–142 (2018).

[78] Kopelent, R. *et al.* Catalytically Active and Spectator Ce^{3+} in Ceria-Supported Metal Catalysts. *Angewandte Chemie International Edition* **54**, 8728–8731 (2015).

[79] Lykhach, Y. *et al.* Counting electrons on supported nanoparticles. *Nature Materials* **15**, 284–288 (2015).

[80] Campbell, C. T. Catalyst-support interactions: Electronic perturbations. *Nature Chemistry* **4**, 597–598 (2012).

[81] Bruix, A. *et al.* A New Type of Strong Metal–Support Interaction and the Production of H_2 through the Transformation of Water on Pt/CeO_2 (111) and Pt/CeO_x /TiO_2 (110) Catalysts. *Journal of the American Chemical Society* **134**, 8968–8974 (2012).

[82] Bruix, A. *et al.* Effects of deposited Pt particles on the reducibility of CeO_2(111). *Physical Chemistry Chemical Physics* **13**, 11384 (2011).

[83] Vayssilov, G. N. *et al.* Support nanostructure boosts oxygen transfer to catalytically active platinum nanoparticles. *Nature Materials* **10**, 310–315 (2011).

[84] Tauster, S. J., Fung, S. C. & Garten, R. L. Strong metal-support interactions. Group 8 noble metals supported on titanium dioxide. *Journal of the American Chemical Society* **100**, 170–175 (1978).

[85] Tauster, S. J. Strong Metal-Support Interactions. *American Chemical Society* **87**, 389–394 (1987).

[86] Farmer, J. A. & Campbell, C. T. Ceria Maintains Smaller Metal Catalyst Particles by Strong Metal-Support Bonding. *Science* **329**, 933–936 (2010).

[87] Penschke, C. & Paier, J. Reduction and oxidation of Au adatoms on the CeO_2 (111) surface – DFT+U versus hybrid functionals. *Phys. Chem. Chem. Phys.* **19**, 12546–12558 (2017).

[88] Hu, P. *et al.* Electronic Metal-Support Interactions in Single-Atom Catalysts. *Angewandte Chemie* **126**, 3486–3489 (2014).

[89] Hansen, T. W., DeLaRiva, A. T., Challa, S. R. & Datye, A. K. Sintering of Catalytic Nanoparticles: Particle Migration or Ostwald Ripening? *Accounts of Chemical Research* **46**, 1720–1730 (2013).

[90] Ouyang, R., Liu, J. X. & Li, W. X. Atomistic theory of ostwald ripening and disintegration of supported metal particles under reaction conditions. *Journal of the American Chemical Society* **135**, 1760–1771 (2013).

[91] Jones, J. *et al.* Thermally stable single-atom platinum-on-ceria catalysts via atom trapping. *Science* **353**, 150–154 (2016).

[92] Dvořák, F. *et al.* Creating single-atom Pt-ceria catalysts by surface step decoration. *Nature Communications* **7**, 10801–10808 (2016).

[93] Neitzel, A. *et al.* Atomically Dispersed Pd, Ni, and Pt Species in Ceria-Based Catalysts: Principal Differences in Stability and Reactivity. *The Journal of Physical Chemistry C* **120**, 9852–9862 (2016).

[94] Ortuño, M. A., Conejero, S. & Lledós, A. True and masked three-coordinate T-shaped platinum(II) intermediates. *Beilstein Journal of Organic Chemistry* **9**, 1352–1382 (2013).

[95] Wang, C. *et al.* Water-Mediated Mars–Van Krevelen Mechanism for CO Oxidation on Ceria-Supported Single-Atom Pt_1 Catalyst. *ACS Catalysis* **7**, 887–891 (2017).

[96] Datye, A. K. & Wang, Y. Atom trapping: a novel approach to generate thermally stable and regenerable single-atom catalysts. *National Science Review* **5**, 630–632 (2018).

[97] Pereira Hernandez, X. I. *et al.* Tuning Pt-CeO_2 interactions by high-temperature vapor-phase synthesis for improved reducibility of lattice oxygen. *Nature Communications* **10**, 1358 (2019).

[98] Capdevila-Cortada, M. & López, N. Entropic contributions enhance polarity compensation for CeO_2 (100) surfaces. *Nature Materials* **16**, 328–334 (2017).

[99] Bugnet, M., Overbury, S. H., Wu, Z. L. & Epicier, T. Direct Visualization and Control of Atomic Mobility at {100} Surfaces of Ceria in the Environmental Transmission Electron Microscope. *Nano Letters* **17**, 7652–7658 (2017).

[100] Kunwar, D. *et al.* Stabilizing High Metal Loadings of Thermally Stable Platinum Single Atoms on an Industrial Catalyst Support. *ACS Catalysis* **9**, 3978–3990 (2019).

[101] Ding, K. *et al.* Identification of active sites in CO oxidation and water-gas shift over supported Pt catalysts. *Science* **350**, 189–192 (2015).

[102] Nie, L. *et al.* Activation of surface lattice oxygen in single-atom Pt/CeO_2 for low-temperature CO oxidation. *Science* **358**, 1419–1423 (2017).

[103] Kato, S. *et al.* Quantitative depth profiling of Ce3+ in Pt/CeO_2 by in situ high-energy XPS in a hydrogen atmosphere. *Physical Chemistry Chemical Physics* **17**, 5078–5083 (2015).

[104] Zhang, D., Han, Z.-K., Murgida, G. E., Ganduglia-Pirovano, M. V. & Gao, Y. Oxygen-Vacancy Dynamics and Entanglement with Polaron Hopping at the Reduced CeO_2 (111) Surface. *Physical Review Letters* **122**, 096101 (2019).

[105] Walsh, A., Sokol, A. A., Buckeridge, J., Scanlon, D. O. & Catlow, C. R. A. Oxidation states and ionicity. *Nature Materials* **17**, 958–964 (2018).

[106] Wu, T. *et al.* Investigation of the Redispersion of Pt Nanoparticles on Polyhedral Ceria Nanoparticles. *The Journal of Physical Chemistry Letters* **5**, 2479–2483 (2014).

[107] Therrien, A. J. *et al.* An atomic-scale view of single-site Pt catalysis for low-temperature CO oxidation. *Nature Catalysis* **1**, 192–198 (2018).

[108] Bagus, P. S., Nelin, C. J., Hrovat, D. A. & Ilton, E. S. Covalent bonding in heavy metal oxides. *The Journal of Chemical Physics* **146**, 134706 (2017).

[109] Das, M. P. & Green, F. Revisiting the Fermi Surface in Density Functional Theory. *Journal of Physics: Conference Series* **726** (2016).

[110] Aizawa, H. & Tsuneyuki, S. First-principles study of CO bonding to Pt(111): validity of the Blyholder model. *Surface Science* **399**, L364–L370 (1998).

[111] Tang, Y., Wang, Y.-G. & Li, J. Theoretical Investigations of $Pt_1k@CeO_2$ Single-Atom Catalyst for CO Oxidation. *The Journal of Physical Chemistry C* **121**, 11281–11289 (2017).

[112] Plata, J. J., Márquez, A. M. & Sanz, J. F. Electron Mobility via Polaron Hopping in Bulk Ceria: A First-Principles Study. *The Journal of Physical Chemistry C* **117**, 14502–14509 (2013).

[113] Naghavi, S. S. *et al.* Giant onsite electronic entropy enhances the performance of ceria for water splitting. *Nature Communications* **8**, 285–291 (2017).

[114] Clerc, J. C. Catalytic diesel exhaust aftertreatment. *Applied Catalysis B: Environmental* **10**, 99–115 (1996).

[115] Bliem, R. *et al.* Dual role of CO in the stability of subnano Pt clusters at the Fe 3 O 4 (001) surface. *Proceedings of the National Academy of Sciences* **113**, 8921–8926 (2016).

[116] Liang, S., Hao, C. & Shi, Y. The Power of Single-Atom Catalysis. *ChemCatChem* **7**, 2559–2567 (2015).

[117] Collman, J. P. Patterns of organometallic reactions related to homogeneous catalysis. *Accounts of Chemical Research* **1**, 136–143 (1968).

[118] Kramida, A., Ralchenko, Y., Reader, J. & Team, N. A. NIST Atomic Spectra Database (ver. 5.5.6) (2018).

[119] Zhou, Y. & Zhou, J. Interactions of Ni Nanoparticles with Reducible CeO_2 (111) Thin Films. *The Journal of Physical Chemistry C* **116**, 9544–9549 (2012).

[120] Wang, X. *et al.* The synergy between atomically dispersed Pd and cerium oxide for enhanced catalytic properties. *Nanoscale* **9**, 6643–6648 (2017).

[121] Su, Y.-Q., Filot, I. A. W., Liu, J.-X. & Hensen, E. J. M. Stable Pd-Doped Ceria Structures for CH_4 Activation and CO Oxidation. *ACS Catalysis* **8**, 75–80 (2018).

[122] Birch, F. The effect of pressure upon the elastic parameters of isotropic solids, according to Murnaghan's theory of finite strain. *Journal of Applied Physics* **9**, 279–288 (1938).

[123] Voloshina, E. & Paulus, B. Influence of electronic correlations on the ground-state properties of cerium dioxide. *Journal of Chemical Physics* **124** (2006).

[124] Stecura, S. & Campbell, W. J. Thermal expansion and phase inversion of rare-earth oxides. *US Bureau of Mines Report Number 5847* 1–46 (1961).

[125] Lipp, M. J. *et al.* Comparison of the high-pressure behavior of the cerium oxides Ce_2O_3 and CeO_2. *Physical Review B* **93**, 1–8 (2016).

[126] Singraber, A., Behler, J. & Dellago, C. Library-Based LAMMPS Implementation of High-Dimensional Neural Network Potentials. *Journal of Chemical Theory and Computation* **15**, 1827–1840 (2019).

[127] Zhu, H. *et al.* Charge transfer drives anomalous phase transition in ceria. *Nature Communications* **9**, 5063 (2018).

[128] Hellström, M., Quaranta, V. & Behler, J. One-dimensional vs. two-dimensional proton transport processes at solid–liquid zinc-oxide–water interfaces. *Chemical Science* **10**, 1232–1243 (2019).

[129] Yang, C. *et al.* Surface Faceting and Reconstruction of Ceria Nanoparticles. *Angewandte Chemie International Edition* **56**, 375–379 (2017).

[130] Murgida, G. E. & Ganduglia-Pirovano, M. V. Evidence for Subsurface Ordering of Oxygen Vacancies on the Reduced CeO_2 (111) Surface Using Density-Functional and Statistica. *Physical Review Letters* **110**, 246101 (2013).

Appendices

UNIVERSITAT ROVIRA I VIRGILI
THEORETICAL INVESTIGATIONS INTO SINGLE-ATOM CATALYSTS ON CERIUM DIOXIDE: DEPOSITION AND ACTIVATION.
Nathan Daelman

Appendix A

HDNNP simulations

This appendix lists all Large-scale Atomic/Molecular Massively Parallel Simulator (LAMMPS) simulations for the HDNNPs setups 3 and 4, as presented in chapter 4.2. It is their stabilities that were used as input for the top panel in figure 4.7. To reiterate, setup 3 contains bulk only data from within 5% expansion/compression of the equilibrium. Setup 4 adds on 3 with the (2×2) slabs for pristine (100) and slabs with peroxo-groups. Both setups use SymFuncs that scan over the peaks (r_s) of the Gaussian radial distribution and two complementary angular SymFuncs.

The NVT simulations all start after 0.2 fs of heating up and span 1.0 fs, analogous to the bottom panel in figure 4.7. The temperature and dataset are marked in the header. They contain the (normally) anti-symmetric potential (red) and kinetic energy (orange), as well as the total energy (green) for stability reference. The y-axes may differ between figures individually, but the potential an kinetic energies of a single figure always have the same span.

Note how setup 3 always break down before the 1.0 fs mark, with the exception of the run at 150 K. The inverse is true for setup 4, with again an exception of 900 K. Setups 1 an 2 are not shown since they break down during to heating.

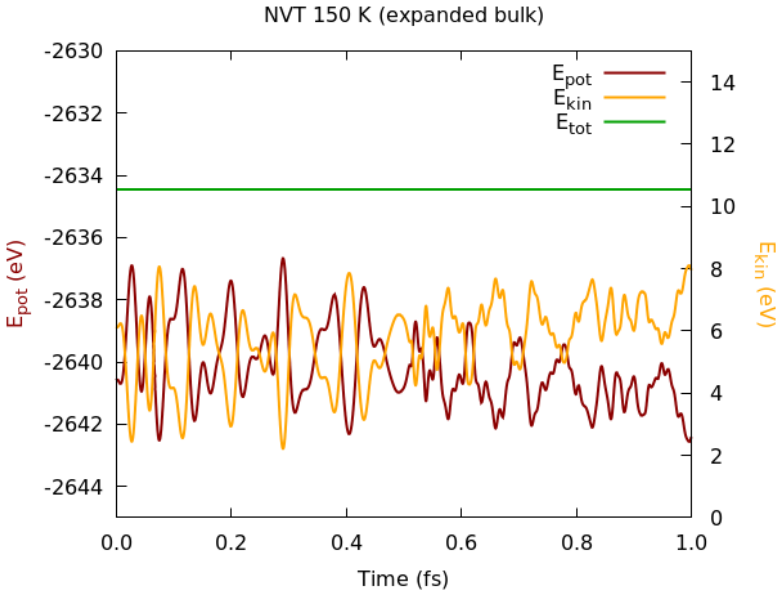
NVT 150 K (expanded bulk)
E_pot
E_kin
E_tot
E_pot (eV)
E_kin (eV)
Time (fs)
-2630
-2632
-2634
-2636
-2638
-2640
-2642
-2644
14
12
10
8
6
4
2
0
0.0
0.2
0.4
0.6
0.8
1.0

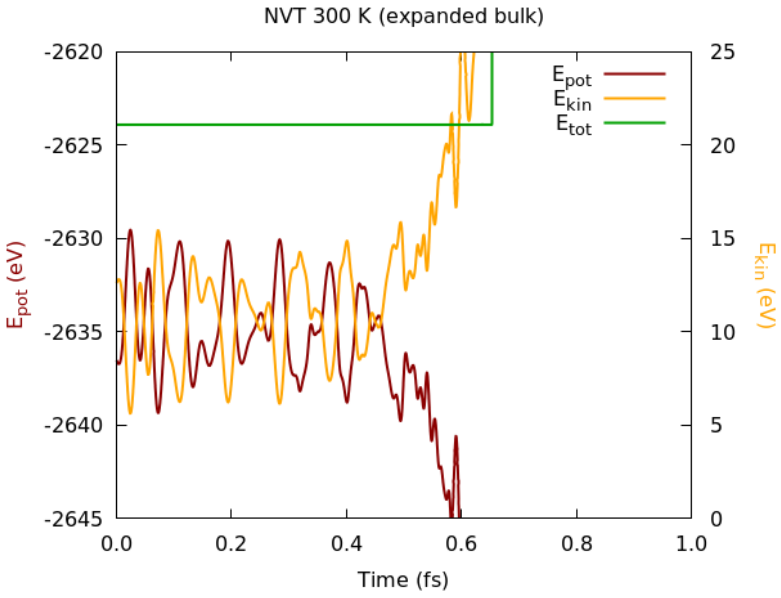
NVT 300 K (expanded bulk)
E_pot
E_kin
E_tot
E_pot (eV)
E_kin (eV)
Time (fs)
-2620
-2625
-2630
-2635
-2640
-2645
25
20
15
10
5
0
0.0
0.2
0.4
0.6
0.8
1.0

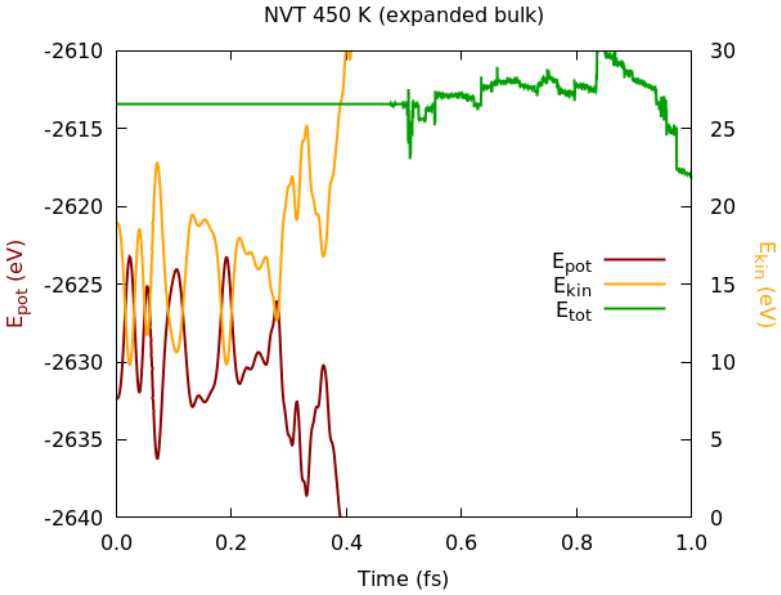
NVT 450 K (expanded bulk)
-2610
-2615
-2620
-2625
-2630
-2635
-2640
30
25
20
15
10
5
0
0.0
0.2
0.4
0.6
0.8
1.0
Time (fs)
E_pot (eV)
E_kin (eV)
E_pot
E_kin
E_tot

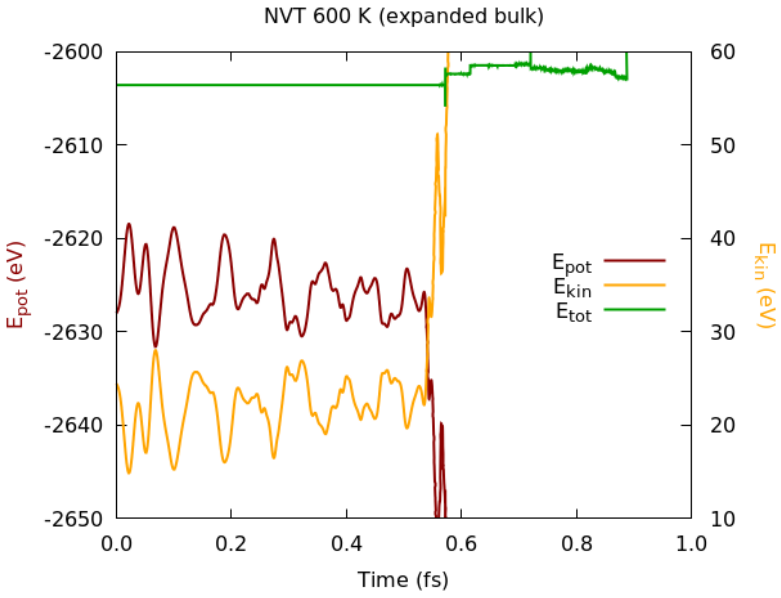
NVT 600 K (expanded bulk)
-2600
-2610
-2620
-2630
-2640
-2650
60
50
40
30
20
10
0.0
0.2
0.4
0.6
0.8
1.0
Time (fs)
E_pot (eV)
E_kin (eV)
E_pot
E_kin
E_tot

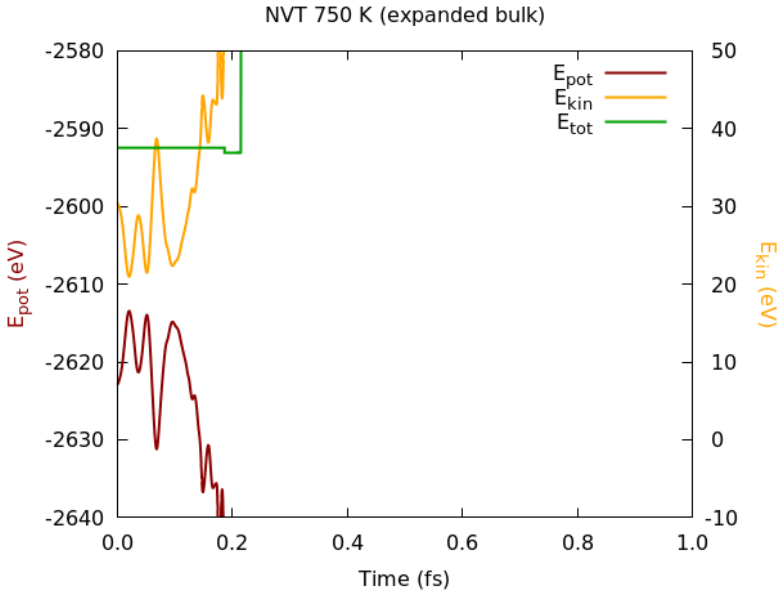
NVT 750 K (expanded bulk)
E_pot
E_kin
E_tot
E_pot (eV)
E_kin (eV)
Time (fs)
-2580
-2590
-2600
-2610
-2620
-2630
-2640
50
40
30
20
10
0
-10
0.0
0.2
0.4
0.6
0.8
1.0

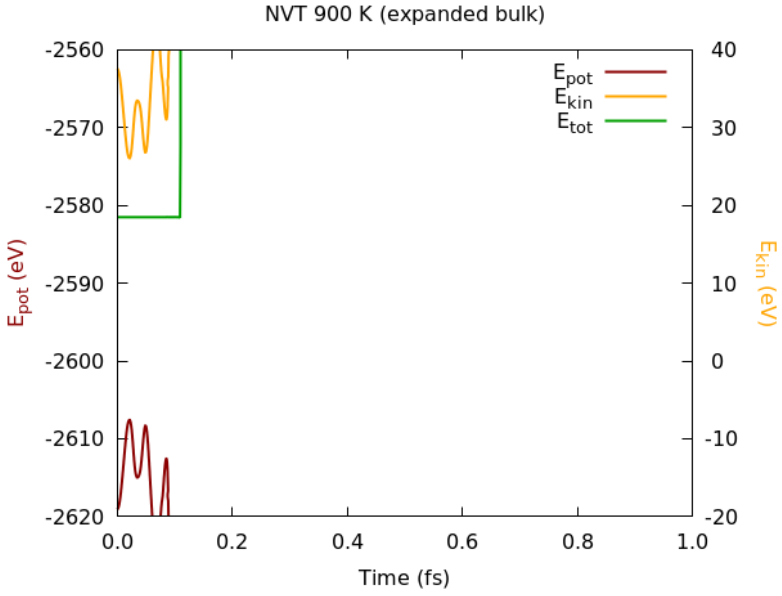
NVT 900 K (expanded bulk)
E_pot
E_kin
E_tot
E_pot (eV)
E_kin (eV)
Time (fs)
-2560
-2570
-2580
-2590
-2600
-2610
-2620
40
30
20
10
0
-10
-20
0.0
0.2
0.4
0.6
0.8
1.0

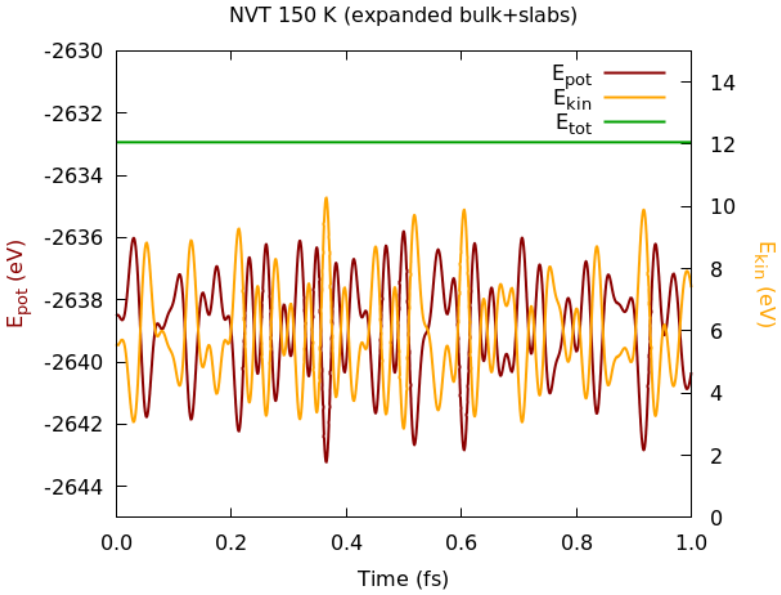
NVT 150 K (expanded bulk+slabs)
E_pot
E_kin
E_tot
E_pot (eV)
E_kin (eV)
Time (fs)
-2630
-2632
-2634
-2636
-2638
-2640
-2642
-2644
14
12
10
8
6
4
2
0
0.0
0.2
0.4
0.6
0.8
1.0

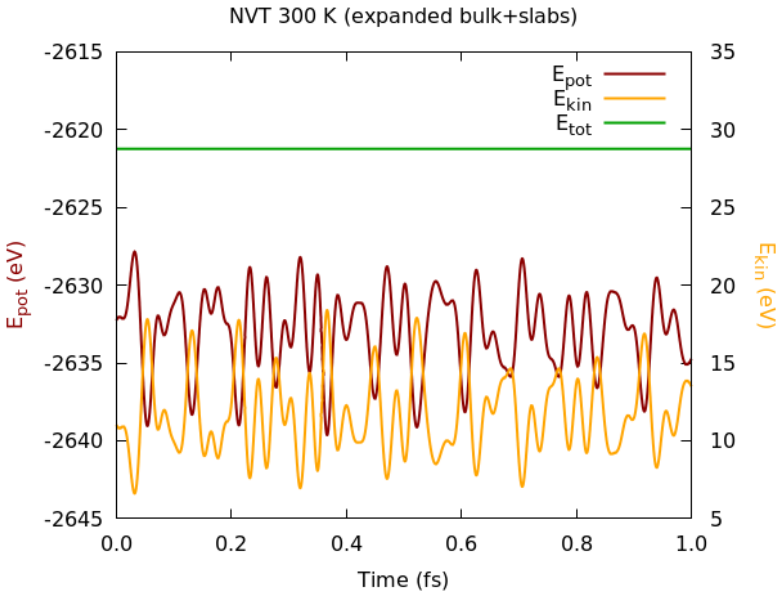
NVT 300 K (expanded bulk+slabs)
E_pot
E_kin
E_tot
E_pot (eV)
E_kin (eV)
Time (fs)
-2615
-2620
-2625
-2630
-2635
-2640
-2645
35
30
25
20
15
10
5
0.0
0.2
0.4
0.6
0.8
1.0

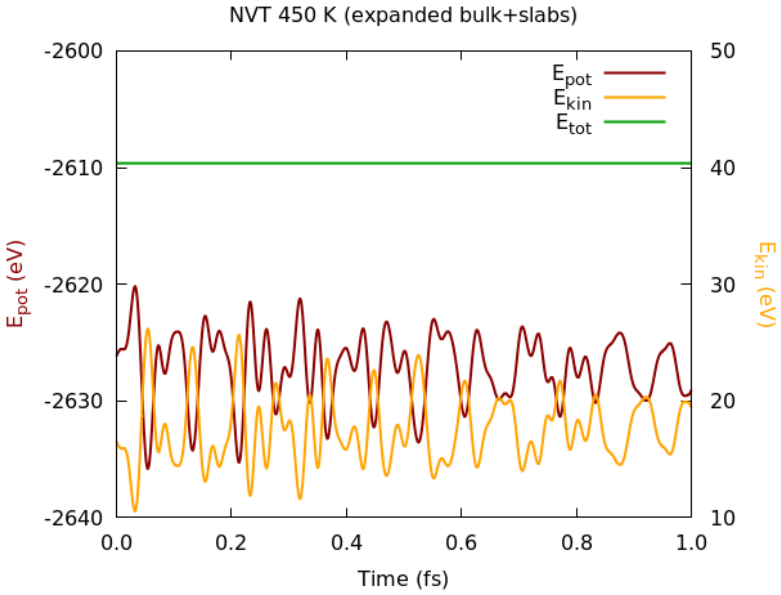
NVT 450 K (expanded bulk+slabs)
E_pot
E_kin
E_tot
E_pot (eV)
E_kin (eV)
-2600
-2610
-2620
-2630
-2640
50
40
30
20
10
0.0
0.2
0.4
0.6
0.8
1.0
Time (fs)

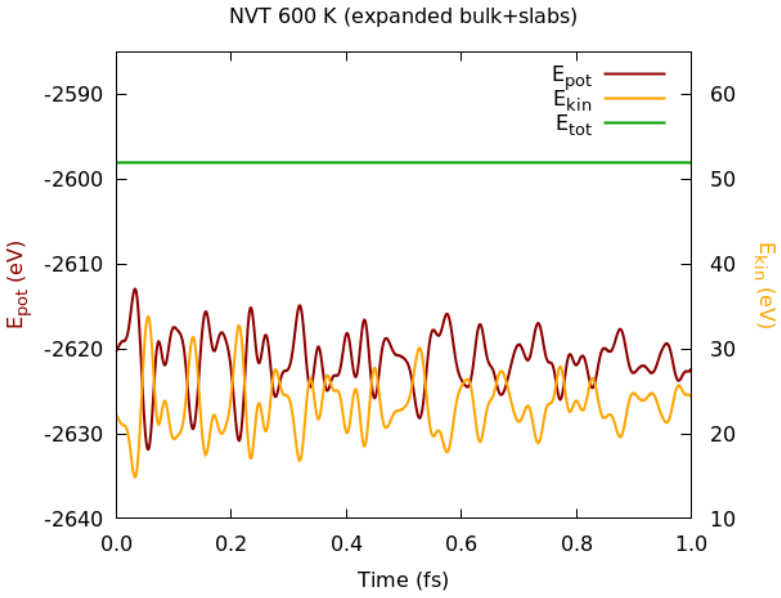
NVT 600 K (expanded bulk+slabs)
E_pot
E_kin
E_tot
E_pot (eV)
E_kin (eV)
-2590
-2600
-2610
-2620
-2630
-2640
60
50
40
30
20
10
0.0
0.2
0.4
0.6
0.8
1.0
Time (fs)

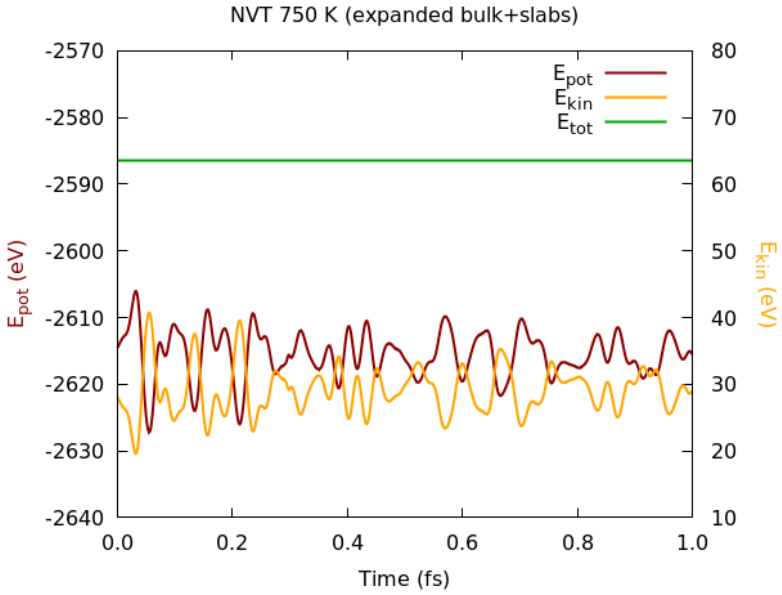
NVT 750 K (expanded bulk+slabs)
E_pot
E_kin
E_tot
E_pot (eV)
E_kin (eV)
Time (fs)
-2570
-2580
-2590
-2600
-2610
-2620
-2630
-2640
80
70
60
50
40
30
20
10
0.0
0.2
0.4
0.6
0.8
1.0

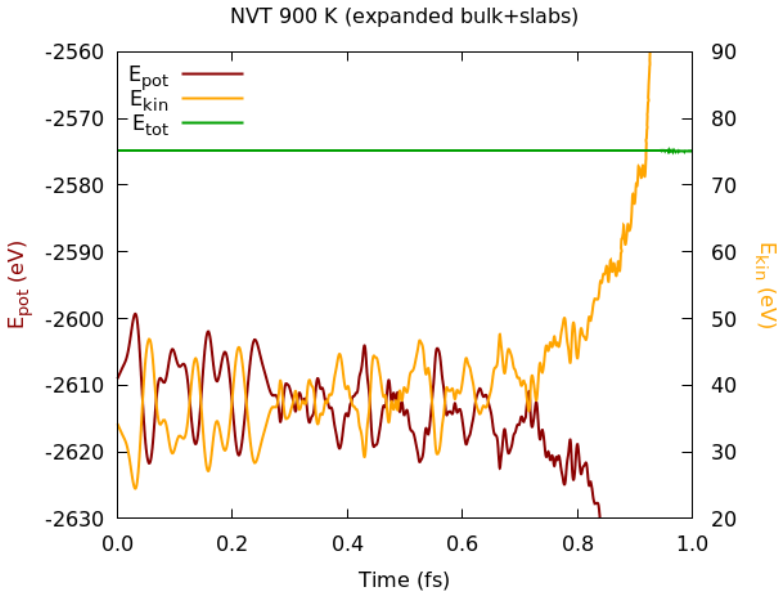
NVT 900 K (expanded bulk+slabs)
E_pot
E_kin
E_tot
E_pot (eV)
E_kin (eV)
Time (fs)
-2560
-2570
-2580
-2590
-2600
-2610
-2620
-2630
90
80
70
60
50
40
30
20
0.0
0.2
0.4
0.6
0.8
1.0

Included Papers

nature materials

ARTICLES

https://doi.org/10.1038/s41563-019-0444-y

Dynamic charge and oxidation state of Pt/CeO_2 single-atom catalysts

Nathan Daelman, Marçal Capdevila-Cortada and Núria López*

The catalytic activity of metals supported on oxides depends on their charge and oxidation state. Yet, the determination of the degree of charge transfer at the interface remains elusive. Here, by combining density functional theory and first-principles molecular dynamics on Pt single atoms deposited on the CeO_2 (100) surface, we show that the common representation of a static metal charge is oversimplified. Instead, we identify several well-defined charge states that are dynamically interconnected and thus coexist. The origin of this new class of strong metal–support interactions is the relative position of the Ce(*4f*) levels with respect to those of the noble metal, allowing electron injection to (or recovery from) the support. This process is phonon-assisted, as the Ce(*4f*) levels adjust by surface atom displacement, and appears for other metals (Ni) and supports (TiO_2). Our dynamic model explains the unique reactivity found for activated single Pt atoms on ceria able to perform CO oxidation, meeting the Department of Energy 150 °C challenge for emissions.

Harnessing the properties of metal/oxide structures lies at the core of materials science, since such interfaces appear in many technological applications[1]. At the interface, diverse amounts of charge may transfer to and from the metal. The excess (defect) charge can then be employed by the metal to donate (accept) charge density to (from) reactants and activate them. Therefore, the charge transfer at the metal/oxide interface controls the catalytic activity. Counting the number of electrons transferred becomes imperative, even though it remains difficult to measure experimentally[2–5].

The most interesting metal/oxide interfaces appear when the metal-to-metal and metal-to-oxide bonds are of similar bond strength, preventing phase separation. In particular, strong metal–support interactions[6] occur when the oxides acting as a support partially cover the metal nanoparticle on reduction[7,8]. However, if the bond between the metal and the oxide is stronger than that of the metal itself, atoms can be dispersed onto the oxide matrix[9]. Recently, this category has been redefined as single-atom catalysts (SACs)[10,11]. Reducible semiconductor oxides are suitable scaffolds for SACs, and examples with TiO_2[9], FeO_x[10], Cu_2O[12] and CeO_2 as supports and Au, Pd or Pt as metals have been reported[13–15]. For scarce metals, the atom economy deployed by SACs is the most cost effective while guaranteeing selective processes in hydrogenation, oxidation and other reactions[10–12,16–18].

Synthesis procedures can target different nanostructures with variable ratios of exposed (111), (110) and (100) surfaces[19,20]. On these ceria supports, Pt nanoparticles can be deposited and, by oxidizing them over an airflow, the volatile PtO_2 units disperse out as single atoms[13,21] with loadings of up to 3 wt.%[22]. Pt atoms have been found at grain boundaries[23] and (111) steps[22,24], and atop very small (<3 nm) nanoparticles[25]. All of these environments provide a (100)-like, square-planar coordination.

The Pt/CeO_2 system has been proposed among the most promising candidates to meet the Department of Energy 150 °C challenge[13–15,22] (that is, achieving 90% conversion of all critical pollutants in exhaust emissions at 150 °C[26]). The catalytic activity is believed to be related to well-dispersed single atoms or low-nuclearity clusters. We have gathered the following observations from the literature on this material: (1) Pt disperses or agglomerates as a function of the environment[14,15,21,27–29]; (2) isolated Pt atoms, as prepared, have been proposed and discarded as potential catalytic centres[25,30]; (3) short-pulse treatments are needed to render the Pt catalyst active[14]; and (4) the nature of the active site remains unknown.

Ceria presents low-energy electron transport mediated by polarons[31,32]. Therefore, the properties at the metal/ceria interface might depart from the static interpretations due to electron dynamics. In the present work, we have performed extensive first-principles molecular dynamics to unravel the role of charge transfer at the interface. We identify several metal oxidation and charge states, reachable at moderate temperatures, and show how they impact the reactivity and, in particular, how they meet the requirements for low-temperature (<150 °C) oxidation.

The three lowest-energy surface facets of ceria are (111), (110) and the polar (100). Platinum adsorption was tested on all of them using the Perdew–Burke–Ernzerhof functional together with the Hubbard *U* correction, PBE+U (Supplementary Table 1). Our results agree with previous findings[21,24,25]. The (111) and (110) surfaces cannot stabilize single-atom Pt, thus metal nanoparticles form instead. Only the (100) surface can stabilize isolated Pt. Therefore, we focus on these slabs as models for local, nanostructured regions (for example, step or edge sites)[24]. The low coordination of the surface oxygen atoms on the oxygen-terminated version increases their mobility[33]. As such, (100) restructures into various coexisting patterns at elevated temperatures encountered during pretreatment. Due to this collection of oxygen distributions, Pt adsorbs on the surface surrounded by a variable number of oxygen ligands (*n*) in the first coordination sphere, denoted as Pt–*n*O (*n* = 2, 3 or 4) (Fig. 1b–d).

When the Pt atom is charged, it transfers one or more electrons to the surface, which can localize on any cerium atom. All possible electronic and coordination configurations were sampled via geometry relaxation and we retained only the stable local minima. Their adsorption energies are shown in Fig. 1a, grouped by coordination (Pt–*n*O) and oxidation state (Pt^0, Pt^+ or Pt^{2+}). To properly assign the nature of the adsorbed atom, we initially employed Bader charges, but they are a poor descriptor of oxidation states[34]. The Pt magnetic moment (Supplementary Note 1 and Supplementary Fig. 1) and

Institute of Chemical Research of Catalonia, The Barcelona Institute of Science and Technology, Tarragona, Spain. *e-mail: nlopez@iciq.es

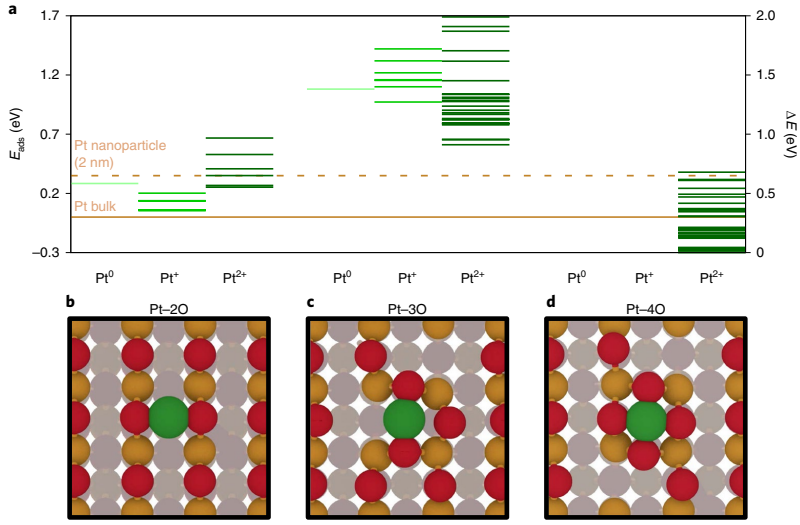

Fig. 1 | Static PBE + *U* Pt adsorption energies on CeO_2 (100). a, Adsorption energy (E_{ads}) of Pt on CeO_2 (100), for the different oxidation states (mOSs) on the surfaces, with distributions stemming from the surface oxygen mobility[23]. E_{ads} (left *y* axis) is with respect to the resting 2O surface, while ΔE (right *y* axis) is with respect to the most stable Pt–*n*O configuration. **b**–**d**, Three Pt coordination environments (Pt–*n*O, where *n* is two (**b**), three (**c**) or four (**d**) O atoms acting as ligands) appear, where O, Ce and Pt are red, yellow and green, respectively. In **a**, mOSs are assigned employing Ce magnetization as a proxy[2]. Each energy level corresponds to a local minima with a fixed Ce^{3+} localization (see Supplementary Fig. 3 for examples). Pt–4O only resides in the Pt^{2+} state. The horizontal lines present the thermodynamic stability with respect to the Pt bulk and 2-nm-diameter nanoparticle (Supplementary Fig. 4). Benchmarks with different *U* values and HSE and RPA functionals are presented in Supplementary Fig. 5 and Supplementary Tables 3–5, and discussed in the Methods.

X-ray photoelectron spectroscopy (XPS) features (Supplementary Fig. 2) also depend on the oxidation state. The latter can be mapped to the experimental XPS spectrum[30]. The spectral shift from Pt^0 to Pt^{2+} matches the experimental one[35]. Note that the peak in between is assigned there to an intermediate species, which we identify as Pt^+. However, the inhomogeneities and final state effects can make assignment difficult. Instead, for a most robust fingerprint identification, and considering that single-atom Pt is the sole possible source of electrons in these models, we can count the number of Ce^{3+}. This corresponds to the number of electrons lost by the metal atom. Ce^{3+} presents a magnetic moment of ~1 μ_B on the 4*f* orbitals (compared with 0 μ_B of Ce^{4+}), which has already been employed in the literature[2]. Therefore, this descriptor is used to trace the metal oxidation state (mOS) of the Pt atom.

The Pt–4O structure encompasses the lowest energy states of all geometric and electronic configurations. Its mOS is always confined to Pt^{2+}, with two surface Ce^{4+} reduced. This behaviour coincides with the coordination rules in coordination chemistry[36]. The multiple Ce^{3+} configurations show a very fine energy distribution, with spacings of just a few meV (Supplementary Fig. 3). Moreover, this structure is thermodynamically favourable compared with the cohesive energy of bulk Pt (horizontal orange line), thus the SAC is stable against agglomeration[37]. This explains why Pt–4O species can be generated from the regular ceria 2O trenches that incorporate volatile PtO_2 species[38], making for excellent precursors to the SAC.

Pt–2O is next in energy, with Pt^+ being the most stable mOS within the potential energy manifold associated with this geometry. Yet, all of these structures are only stable compared with the cohesive energy of a 2-nm-diameter Pt nanoparticle (Supplementary Fig. 4). This means that isolated atoms are stable against the initial states of agglomeration, and even dimerization is unfavoured (Supplementary Table 2). Comparing all three mOSs on Pt–2O, the (near-)degeneracy of the electron distributions overlap irrespective of the functional employed (see Methods, Supplementary Fig. 5 and Supplementary Tables 3–5). Pt–3O exhibits even larger overlap, but the coordination as a whole is unstable with respect to agglomeration.

The reason different electronic configurations coexist can be traced back to the interplay between the ionization potentials of the isolated gas-phase Pt atoms, surface reduction and distortion, and changes in electrostatic interactions. This is shown in the Born–Haber cycle (Supplementary Note 2 and Supplementary Fig. 6), which starts with an isolated Pt atom and the pristine CeO_2 (100) surface. When Pt adsorbs as Pt^0 on the regular 2O surface, the resulting covalent contribution is −1.93 eV, as calculated by the formation of two Pt–O bonds in $Pt(H_2O)_2$. In parallel, the gas-phase ionization of a Pt atom to Pt^+ requires 8.96 eV[39]. Assuming that the covalent contribution persists throughout the oxidation steps, the energy compensation needs to come either from the surface reduction[40] and/or the changes in the electrostatic contributions. The Coulomb interaction[41] between the Pt–O and Ce–O pairs stands out with a value of 9.73 eV. This term is calculated from the charges and the first neighbour distances of the Pt^0–2O and Pt^+–2O (Supplementary Table 6). Adding up these contributions, the step from Pt^0 to Pt^+ on Pt–2O is slightly endothermic by 0.3 eV. Indeed, even this simple thermodynamic cycle highlights that the change in mOS is compensated for by the electrostatic contributions.

To verify whether the charge transfer processes presented above are kinetically attainable, first-principles Born–Oppenheimer molecular dynamics (BOMD) were performed on all three Pt–*n*O structures, following an approach similar to that described in ref. [42] (Fig. 2, Supplementary Fig. 7 and Supplementary Videos 1–3). BOMD simulations are computationally very demanding; thus, the

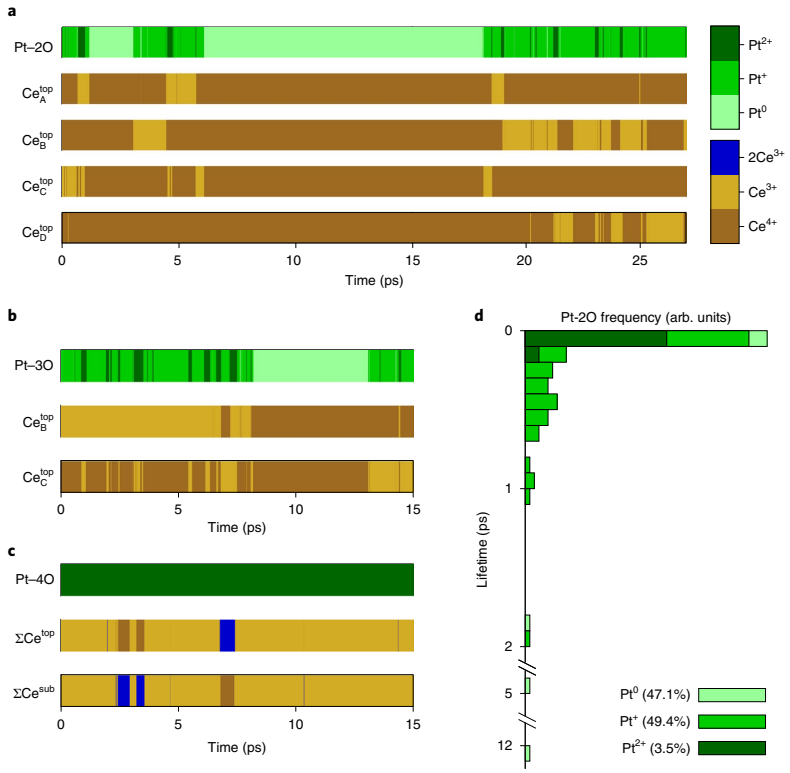

Fig. 2 | BOMD simulations of the Pt–*n*O systems. a–c, Time evolution at 600 K of the atom-resolved oxidation states of the Pt and surface Ce atoms, for Pt-2O (**a**), Pt-3O (**b**) and Pt-4O (**c**). The assignment of Ce^{3+} is discussed in Supplementary Note 3. In **c**, the oxidation states of Ce are summed together for the top layer ($\sum Ce^{top}$) and subsurface layer $\sum Ce^{sub}$, respectively. **d**, Lifetime distribution of the various mOSs for the Pt-2O structures. The Pt-3O trajectory has been included after conversion to Pt-2O (occurring at ~486 K). Trajectories are shown in Supplementary Videos 1–3.

Pt–*n*O structures were simulated in (2×2) supercells. Before that, it was assessed that the patterns in Fig. 1 are still properly represented in the smaller cell (Supplementary Fig. 8). Vice versa, a short heating simulation of Pt–2O in the (3×3) slabs also confirmed the polaron-induced charge transfer for larger supercells (Supplementary Video 4).

Figure 2a shows the oxidation state per atom, gathered for the Pt–2O system over a 27-ps time period after heating up to 600 K. The simulation exhibits an alternating number of Ce^{3+} centres, confirming the dynamic nature of the mOS directly. A visualization of the trajectory is shown in Supplementary Video 1, where the smooth nature of the electron transfer events can be observed. An individual transfer is captured in Supplementary Fig. 7, with the electron in Ce_C^{top} moving to Ce_A^{top} by temporarily crossing over Pt. In the case of Pt–3O (Fig. 2b), the coordination shell starts opening at ~300 K during the heating process. On opening, the oxygen atoms adopt the regular row pattern of the Pt–2O configuration. This corroborates that Pt–3O is a metastable state, as found in Fig. 1a. Remarkably, Pt–3O does not reconstruct to the global minimum, namely Pt–4O. Finally, the Pt–4O system (Fig. 2c) remains stable with respect to its coordination, and maintains the mOS in accordance with Fig. 1a. Since the extra surface electrons for Pt–4O reside in the slab throughout the full simulation, they have the opportunity to exchange with the subsurface centres reducing the Ce^{3+}–Ce^{3+}repulsion.

Considering that Pt–3O transforms into the Pt–2O coordination, their data can be analysed together to illustrate the persistence of different oxidation and charge states. The frequency histogram in Fig. 2d presents their lifetimes (that is, the time interval that Pt resides uninterruptedly in a single mOS (Supplementary Note 3)). Even though Pt^0 and Pt^+ take up almost equal portions of time (47 and 49%, respectively), Pt^0 can vastly outlive Pt^+, with outliers of up to 5 and 12 ps. Therefore Pt^+—the most stable state at 0 K—is no longer the longest-living species at 600 K.

To understand the origin of the Pt mOS dynamics on the CeO_2 (100) surface, the density of states (DOS) of the full Pt–2O system is decomposed into the metal and oxide units at the geometries of the different lowest-energy mOSs (Fig. 3). The DOS diagram features the filled O(2*p*) valence band (red) and the empty Ce(4*f*) levels (orange) placed in the band gap. Figure 3a shows the 2O-terminated CeO_2 (100), while Fig. 3f corresponds to the isolated, gas-phase Pt atom in a d^9s^1 electronic configuration in a structure where Pt is far away from the surface. All systems are aligned according to the 2*s* band centre of the central oxygen atoms in the slab. As in the Born–Haber cycle, the isolated Pt atom is first allowed to interact with two water molecules, forming Pt–$(H_2O)_2$ in Fig. 3e. The Pt levels shift higher up to the Fermi level (green line) due to the covalent (antibonding) interaction. In the simulations for the Pt–2O system, we identified that the presence of Pt distorts the CeO_2 surface to

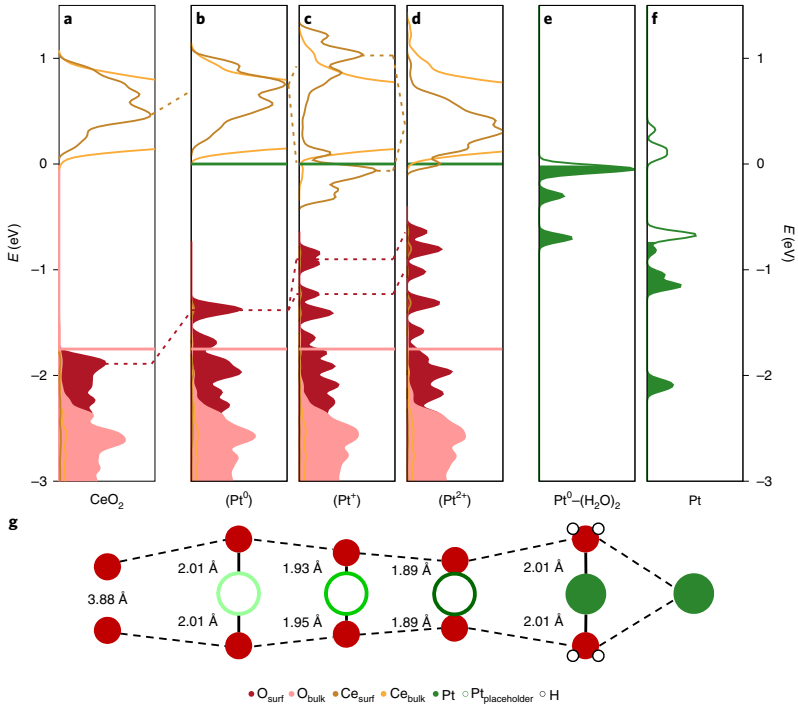

Fig. 3 | DOS decomposition for the Pt–2O systems with different oxidation states. a, DOS of the pristine CeO_2 surface, showing the filled valence band (red) and empty Ce(4*f*) bands (orange). **b**–**d**, DOSs of 2O systems with oxide geometries of Pt^0–2O (**b**), Pt^+–2O (**c**) and Pt^{2+}–2O (**d**). The lowering of the Ce(4*f*) levels allows electron injection from the higher Pt-filled states, as indicated by the Fermi level in **e** (green line). **e**,**f**, Gas-phase Pt levels when covalently interacting with water (**e**) or when isolated (**f**). The gas-phase systems are separated by more than 7 Å from any side of the slabs. All systems are aligned according to the 2*s* band centre of the central oxygen layer in the slab. **g**, Local coordination of the unrelaxed oxygen ligands around the Pt vacancy. Each coordination is aligned with its respective DOS panels. Tests with different functionals show no significant changes (see Supplementary Fig. 9).

different extents depending on the mOS. Therefore, the electronic structure of the oxide in the geometry corresponding to the lowest energy configuration of each Pt-2O mOS occupies the panels shown in Fig. 3b–d. Surface distortions push the ligand O(2*p*) levels up to higher energies. Concomitantly, the cation cavity increases, the repulsion with their O neighbours decreases, and the Ce(4*f*) states drop below the Fermi level of Pt–$(H_2O)_2$. This establishes the driving force for electron transfer from Pt to the oxide. Our results are robust compared with other functionals (Supplementary Fig. 9 and Supplementary Note 4). Therefore, electron transfer at the Pt–*n*O interface can be understood as a phonon-assisted metal-support interaction that can appear when: (1) the metal levels lie either in the band gap or closely above the Fermi level of the reducible semiconductor; (2) the surface is flexible enough to allow surface distortions; and (3) empty cation states appear in the band gap within an energy range accessible as a consequence of the geometric distortion. To assess the scope of phonon-assisted metal-support interaction, we performed a scan (similar to Fig. 1) for Ni on the same CeO_2 surface or for the same metal on a different oxide rutile TiO_2 (110). Supplementary Fig. 10 suggests the coexistence of multiple oxidation states for these systems as well.

The variable coordination and oxidation states affect the reactivity (Fig. 4). Pt^{2+}–4O is the most robust state, in agreement with the ionic nature identified in experiments[21,28], and breaking this coordination by removing an oxygen is very endothermic (~1.84 eV). Thus, Pt^{2+}–4O is the resting state of the material under most conditions (in particular, under the oxidative preparation route from the metal nanoparticles that results in PtO_2 volatilization and deposition). Under mild, reducing conditions and medium to high temperatures, like the pulses employed in catalytic activation, both H_2 and CO can open up Pt–4O (Fig. 4a (cycle 1) and Supplementary Table 7). In Fig. 4a, molecular hydrogen has to overcome a relatively large activation barrier[35] (1.35 eV) to split over Pt and O (−0.67 eV below reactants). Next, the hydrogen and hydroxyl group recombine to form a water molecule, which readily leaves the surface. H_2 dissociates over the regular O-termination pristine CeO_2 via a transition state at 0.82 eV, with the final state lying −3.00 eV below gas-phase reactants (see ref. [41]). Alternatively, if Pt–4O is reduced by CO, the molecule adsorbs onto a lattice oxygen of this unit and evolves towards CO_2. The highest activation barrier in this path is ~1 eV and the final state is −1.23 eV below reactants. Therefore, the relative inertness of Pt SACs against H_2, and the low CO uptake in the temperature programmed desorption experiments, are related to the low pressures employed in ultra-high vacuum experiments[21,30]. The activation process, as described here, is reversible in an oxidizing environment. A deactivation switch is what sets this system apart from other catalysts, such as nanoclusters, which can be prepared using oxidizing

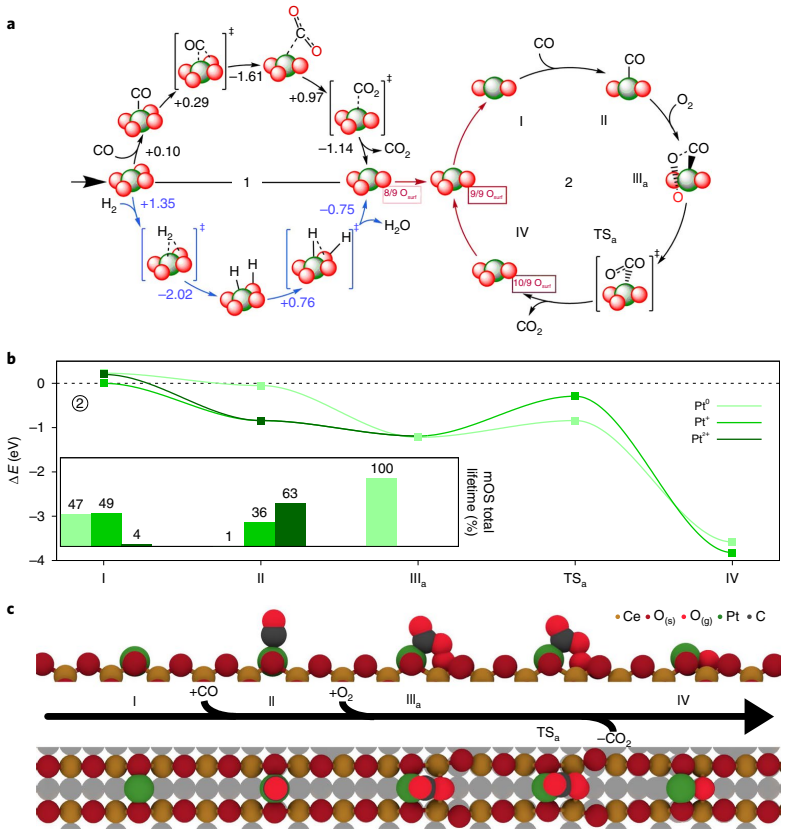

Fig. 4 | CO oxidation on Pt-*n*O structures. a, Reaction energy cycles (in eV) for surface reduction (cycle 1; black by CO; blue by H_2) and CO oxidation (cycle 2), with red spheres denoting the Pt coordination. The dagger represents the transition states. Oxygen exchange/diffusion processes are marked in red, and the boxes below the Pt–3O structures denote the ratio of surface oxygen atoms in the (3×3) supercell. The numerals in cycle 2 refer to the reaction path of CO oxidation on Pt–2O in **b** and **c**. **b**, Reaction profile of cycle 2 for each oxidation state of Pt. The mOS lifetimes are presented in the inset, as retrieved from BOMD 10.5-ps trajectories of the reaction intermediates. In step II, Pt^+ and Pt^{2+} collapse to the same energy level. The inset supports this by showing that both mOSs coexist and are dynamically connected. **c**, Side (top) and top (bottom) views of the reaction steps. Dark red denotes oxygen from the bulk phase (s) and bright red denotes oxygen from the gas phase (g).

airflow[43]. After the CO or H_2 treatment, the Pt–4O coordination is reduced to Pt–3O.

The Pt–3O system is labile with respect to oxygen diffusion, as shown by the molecular dynamics simulations, where it converts into Pt–2O in <0.5 ps at 300 K. Therefore, our results show that reducing atmospheres convert the resting Pt–4O state into Pt–2O species. This explains why recent experiments need short, reducing pulses at 250 °C to generate the active platinum species[14] that we can now identify as Pt–2O. The barriers of ~1 eV explain why temperatures of at least 250 °C are required during activation, while higher exposure times to reducing atmospheres induce Pt agglomeration. However, the transient nature of Pt–2O makes it difficult to characterize it experimentally, even under operando conditions. Note that even single atoms have only recently been clearly identified in microscopy[10].

The system then enters cycle 2 of Fig. 4a,b. Complementary data for the elementary steps, alternative routes and structures can be found in Supplementary Fig. 11 and Supplementary Table 8. On Pt–2O state I in Fig. 4b, the three mOSs coexist and have been investigated separately for CO reduction. Overall, CO adsorption is relatively weak, but the gas-phase CO pressures are large under low-temperature (<150 °C) conditions and ionic Pt has the largest adsorption energies. Indeed, charge dependence for CO adsorption on SACs was also reported for Pt_1/TiO_2 anatase[44]. The CO vibrational shift for this state is around 60 cm^{-1}, similar to the experimental value reported (75 cm^{-1})[21] (see Supplementary Table 9). The BOMD for this intermediate shows larger lifetimes for the ionic Pt configurations (with a 1:2 ratio between Pt^+ and Pt^{2+}). Then, O_2 can adsorb, forming a percarbonate species with an O–O bond distance of 1.452 Å. In the BOMD, this state of the SAC corresponds to no electron transfer to the Ce^{4+} centres. However, in this particular coordination, the formal oxidation state of the metal is Pt^{2+}, regardless of its previous state. Hence, the O_2 adsorption energy depends on the electronic state of configuration (II), and can be as large as −1.20 eV. From this configuration on, CO_2 formation easily pushes the system to the low-lying Pt^0 state. The barrier for this step is about 0.56 eV. To evolve to Pt^+, the energy required is much larger (namely, 1.11 eV). Therefore, during the CO oxidation cycle in the

Pt–2O structure, the electronic structure of the material needs to be dynamic to allow both the adsorption of CO (occurring at ionic states) and oxidation (occurring at the neutral state) elementary steps in the mechanism. Separate BOMD runs were also performed on the reaction intermediates, showing that some of them exhibit dynamic electron transfer (see insets in Fig. 4b and Supplementary Fig. 11b). We have added the weights (percentage of lifetimes) of the different mOSs in the band below each structure, indicating that for some intermediates (CO) dynamic electron transfer occurs, while with others (percarbonate) a single electronic configuration is more likely.

Regarding the stability of Pt–2O (and Pt–4O), Pt diffusion is impeded by 2.9 eV. Dimerization on the trenches is also endothermic, regardless of mOS (see Supplementary Note 5 and Supplementary Table 2). This reinforces the role of isolated Pt atoms in CO oxidation. If CO is adsorbed, the barriers slightly lower, but dimerization remains difficult in most cases. Volatilization of Pt as molecular PtO_2 is also endothermic (by ~1 eV); thus, volatilization is negligible at the reaction temperatures employed in low-temperature CO oxidation, and only taking place in oxidizing conditions that lock Pt in the Pt–4O coordination.

Therefore, the Pt/CeO_2 behaviour can be summarized as follows: Pt^0–2O is the longest-lasting state in the molecular dynamics simulations, but its ability to trap CO is low. In turn, the short lifetime of the Pt^+ species will impact the reactivity of the SAC. Addressing the microkinetics of the Pt/CeO_2 system thus requires the use of accessible ensemble concepts[45]. The overall CO oxidation reaction barrier is ~0.56 eV; this energy is compatible with the high activity observed at temperatures lower than the 150 °C requirement of the exhaust emission challenge.

In summary, the common assignment of a fixed oxidation state in single-atom catalysts is exceedingly simple. Depending on the metal/oxide combination, a dynamic charge transfer between the metal and the oxide appears instead. The electron transfer is assisted by phonons and stems from the level alignment between the metal and the defect states in the oxide. As a result, several oxidation and charge states might coexist, enriching the chemistry of single atoms on oxide surfaces. We demonstrated how the reactivity is closely related to the dynamic behaviour. Our results explain the latest experimental observations that indicate the need for short pulses to redisperse Pt nanoparticles in order to be activated as single atoms to perform low-temperature oxidations (in the 150 °C challenge). We identify how the metal/oxide dynamic charge transfer is crucial to understanding the nature of the active site and the mechanism in these SACs. This newly gained degree of freedom, introduced by the presence of the reducible support, might break linear scaling relationships and thus open the path to more active and selective catalysts.

Online content

Any methods, additional references, Nature Research reporting summaries, source data, statements of code and data availability and associated accession codes are available at https://doi.org/10.1038/s41563-019-0444-y.

Received: 22 July 2018; Accepted: 24 June 2019;
Published online: 05 August 2019

References

1. Stair, P. C. Metal-oxide interfaces: where the action is. *Nat. Chem.* **3**, 345–346 (2011).
2. Lykhach, Y. et al. Counting electrons on supported nanoparticles. *Nat. Mater.* **15**, 284–288 (2015).
3. Schneider, W.-D., Heyde, M. & Freund, H.-J. Charge control in model catalysis: the decisive role of the oxide–nanoparticle interface. *Chemistry* **24**, 2317–2327 (2018).
4. Kumar, G. et al. Evaluating differences in the active-site electronics of supported Au nanoparticle catalysts using hammett and DFT studies. *Nat. Chem.* **10**, 268–274 (2018).
5. Campbell, C. T. Catalyst–support interactions: electronic perturbations. *Nat. Chem.* **4**, 597–598 (2012).
6. Tauster, S. J., Fung, S. C. & Garten, R. L. Strong metal–support interactions. Group 8 noble metals supported on titanium dioxide. *J. Am. Chem. Soc.* **100**, 170–175 (1978).
7. Rodríguez, J. A. et al. Activity of CeO_x and TiO_x nanoparticles grown on Au(111) in the water–gas shift reaction. *Science* **318**, 1757–1760 (2007).
8. Divins, N. J., Angurell, I., Escudero, C., Perez-Dieste, V. & Llorca, J. Influence of the support on surface rearrangements of bimetallic nanoparticles in real catalysts. *Science* **346**, 620–623 (2014).
9. Fu, Q., Saltsburg, H. & Flytzani-Stephanopoulos, M. Active nonmetallic Au and Pt species on ceria-based water–gas shift catalysts. *Science* **301**, 935–938 (2003).
10. Qiao, B. et al. Single-atom catalysis of CO oxidation using Pt_1/FeO_x. *Nat. Chem.* **3**, 634–641 (2011).
11. Cargnello, M. et al. Control of metal nanocrystal size reveals metal–support interface role for ceria catalysts. *Science* **341**, 771–773 (2013).
12. Therrien, A. J. et al. An atomic-scale view of single-site Pt catalysis for low-temperature CO oxidation. *Nat. Catal.* **1**, 192–198 (2018).
13. Nagai, Y. et al. In situ redispersion of platinum autoexhaust catalysts: an on-line approach to increasing catalyst lifetimes? *Angew. Chem. Int. Ed.* **47**, 9303–9306 (2008).
14. Gänzler, A. M. et al. Tuning the structure of platinum particles on ceria in situ for enhancing the catalytic performance of exhaust gas catalysts. *Angew. Chem. Int. Ed.* **56**, 13078–13082 (2017).
15. Nie, L. et al. Activation of surface lattice oxygen in single-atom Pt/CeO_2 for low-temperature CO oxidation. *Science* **358**, 1419–1423 (2017).
16. Lin, J. et al. Remarkable performance of Ir_1/FeO_x single-atom catalyst in water gas shift reaction. *J. Am. Chem. Soc.* **135**, 15314–15317 (2013).
17. Liu, P. et al. Photochemical route for synthesizing atomically dispersed palladium catalysts. *Science* **352**, 797–800 (2016).
18. Wei, H. et al. FeO_x-supported platinum single-atom and pseudo-single-atom catalysts for chemoselective hydrogenation of functionalized nitroarenes. *Nat. Commun.* **5**, 5634 (2014).
19. McCabe, R. W. & Trovarelli, A. Forty years of catalysis by ceria: a success story. *Appl. Catal. B Environ.* **197**, 1 (2016).
20. Trovarelli, A. & Llorca, J. Ceria catalysts at nanoscale: how do crystal shapes shape catalysis? *ACS Catal.* **7**, 4716–4735 (2017).
21. Jones, J. et al. Thermally stable single-atom platinum-on-ceria catalysts via atom trapping. *Science* **353**, 150–154 (2016).
22. Kunwar, D. et al. Stabilizing high metal loadings of thermally stable platinum single atoms on an industrial catalyst support. *ACS Catal.* **9**, 3978–3990 (2019).
23. Zhou, G., Li, P., Ma, Q., Tian, Z. & Liu, Y. Density functional theory plus Hubbard U study of the segregation of Pt to the CeO_{2-x} grain boundary. *Nano Lett.* **18**, 1668–1677 (2018).
24. Dvořák, F. et al. Creating single-atom Pt-ceria catalysts by surface step decoration. *Nat. Commun.* **7**, 10801–10808 (2016).
25. Bruix, A. et al. Maximum noble-metal efficiency in catalytic materials: atomically dispersed surface platinum. *Angew. Chem. Int. Ed.* **53**, 10525–10530 (2014).
26. Zammit, M. et al. *Future Sutomotive Aftertreatment Solutions: the 150 °C Challenge Workshop Report* Technical Report (Pacific Northwest National Laboratory, 2013).
27. Farmer, J. A. & Campbell, C. T. Ceria maintains smaller metal catalyst particles by strong metal-support bonding. *Science* **329**, 933–936 (2010).
28. Wu, T. et al. Investigation of the redispersion of Pt nanoparticles on polyhedral ceria nanoparticles. *J. Phys. Chem. Lett.* **5**, 2479–2483 (2014).
29. Pereira Hernandez, X. I. et al. Tuning Pt–CeO_2 interactions by high-temperature vapor-phase synthesis for improved reducibility of lattice oxygen. *Nat. Commun.* **10**, 1358 (2019).
30. Neitzel, A. et al. Atomically dispersed Pd, Ni, and Pt species in ceria-based catalysts: principal differences in stability and reactivity. *J. Phys. Chem. C* **120**, 9852–9862 (2016).
31. Plata, J., Márquez, A. M. & Sanz, J. F. Electron mobility via polaron hopping in bulk ceria: a first-principles study. *J. Phys. Chem. C* **117**, 14502–14509 (2013).
32. Reticcioli, M. et al. Polaron-driven surface reconstructions. *Phys. Rev. X* **7**, 031053 (2017).
33. Capdevila-Cortada, M. & López, N. Entropic contributions enhance polarity compensation for CeO_2 (100) surfaces. *Nat. Mater.* **16**, 328–334 (2017).
34. Walsh, A., Sokol, A. A., Buckeridge, J., Scanlon, D. O. & Catlow, C. R. A. Oxidation states and ionicity. *Nat. Mater.* **17**, 958–964 (2018).
35. Lykhach, Y. et al. Reactivity of atomically dispersed Pt^{2+} species towards H_2: model Pt–CeO_2 fuel cell catalyst. *Phys. Chem. Chem. Phys.* **18**, 7672–7679 (2016).
36. Greenwood, N. N. & Earnshaw, A. Chemistry of the Elements. 2nd edn, (Elsevier: 1997).

37. Ouyang, R., Liu, J.-X. & Li, W.-X. Atomistic theory of Ostwald ripening and disintegration of supported metal particles under reaction conditions. *J. Am. Chem. Soc.* **135**, 1760–1771 (2013).
38. Datye, A. K. & Wang, Y. Atom trapping: a novel approach to generate thermally stable and regenerable single-atom catalysts. *Natl Sci. Rev.* **5**, 630–632 (2018).
39. Kramida, A., Ralchenko, Y., Reader, J. & Team, N. A. *Atomic Spectra Database* (version 5.5.6) (National Institute of Standards and Technology, 2018); https://physics.nist.gov/cgi-bin/ASD/ie.pl
40. Capdevila-Cortada, M., García-Melchor, M. & López, N. Unraveling the structure sensitivity in methanol conversion on CeO_2: a DFT + *U* study. *J. Catal.* **327**, 58–64 (2015).
41. Andersin, J., Nevalaita, J., Honkala, K. & Häkkinen, H. The redox chemistry of gold with high-valence doped calcium oxide. *Angew. Chem. Int. Ed.* **52**, 1424–1427 (2013).
42. Kowalski, P. M., Camellone, M. F., Nair, N. N., Meyer, B. & Marx, D. Charge localization dynamics induced by oxygen vacancies on the TiO_2 (110) surface. *Phys. Rev. Lett.* **105**, 146405 (2010).
43. Pilger, F. et al. Size control of Pt clusters on CeO_2 nanoparticles via an incorporation–segregation mechanism and study of segregation kinetics. *ACS Catal.* **6**, 3688–3699 (2016).
44. DeRita, L. et al. Structural evolution of atomically dispersed Pt catalysts dictates reactivity. *Nat. Mater.* **18**, 746–751 (2019).
45. Ha, M.-A., Baxter, E. T., Cass, A. C., Anderson, S. L. & Alexandrova, A. N. Boron switch for selectivity of catalytic dehydrogenation on size-selected Pt clusters on Al_2O_3. *J. Am. Chem. Soc.* **139**, 11568–11575 (2017).

Acknowledgements
This research has been supported by the Ministerio de Economía y Competitividad (CTQ2015-68770-R). The authors acknowledge BSC-RES and BIFI for providing generous computational resources. We also thank A. Bruix for critically reading the manuscript, and T. Schäfer for help with the random phase approximation (RPA) methodology.

Author contributions
N.D. performed the calculations. N.D., M.C.-C. and N.L. analysed the data and prepared the manuscript.

Competing interests
The authors declare no competing interests.

Additional information
Supplementary information is available for this paper at https://doi.org/10.1038/s41563-019-0444-y.

Reprints and permissions information is available at www.nature.com/reprints.

Correspondence and requests for materials should be addressed to N.L.

Publisher's note: Springer Nature remains neutral with regard to jurisdictional claims in published maps and institutional affiliations.

Methods

Slab preparation. Bulk CeO_2 has a fluorite crystal structure with an experimental lattice parameter of 5.497 Å. When optimized at the PBE+U level, the bulk yields a theoretical lattice parameter of 5.410 Å. Slabs were cleaved at the (111), (110) and (100) Miller indices. For the (100) surface, half of the topmost oxygens were moved from the surface top layer to the bottom layer in order to reduce the polarity and render the system stoichiometric. Starting from this trench-like structure, two other low-energy reconstructions were investigated[33]. Each of these reconstructions allows for a different coordination shell around single-atom Pt. To support these reconstructions, the slabs have to span at the least a (2×2) supercell. In this work, they were extended to (3×3) supercells ((2×3) in the case of (110)) to sample lower Pt loadings. Along the vertical axis, the slabs are nine atom layers thick, with the five top layers allowed to relax, and a 15 Å vacuum.

Density functional theory computational methods. All calculations were performed at density functional theory+U level, as implemented by the Vienna Ab initio Simulation Package (VASP; version 5.4.4)[46–48]. The PBE functional[49] was used together with a Hubbard U term to enforce charge localization at the atom centres following the approach of Dudarev et al.[50]. For the cerium 4*f* orbitals, U=4.5 eV was used, based on the work in ref. [51]. Projector-augmented waves were employed to describe the core electrons, while the valence electrons were expanded in a plane-wave basis set with a cut-off energy of 500 eV. Unless stated otherwise, a gamma-centred k-mesh of (3×3×1) was used for (2×2) and (3×3) supercells alike. All of the systems considered are neutral. Spin polarization was accounted for where necessary. We assessed the influence of surface reduction on the mOS by either adsorbing a hydrogen atom as a surface hydroxyl group (one additional electron stored in the oxide) or generating a surface oxygen vacancy (two) (see Supplementary Note 6 and Supplementary Fig. 12). The latter would be akin to the surface state directly after the activation step. In all cases, different oxidation states for Pt exist and their variability depends on the nature of the surface modification. The electronic entropy contributions of the newly created Ce^{3+} centres never exceed 1 meV K^{-1} at 600 K when using Fig. 1 in ref. [52]. To account for the role of dispersion in the binding energy of CO, the van der Waals contributions were modelled using the D3 model. When applied to the adsorption of CO, it was found to contribute less than 0.1 eV and was hence disregarded in the remainder of this work (Supplementary Table 9). The 2-nm nanoparticle was built as a cuboctahedron with a final stoichiometry of Pt_{935} and was calculated in a cubic box with 35-Å edges (Supplementary Fig. 4).

Benchmarking. We verified the robustness of our model with respect to different functionals, examining three routes: (1) different Hubbard parameters (U=3.5, 4.5 and 5.5 eV; Supplementary Fig. 5); (2) two hybrid functionals (namely, Heyd–Scuseria–Ernzerhof (HSE-06) and HSE03-13; Supplementary Tables 3 and 4); and (3) the random phase approximation for Pt–2O, starting from PBE+U (U=4.5 eV) at the gamma point for the (3×3×1) supercell (Supplementary Table 5). Overall, multiple coexisting mOSs are recovered using different functionals, although the relative order of the Ce^{3+} distributions can change between functionals. In contrast with HSE, random phase approximation (RPA) favours a strongly ionic character (in this case, Pt^{2+}; ref. [53]), although the other mOSs would still be accessible at elevated temperatures. The hybrid DOSs are presented in Supplementary Fig. 9.

Modelling XPS data. The core-level binding energies were computed for the Pt(4*f*) states, using the Janak–Slater approach with excitation to the vacuum level (ICORELEVEL=2 and CLZ=0.5). To prevent spurious electron transfer, the excited electron was removed from the system. Those core-level binding energies represent the spectral peaks of each electronic configuration, and were averaged over the coordination and oxidation states to obtain the peaks in Supplementary Fig. 2.

Ab initio molecular dynamics simulations. Molecular dynamics simulations were performed within the canonical NVT ensemble (that is, constant number of particles, the system's volume and the temperature) in a smaller (2×2) supercell with a k-mesh of (3×3×1). The trajectories can be found in Supplementary Videos 1–3. The slabs were set up by first heating them from 0–300 K in 0.5 ps, then equilibrating for 1.5 ps, and subsequently further heating from 300–600 K in 0.5 ps. The time step remained 1 fs throughout the set-up. Finally, the data were collected at 600 K with a 3-fs time step. In the case of the (3×3) slab in Supplementary Video 4, the system was heated up from 0–600 K in one session of 0.5 ps. The k-mesh was reduced to a gamma point. In all cases, the electronic structures were well converged to 10^{-7} eV. The temperature in the stable regions was regulated by the Nosé–Hoover thermostat[54]. During the runs, the magnetizations were found to change gradually and continuously, ensuring that the transitions were not the result of any artefacts or poor convergence (Supplementary Figs. 7 and 13). The BOMD runs for the intermediates in CO oxidation were shortened to 10.5 ps, but still managed to show that the dynamics depends on the particular intermediate. The lifetime histogram parameters and the magnetization cut-off were calibrated with a sensitivity test in Supplementary Note 3 and Supplementary Fig. 14.

Data availability

The datasets generated during the current study are available in the ioChem-BD database[55] (https://doi.org/10.19061/iochem-bd-1-78).

References

46. Kresse, G. & Furthmüller, J. Efficiency of ab-initio total energy calculations for metals and semiconductors using a plane-wave basis set. *Comput. Mater. Sci.* **6**, 15–50 (1996).
47. Blöchl, P. E. Projector augmented-wave method. *Phys. Rev. B* **50**, 17953–17979 (1994).
48. Kresse, G. & Joubert, D. From ultrasoft pseudopotentials to the projector augmented-wave method. *Phys. Rev. B* **59**, 1758–1775 (1999).
49. Perdew, J. P., Burke, K. & Ernzerhof, M. Generalized gradient approximation made simple. *Phys. Rev. Lett.* **77**, 3865–3868 (1996).
50. Dudarev, S. L., Botton, G. A., Savrasov, S. Y., Humphreys, C. J. & Sutton, A. P. Electron-energy-loss spectra and the structural stability of nickel oxide: an LSDA+U study. *Phys. Rev. B* **57**, 1505–1509 (1998).
51. Fabris, S., de Gironcoli, S., Baroni, S., Vicario, G. & Balducci, G. Taming multiple valency with density functionals: a case study of defective ceria. *Phys. Rev. B* **71**, 041102 (2005).
52. Naghavi, S. S. et al. Giant onsite electronic entropy enhances the performance of ceria for water splitting. *Nat. Commun.* **8**, 285–291 (2017).
53. Penschke, C. & Paier, J. Reduction and oxidation of Au adatoms on the CeO_2(111) surface—DFT+U versus hybrid functionals. *Phys. Chem. Chem. Phys.* **19**, 12546–12558 (2017).
54. Hoover, W. G. Canonical dynamics: equilibrium phase–space distributions. *Phys. Rev. A* **31**, 1695–1697 (1985).
55. Álvarez-Moreno, M. et al. Managing the computational chemistry big data problem: the ioChem-BD platform. *J. Chem. Inf. Model.* **55**, 95–103 (2015).

nature materials

SUPPLEMENTARY INFORMATION
https://doi.org/10.1038/s41563-019-0444-y

In the format provided by the authors and unedited.

Dynamic charge and oxidation state of Pt/CeO_2 single-atom catalysts

Nathan Daelman, Marçal Capdevila-Cortada and Núria López*

Institute of Chemical Research of Catalonia, The Barcelona Institute of Science and Technology, Tarragona, Spain. *e-mail: nlopez@iciq.es

Supplementary Information: Dynamic charge and oxidation state of Pt/CeO_2 single-atom catalysts

Nathan Daelman[1], Marçal Capdevila-Cortada[1] & Núria López[1]

[1]*Institute of Chemical Research of Catalonia (ICIQ), The Barcelona Institute of Science and Technology, Av. Països Catalans 16, 43007 Tarragona, Spain.*

Contents

Supplementary Note 1

Throughout this work, the adsorbed metal oxidation state (mOS) has been consistently categorized by counting the number of reduced Ce^{3+}. Since not all Ce^{3+} combinations form stable local minima, only well-converged results were accounted for. Hence the number of Ce^{3+} centres is coordination-dependent. These are distinguishable by means of their magnetic moment of ~ 1 μ_B. The Pt magnetic moment on the other hand, correlates with mOS as well. The mOS is projected onto a continuous variable, namely the sum over the absolute Ce^{3+} magnetic momenta ($\sum|\mu_{Ce^{3+}}|$). Supplementary Fig. 1 then compares it to Pt ($|\mu_{Pt}|$). The details of the correlation appear coordination-sensitive. In Pt-2O, the relationship scales linearly along a (2:1) line. In Pt-4O only Pt^{2+} exists and a Pt magnetization signal is consistently absent. This indicates a singlet state and suggests a break in chemical behaviour, most noticeably in reactions with other open-shell systems. Pt-3O also relates better to the discrete view of the mOS, with Ce^{3+} centred around 0, 1 and 2 μ_B. Pt^{+}-3O then bears a magnetic moment of around 0.4 μ_B, similar to the 0.5 μ_B of Pt^{+}-2O. The signal vanishes again however at Pt^{2+}-3O. The system thus behaves as a mixture of Pt-2O and Pt-4O, depending on the mOS.

Supplementary Note 2

The thermodynamics of multiple mOS are modelled with a Born-Haber scheme in Supplementary Fig. 6. The model variables are tabulated in Supplementary Table 6. The interactions at play include: (i) the separated redox terms for the ion and the surface; (ii) the energy contributions

to distort the surface from the pristine termination to the final structure for the different OS Pt configurations ($E_{Distorsion}$); (iii) the covalent Pt-O bond ($E_{Covalent\ Pt\text{-}O}$), which was calculated as the energy gained from the Pt-$(H_2O)_2$ formation out of water and an isolated Pt atom; (iv) the differential Coulomb interaction ($E_{Coulomb}$) calculated for the first (Pt-O) and second coordination spheres (reduced Ce-O pairs):

$$E_{Coulomb} = E^{Pt\text{-}O}_{Coulomb} + \Delta E^{Ce\text{-}O}_{Coulomb} = k \sum_{O_i \in O^{top}_{ligand}} \left[\frac{Q^{Pt}_{Bader} \times Q^{O_i}_{Bader}}{r_{Pt\text{-}O_i}} + Q^{O_i}_{Bader} \times \left(\frac{Q^{Ce^{3+}}_{Bader}}{r_{Ce^{3+}-O_i}} - \frac{Q^{Ce^{4+}}_{Bader}}{r_{Ce^{4+}-O_i}} \right) \right]$$

where $k = 14.40$ eV Å$/Q^2_{e^-}$ stands for the Coulomb constant; $E^{Pt\text{-}O}_{Coulomb}$ and $\Delta E^{Ce\text{-}O}_{Coulomb}$ for the 1st and 2nd coordination sphere respectively; O^{top}_{ligand} for the bonding oxygen atoms of the 1st sphere; Q^{Pt}_{Bader}, $Q^{O_i}_{Bader}$, $Q^{Ce^{3+}}_{Bader}$ and $Q^{Ce^{4+}}_{Bader}$ for the Bader charges of the Pt atom and the coordinating O, Ce^{3+} and Ce^{4+}; and , $r_{Ce^{3+}-O_i}$ and $r_{Ce^{4+}-O_i}$ for the inter-atomic distances between Pt and O, O and Ce^{3+}, and O with Ce^{4+}.

The leading endothermic terms in the cycles are both Pt ionization potentials (i) and are balanced by the large exothermic electrostatic contributions (iv). From these results, the energy difference between Pt^0 and Pt^+ is close to 0.3 eV, which for the simplicity of the concepts involved qualitatively allows both coordinations to coexist. The deviations on Pt^{2+} to the DFT values are larger. Still, the relevance of the Coulombic terms remains clear.

Supplementary Note 3

Aside from establishing the dynamical aspect in the mOS, the MD simulations provide other useful information regarding the lifetime of these states. In the case of Pt-4O, the system has a fixed mOS

(within the conditions tested) and the coordination should first be broken before it could fluctuate. Pt-3O on the other hand converts readily into Pt-2O. Therefore, the concept of oxidation state stability does not apply here. Lastly Pt-2O has been demonstrated to have time-dependent mOS, for which a total of 42 ps have been simulated. As a measure of stability we introduce *lifetime*, defined as the sum of successive time intervals for which Pt resides in a single mOS. Here, the sum of magnetic moments over Ce ($\sum |\mu_{\text{Ce}}|$) is used as a proxy for the mOS. To discern between Ce^{3+} and Ce^{4+}, a cutoff value has to be calibrated ($\text{OS}_{\text{Ce}} : \{\mu_{\text{Ce}} \leq \mu_{\text{cutoff}} : q \to 4+; \mu_{\text{Ce}} > \mu_{\text{cutoff}} : q \to 3+\}$). Furthermore, visualizing the distribution requires a frequency count of some sort. Since the number of retention periods is finite, these periods can be grouped into a histogram: $f_{life} : t \to \sum_{t \in box}$, where $t = \sum_i \texttt{if}\,[\text{OS}(t_i) == \text{OS}(t_{i-1})]$, i the step index and t_i the corresponding time step. This introduces an additional parameter, namely the box width. Supplementary Fig. 14 shows a scan of various parameter settings. The similarity between the histograms shows the quality of the data and its robustness to parameter changes. Therefore, a single representation as shown in the main text (Fig. 2d) becomes meaningful. The parameters chosen were a cutoff value of 0.8 μ and a box width of 100 fs.

Supplementary Note 4

DFT is known to systematically underestimate the band gap. Therefore, the decomposition in Fig. 3 has been compared to a hybrid functional. The success of HSE03 with 13% exact exchange (HSE03-13) applied to light-harvesting materials[1] carries over to the level alignment in this system. The new decomposition is shown in Supplementary Fig. 9. Firstly, the qualitative effect of the

distortions on the surface ceria (4f)-band is recovered. (Pt^{+}) and (Pt^{2+}) intersect the Pt Fermi-level, allowing for electron donation. At the same time, HSE03-13 is partially filling its 4f orbitals. The state mixing could originate from the larger volume of the valence electrons compared with PBE+U ($U_{eff} = 4.5$ eV). Therefore, the spread and any related effects can be regarded as an artifact from HSE03-13 or the low resolution (due to a gamma-point mesh). The distortion effects on the other hand, are still pronounced enough to corroborate the phonon-induced charge transfer mechanism as proposed in the main text.

Supplementary Note 5

Pt-2O is stable against sintering (Fig. 1), but other surface processes were examined too. The results are collected in Supplementary Table 2. These processes include: (i) the diffusion of the Pt atom over the surface; (ii) it encountering another single-atom Pt (dimerization); or (iii) loss of Pt to the gas phase (volatilization). As for the other coordinations: Pt-3O has already been established to convert at temperatures above 300 K (Fig. 2), while Pt-4O corresponds to the preferred square-planar configuration.

The lowest-energy path for diffusion is between two O-bridge site along the trench. The overall process is thermoneutral due to symmetry. Between both minima, Pt forms a Ce-Pt-Ce bridge to lower the activation energy. When charge is transferred to nearby the Ce centres, these end up distorting the symmetry of the trench and modifying the barrier. Both scenarios are considered. The activation energy is retrieved by $E_{diff} = E_{Pt\text{-}2O@Ce_{bridge}} - E_{Pt\text{-}2O@O_{bridge}}$, where @ refers

to the bridging site. Gas species which are present in the reaction environment, such as CO, can significantly stabilize the intermediate. Here, the activation energy accounts for the CO adsorbing prior to diffusing: $E_{\text{diff-CO}} = E_{\text{PtCO-2O@Ce}_{\text{bridge}}} - E_{\text{PtCO-2O@O}_{\text{bridge}}}$. Only for Pt^{+} and Pt^{2+} does this lower the barrier significantly to ~ 0.4 eV.

Pt dimers are not thermodynamically stable. They can become stable however when both ends are confined by oxygen, forming a $(PtO_3)_2$ coordination. The reaction energies are compared to the square-planar system: $E_{\text{dimer}} = E_{(PtO_3)_2} - 2E^{\text{min}}_{\text{Pt-4O}} - E_{\text{2O}} - E_{\text{Pt,(g)}}$. Volatilization on the other hand is considered as a direct deposition: $E_{\text{vol}} = E_{PtO_2\text{,(g)}} + E_{\text{2O}} - E^{\text{min}}_{\text{Pt-2O}} - E_{O_2\text{,(g)}}$.

Supplementary Note 6

In Fig. 1 and Supplementary Fig. 3, 5 and 8 a single base reference line was used with respect to 2O and Pt-bulk. With respect to this baseline, two factors influencing the dispersion energy are mapped out: (i) the oxidation state of the Pt SAC (horizontally), and (ii) electron localization (vertically). When examining the effect of surface reduction, we only want to account for those two factors. Applying the previous reference to both systems in Supplementary Fig. 12 would introduce an additional factor: (iii) the chemical reaction underpinning the surface reduction, i.e. the addition of a single hydrogen atom $\left(+\frac{1}{2}H_2\right)$ or abstraction of a single oxygen atom $\left(-\frac{1}{2}O_2\right)$. This would shift all states vertically by their respective reaction energies. In order to exclude the contribution from (iii), the reaction energy thus has to be integrated into the baseline by replacing 2O with its reduced counterparts. Since the residing electron(s) can localize at various cerium

centres, we obtain a set of Pt-free reference systems. Any of these systems can be a starting point for metal dispersions and thus the full range is marked. In other words, no single model system can represent a reduced surface. States above the reference region present energetically unstable dispersion, while those below are stable. An analogous reasoning applies to the 2O + Pt nanoparticle reference line as well.

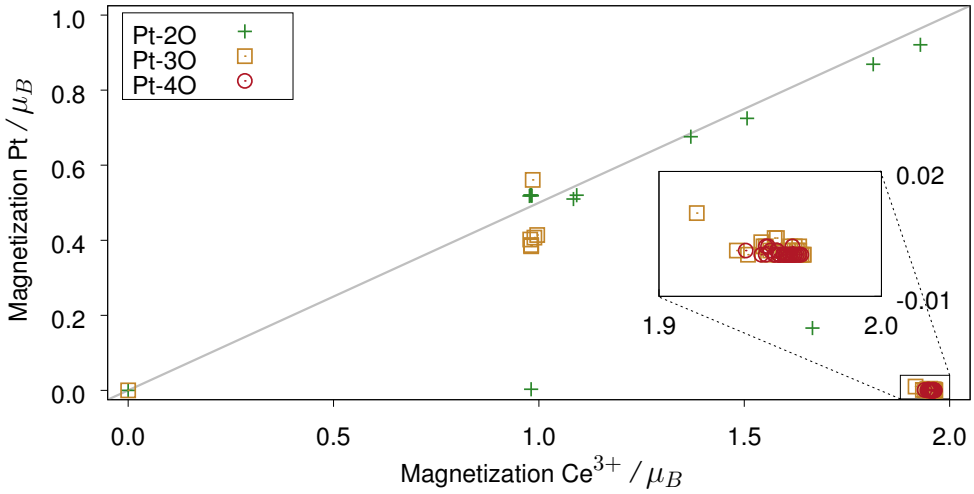

Supplementary Fig. 1 | Oxidation to magnetization. Correlation between the Pt magnetization ($\sum|\mu_{Pt}|$) as a function of the Ce^{3+} magnetization ($\sum|\mu_{Ce^{3+}}|$) per Pt-nO coordination. The grey line serves as a visual aid for a perfect correlation (2:1). The inset shows a zoom-in of the Pt^{2+}-3O and Pt^{2+}-4O data. For a discussion on their vanishing magnetization, see Supplementary Note 1.

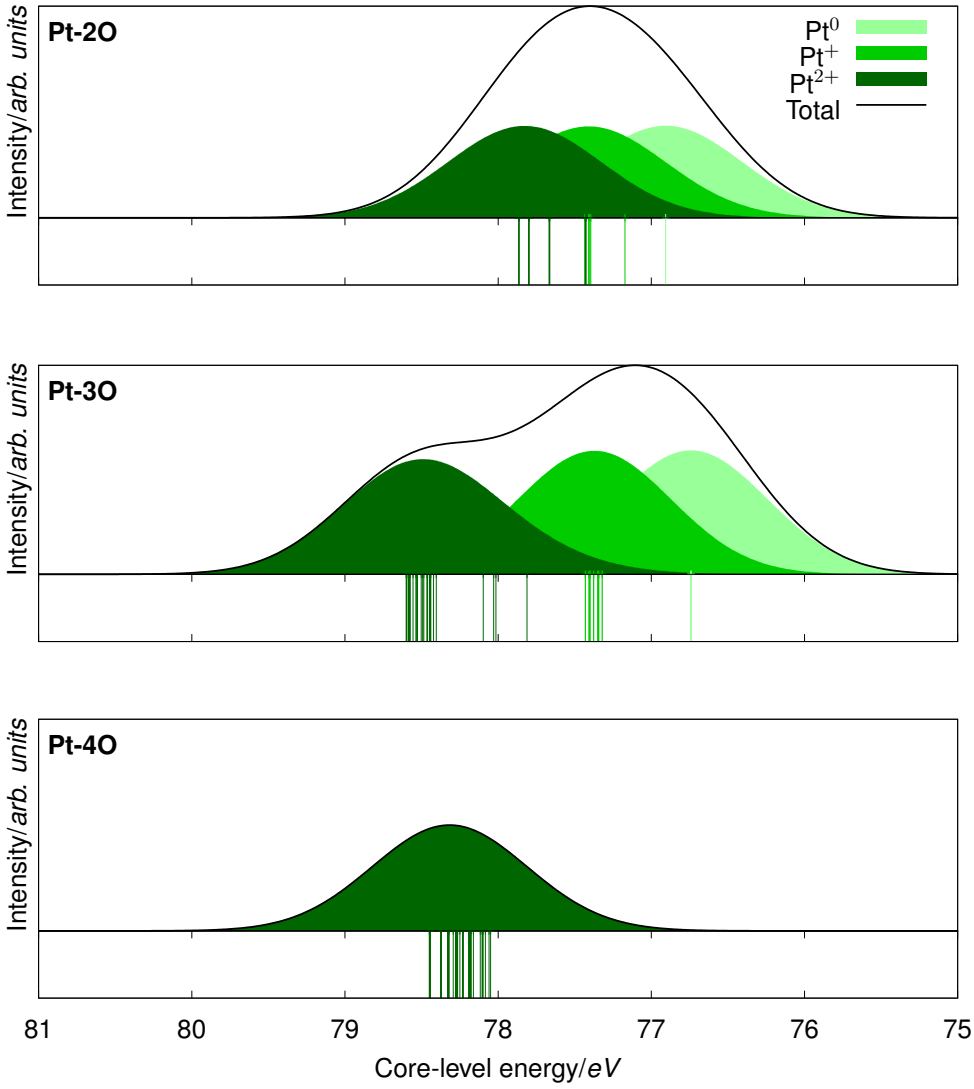

Supplementary Fig. 2 | Core-level energies. XPS spectra by Pt-nO coordination and mOS. The bars underneath the spectra correspond to the peaks of each charge distribution. The curves are the corresponding Boltzmann distributions per mOS.

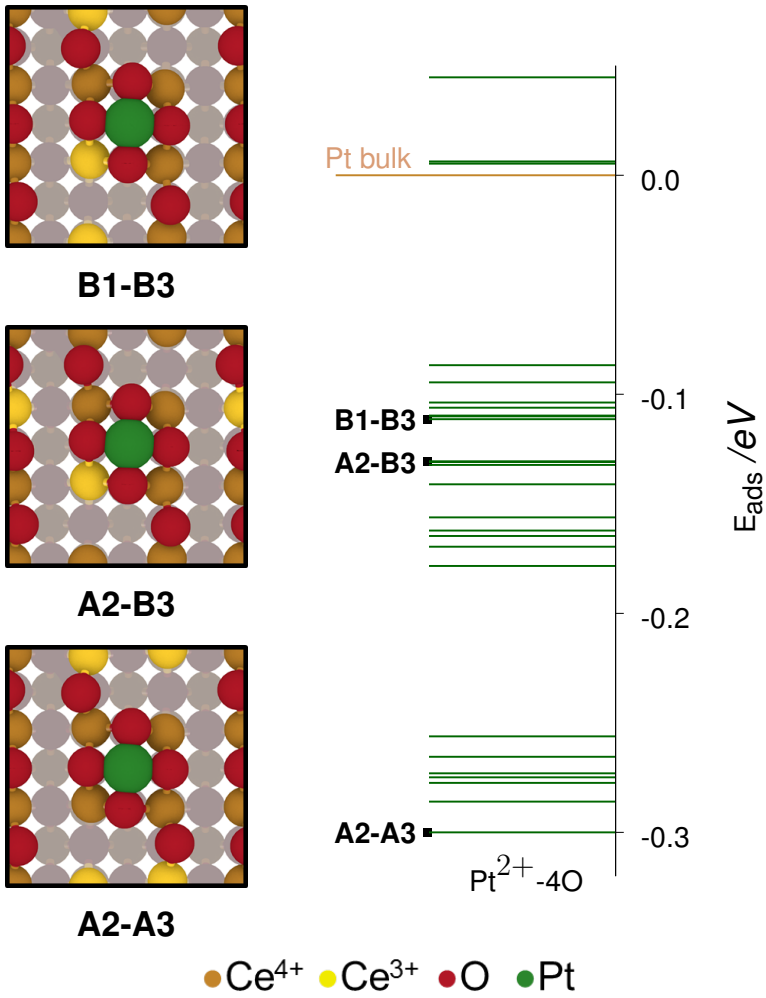

Supplementary Fig. 3 | Electron transfer spectrum. Zoom-in of the far-right column in Fig. 1, namely Pt^{2+}-4O. On the left-hand side is a sampling of different electron localization patterns, each of which a local minimum. The labels below them denote the Ce^{3+} indexes and map to the points on the energy spectrum at the right-hand side.

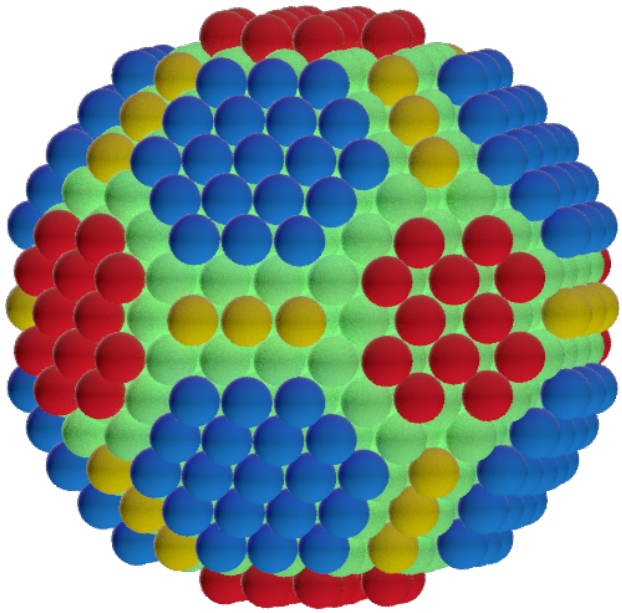

Supplementary Fig. 4 | Pt nanoparticle. A cuboctahedral Pt metal nanoparticle with a 20 Å diameter. The particle contains 935 atoms, 152 of which are {111}-terminated (blue) and 54 {100}-terminated (red). Surface edge sites are denoted in orange and the bulk in green.

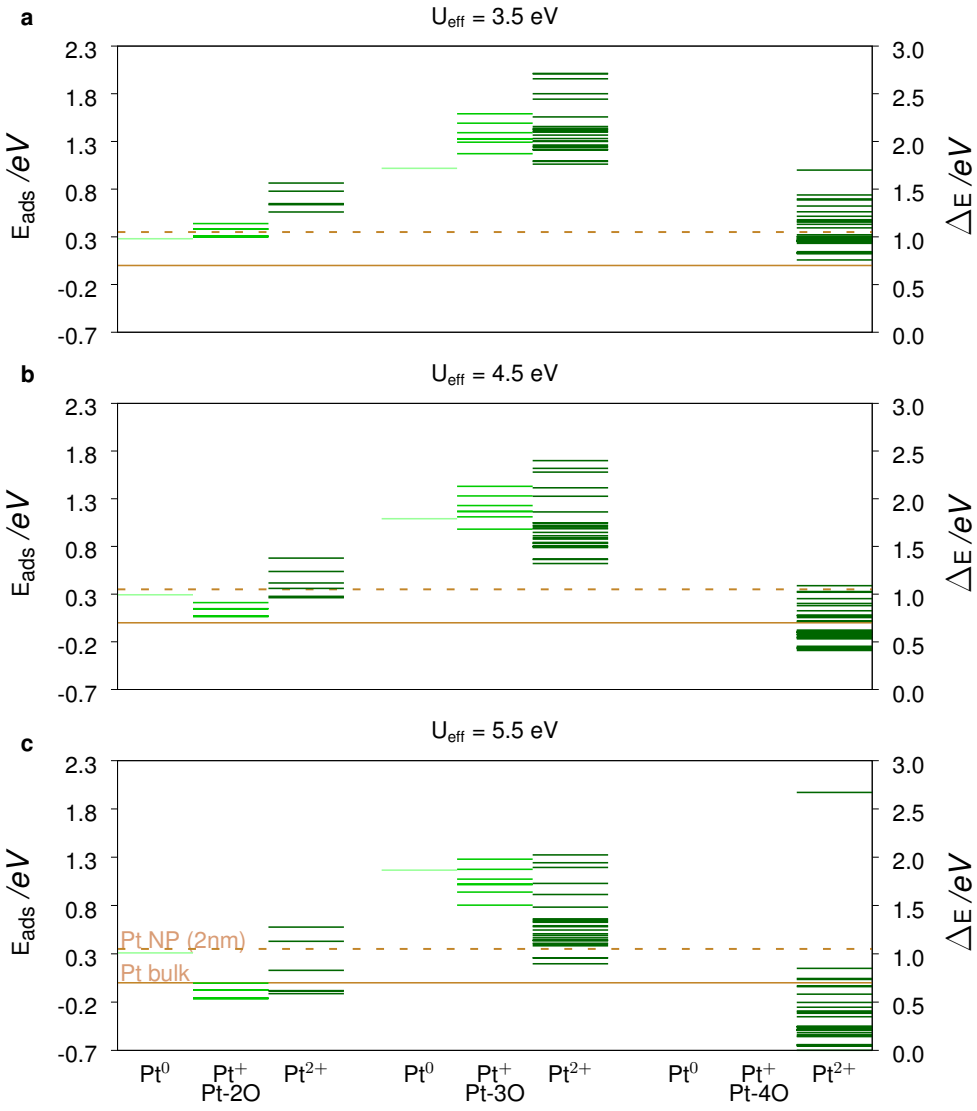

Supplementary Fig. 5 | Hubbard calibration. Pt-nO (3×3) is tested for different Hubbard parameters (U_{eff}). In top-down order these are 3.5, 4.5 and 5.5 eV.

The orange, full (dashed) line denotes equilibrium with the Pt bulk (a Pt nanoparticle of 2 nm in diameter (see Supplementary Fig. 4)) on top of the 2O surface with matching Hubbard parameter. Note that the ionic Pt states are susceptible to the Hubbard parameter. More specifically, they are better stabilized with an increasing U value. Irrespective of this dependency, the energy spans of the mOS of a single coordination environment always overlap. As such, thermal energy suffices to activate electron transfer, fulfilling a main requirement for PAMSI.

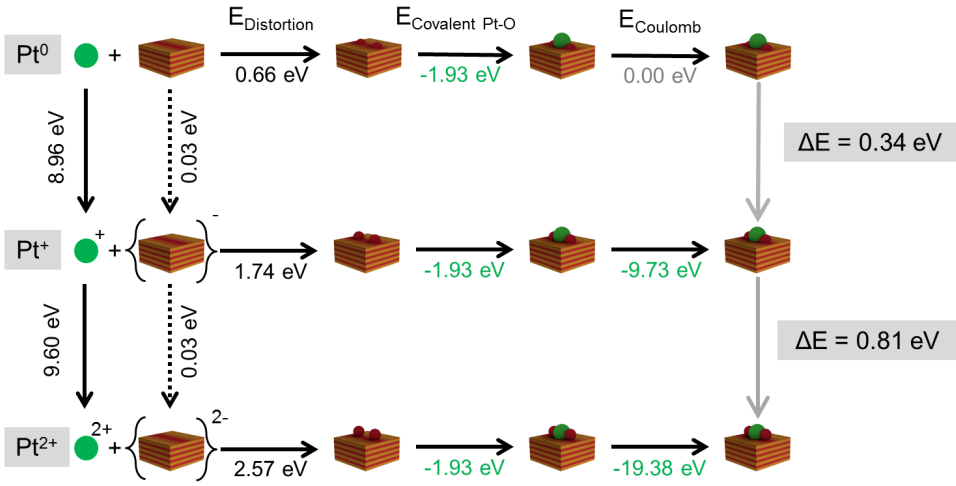

Supplementary Fig. 6 | Born-Haber cycle. A schematic breakdown of the physical interactions introduced when adsorbing a single Pt atom on the CeO_2 (100) surface. Each row corresponds to a mOS. Green numbers show stabilizing interactions, black to destabilizing and grey to non-interacting. ΔE represents the final relative stabilities. For a methodology we refer the reader to Supplementary Note 2 and to Supplementary Table 6 for the model input variables.

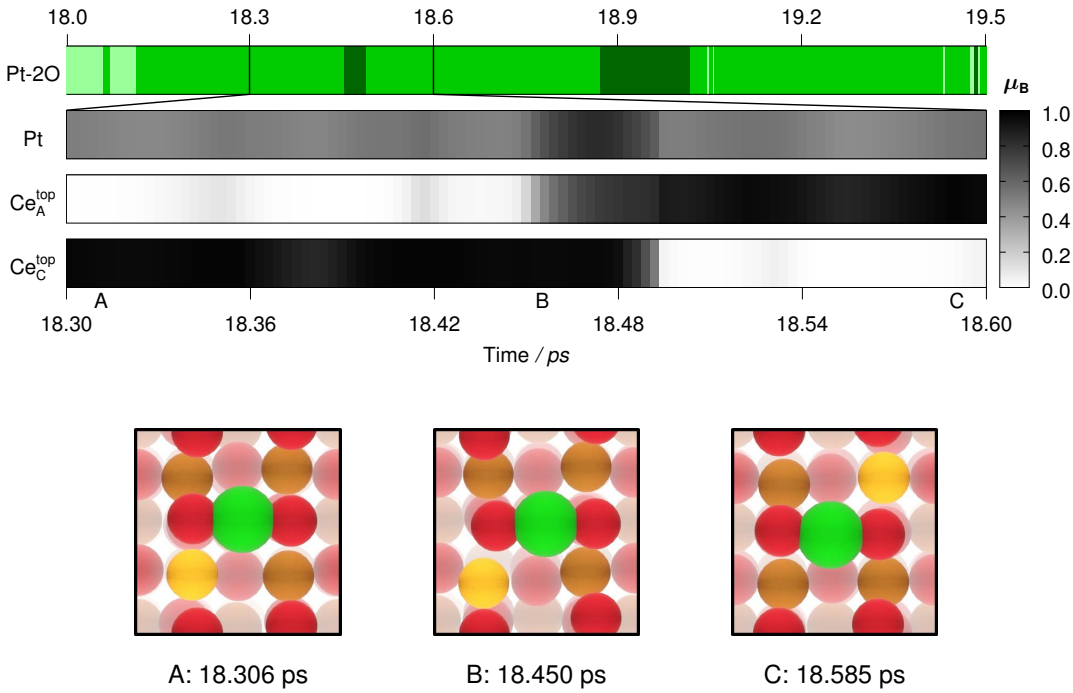

Supplementary Fig. 7 | Polaron movement (2×2). A single polaron diffusion event on Pt-2O with a (2×2) supercell is depicted. The topmost, green band is an enlargement of the Pt mOS in Fig. 2a, between 18.0 and 19.5 ps. The black-and-white bands below denote the magnetic moment (a descriptor for the mOS) of Pt, Ce_A^{top} and Ce_C^{top} in top-down order. The polaron movement progresses from Ce_C^{top} over Pt to Ce_A^{top} and lasts for 45 fs. Therefore, the bands are further zoomed in from 18.30 to 18.60 ps, up to when the individual MD steps become distinguishable. The labels below the Ce_C^{top} band mark the three snapshots of Supplementary Video 1 at the bottom, at 18.306, 18.450 and 18.585 ps.

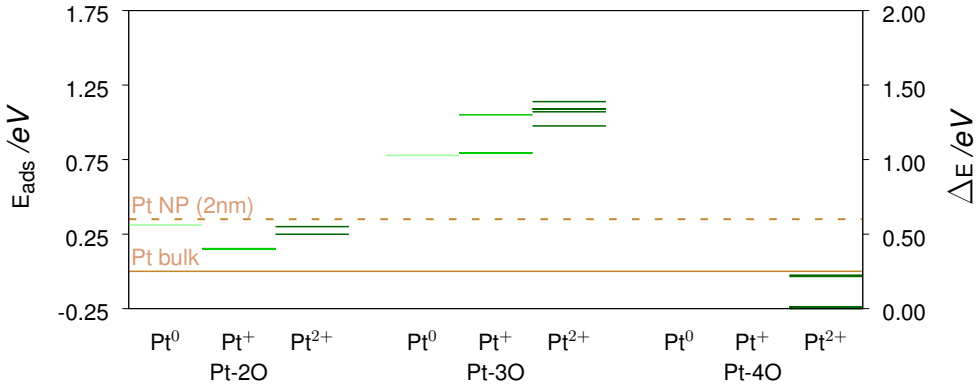

Supplementary Fig. 8 | Pt adsorption energies on CeO_2 (100) supercell of (2×2). a, Adsorption energy of Pt on CeO_2 (100), for multiple mOS on different surface nO configurations. As surface oxygens were demonstrated to be mobile on this facet[2], three possible Pt environments have been considered, denoted as Pt-nO where n is the number of O atoms in the immediate vicinity of Pt. For each case involving Pt^+ or Pt^{2+} all possible Ce^{3+} distributions were considered. For Pt-4O, only Pt^{2+} configurations were stable. Adsorption energies with respect to the regularly oxygen-terminated CeO_2 (100) and Pt bulk are shown in the left axis (E_{ads}), while the values relative to the most stable configuration can be read on the right axis (ΔE). The orange, full (dashed) line denotes equilibrium with the Pt bulk (a Pt nanoparticle of 2 nm in diameter (see Supplementary Fig. 4)).

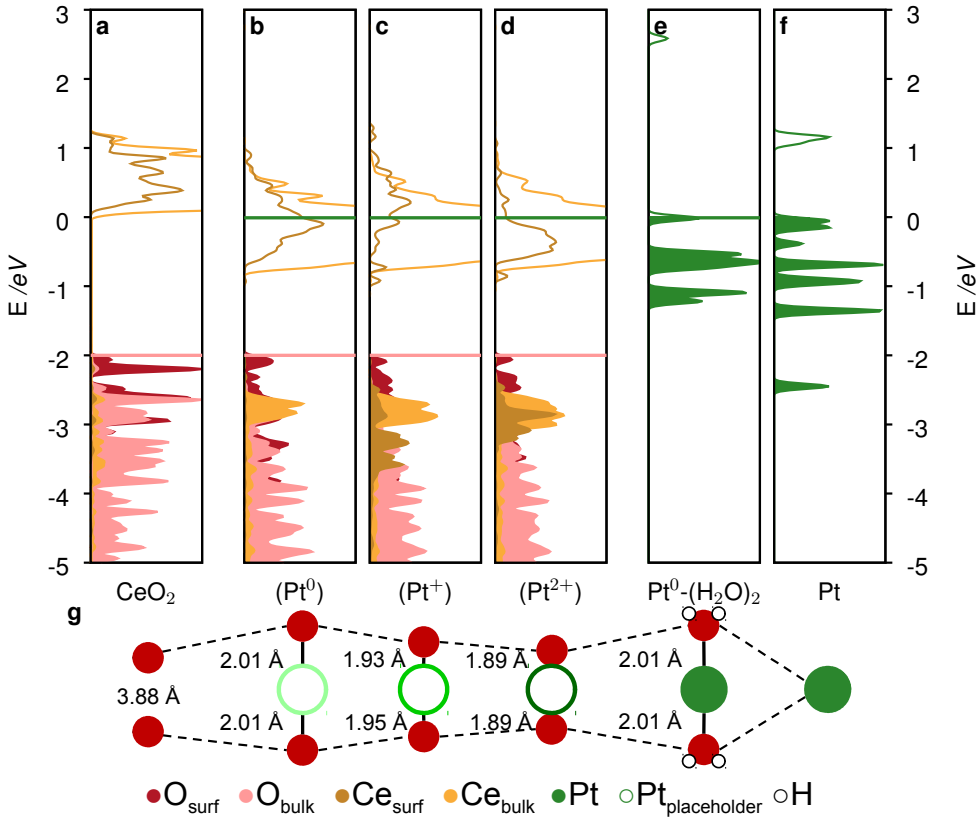

Supplementary Fig. 9 | HSE03-13, gamma point Density of States decomposition for the Pt-2O systems with different oxidation states. **a,** DOS for the pristine CeO_2 surface showing the filled Valence Band and empty Ce(4f) bands. **b-d**, oxide-only (once Pt is removed) DOS obtained at the geometries of the Pt-2O configurations with different mOS: **b,** neutral Pt^0; **c,** single-electron transfer Pt^+; **d,** double metal-to-surface electron transfer Pt^{2+}. The lowering of the Ce(4f) levels allows the injection from the higher Pt filled states as indicated by the Fermi level in **e** (green line).

e-**f**, gas-phase Pt levels when covalently interacting with water or when isolated, respectively. The gas-phase systems are separated 7.1 Å from the top and 8.2 Å from the bottom of two undistorted 2O slabs. All systems were aligned according to the 2s-band center of the central oxygen layer in the slab. **g,** local geometries.

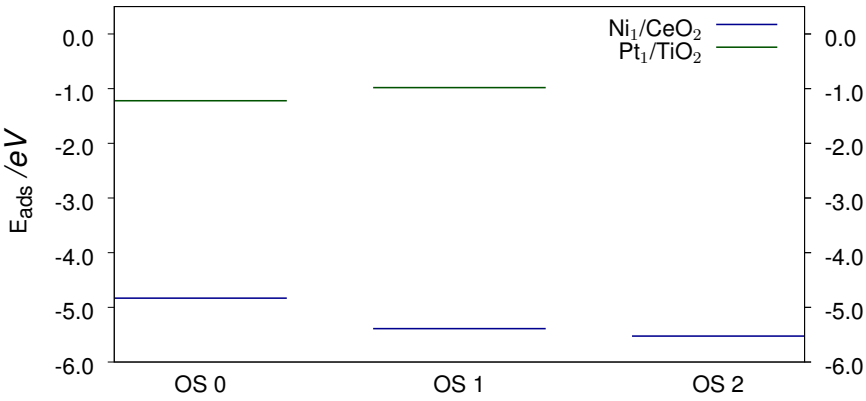

Supplementary Fig. 10 | PAMSI scope. Two sample systems are shown where preliminary data suggests PAMSI to occur. The energies per mOS are given in eV with respect to the pristine surfaces (rutile $TiO_2(110)$ or $CeO_2(100)$) and metal atom (Pt or Ni). Remark that both systems contain either the dispersed metal or metaloxide component overlapping with the focus in this paper, namely Pt_1/CeO_2.

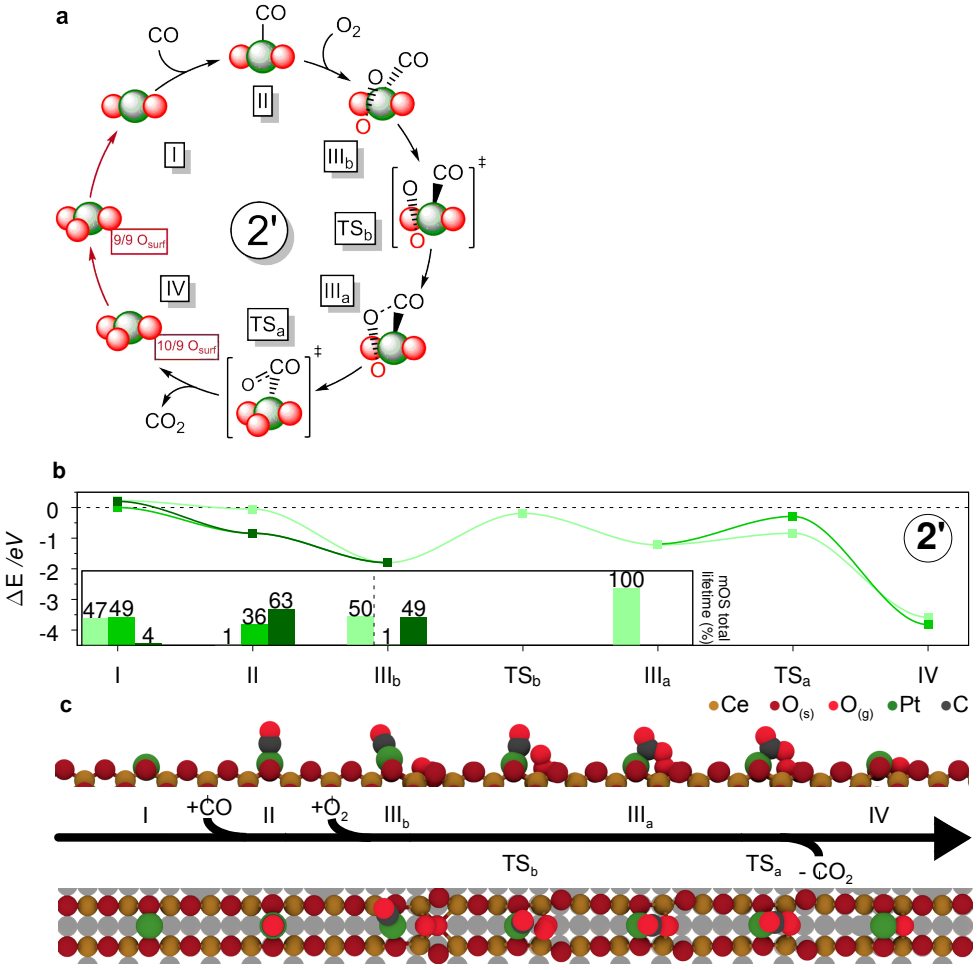

Supplementary Fig. 11 | Alternative CO oxidation route. Parallel to the reaction presented in cycle 2 in Fig. 4a and Fig. 4b, CO can align itself under a 118° angle to the peroxo group (III_b). From there on, it either desorbs again or converts to the percarbonate from Fig. 4 (III_a).

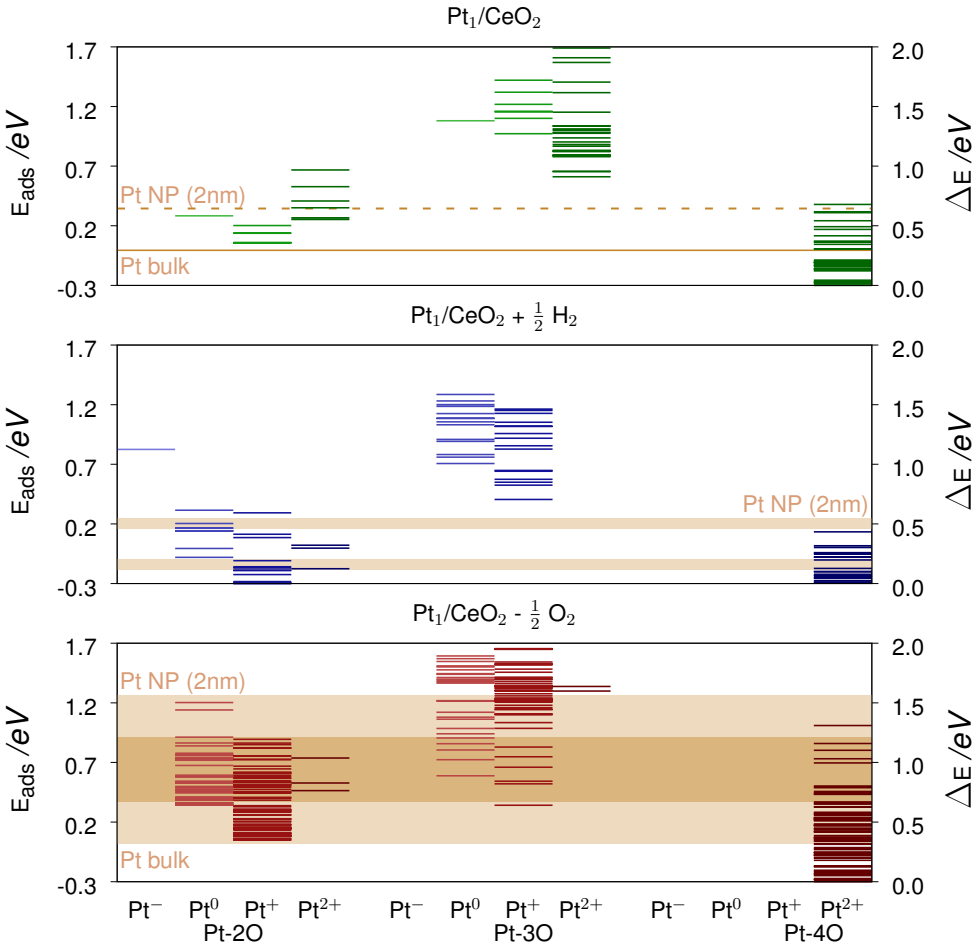

Supplementary Fig. 12 | Chemically induced surface reduction. The influence of surface reduction on PAMSI was investigated for the (3×3) slab model. The reduction was modelled by either adding a H atom (forming a hydroxyl group) or abstracting a surface oxygen to inject one or two more electrons into the surface, respectively. The new energy spectra are shown in top-down order, with the regular surface on top.

Due to different possible charge localization sites, there is no longer a single reference, see Supplementary Note 6 for more information. Instead the full energy range is denoted, in comparison with the Pt bulk (below) and a Pt nanoparticle (above) with a 2 nm diameter as shown in Supplementary Fig. 4. Note how PAMSI manages to persist with surface oxygen vacancy concentrations of up to $\theta = \frac{1}{9}$. In some states the reduced Ce^{3+} centers localize onto lower surface layers as well, similar to what has been reported in experiments[3].

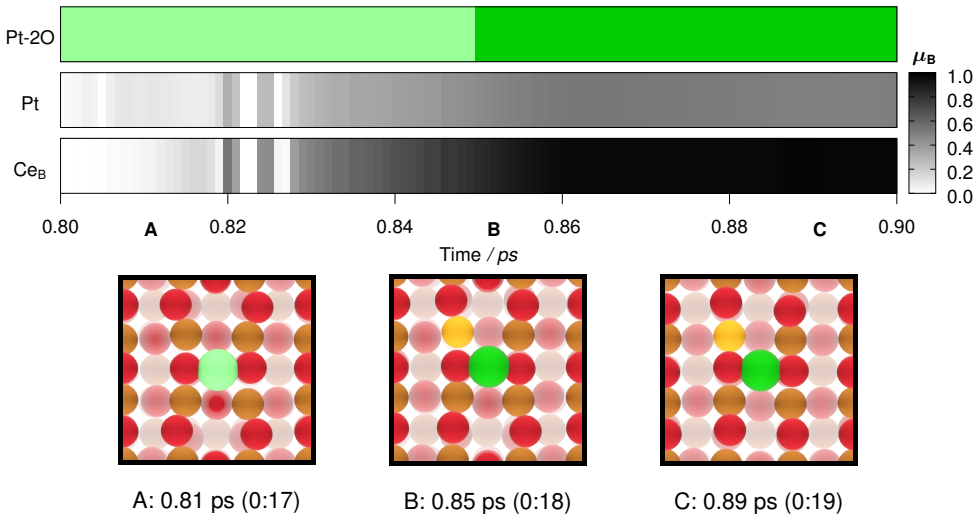

Supplementary Fig. 13 | Polaron movement (3×3). A single polaron diffusion event on Pt-2O with a (3×3) supercell is traced. This event occurs during the MD simulation in Supplementary Video 4. The top band denotes the mOS, while the bands below denote the magnetization in grey on the Pt atom and the host cerium centre, respectively. Below are three snapshots from the Video, each labelled according to simulated time (ps) and with the Video runtime between brackets. The snapshots have also been placed along the time axis. Both panels show this extended reaction mechanism. The dashed line from III_a to IV denotes higher, alternative reaction barrier. The grey band at the bottom shows the lifetimes of each mOS. The lifetimes were accumulated over 13.5 ps of MD simulation for each intermediate.

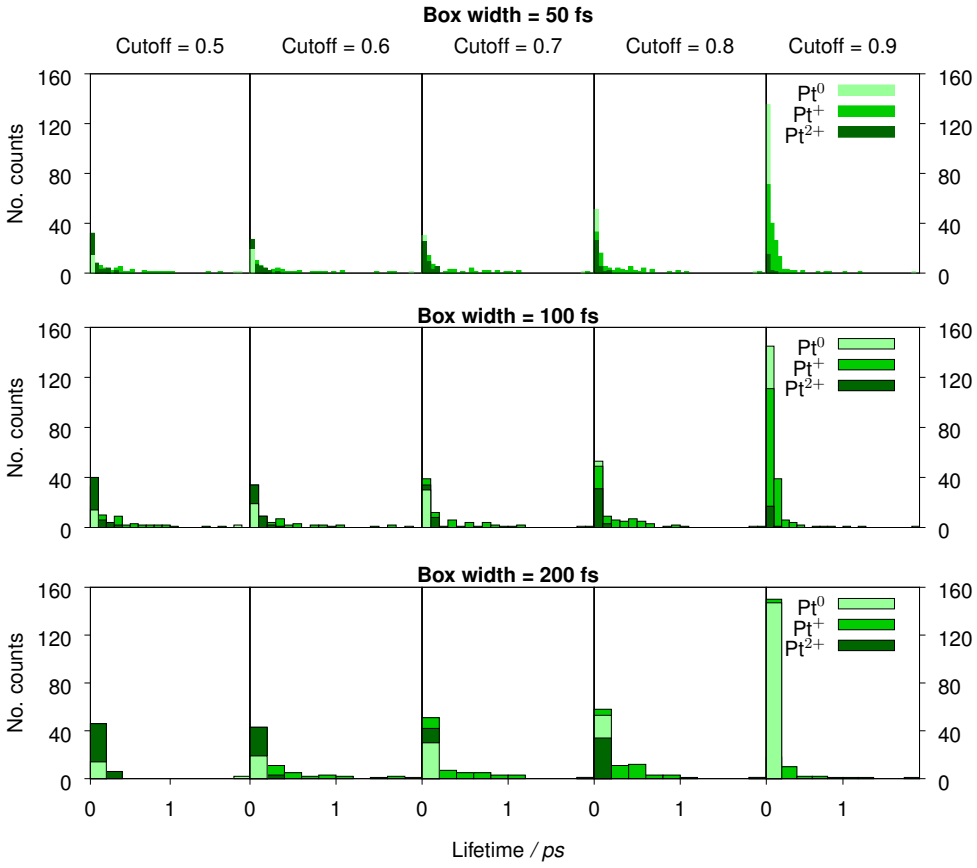

Supplementary Fig. 14 | Lifetime from Molecular Dynamics. Sensitivity test of the MD statistics to the histogram lifetime parameters. These parameters cover the lifetime intervals (box width) per row and the magnetization cut-off, varying horizontally. From this scan, a box width of 100 fs was chosen with a cut-off value of $0.8\ \mu_B$. For more information, see Supplementary Note 3.

The black line in the grey band at III_b indicates that the mOS belong to different simulations and have not been found to be dynamically linked.

Supplementary Table 1 | Single-atom Pt adsorption on CeO_2. Scan of CeO_2 (2×2) surfaces for (111), (110) and (100). This yields the mOS and adsorption energies, E_{ads} (eV) with respect to bulk Pt (E_{ads} = E - E_{surf} - $E_{bulk\ Pt}$). The figures below present a top view of the (2×2) surfaces.

	(111)		(110)		(100)	
Adsorption site	mOS	E_{ads}	mOS	E_{ads}	mOS	E_{ads}
Ce_{top}	0	4.29	0	4.93	1	2.33
Ce_{sub}	-	-	0	1.45	0	0.32
O_{top}	0	3.05	0	2.69	1	0.65
O_{bridge}	1	2.39	0	3.41	-	-
$O_{hexagon}$	1	2.49	2	0.63	-	-

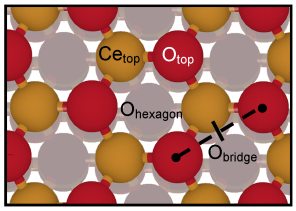

(111)

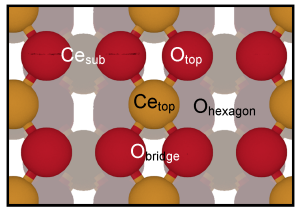

(110)

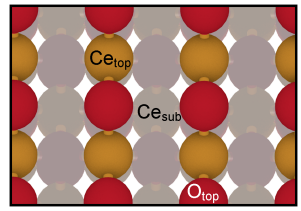

(100) O-terminated

Supplementary Table 2 | Stability check. The stability of the Pt-2O coordination is verified with respect to Pt diffusion, volatilization and dimerization. The energies (eV) are shown for each mOS minimum.

Reaction		E_{Pt^0}	E_{Pt^+}	$E_{Pt^{2+}}$
Pt diffusion	Ce^{3+} direction	-	3.15	2.89
	Ce^{4+} direction	2.95	3.17	2.99
CO-assisted Pt diffusion	Ce^{3+} direction	-	0.43	0.35
	Ce^{4+} direction	1.92	0.42	2.55
Volatilization		0.92	1.15	0.95
		$E_{Pt_2^0}$	$E_{Pt_2^{2+}}$	$E_{Pt_2^{3+}}$
Dimerization		1.84	0.32	0.29

Supplementary Table 3 | Functional energy benchmark. Pt adsorption energy comparison (eV) between PBE+U (U = 4.5 eV), HSE06 and HSE03-13[1] with respect to the 2O surface. The scope is restricted to the local minima of the (3×3) supercells at PBE+U level.

Coord	Pt OS	$E^{PBE+U}_{Pt\text{-}atom}$	$E^{HSE06}_{Pt\text{-}atom}$	$E^{HSE03\text{-}13}_{Pt\text{-}atom}$
Pt-2O	0	−5.28	−4.57	−4.85
	1	−5.50	−4.61	−4.47
	2	−5.31	−4.08	−4.10
Pt-3O	0	−4.48	−4.14	−4.39
	1	−4.59	−3.88	−3.78
	2	−4.95	−3.75	−3.29
Pt-4O	2	−5.86	−4.85	−4.38

Supplementary Table 4 | Functional Benchmark. Comparison between the electronic properties of PBE+U ($U_{eff} = 4.5$ eV), HSE06 and HSE03-13[1] for the (3×3) supercell model of the local minima. This entails Bader charges ($|e^-|$) for the Pt atom and neighbouring Ce atoms and the latter's magnetization (μ_B) obtained. The magnetic moments of the Ce^{3+} centres act as a proxy for the mOS.

Coord	mOS	Pt_{Bader}^{PBE+U}	Pt_{Bader}^{HSE06}	$Pt_{Bader}^{HSE03-13}$	$Ce_{Bader}^{3+,PBE+U*}$	$Ce_{Bader}^{3+,HSE06**}$	$Ce_{Bader}^{3+,HSE03-13***}$	$\sum\lvert\mu_{Ce^{3+}}^{PBE+U}\rvert$	$\sum\lvert\mu_{Ce^{3+}}^{HSE06}\rvert$	$\sum\lvert\mu_{Ce^{3+}}^{HSE03-13}\rvert$
Pt-2O	0	0.10	0.11	0.14	-	-	-	0.00	0.00	0.00
	1	0.19	0.44	0.41	2.30	2.16	2.18	0.99	0.96	0.78
	2	0.46	0.47	0.42	2.07/2.14	2.19/2.26	2.16/2.23	1.67	1.420	1.11
Pt-3O	0	0.04	0.50	0.53	-	-	-	0.00	0.00	0.00
	1	0.21	0.44	0.41	2.06	2.28	2.30	0.99	0.97	0.76
	2	0.53	0.69	0.69	2.04/2.07	2.17/2.20	2.17/2.21	1.96	1.93	1.63
Pt-4O	2	0.74	0.81	0.82	2.01/2.01	1.91/2.21	1.91/2.22	1.96	1.93	1.60

* for reference only, $Ce_{top}^{4+,PBE+U}$ has an average Bader charge of 1.9 $|e|^-$ on the 2O surface.

** for reference only, $Ce_{top}^{4+,HSE06}$ has an average Bader charge of 2.0 $|e|^-$ on the 2O surface.

*** for reference only, $Ce_{top}^{4+,HSE03-13}$ has an average Bader charge of 3.0 $|e|^-$ on the 2O surface.

Supplementary Table 5 | Comparison to RPA. Comparison of the adsorption energies according to PBE+U (U = 4.5 eV) and the Random Phase Approximation (RPA). Due to the computational requirements of RPA, the scope was limited to the PBE+U local minima on Pt-2O (see Supplementary Fig. 3).

Coord	Pt OS	$E^{PBE+U}_{Pt\text{-}atom}$	$E^{RPA}_{Pt\text{-}atom}$
Pt-2O	0	−5.28	−4.77
	1	−5.50	−4.53
	2	−5.31	−5.27

Supplementary Table 6 | Born-Haber input. The model input variables for the 2O Born-Haber cycle, as presented in Supplementary Fig. 6 and discussed in Supplementary Note 2, are tabulated here. The top-left table contains the Bader charges (Q_{Bader} in $|e^-|$) for each mOS, while the top-right and bottom table list the implemented atomic distances (d_{atomic} in Å), again per mOS as denoted by the Pt superscript in the header. Pt^* refers to the relevant mOS. The subscripts distinguish between O and Ce and are unrelated to the any of the Molecular Dynamics simulations. Note that Q_{Bader} only contains ionic Pt, since the differences in electrostatic energy due to electron transfer are being considered. All the while, d_{atomic} is still relevant for Pt^0 in order to compute the relative atomic movement.

Q_{Bader}	OS 1	OS 2
Pt	0.19	0.46
O_A	−1.02	−1.02
O_B	−1.19	−1.19
Ce_A	2.07	2.16
Ce_B	2.14	2.23

d_{atomic}	Pt^0	O_A	O_B	Ce_A	Ce_B
Pt^*	0.000	2.011	2.011	-	-
O_A	2.011	0.000	-	2.351	-
O_B	2.011	-	0.000	-	2.351
Ce_A	-	2.351	-	0.000	-
Ce_B	-	-	2.351	-	0.000

d_{atomic}	Pt^+	O_A	O_B	Ce_A	Ce_B	Pt^{2+}	O_A	O_B	Ce_A	Ce_B
Pt^*	0.000	1.931	1.948	-	3.279	0.000	1.892	1.892	3.303	3.303
O_A	1.931	0.000	-	2.555	-	1.892	0.000	-	2.561	-
O_B	1.948	-	0.000	-	2.417	1.892	-	0.000	-	2.561
Ce_A	-	2.555	-	0.000	-	3.303	2.561	-	0.000	3.864
Ce_B	3.279	-	2.417	-	0.000	3.303	-	2.561	3.864	0.000

Supplementary Table 7 | Pt-4O reaction diagram. The CO oxidation and H_2 reduction energies from Fig. 4a, circle 1 are covered: the energy relative to the minimum of the Pt-4O surface $\left(\mathrm{E} = \mathrm{E}_i - \mathrm{E}_{\mathrm{CO}} - \mathrm{E}_{\mathrm{O}_2} - \mathrm{E}^{\mathrm{min}}_{\text{Pt-4O}}\right)$, the reaction energy $(\Delta\mathrm{E} = \mathrm{E}_i - \mathrm{E}_{i-1})$, the activation energy $(\mathrm{E_a})$ and imaginary frequency (ν_i) of any transition state. All energies are in eV, while the frequencies are in cm^{-1}. The subscript (g) refers to the gas phase.

Reaction	E	ΔE	E_a	ν_i
PtO_4 + $CO_{(g)}$ $\rightarrow$ PtCOO	0.10	0.10	0.39	170
$PtO_4CO \rightarrow PtO_5C$	−1.23	−1.33	1.14	123
$PtO_5C \rightarrow PtO_3$ + $CO_{2,(g)}$	−1.39	−0.16	-	-
PtO_4 + $H_{2,(g)}$ $\rightarrow$ $HPtO_4H$	−0.68	−0.68	1.33	1535
$HPtO_4H \rightarrow PtO_3$ + $H_2O_{(g)}$	−0.68	0.00	0.76	880

Supplementary Table 8 | Pt-2O reaction diagram. The CO oxidation energies on Pt-2O from Fig. 4a, circle 2 and Supplementary Fig. 11, circle 2' are covered: the energy relative to the minimum of the Pt-2O surface $\left(\mathrm{E} = \mathrm{E}_i - \mathrm{E}_{\mathrm{CO}} - \mathrm{E}_{\mathrm{O}_2} - \mathrm{E}^{\mathrm{min}}_{\mathrm{Pt\text{-}2O}}\right)$, the reaction energy $(\Delta\mathrm{E} = \mathrm{E}_i - \mathrm{E}_{i-1})$, the activation energy $(\mathrm{E_a})$ and imaginary frequency (ν_i) of any transition state. All energies are in eV, while the frequencies are in cm^{-1}. The subscript (g) refers to the gas phase.

OS	F4, SF11	Reaction	E	ΔE	E_a	ν_i
0	2.I-II	$PtO_2 + CO_{(g)} \rightarrow PtO_2CO$	-0.06	-0.29	-	-
	2.II-III$_a$	$PtO_2CO + O_{2,(g)} \rightarrow PtO_3CO_2$	-1.40	-1.35	-	-
	2.III$_a$-IV	$PtO_3CO_2 \rightarrow PtO_3 + CO_{2,(g)}$	-3.58	-2.18	0.56	598
	2.II-III$_b$	$PtO_2CO + O_{2,(g)} \rightarrow PtO_3OCO$	-1.81	-1.75	-	-
	2.III$_b$-III$_a$	$PtO_3OCO \rightarrow PtO_3CO_2$	-1.20	0.61	1.60	166
1	2.I-II	$PtO_2 + CO_{(g)} \rightarrow PtO_2CO$	-0.84	-0.84	-	-
	2.II-III$_a$	$PtO_2CO + O_{2,(g)} \rightarrow Pt^0O_3CO_2$	-1.40	-0.56	-	-
	2.III$_a$-IV	$Pt^0O_3CO_2 \rightarrow PtO_3 + CO_{2,(g)}$	-3.82	-2.42	1.11	837
	2.II-III$_b$	$PtO_2CO + O_{2,(g)} \rightarrow PtO_3OCO$	-1.81	-0.97	-	-
2	2.I-II	$PtO_2 + CO_{(g)} \rightarrow PtO_2CO$	-0.84	-1.04	-	-
	2.II-III$_a$	$PtO_2CO + O_{2,(g)} \rightarrow Pt^0O_3CO_2$	-1.40	-0.56	-	-
	2.II-III$_b$	$PtO_2CO + O_{2,(g)} \rightarrow PtO_3OCO$	-1.81	-0.97	-	-

Supplementary Table 9 | CO adsorption. Adsorption energies (eV) and stretching frequencies (cm^{-1}) of CO on Pt-2O and Pt-4O. The adsorption energies are compared to several references: $\mathrm{E_{OS}} = \mathrm{E} - \mathrm{E}^{\mathrm{min}}_{\mathrm{Pt^*\text{-}nO}} - \mathrm{E_{CO}}$, $\mathrm{E_{surface}} = \mathrm{E} - \mathrm{E}^{\mathrm{min}}_{\mathrm{Pt\text{-}nO}} - \mathrm{E_{CO}}$ and $\mathrm{E_{global}} = \mathrm{E} - \mathrm{E}^{\mathrm{min}}_{\mathrm{Pt\text{-}4O}} - \mathrm{E_{CO}}$. At the bottom are the reference frequencies for gas-phase CO, used in the gas-phase shift. The Boltzmann weighted shift of $33\ \mathrm{cm}^{-1}$ from Pt^0 to Pt^{2+} (PBE+U) is comparable with the experimental shift of $31\ \mathrm{cm}^{-1}$ from metallic $(2064\ \mathrm{cm}^{-1})$ to ionic Pt $(2095\ \mathrm{cm}^{-1})$ [4].

Surface	OS	Ce^{3+}	E_{OS}	$E_{surface}$	E_{global}	ν_{CO}^{PBE+U}	E_{OS}^{VDW}	$E_{surface}^{VDW}$	E_{global}^{VDW}	$\nu_{CO}^{PBE+U\ VdW}$
Pt-2O	0	-	-0.29	-0.06	0.30	2025	-0.36	-0.18	0.22	2030
	2	$28, 29$	-1.04	-0.84	-0.49	2043	-1.09	-0.94	-0.54	2046
	2	$29, 34$	-1.26	-1.35	-0.91	2058	-1.50	-1.35	-0.95	2056
Pt-4O	2	$31, 32$	0.10	0.10	0.10	2050	-0.14	-0.14	-0.14	2077

* CO gas-phase: $\nu_{CO}^{theor} = 2117\ \mathrm{cm}^{-1}$

** CO gas-phase: $\nu_{CO}^{exp} = 2170\ \mathrm{cm}^{-1}$ from NIST[5]

Supplementary video captions

Supplementary Video 1 | Molecular Dynamics simulation of polaron-induced electron transfer between a single Pt atom and its support, a (2×2) CeO_2 supercell with a 2O termination. The colour code is similar to that of Fig. 1: O, red; Ce^{4+}, orange; Ce^{3+}, yellow; Pt^0, light-green; Pt^+, green; Pt^{2+}, dark-green. The colour code for cerium and mOS are also listed in the legend at the top-right corner. Subsurface atoms appears fainter due to a mist effect. The mOS is determined by the number Ce^{3+} atoms, which have a magnetic cut-off of $0.8\ \mu_B$ (see Supplementary Fig. 14 and Supplementary Note 3). The camera is centred on the Pt atom, which is thus perceived as frozen. The corresponding cell boundaries, denoted by the black lines, are therefore also frozen. The system was prepared by a two-stage heating process from 0 to 600 K and incremental temperature steps of 1 K, interspersed with an equilibration stage. The video starts right hereafter. An average temperature of 600 K is maintained by the Nosé-Hoover thermostat with a period of 40 steps. For more technical details, the reader is referred to the Methods section. A full overview of the atom-resolved oxidation states and their time-evolution can be found Fig. 2. The time-evolution bands from the figure have been inserted at the bottom and a red line traces the progress of time over them.

Supplementary Video 2 | Molecular Dynamics simulation of polaron-induced electron transfer between a single Pt atom and its support, a (2×2) CeO_2 supercell with a 3O termination. The same formatting applies as in Supplementary Video 1. Note however that in this video both heating stages, the equilibration stage, and the final run at 600 K are shown. Each stage is delimited with a black line in the time-evolution bands. This is because the surface undergoes severe restructuring

at the onset: first one ligand oxygen diffuses at a temperature of ~ 300 K ($0:03$ min.), followed by another surface oxygen diffusing at ~ 486 K ($0:16$ min.) As such, Pt-3O converts into Pt-2O. From that point on the simulation proceeds in a similar fashion as in Supplementary Video 1.

Supplementary Video 3 | Molecular Dynamics simulation of polaron-induced electron transfer between a single Pt atom and its support, a (2×2) CeO_2 supercell with a 4O termination. The same formatting applies as in Supplementary Video 1. Here the mOS remains $2+$ throughout the run, although electrons can briefly delocalise over the Pt centre while hopping. Instead, all electron transfer happens between cerium atoms only, both at the first and second surface layer.

Supplementary Video 4 | Molecular Dynamics simulation of polaron-induced electron transfer between a single Pt atom and its support, a (3×3) CeO_2 supercell with a 2O termination. Only the colour code and cell boundaries from Supplementary Video 1 apply here. No time-evolution bands are present. Here, only the heating stage was executed, without any equilibration period. The same incremental temperature steps of 1 K were used and the whole simulation lasted 0.5 ps. At ~ 510 K ($0:18$ min) Pt^0 transitioned into Pt^+, while donating an electron to the top surface layer. The shifting colours indeed validate that PAMSI is not an artefact of the (2×2) supercell.

Supplementary References

1. Hegner, F. S., Cardenas-Morcoso, D., Giménez, S., López, N. & Galan-Mascaros, J. R. Level Alignment as Descriptor for Semiconductor/Catalyst Systems in Water Splitting: The Case of Hematite/Cobalt Hexacyanoferrate Photoanodes. *ChemSusChem* **10**, 4552–4560 (2017).

2. Capdevila-Cortada, M. & López, N. Entropic contributions enhance polarity compensation for CeO_2 (100) surfaces. *Nature Materials* **16**, 328–334 (2017).

3. Kopelent, R. *et al.* Catalytically Active and Spectator Ce 3+ in Ceria-Supported Metal Catalysts. *Angewandte Chemie International Edition* **54**, 8728–8731 (2015).

4. Jones, J. *et al.* Thermally stable single-atom platinum-on-ceria catalysts via atom trapping. *Science (New York, N.Y.)* **353**, 150–154 (2016).

5. Kramida, A., Ralchenko, Y., Reader, J. & Team, N. A. NIST Atomic Spectra Database (ver. 5.5.6) (2018).

Index

CeO_2 cerium dioxide. 2, 70, 84, 86, 89, 105–107, 110, 114–116, 120

CH_4 methane. 4, 5

CI-NEB climbing-image nudged elastic band method. 54–56, 92

CM classical mechanics. 19

CNN convolutional neural network. 73

CO carbon monoxide. 1, 4, 5, 40, 75, 76, 81, 82, 89–91, 93, 94, 96, 97, 103, 104

CO_2 carbon dioxide. 4, 5, 75, 81, 89, 94

CP2K Car-Parrinello code for the new Millenium. 18

CSTR continuously stirred tank reactor. 64

Cu copper. 40, 76

DET dynamic electron transfer. 95, 101, 102

DFT density functional theorem. 2, 6, 7, 20, 30, 41, 44, 45, 64, 76, 88, 93, 112

DFT+U density functional theorem equiped with a Hubbar correction. 7, 88, 105, 106

DM dimer method. 56, 58

DNN deep neural network. 66

DOE US Department of Energy. 1, 4, 95, 120

DOF degrees of freedom. 58, 92

DOS Density of States. 22, 85, 88, 102

E_a activation energy. 82

EC electron(ic) configuration. 80, 83, 92, 93

EMSI Electronic Metal-Support Interactions. 76, 78, 103

ET electron transfer. 78, 87–90, 99, 100, 102, 105

ET dynamics electron transfer dynamics. 90, 103

EU European Union. 3, 4

fCN fractional coordination number. 46

FD fluctuation-dissipation. 39

FFT Fast Fourier Transform. 23, 24

FM ferromagnetic. 108, 109

FORA first order relativistic approximation. 13

FTIR Fourier-Transformed Infrared Resonance. 103, 104

GGA Generalized Gradient Approximation. 7, 31–34, 36, 38, 40, 42

GW single-particle Green functions G multiplied with the screened interaction matrix W. 39, 48, 49, 105

H_2 dihydrogen. 1, 81, 82, 84

Hb hemoglobin. 4

HDNNP High-Dimensional Neural Network Potential. 67, 68, 71, 110–117, 120, 121, 133

HF Hartree-Fock. 19, 21, 22, 24–27, 36, 38, 39, 41, 42, 89, 105–107, 109, 120

HOMO highest occupied molecular orbital. 77, 98

HP hyperparameter. 66

HSE Heyd–Scuseria–Ernzerhof functional. 41–43, 89

HSE03 Heyd–Scuseria–Ernzerhof functional with the cutoff radius at 0.3 Åand 13% of exact exchange. 42, 89

HSE03 Heyd–Scuseria–Ernzerhof functional with the cutoff radius at 0.3 Å. 2, 41, 106–109, 120

HSE06 Heyd–Scuseria–Ernzerhof functional with the cutoff radius at 0.2 Å. 41, 89

hyper-GGA hyper-generalized Gradient Approximation. 33

IDM improved dimer method. 57

IPCC Intergovernmental Panel on Climate Change. 3

KMC kinetic Monte-Carlo. 63, 110

KS Kohn-Sham. 27, 28, 32, 33, 39

LAMMPS Large-scale Atomic/Molecular Massively Parallel Simulator. 133

LDA Local Density Approximation. 6, 30, 31, 33–35, 37, 38, 40, 42

LDOS local Density of States. 1, 87, 101–103

LPT linear response theory. 37

LR long-range. 41, 42, 44

LRT linear response theory. 88, 89

LTMP2 Laplace-transformed second order Møller-Plesset perturbation theory. 23–26, 41, 105–108, 120

LUMO lowest occupied molecular orbital. 77

MD Molecular Dynamics. 1, 2, 57, 65, 111

MEP minimum energy path. 53, 55, 56, 58, 61

meta-GGA meta-generalized Gradient Approximation. 31–33, 35, 36

ML monolayer. 79, 94, 97

MM molecular mechanics. 110, 116

mOS metal oxidation state. 81–90, 92–101, 103, 109, 116

MP Møller-Plesset perturbation theory. 22

MP2 second order Møller-Plesset perturbation theory. 2, 23, 25, 26, 39–41, 44, 49, 105, 107–109, 120

MvK Mars-van Krevelen. 91

N_2O nitrous oxide. 4, 5

NCPP norm-conserving pseudopotential. 48, 49

NEB nudged elastic band method. 53–56, 58

Ni nickel. 1, 2, 76, 99–103, 110, 120

NN Neural Network. 7, 65–67, 69, 71–73, 110–112, 117

NNP Neural Network Potential. 2, 67, 69–71, 73, 116, 120

NP nanoparticle. 64, 75–79, 81, 86, 96, 97, 103, 115–117, 120

O_2 dioxygen. 4, 90, 93–95, 97

OS oxidation state. 1, 81, 84–86, 90, 92, 100, 101, 120

OS dynamics oxidation state dynamics. 1

OSC oxygen storage capacity. 80

PAMSI Phonon-Assisted Metal-Support Interaction. 2, 88–90, 93–95, 98, 99, 101, 103, 109, 117, 120

PAW projector augmented wave. 41, 45, 48, 49

PBC periodic boundary condition. 18, 23, 64

PBE Perdew, Burke and Ernzerhof functional. 31, 34, 35, 40–42, 89, 103

PBE+U Perdew, Burke and Ernzerhof functional equiped with a Hubbard correction. 88, 89, 106, 110

PBE0 PBE0. 40, 42, 43

PBEsol Perdew, Burke and Ernzerhof functional adapted for solids. 34, 35

Pd palladium. 2, 75, 78, 99–104, 120

PES potential energy surface. 15, 25, 50, 52–54, 56–58, 65, 67, 91, 92

pFig. paper figure. 80–82, 85–87, 89, 91, 101, 109

PFR plug flow reactor. 64, 93, 95

PIP permutation invariant polynomia. 68

post-DFT post-processing methods for density functional theory. 7, 38, 49, 89

post-HF postprocessing methods for Hartree-Fock. 7, 25, 49, 105–107

PP pseudopotential. 45, 47, 48

PS pseudo-. 48

pSFig. paper supplementary figure. 83–88, 92, 97

pSTab. paper supplementary table. 89

Pt platinum. 1, 75–77, 79–91, 93, 95, 97–104, 109, 110, 119, 120

QM quantum mechanics. 12, 13, 19, 28

RMS root mean square. 111, 118

RPA Random Phase Approximation. 2, 7, 33, 37–41, 44, 49, 89, 105–109, 120

Ru ruthenium. 75

RXES resonant X-ray emission spectroscopy. 76

SA single-atom. 1, 2, 77, 79–84, 86–91, 93, 95–104, 109, 110, 116, 118–120

SAC single-atom catalyst. 1, 2

SCAN strongly constrained and appropriately normed. 35

SMSI Strong Metal-Support Interactions. 76, 78, 88, 98, 101

SOAP Smooth Overlap of Atomic Positions. 68

SP single-point. 113, 117

SR short-range. 40–42, 117

stochatic MP2 second order Møller-Plesset perturbation theory with stochastic orbitals. 26, 41

SymFunc symmetry function. 68–70, 72, 111–113, 115, 120, 133

SymVec symmetry vector. 70–73, 110

TiO_2 titania. 76, 78

TOF turn-over frequency. 91

tOS total compound oxidation state. 90–95

TS transition state. 61, 91

TST transition state theory. 52, 53, 61, 62

UHV ultra-high vacuum. 76

USA United States of America. 3, 4

USPP ultrasoft pseudopotential. 47–49

VASP Vienna Ab initio simulation package. 7, 18, 47, 48, 50, 52, 60, 104, 105

vdW van der Waals. 44, 71

WGS water-gas shift reaction. 76

xc exchange-correlation. 27, 28, 32–34, 36, 39, 40, 42

XPS X-ray photo-emission spectroscopy. 85, 90

XXMC Exact exchange and compatible correlation. 32

ZORA zeroth order relativistic approximation. 13, 14

ZPE zero-point energy. 15, 93

UNIVERSITAT ROVIRA I VIRGILI
THEORETICAL INVESTIGATIONS INTO SINGLE-ATOM CATALYSTS ON CERIUM DIOXIDE: DEPOSITION AND ACTIVATION.
Nathan Daelman

UNIVERSITAT
ROVIRA i VIRGILI